IntechOpen

Modeling and Simulation for Electric Vehicle Applications

Edited by Mohamed Amine Fakhfakh

MODELING AND SIMULATION FOR ELECTRIC VEHICLE APPLICATIONS

Edited by **Mohamed Amine Fakhfakh**

Modeling and Simulation for Electric Vehicle Applications
http://dx.doi.org/10.5772/61918
Edited by Mohamed Amine Fakhfakh

Contributors

Varga Bogdan Ovidiu, Moldovanu Dan, Mariașiu Florin, Iclodean Călin Doru, Yangang Wang, Muhammad Aziz, Takuya Oda, Pablo Moreno-Torres, Daniel Fodorean, Mahmoud Ghofrani, Marcos Lafoz, Marcos Blanco, Gustavo Navarro, Jorge Torres, Luis García-Tabarés

Notice

First published in Croatia, 2016 by INTECH d.o.o.
eBook (PDF) Published by IN TECH d.o.o.
Place and year of publication of eBook (PDF): Rijeka, 2019.
IntechOpen is the global imprint of IN TECH d.o.o.
Printed in Croatia

Legal deposit, Croatia: National and University Library in Zagreb

Additional hard and PDF copies can be obtained from orders@intechopen.com

Modeling and Simulation for Electric Vehicle Applications
Edited by Mohamed Amine Fakhfakh

p. cm.

Print ISBN 978-953-51-2636-2

Online ISBN 978-953-51-2637-9

eBook (PDF) ISBN 978-953-51-6678-8

Meet the editor

Mohamed Amine Fakhfakh was born in Sfax, Tunisia, in 1981. He received the Electrical Engineering degree from the Ecole National d'Ingenieur de Sfax (ENIS), in 2005, the Electronic Master degree from the ENIS, in 2006, and the PhD degree in electrical engineering from the ENIS, in 2011. he joined the Higher Institute of Applied Science and Technology of Gafsa, Tunisia, In 2011, where he is an assistant professor. His current research interests are power semiconductor device modeling, the electrothermal modelization, power electronic applications to electrical vehicles,and renewable energy. He is a member of the organizing and reviewing committees of several conferences.

Contents

Preface

Due to pollution, greenhouse gases, and the depletion of fossil fuel resources, electric vehicles (EVs) are increasingly used because they use electricity as an energy source. EVs are divided into three categories: the pure EV, the hybrid EV, and the fuel cell EV. Although these three types of electric vehicle have different system configuration, one (or more) motor drive system is always needed to convert electrical power into mechanical ones. Among the drive systems used for EV, induction motor system and permanent magnet motor system are mostly used for their high power density and high efficiency.

Nowadays, industry and academic research seek to overcome the obstacles that block the widespread use of electric vehicles, such as life, energy density, power density, and weight and cost of batteries. For this, there is a great demand for knowledge to model and optimize electric vehicles.

This book consists of seven chapters written by leading researchers and professionals from industry and academia. It presents interesting topics from the area of modeling and simulation of electric vehicles.

Chapter 1 explains all the necessary steps to create a model of electric vehicle and run it in IPG Car Maker simulator.

Chapter 2 discusses the importance and functionality of power electronics and module in HEV/EV power train system and summarized the performance requirements by automotive industry.

Chapter 3 presents the importance to study the magnetic field when designing electric vehicles and their components.

Chapter 4 proves the advantage of using magnetic gears (MGs) for transportation applications. It presents a state-of-the-art on the available MGs, with fixed or variable transmission ratio, pointing out their applicability.

Chapter 5 analyses the switched reluctance drives for traction applications and focusing on their capability to operate in degraded mode.

Chapter 6 discusses the enhanced utilization of EVs and their used batteries to participate in ancillary service to support the electricity, especially in a small-scale EMS.

Chapter 7 outlines the means of electrical vehicle to smart grid interactions and how attaining a synergistic relationship is vital for improving the way power is distributed.

This book will be useful for students of Electrical Engineering; it will help them solve practical problems.

Finally, I thank everyone who has contributed to this book. All the results of your work will be useful for a lot of readers.

Dr. Mohamed Amine Fakhfakh
Electrical Engineering Department,
University of Sfax,
Tunisia

Chapter 1

Simulation in the Loop of Electric Vehicles

Bogdan Ovidiu Varga, Dan Moldovanu,
Florin Mariaşiu and Călin Doru Iclodean

Additional information is available at the end of the chapter

http://dx.doi.org/10.5772/64295

Abstract

The objective of this chapter is to underline the importance of pre-production and prototyping simulation in the loop of electric vehicles, by considering as many vehicle characteristics as possible. Basic simulations were made, using IPG CarMaker, to simulate electric vehicles with different properties for batteries, transmission, electric motors, aerodynamics of the vehicle, and most importantly, driver properties. This chapter also explains all the necessary steps to create a model and run it in IPG CarMaker, including data exports, so that the results could be reproduced easily. This chapter underlines the importance of batteries and answers the questions: what is the correct number of batteries that a vehicle must equip in order to have a bigger range? Basically, one should carry more batteries that add weight but at what range in price.

Keywords: electric vehicles, battery size, simulation in the loop, IPG CarMaker

1. Introduction

IPG CarMaker is a simulation environment used to simulate a computer representation of a real vehicle with the behaviour matching the real vehicle. In this environment, the user creates the vehicle using mathematical models that contain equations of motion kinematics, but also a multi-body definition of the system. The parameters are modified in accordance with the real vehicle to be studied [1].

IPG CarMaker is also used for other purposes than just pure simulation, which are as follows: it is coupled with MATLAB in order to implement new algorithms, for example vehicle state estimation using an integrated Kalman filter scheme for vehicle dynamics estimation (side slip) [2]; it is used as model-predicting control for fuel consumption optimization of a range

extender for a hybrid vehicle architecture (state of charge trajectory estimation) [3]; it is used as a validation of a controller for variable steering ratio of a front steering system, tested on a virtual road for driving comfort improvement [4]; it is used for solving challenging problems such as wheel slip control for electric powertrain vehicles, for anti-lock brake and traction control functional validation (hardware-in-the-loop (HIL) using IPG CarMaker coupled with dSPACE) [5] and complex hardware-in-the-loop system (MATLAB Simulink model coupled with IPG CarMaker multibody vehicle model, dSPACE electronic control unit, and a real friction brake unit) for brake friction optimization and lower energy consumption [6].

Using this knowledge, it is possible to simulate any vehicle in IPG CarMaker, as long as the user knows all the necessary data. The same behaviour can be simulated for any vehicle, on the same road, with the same manoeuvres, just by changing the vehicle properties. The vehicle contains all components from the real vehicle, such as powertrain, chassis, tires, brakes, but also controllers, such as ABS (Anti-Lock Braking System), ESP (Electronic Stability Program), ACC (Adaptive Cruise Control), or other user-modelled systems.

After defining the virtual vehicle, the user must characterize the road, that is a digitized or computer-modelled representation of the real road (usual road, track, or course), which simulates the road and it is generated for testing. CarMaker can generate the road using the following two methods:

- An easy method that combines individual road segments, such as straights and curves, to form a continuous road, where all the parameters interconnect. For each segment, the user can define all the data such as angle, slope, pitch, friction coefficient, length, and width.
- The second method involves an existing road file (already digitized data), generated by a direct measurement from a GPS device, Google Earth, or other. The file can be opened by CarMaker and used as the road or track during simulation.

The third step is defining the virtual driver, which simulates the actions of a real driver. All the parameters would normally be controlled by a real driver, such as turning/steering or operating the gas, brake and clutch pedals, shifting gears (for manual transmission). For the virtual driver, there are two approaches in CarMaker:

- A simply controlled driver, for which the user can specify at each step what the virtual driver should do.
- An IPG driver, a smart-controlled driver, which tries to maintain the given trajectory and operate within specified limits. As an example, the reaction time can be modified.

Altogether, the virtual vehicle, the virtual driver, and the virtual road form the virtual vehicle environment.

CarMaker also has the CIT (CarMaker interface toolbox) that consists of a number of tools that run on a host computer, namely:

- IPG control—it is a visualization and analysis tool that can monitor quantities in real-time, load post-simulation data, plot, and export results;

http://dx.doi.org/10.5772/64295

- CarMaker GUI—it is a main graphical user interface that controls the virtual vehicle environment, where the user can select all the virtual parameters (virtual vehicle, virtual road, virtual driver parameters, load manoeuvres);
- Vehicle data set editor—it allows the user to control and modify all the parameters of the vehicle;
- IPGMovie—it shows a real-time 3D animation of the vehicle performing the desired manoeuvres on the specified road;
- Instrumentsit shows the important instruments like dials, and information about driving conditions such as position on the pedals, ABS warning lamp, brake light and others;
- Direct variable access (DVA)—allows the simulation quantities to be viewed and modified interactively;
- ScriptControl—it is a test automation utility that allows scripts to be defined, edited, and executed. All the functions of the CIT can be controlled automatically using ScriptControl;
- TestManager—it is another utility for test automation. A mixture of script and GUI-based creation and execution of test series.

The vehicle that was chosen for the simulation is a Tesla Model S because it is an electric car with a good range (currently using an 85-kWh battery, from which a range of 426 km can be achieved and an energy consumption of 237.5 Wh/km) [7].

2. Creating a simulation

Creating a simulation involves using the CIT to create the desired model of the real situation that needs to be simulated, choosing the vehicle (with all its properties), the driver, the road, the manoeuvres and the load (**Figure 1**).

Figure 1. IPG CarMaker main window.

Before actually starting the simulation, the Instruments window should be activated (**Figure 2**), the IPGMovie window to visualize the status in real time (or faster) and more importantly (**Figure 3**), and the IPG Control Data window to observe the evolution of certain parameters and save results.

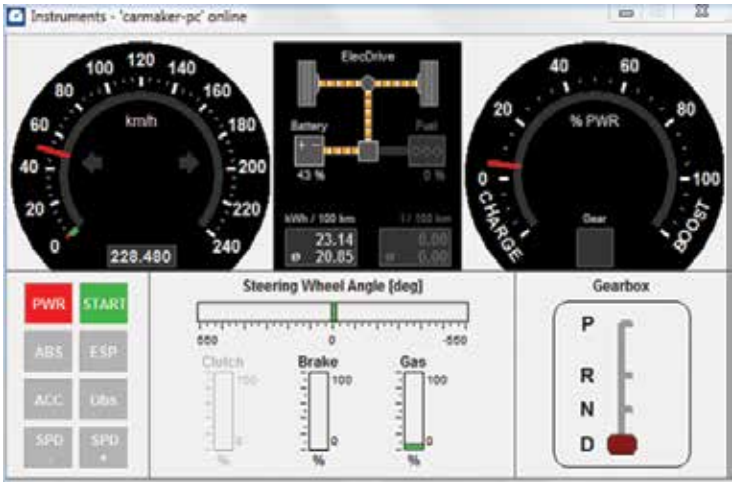

Figure 2. Instruments window—IPG CarMaker.

Figure 3. IPGMovie window.

In order to emphasize the influence of the battery on the E-motor power consumption, several simulations were made where the variables are the battery pack power, which leads to a different current, but the same voltage, and most importantly a different mass, as given in **Table 1**.

Properties/battery	Battery 1	Battery 2	Battery 3
Power [kW]	85	51	25.5
Current [Ah]	210	127.5	63.7
Voltage [V]	400	400	400
Mass of the vehicle [kg]	2108	1842	1770
Energy [MJ]	302	184	92

Table 1. Properties of the used batteries.

Also, to monitor the energy consumption and the current on the same vehicle with the same load, a different state of charge was used for each battery pack.

When creating a desired vehicle in IPG CarMaker, several sets of data must be set so that the simulation is as close as possible to the real vehicle, with as few approximations as possible.

Figure 4 shows the vehicle body in the vehicle data set: in this, a flexible body is used, where the masses of the two bodies are introduced and placed in an x-y-z coordinate system. The joint is also defined, which implies that the properties of the stiffness (torsion and bending), damping and occurring amplifications must be defined as well.

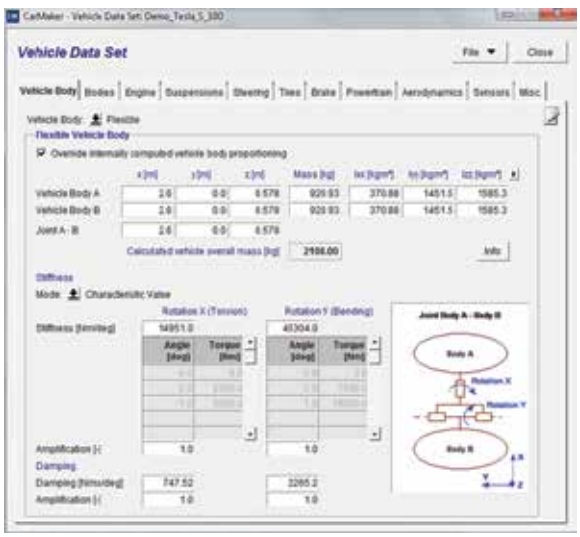

Figure 4. Vehicle data set—vehicle body menu.

After the properties of the vehicle body are done, the next required input is the vehicle bodies (**Figure 5**), where the required fields are moments of inertia for all wheel carriers, for all the wheels, placements of the wheels, hitch position if required and, if any, trim loads. In this case, there are no trim loads.

Figure 5. Vehicle data set—bodies menu.

Since it is an electric car, no internal combustion engine was input (**Figure 6**). This feature can be used if the simulation requires a hybrid vehicle or a classic vehicle.

Figure 6. Vehicle data set—engine menu.

http://dx.doi.org/10.5772/64295

When simulating an electric vehicle, after introducing the required data for suspension, steering, tires, and brakes, the powertrain data are extremely important: in the general submenu, the number of electric motors is selected—in this case, one electric motor (**Figure 7**).

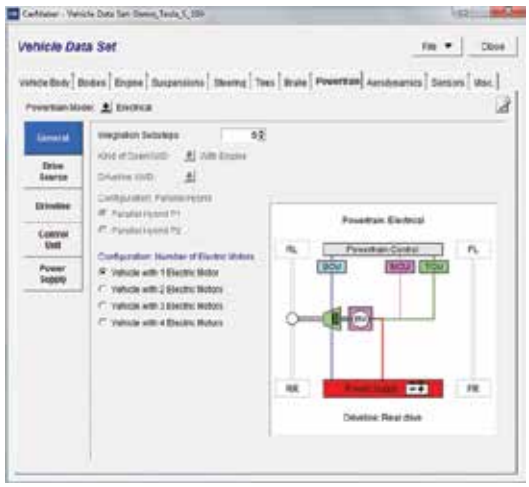

Figure 7. Vehicle data set—powertrain—general menu.

In the second submenu, drive source, the general data are introduced such as moment of inertia for the electric motor, ratio, build-up time, friction coefficient, and voltage level (**Figure 8**), but also the torque (as a characteristic value) for both cases of the electric motor (motor or generator), as shown in **Figure 9**, and the efficiencies of the electric motor in both cases (**Figure 10**).

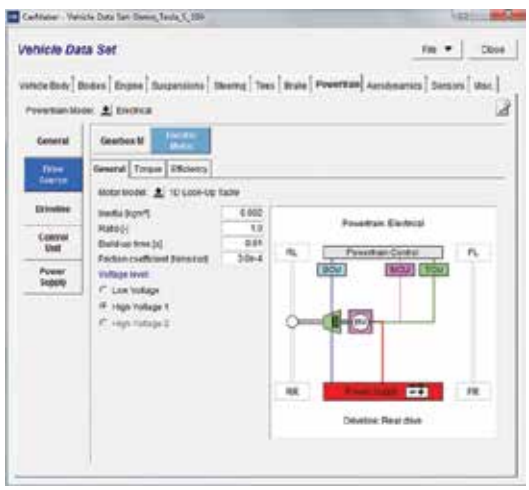

Figure 8. Vehicle data set—powertrain—drive source—general menu.

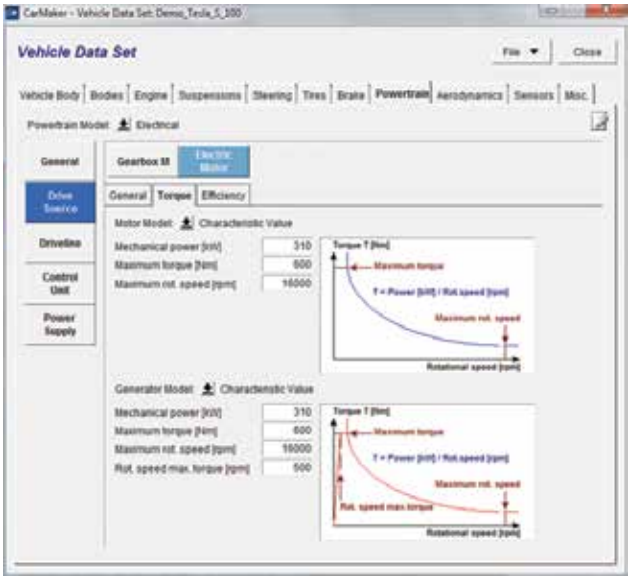

Figure 9. Vehicle data set—powertrain—drive source—torque menu.

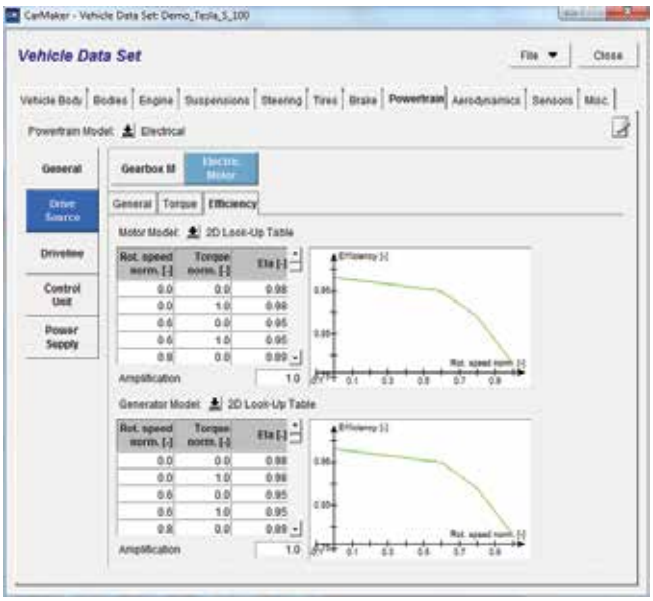

Figure 10. Vehicle data set—powertrain—drive source—efficiency menu.

The next input is the driveline: the rear drive option was selected by this, with no external torque (**Figure 11**), because it is not the case since there is no external torque to the differential or wheels.

http://dx.doi.org/10.5772/64295

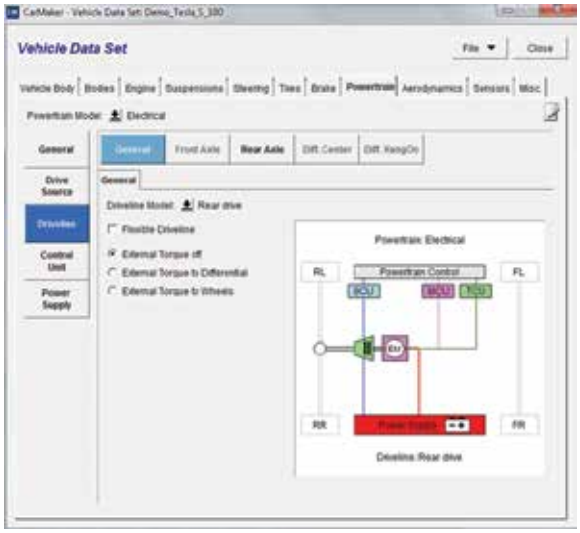

Figure 11. Vehicle data set—powertrain—driveline menu.

For the control unit, first the powertrain control is set to electrical, the engine start with button and not key, and the desired input for the body control unit (BCU), motor control unit (MCU), and traction control unit (TCU), as shown in **Figure 12**.

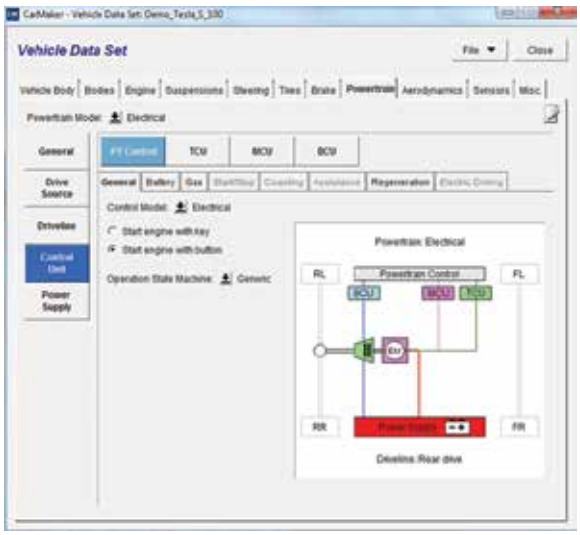

Figure 12. Vehicle data set—powertrain—control unit menu.

For the electric vehicle, the power supply is of most importance: low voltage, high voltage or both low voltage and high voltage can be selected; in this case, low and high voltages were selected with no auxiliary consumer for neither low nor high voltage (**Figure 13**).

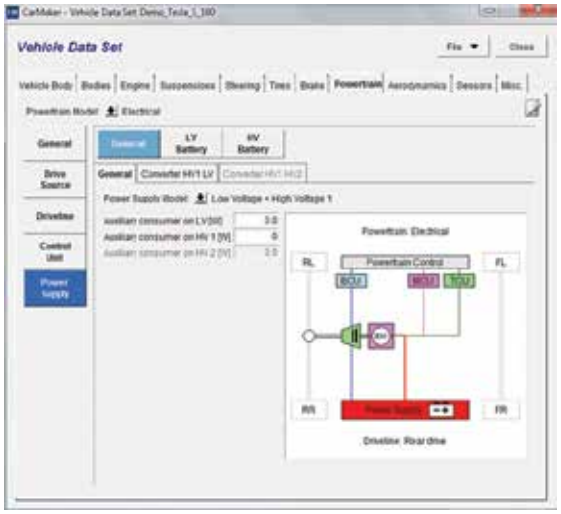

Figure 13. Vehicle data set—powertrain—power supply—general menu.

In the low voltage set-up menu, the main data regarding the LV battery can be introduced, such as capacity, idle voltage, initial state of charge (ISOC), minimum and maximum state of charge, capacities and resistances of the battery (**Figure 14**).

For the high-voltage battery, the current state (as on the real vehicle) is inserted, a battery with the capacity of 210 Ah, 85 kW of power, idle voltage of 400 V, and the specific resistances and capacities of the battery (**Figure 15**).

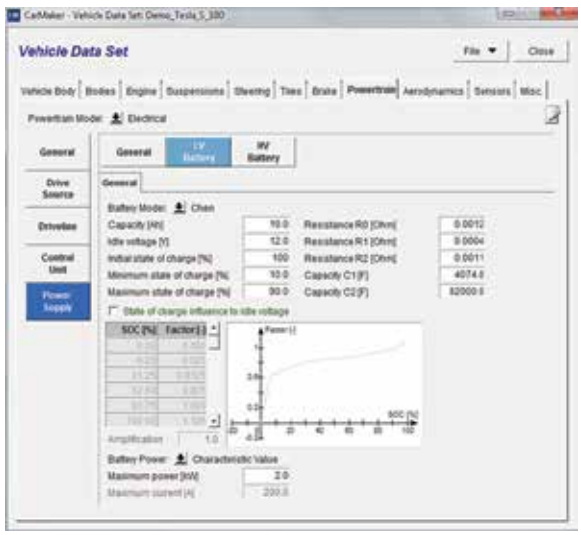

Figure 14. Input data for the low-voltage battery.

http://dx.doi.org/10.5772/64295

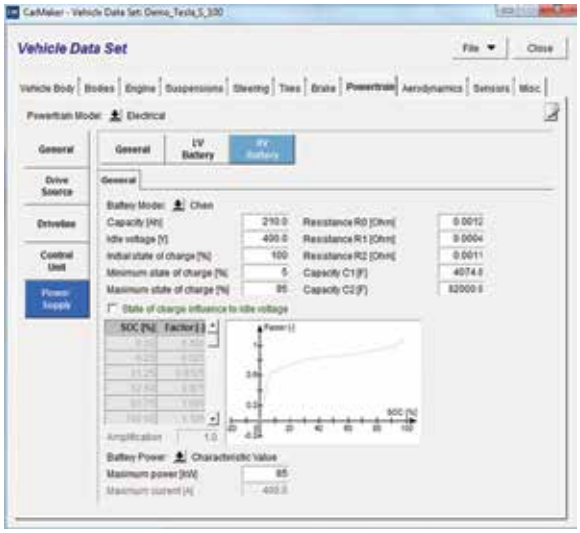

Figure 15. High-voltage battery input data.

In the miscellaneous menu, the vehicle graphics and the movie geometry (in order to create a proper video in real time of the desired vehicle: Tesla Model S) were selected (**Figure 16**).

After the vehicle is ready, the input for the road follows (**Figure 17**) where the driver must maintain a constant speed and the manoeuvres are just to follow the given road.

Figure 16. Miscellaneous input for the Tesla Model S model.

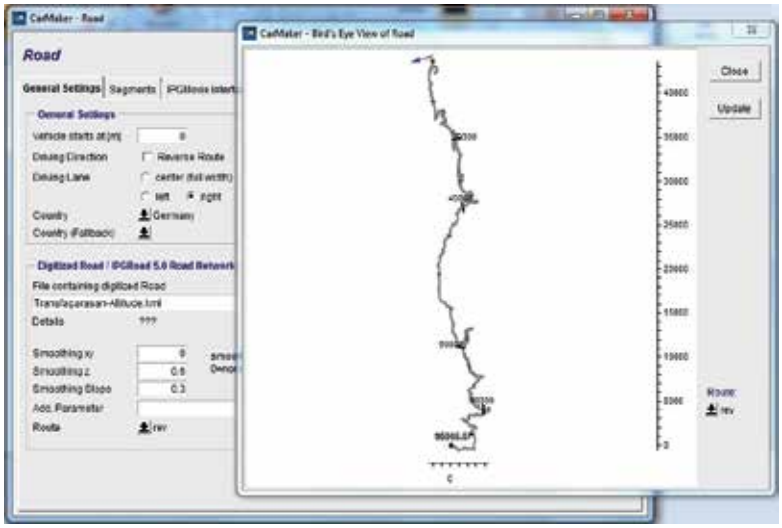

Figure 17. Road generated for the simulation.

3. Simulation cases

In order to underline the range of a specific electric vehicle, the Tesla Model S, the initial case starts with a fully loaded battery, so initial state of charge is set to 100%. In other cases, an ISOC of 60 and 30% was considered, as shown in **Table 2**.

Case/properties	Battery power [kW]	Battery state of charge [%]	Mass of the vehicle [kg]
Case 1	85	100	2108
Case 2	85	60	2108
Case 3	85	30	2108
Case 4	51	100	1892
Case 5	51	60	1892
Case 6	51	30	1892
Case 7	25.5	100	1770
Case 8	25.5	60	1770
Case 9	25.5	30	1770

Table 2. Simulation cases.

After creating the Case 1 Model, the simulation is started, and the results of the battery current and energy can be monitored in the DataWindow (**Figure 18**). After the vehicle stops, the

http://dx.doi.org/10.5772/64295

distance is recorded and the state of charge of the battery is changed (**Figure 19**), with new results (**Figure 20**) and the same is done for case 3 (**Figure 21**).

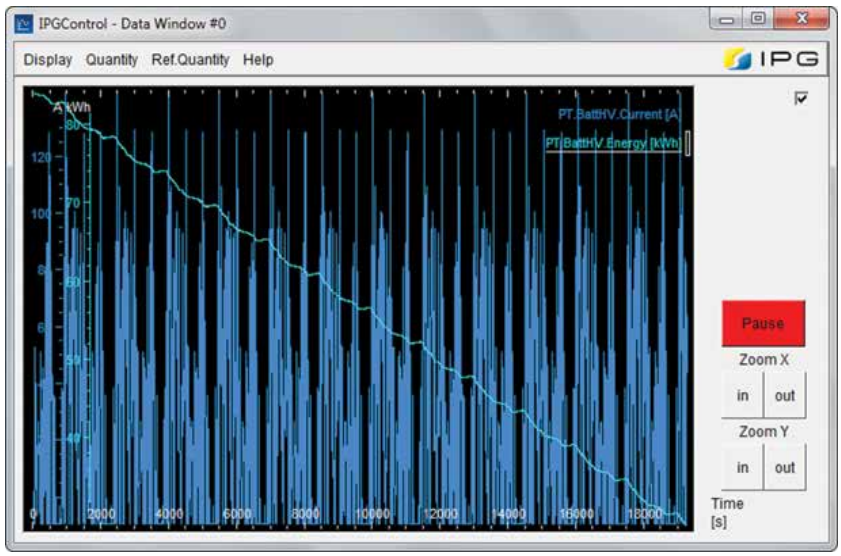

Figure 18. Battery current and energy monitored in the DataWindow, for Case 1.

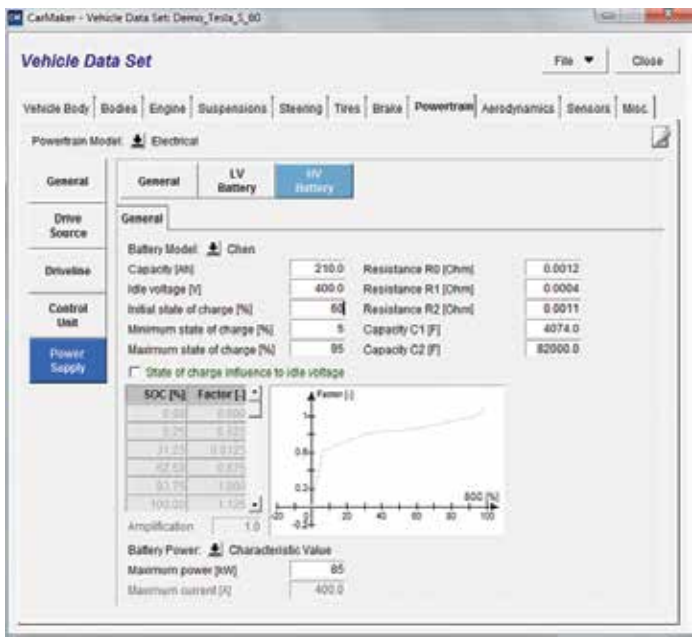

Figure 19. Changing the SOC of the high-voltage battery to 60%.

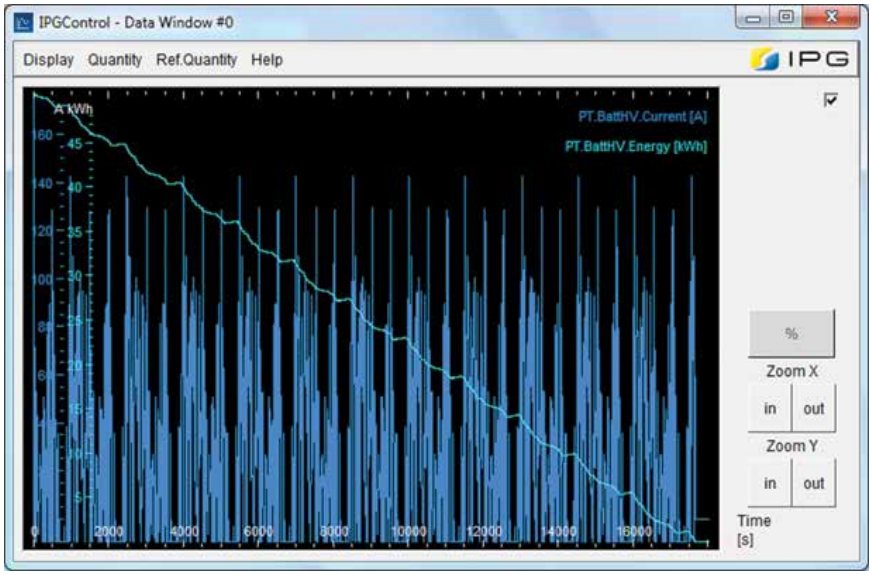

Figure 20. Battery current and energy monitored in the DataWindow, for Case 2.

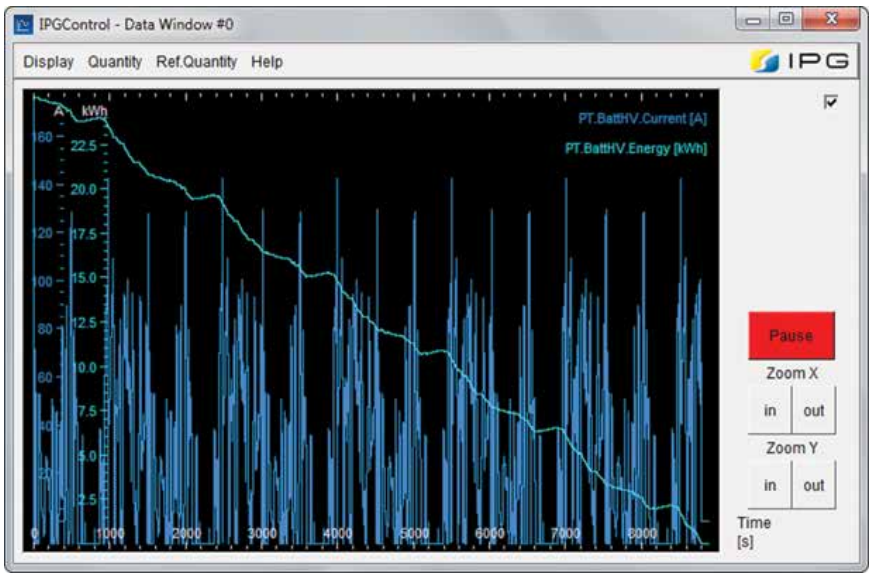

Figure 21. Battery current and energy monitored in the DataWindow, for Case 3.

In order to change the data for Cases 4–6, the mass of the vehicle bodies was modified so that the total mass of the vehicle is correct for these cases (1892 kg) as shown in **Figure 22**, but also the maximum power was reduced to 51 kW (**Figure 23**), with results shown in **Figure 24** (Case 4), **Figure 25** (Case 5), and **Figure 26** (Case 6).

http://dx.doi.org/10.5772/64295

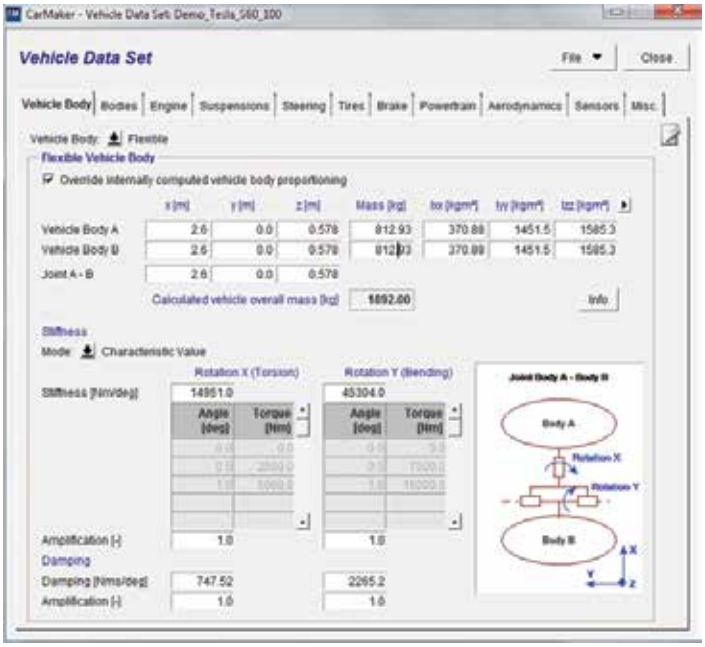

Figure 22. Vehicle bodies change for Cases 4 to 6.

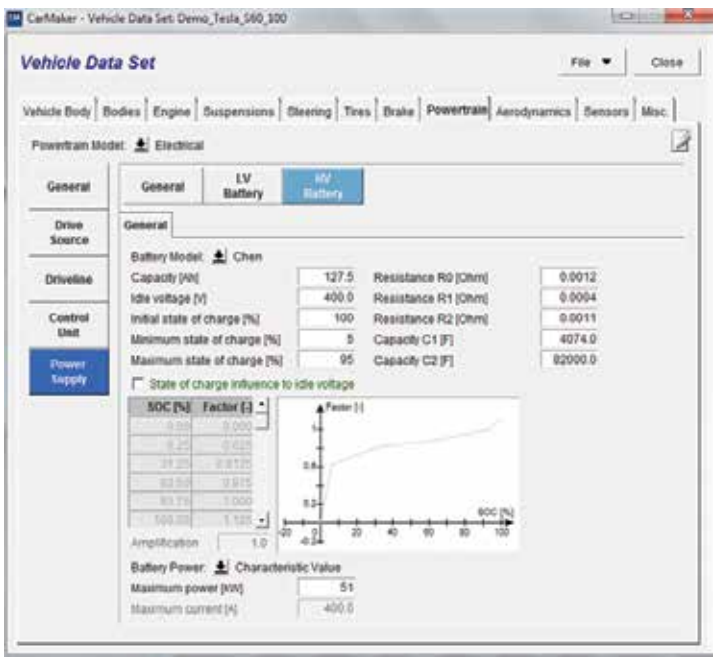

Figure 23. High-voltage battery properties for Case 4.

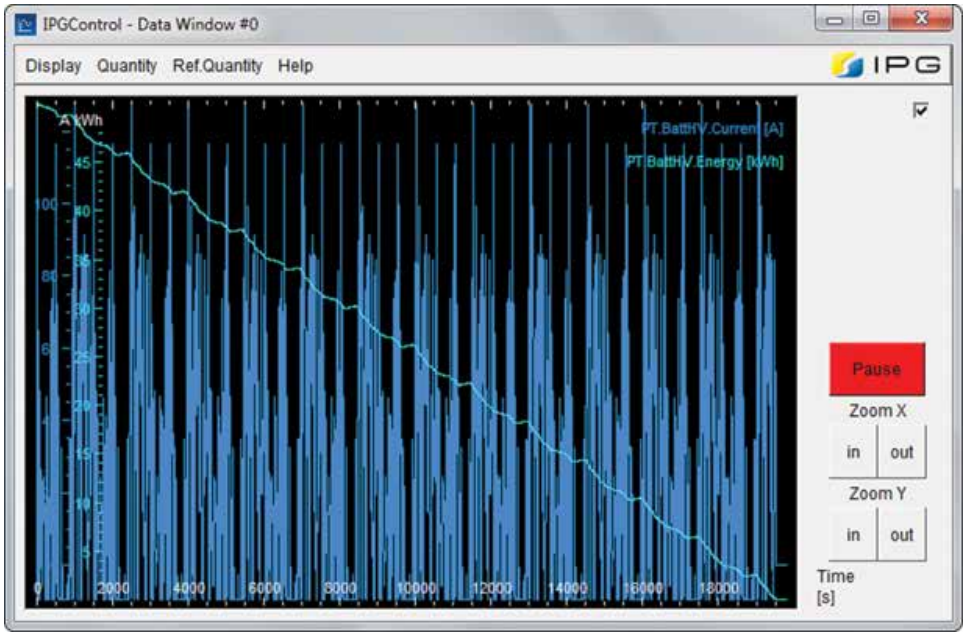

Figure 24. Battery current and energy monitored in the DataWindow, for Case 4.

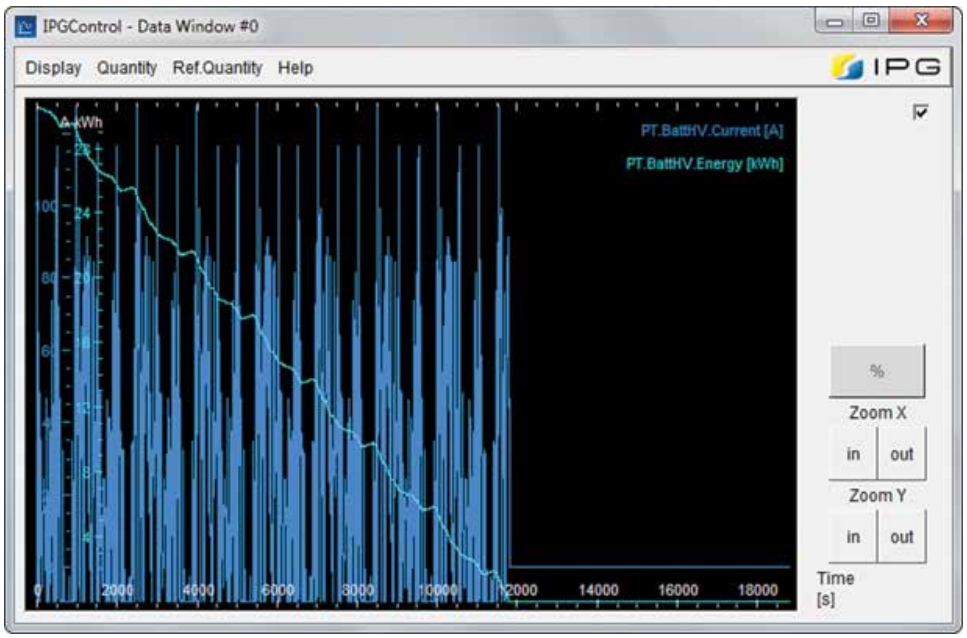

Figure 25. Battery current and energy monitored in the DataWindow, for Case 5.

http://dx.doi.org/10.5772/64295

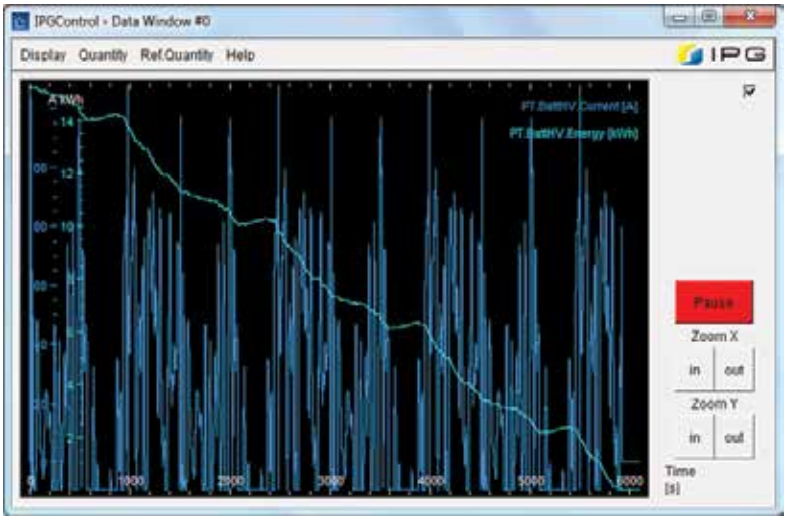

Figure 26. Battery current and energy monitored in the DataWindow, for Case 6.

For Cases 7–9, the mass of the vehicle bodies was modified so that the total mass of the vehicle is correct (1770 kg) as shown in **Figure 27**, but also the maximum power was reduced to 25.5 kW (**Figure 28**), with results shown in **Figure 29** (Case 7), **Figure 30** (Case 8), and **Figure 31** (Case 9).

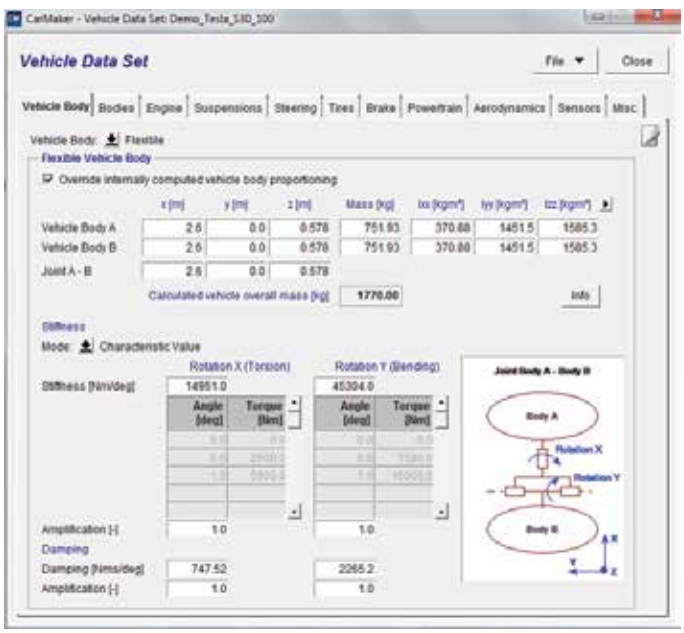

Figure 27. Vehicle bodies change for Cases 7 to 9.

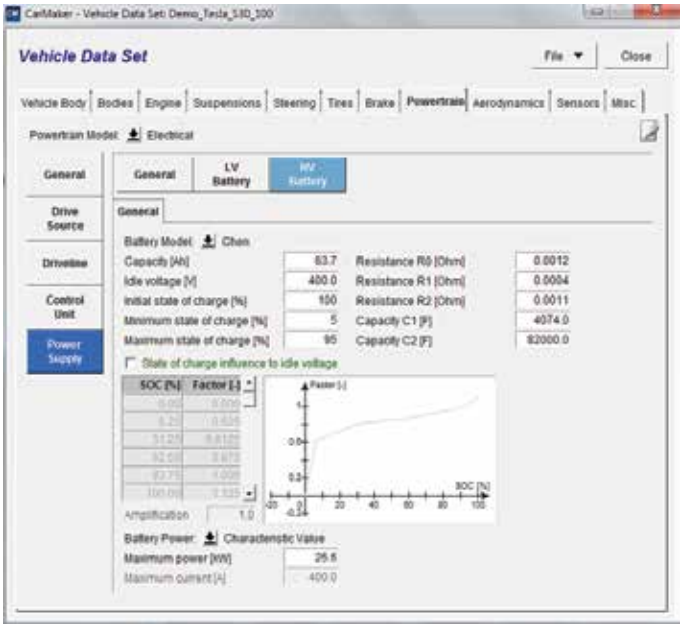

Figure 28. High-voltage battery properties for Case 7.

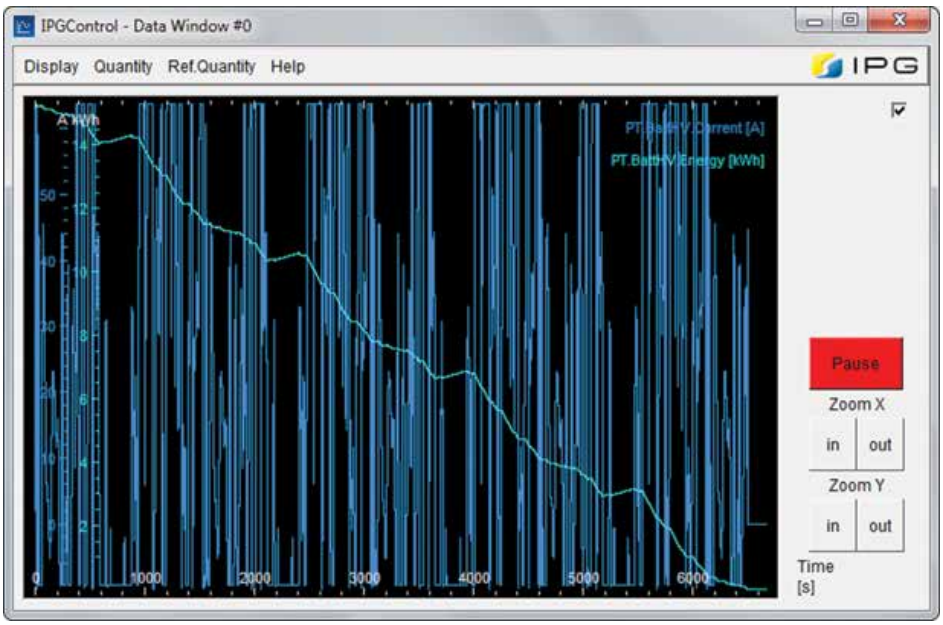

Figure 29. Battery current and energy monitored in the DataWindow, for Case 7.

http://dx.doi.org/10.5772/64295

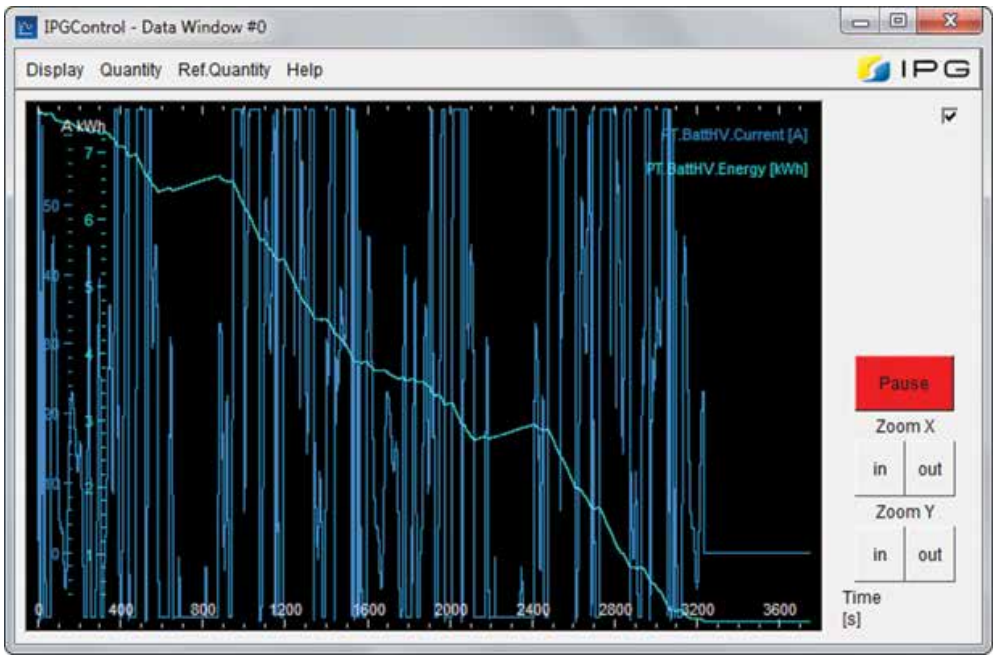

Figure 30. Battery current and energy monitored in the DataWindow, for Case 8.

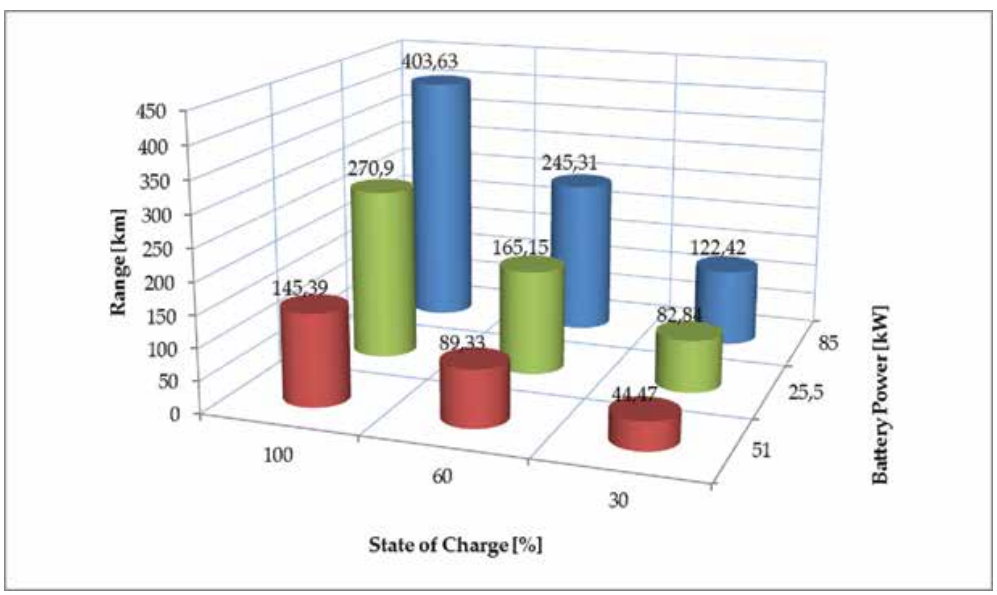

Figure 31. Range results for all simulation cases.

4. Results

After each simulation, the range was recorded, and the battery current and energy were monitored via DataWindow. All data from the DataWindow can be exported as separate files and evaluated.

The results regarding the range are presented in **Table 3**, and as a graph in **Figure 31**.

	Battery power [kW]	State of charge [%]	Range [km]
Case 1	85	100	403.63
Case 2	85	60	245.31
Case 3	85	30	122.42
Case 4	51	100	270.9
Case 5	51	60	165.15
Case 6	51	30	82.84
Case 7	25,5	100	145.39
Case 8	25,5	60	89.33
Case 9	25,5	30	44.47

Table 3. Range results for all simulations.

In order to see how these results were obtained, the energy consumption has to be monitored:

- Energy consumption for all SOC with the 25.5-kW battery (**Figure 32**);
- Energy consumption for 30% SOC with all batteries (**Figure 33**).

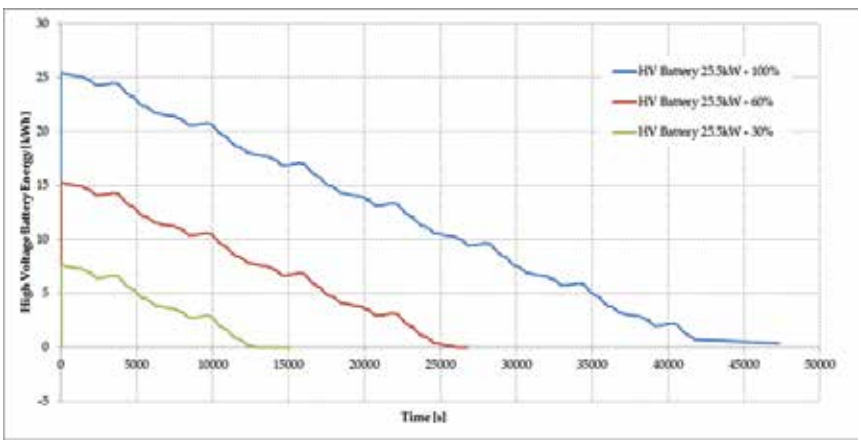

Figure 32. Energy consumption for all SOC with the 25.5-kW battery.

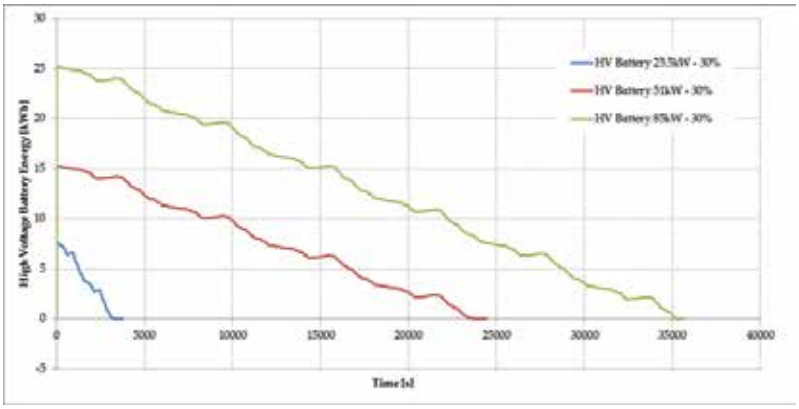

Figure 33. Energy consumption for 30% SOC with all batteries.

5. Conclusion

IPG CarMaker is a powerful simulation tool that can estimate, due to its complexity and number of input factors, output values very close to reality; just as in Case 1, where the maximum range of the Tesla Model S is 403.63 km, close to the specifications of the producer [7].

It can be seen in the simulations that the range of the vehicle increases with the state of charge of the battery; when the power of the battery is decreased, the range decreases because of the lower power, but also increases due to the lower weight of the vehicle; overall, the range decreases.

When analysing **Figure 33**, the energy of the batteries has similar slopes for the 85 and 51 kW batteries, but the slope for the smallest battery, 25.5 kW is more abrupt, decreasing fast in comparison to the others.

The answer to the initial question—what is the correct number of batteries that a vehicle must equip in order to have a bigger range—is as many as possible, limited by the final price of the vehicle, even though the tendencies in the batteries domain are to reduce the weight as much as possible and store as much energy as possible.

IPG CarMaker is a SIL (simulation in the loop) software that takes into account all reactions from the road and from the transmission and adapts the driver behaviour.

By connecting it to a real engine testbed or powertrain testbed, the IPG CarMaker can be transformed into a HIL (hardware-in-the-loop) simulation, where the behaviour of the real engine is controlled by the virtual driver, on the virtual road, from the virtual vehicle and the response of the load is controlled by adjusting the dynamometer load.

Author details

Bogdan Ovidiu Varga*, Dan Moldovanu, Florin Mariaşiu and Călin Doru Iclodean

*Address all correspondence to: bogdan.varga@auto.utcluj.ro

Automotive Engineering and Transport Department, Faculty of Mechanics, Technical University of Cluj-Napoca, Cluj-Napoca, Romania

References

[1] Bogdan Ovidiu Varga, Florin Mariasiu, Dan Moldovanu, Calin Iclodean. Electric and Plug-In Hybrid Vehicles: Advanced Simulation Methodologies. 1st ed. Springer; 2015. pp. 524 p. doi:10.1007/978–3–319–18639–9, http://link.springer.com/book/10.1007/978–3–319–18639–9.

[2] King Tin Leunga, James F. Whidbornea, David Purdyb, Phil Barberc. Road vehicle state estimation using low-cost GPS/INS. Mechanical Systems and Signal Processing. 2011;25(6):1988–2004. doi:10.1016/j.ymssp.2010.08.003

[3] Daliang Shen, Valerie Bensch, Steffen Miiller. Model predictive energy management for a range extender hybrid vehicle using map information. IFAC-PapersOnLine. 2015;48(15):263–270. doi:10.1016/j.ifacol.2015.10.038

[4] Zhenhai Gaoa, Jun Wanga, Deping Wangb. Dynamic modeling and steering performance analysis of active front steering system. Procedia Engineering. 2011;15(1):1030–1035. doi:10.1016/j.proeng.2011.08.190

[5] Valentin Ivanova, Dzmitry Savitskia, Klaus Augsburga, Phil Barberb, Bernhard Knauderc, Josef Zehetnerc. Wheel slip control for all-wheel drive electric vehicle with compensation of road disturbances. Journal of Terramechanics. 2015;61(4):1–10. doi: 10.1016/j.jterra.2015.06.005

[6] Barys Shyrokaua, Danwei Wangb, Dzmitry Savitskic, Kristian Hoeppingc, Valentin Ivanovc. Vehicle motion control with subsystem prioritization. Mechatronics. 2015;30(1):297–315. doi:10.1016/j.mechatronics.2014.11.004

[7] Tesla Motors. Tesla Model S Specifications [Internet]. Available from: https://www.teslamotors.com/support/model-s-specifications [Accessed: 23.03.2016]

Chapter 2

Status and Trend of Power Semiconductor Module Packaging for Electric Vehicles

Yangang Wang, Xiaoping Dai, Guoyou Liu,
Yibo Wu, Yun Li and Steve Jones

Additional information is available at the end of the chapter

http://dx.doi.org/10.5772/64173

Abstract

Power semiconductor modules are the core components in power-train system of hybrid and electric vehicles (HEV/EV). With the global interests and efforts to popularize HEV/EV, automotive module has become one of the fast growing sectors of power semiconductor industry. However, the comprehensive requirements in power, frequency, efficiency, robustness, reliability, weight, volume, and cost of automotive module are stringent than industrial products due to extremely high standards of vehicle safety and harsh environment. The development of automotive power module is facing comprehensive challenges in designing of structure, material, and assembly technology. In this chapter, the status and trend of power semiconductor module packaging for HEV/EV are investigated. Firstly, the functionality of power electronics and module in HEV/EV power-train system, as well as the performance requirements by automotive industry, is addressed. A general overview of HEV/EV module design and manufacturing is discussed. Then, the typical state-of-the-art commercial and custom HEV/EV power modules are reviewed and evaluated. Lastly, the packaging trends of automotive module are investigated. The advanced assembly concept and technology are beneficial to thermal management, minimized parasitic parameters, enhancement of thermal and mechanical reliability, and the reduction of weight, volume, and cost.

Keywords: hybrid and electric vehicles, insulated gate bipolar transistor, packaging, power module, reliability

1. Introduction

During the last few decades, people have made great efforts on exploiting sustainable and clean energy to mitigate the global crisis of fossil energy and deterioration of environment. Accordingly, the application systems powered by new and clean energy are developed with high interests. One of the crucial systems is hybrid and electric vehicles (HEV/EVs), which rely fully or partly on electricity which transformed from renewable and clean energy such as solar, wind, and nuclear powers. Therefore, HEV/EV is regarded as environmental-friendly product for the reduction of CO_2 and noise remarkably. Furthermore, the development of HEV/EV is becoming a main policy of most governments and automotive industry, leading to worldwide extensive research and development [1].

Performance		Temp	Reliability	Efficiency	Size/weight	Cost
Power device	High T_{jmax}	√	√		√	√
	Low loss	√	√	√	√	√
Module packaging	Low R_{th}	√	√		√	
	Low R, L	√	√	√		
	No base	√			√	√
	Direct cooling	√	√		√	
	Planar contact	√	√	√	√	
	Ultrasonic welding		√			
	New interconnection	√	√			
	New housing	√	√		√	

Table 1. Dependence of IGBT module performance on power device and assembly.

HEV has dual power sources of internal combustion engine and electric motor, while EV uses electric motor to power only. In both cases, the electric motor is essential to the systems. The motor, on the other hand, acts as a generator for regenerative breaking. The importance of motor in HEV/EV results in high-level significance of power-train system of which the main element is DV/AC inverter. The inverter controls power conversion from battery to motor by power semiconductor devices. Therefore, the core component in the power system of HEV/EV is power semiconductor switches, which are normally insulated gate bipolar transistor (IGBT) and free-wheeling diode (FWD) at the moment [2]. For increasing power, reliability, and prolonging lifetime, IGBT and FWD chips are packaged to module with multiple devices, isolation layer, and protection parts [2–9].

The great interest of developing HEV/EV across the world has motivated massive effort on improving and optimizing automotive modules. These modules always work in harsh environment of high temperature, humidity, mechanical vibration, and shock, and the possibility of chemical contamination. As limited by the space and weight in HEV/EV system,

http://dx.doi.org/10.5772/64173

the module and inverter system should have light and compact packaging. Hence, for driving and controlling HEV/EV efficiently, IGBT modules with high power, efficiency, reliability, light weight, and small size are required, which result in huge challenges to power device and packaging technologies [9, 10–13]. The power module overall performances are determined to a large extent by the electrical, thermal, and mechanical characteristics of both power chips and the way of chips packaging. **Table 1** shows the dependence of IGBT module performance on power device itself and the assembly technologies.

To meet the series of challenges as mentioned above to automotive module packaging, power semiconductor and automotive industries are developing automotive-qualified power chip and module. The advanced power device could not guarantee superior output from a power module, and much of the harsh requirements from HEV/EV systems can be satisfied by the optimized packaging concepts, structures, materials, and technologies together with novel power devices [14, 15]. In this work, the status and trend of power semiconductor module packaging for HEV/EV are investigated. Section 2 addresses the functionality and requirements of power electronics and module in HEV/EV system. A general overview of HEV/EV module design in terms of structure, material, and packaging technologies is discussed in Section 3. In Section 4, the typical state-of-the-art commercial and custom HEV/EV power modules are reviewed and evaluated. The packaging trends of automotive power module are investigated in Section 5.

2. Power semiconductor module in HEV/EV

It is expected that the HEV/EV will be one of the strong growth points for automotive industry in the next few decades with the improvement of performance, evolvement of technologies, and reduction of cost of ownership [1]. **Figure 1** shows the annual light-duty vehicle sales prediction by technology type. Based on Energy Technology Perspectives forecast, EV, Plug-in HEV (PHEV), and HEV will reach sales of 2.5, 5.0, and 10.0 M, respectively, per year by 2020, making the total sales of low carbon vehicles about 18% of the annual sales. By 2030, EV, PHEV, and HEV are expected to sell 9, 25, and 26 M units, respectively, corresponding to 50% of annual automotive market. And by 2050, sales of all kinds of low carbon vehicles will occupy more than 80% of the whole automotive sales [1]. Yole Development suggests that about 25 M cars manufactured will be electrified in 2016, with the majority of them being micro-HEV with low level of electrification, and 5 M will be full HEV, PHEV or EV [16].

With rapid ramp-up sales of HEV/EV in the last decade, power semiconductor industry has seen huge opportunity of power components and system supply. DC/AC inverter market will grow from $45 bn in 2012 to $71 bn in 2020 with more than 28 M units of 2012 and 80 M in 2020 [17]. HEV/EV represents one of the biggest markets for power device and system manufacturers together with the other most attractive motion and conversion applications of photovoltaics (PVs), wind turbines, rail traction, motor drives, and uninterruptible power supplies (UPSs) [17].

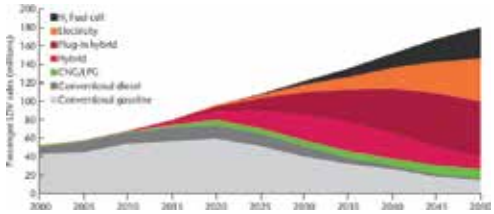

Figure 1. Annual light-duty vehicle sales by technology type, source: IEA 2010.

Power electronics is one of the essential technologies in HEV/EV research and development. The electricity for driving HEV/EV from grid is needed to be converted a few times before reaching electric motor and accessory appliances. These procedures are controlled by power electronic systems of which the main components are power IGBT modules [4, 5, 9]. **Figure 2** shows the schematic of power-train system in the EV showing the power control systems of converters and inverters. For HEV, the battery could be charged by both the electric grid and the internal combustion engine.

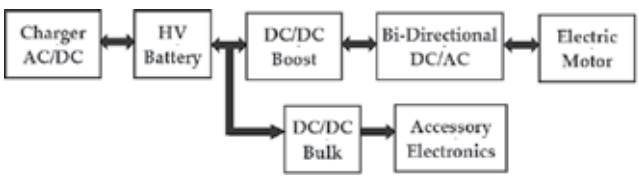

Figure 2. Schematic of power train in the EV.

Power modules are the core parts of inverter and converter systems in **Figure 2**, which dominate the system performance, reliability, size, weight, and the cost. **Figure 3** is an example of an inverter cost breakdown, showing that power module accounts for 30% of the whole cost and its cost reduction is critical to the system. To save size and weight of power systems, the cooling technology and system must be improved as it accounts for about 15% of cost and 30% of weight of the whole system. In 2012, the market was $1.9 bn for power modules which were mostly made with IGBT. At the moment, the average cost of a power module is above $500 in HEV, making a few billions of market in the next few years [17].

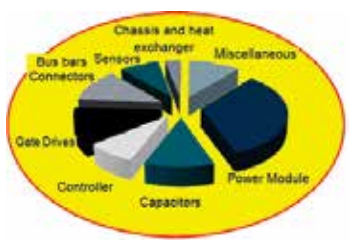

Figure 3. Cost breakdown of an HEV/EV inverter.

In HEV/EV application, the work environment of power system and module is harsh than industry applications. For example, the ambient temperature under the hood may reach 100°C with higher humidity; the HEV manufacturer is looking for sharing engine coolant with power module so the coolant temperature will be up to 105°C; the mechanical vibration and shock are usually strong and unpredictable during the vehicle running. In addition, the reliability, size, weight, and cost are challenges to power module development as the limited space and cost objectives of HEV/EV [9, 10–13]. **Table 2** shows the technology targets for both the power electronics and electric motors in HEV/EV [15].

	Power electronics				**Motors**		
Year	**$/kW**	**kW/kg**	**kW/L**	$T_{coolant}$	**$/kW**	**kW/kg**	**kW/L**
2010	7.9	10.8	8.7	90°C	11.1	1.2	3.7
2015	5.0	12.0	12.0	105°C	7.0	1.3	5.0
2020	3.3	14.1	13.4	105°C	4.7	1.6	5.7

Table 2. Technology targets for HEV/EV.

The major criteria for evaluating an automotive power module such as the performance, efficiency, reliability, cost, and volume/weight are generally determined by power semiconductor devices, packaging, and manufacturing technology. These criteria can be characterized by a series of technical parameters in aspects of the power module's electrical, thermal, thermomechanical, and mechanical properties, as well as packaging materials and processing techniques. The parameters determining the overall performance of a power module are thermal impedance (resistance and capacitance), operating and maximum junction temperature ($T_{j\,op}$, T_{jmax}), parasitic resistance and inductance, power cycling, thermal cycling/shock, vibration ruggedness, etc. [2–13]. People have made numerous technical advancements to improve these parameters through material and processing development and package structure optimization. **Table 1** lists the potential available solutions to meet the challenges of automotive packaging in the aspects of power semiconductor devices, and power modules packaging. It is supposed that improvement in one technology area is not sufficient at all to overcome all the difficulties and a comprehensive approach is required, and it may be not possible to achieve all the market and technical goals by making improvement to the existing technologies.

3. Overview of design for HEV/EV module

In HEV/EV applications, power modules must have superior performance and reliability than industrial products as the working environment is harsh in temperature, humidity, and vibration [9, 10–13]. The power modules are stressed heavily and frequently by electrical, thermal, and mechanical actions, so the device itself and the packaging parts are required to be robust enough during their operational life. Moreover, the system and device are restricted

by space, weight, and cost of the whole vehicle [2–4]. For these reasons, extensive efforts have been taken to improve the performance and reliability of automotive modules, and a series of optimized design and packaging solutions have been proposed [18–26].

The design of automotive power module should address the performance and reliability issues related to electrical, thermal, and mechanical. They are the main functional aspects that a power module has to serve. The power devices, module structure, materials, and packaging technologies are responsible for these performances, reliability, cost, volume, and weight. The components and technologies affecting power module's overall performance are listed in **Table 3**, and the module's reliability and lifetime are limited by the most unstable parts in the packaging.

Reliability issues		**Design optimization**
Electrical performance	Blocking	Chip field depletion, passivation
	Gate leakage	Gate oxide, packaging cleanness
	Power loss	Gate, field stop, thickness, parasitics
	Frequency/SOA	Power chip, parasitics
Thermal performance	Resistance, R_{th}	Module structure, material, technology
	Storage	Integrity of plastic, passivation, glue, gel
	Temperature cycling/shock	Joining, interconnection, materials
	Power cycling	Joining, interconnection
Mechanical	Shock/vibration	Bonding, housing

Table 3. Performance and reliability design on automotive power module.

The electrical performance is essential to power module application, with the main parameters affecting system performance are power density, operation temperature, blocking voltage, switching frequency, power dissipation/efficiency, and reverse/short-circuit safety-operating areas (RB/SCSOA). These performances are affected primarily by IGBT and FWD chips. However, the thermal and mechanical performances are mainly dependent on module packaging aspects. Thermal design is a critical step for the enhancement and optimization of thermal resistance, high-/low-temperature storage, thermal cycling, and power cycling, and the mechanical design is beneficial to the module resistant to shock and vibration [14].

3.1. Power chips for HEV/EV module

It is generally believed that the electrical performance and reliability are mainly controlled by power switches. **Figure 4** shows the vertical structure of an advanced IGBT used in HEV/EV modules. The thin-wafer technology, trench gate, and field stop layer are introduced to trade-off conduction and switching losses by which the frequency and efficiency are improved. The power dissipation results from leakage currents are reduced by the optimization of chip

http://dx.doi.org/10.5772/64173

design. High power density, high RBSOA, and SCSOA capabilities are essential to HEV/EV power train, which are objectives of automotive chip design [2–4, 27–31].

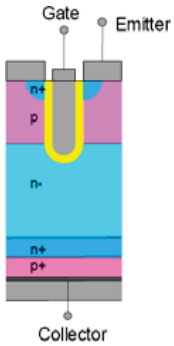

Figure 4. Vertical structure of a trench gate, field stop IGBT in HEV/EV modules [31].

At the moment, the standard fourth-generation IGBT technology is widely adopted by various industries. The thickness of 650 and 1200 V chips is reduced to about 70 and 120 μm, along with trench gate, the saturation voltage and conduction loss are reduced substantially compared to thick and planar gate devices. The frequency and switching loss are also optimized by these structures and field stop layer. Low power dissipation power chips are crucial to HEV/EV industry, which will result in high efficiency and energy saving, low rise of junction temperature (T_j) and therefore the high thermal reliability.

3.2. Design for low stray inductance

The parasitic parameters such as resistance (R), stray inductance (L_S), and capacitance have adverse effects on power dissipation, switching speed, and RB/SCSOA. One of the main objectives of automotive module design is to achieve low parasitic parameters. L_S is considered as the chief factor affecting IGBT module's performance and reliability. During the switching, an overshoot voltage (V_{OS}), equal to the product of L_S and current-varying rate, will be applied on the device terminals. If the sum of V_{OS} and DC-link voltage is higher than that of device-blocking voltage (V_{CES}), IGBT will be broken down. RB/SCSOA is then reduced because of the V_{OS} accordingly. The speed of automotive modules is much higher than industrial applications, resulting in high V_{OS} and reliability problems.

L_S of an IGBT module results from the substrate metal parts, bonding wires, conduct bus bars, control, and auxiliary pins. Design rules for minimizing the parasitic effects are proposed including reductions of current loop geometrical length and area [32], laminated bus bar, planar chip interconnection by using metal lead or PCB [2, 19, 32]. **Figure 5** shows an optimized substrate layout with minimum stray inductance. In this half-bridge substrate, the commutate path and area through DC+ and DC− are reduced to relatively small levels, leading to a small V_{OS} during IGBT switching-off verified by both simulation and module test [32]. It is supposed that the commutation loop length and area are valuable indicators of low L_S substrate design.

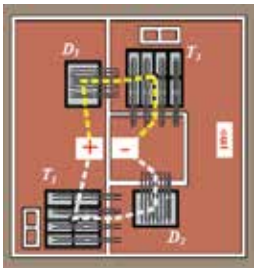

Figure 5. Optimized current loop dimensions with minimum stray inductance (Right) [32].

Thick and short bus bar and wires are effective to minimize L_S of a module. Due to substrate design, this bus bar may not be applicable. Furthermore, the laminated sandwich layout bus bars are verified as effective low L_S design solution [31]. The bonding wire-free concept, such as direct lead bond (DLB) [20, 21], double-side soldering/sintering on PCB or top-layer substrate [31] are good solutions to lower L_S.

Figure 6 shows a novel concept of double-side bonding in which bonding wire is eliminated. Therefore, L_S can be reduced, wire bonds failure is avoided, and the heat transfer efficiency is enhanced significantly by spreading through both sides of the chips. The planar IGBT module has been developed and applied in HEV/EV with great interest by the industry [20, 21].

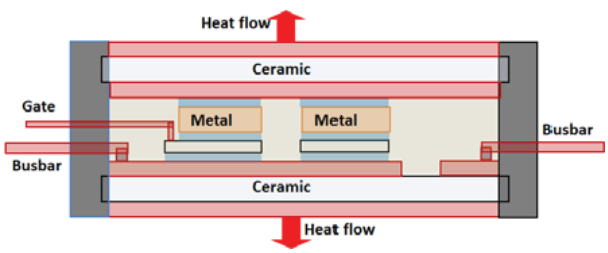

Figure 6. A planar interconnection concept for automotive module assembly [14].

3.3. Thermal design for automotive module

Thermal performance and reliability are of most importance for automotive IGBT modules as the ambient temperature is very high under the hood. On the other hand, the active power cycling and surging are more frequent than other applications that happen in the acceleration and deceleration stages. Therefore, large passive and active temperature excursions always occur in an automotive module operation. For the sake of cost and system complexity, customers prefer the traction inverter to share cooling system with the engine, meaning that the temperature of coolant could be up to 105°C in the near future. The abovementioned problems result in serious reliability problems on power module joining and interconnection parts. The solder layers of chip attach, substrate attach, and bus bar attach are prone to

http://dx.doi.org/10.5772/64173

delamination and failure because of fatigue finally due to high absolute temperature and high temperature swing (ΔT_j), and the bonding wires will be cracked or lifted off [33–35].

Reliability and lifetime of a power module is limited by the weakest point of the above parts. It is reported that power module lifetime reduces exponentially with the minimum/maximum junction temperature (T_{jmin}/T_{jmax}) and temperature swing. An outstanding thermal design gives smaller ΔT_j from the low thermal resistance of junction to case ($R_{th\ j\text{-}c}$) and junction to heat sink ($R_{th\ j\text{-}h}$) and enhances reliability [33–35].

Thermal design of IGBT module lies in the chip and packaging structure and materials. By elevating T_{jmax} of chips, the reliability will be enhanced as the improvement of electrical performance, and the requirement of module design will be mitigated. Currently, the fourth IGBT chips have a T_{jmax} of 150°C, and it is proposed that T_{jmax} of next-generation automotive module should reach 175°C, which requires redesigns in chip-doping profile, passivation, and metal materials.

To enhance reliability and prolong lifetime, power dissipated in chips and parasitic components must be spread with high efficiency, which can be achieved by low $R_{th\ i\text{-}c}$. Design for low $R_{th\ j\text{-}c}$ is dependent on the optimization of module structure and material. The high thermal conductivity ceramic such as AlN and Si_3N_4, and Cu or AlSiC baseplate with optimized thickness, direct cooling structure without using thermal grease are proved effective solutions to reduce the overall $R_{th\ j\text{-}h}$. However, the thermal performance should be traded off with reliability, weight, and cost. **Figure 7(a)** shows that a direct cooling pin-fin baseplate can reduce the $R_{th\ j\text{-}h}$ of conventional module by about 50% because of eliminating the grease layer [4, 18, 22, 23]. The direct liquid cooling (DLC) pin fins can be optimized in terms of efficiency, shape, layout, material, and cost. **Figure 7(b)** shows an automotive IGBT module with optimized Al in-line pin fins, in which the weight and cost are saved by maintaining merits of low thermal resistance and high reliability. Thermal simulation shows that the power switches work at the safe temperature envelop during the highest transient and continuous power output stages of a passenger car sharing 105°C cooling of the engine. Lifetime of the module is predicted under a real mission, which shows that it is capable of meeting the requirements with high coolant temperature [3].

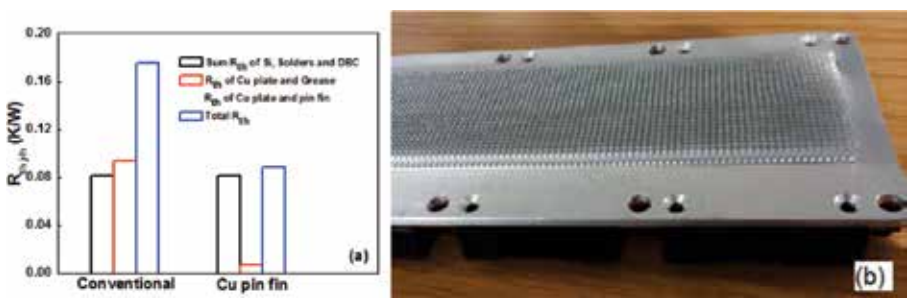

Figure 7. Comparison of $R_{th\ j\text{-}h}$ between conventional and direct cooling modules (a) and automotive IGBT module with optimized Al in-line pin fins (b).

Baseplate free- and double-side-cooling modules are proposed for automotive application for their good thermal performance as shown in **Figure 8** [20, 36]. The baseplate-free module can benefit to $R_{\text{th j-h}}$, weight, and cost, and the double-side-cooling structure can increase further the heat transfer efficiency. Both the modules are successfully applied in HEV/EV.

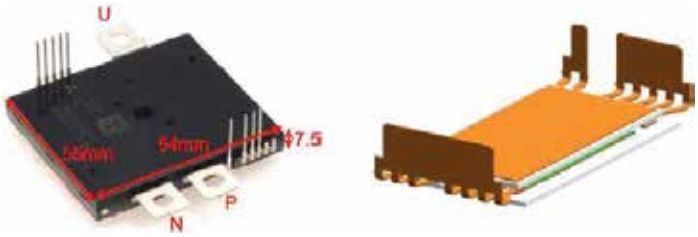

Figure 8. Baseplate-free (Left) [20] and double-side cooling [36] automotive modules.

3.4. Technology design for automotive module

Although low $R_{\text{th j-c}}$ reduces ΔT_{j} at constant power loss level, the high $T_{\text{jmin}}/T_{\text{jmax}}$ together with ΔT_{j} can degrade gradually module's weakest point such as wire bonds, die attach solder layer, conduct lead, and substrate attach solder layer. The planar and next-generation copper-bonding wires with novel soldering technology are effective solutions to this instability. The novel die attachment technologies such as silver sintering and transient liquid phase sintering (TPLS) are verified to improve the power cycling capability by orders of magnitude. **Figure 9** shows lifetime comparison of copper wire incorporated with novel soldering and conventional Al wire and soldering, soldered and sintered die attachment [37, 38].

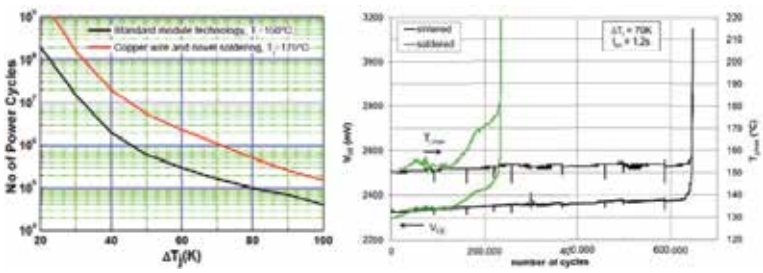

Figure 9. Improvement of lifetime by copper wire with novel soldering (Left) [37], lifetime comparison of modules with soldered and sintered die attach [38].

The mechanical shock and vibration affect mostly on the conduct bus bar and pins, which happen frequently in the running of an automobile. The strength of contacts should be enhanced in order to meet automotive standard that requires the module to be tested for 2 h per axis at more than 10 g for vibration, and three times at each direction and more than 100 g for shock. The ultrasonic welding with injection-molded housing (**Figure 10(a)**) as well as pressure contact is designed for achieving the mechanical reliability standard. **Figure 10(b)**

http://dx.doi.org/10.5772/64173

shows that the reliability of bonding can be enhanced by ultrasonic welding, as negligible degradation of bonding tensile strength was found [39].

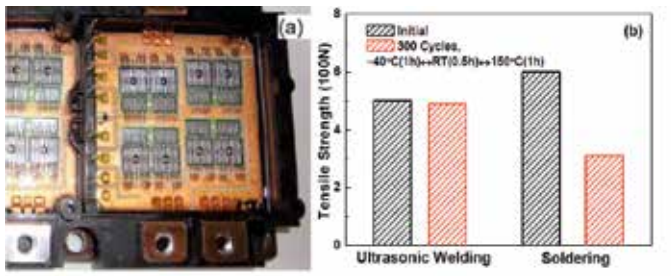

Figure 10. Ultrasonic welded terminals and pins in a HEV/EV module (a), and the reliability comparison with soldered terminals (b) [39].

4. State-of-the-art HEV/EV power module

In this section, the typical state-of-the-art commercial and custom HEV/EV power modules are reviewed and evaluated. The design and manufacture of automotive power module were following industrial power module packaging standard at the beginning. The conventional structure and technologies were applied in automotive module, which was the sandwich structure including plain baseplate and direct bond copper (DBC) substrate interconnected by solder reflowing and wire bonding. The structure and technologies are difficult to meet HEV/EV requirements in thermal and mechanical performance, as well as in the reliability, lifetime, cost, volume, and weight. Therefore, power semiconductor and automotive industry had developed a series of power modules dedicated for HEV/EV application as described in the following.

4.1. Direct liquid-cooled HEV/EV power module

Direct liquid cooling (DLC) was supposed to be an efficient solution to HEV/EV modules with its advantages of efficiency, integration, weight, and size [2–4]. A typical DLC module integrates liquid-cooling structure such as pin fins into the baseplate, which can flow through coolant without an external heat sink. Therefore, the traditional thermal interface layer between baseplate and heat sink is eliminated, and the un-uniformity and degradation of thermal grease will be avoided as well. It is reported that the $R_{\text{th j-h}}$ could be reduced by 50% of plain plate in the application, resulting in much lower ΔT_{j} and reinforcement of the reliability and lifetime. Therefore, the pin-fin DLC IGBT module is a good solution to HEV/EV power systems not only in the aspects of reliability but also performance, cost, and weight [2–4, 18, 22, 23].

DLC module with pin-fin plate is excellent in delivering higher power than plain base or baseplate-free modules, and the converter system with DLC module is compact and reliable.

Figure 11 shows the commercial DLC modules with pin-fin plate. A technology trend for IGBT module cooling in HEV/EV power-train system uses coolant with elevated temperature, so the power device can share cooling system with engine at up to 105°C liquid [3, 8]. This will simplify power electronics system without separate cooling circuit, resulting in the reduction of overall cost, weight, and volume of whole vehicle. However, high-temperature cooling has huge adverse effects on reliability and lifetime of power module, and may result in exceeding of $T_{j\,max}$. The direct liquid cooling is generally believed as an efficient thermal management with high cooling efficiency at high-temperature applications. The application of DLC module in HEV/EV has been widely accepted [3–5, 40].

Figure 11. The commercial DLC modules for HEV/EV power system.

The manufacture complexity and cost of pin-fin baseplate are high compared to plain plate at the moment, and the new technologies are required to integrate DLC structure into external cooling path.

Figure 12 shows an integrated cooler structure [2] with the direct bonded Al (DBA) substrates are directly bonded (by brazing) onto specially fabricated cold plate to realize direct cooling of the power module. The integrated module and cooling structure eliminates the conventional baseplate and thermal interface layer. It achieves 30% improvement in thermal performance. The assembly includes a buffer plate with punched holes for releasing the stresses between the cooler and DBA caused by a coefficient of thermal expansion (CTE) mismatch. The Al ribbons were used to replace Al wires for improving the reliability and electric parasitic parameters of die interconnections.

Figure 12. Integrated automotive power system with baseplate-free module and cold plate [2].

http://dx.doi.org/10.5772/64173

4.2. Baseplate and solder-free automotive power module

The state-of-the-art IGBT modules are based on a solder construction for chips attaching to substrate and substrate attaching to baseplate. Investigations have shown that these solder layers constitute the weakness of power semiconductor module as they demonstrate fatigue when exposed to active and passive temperature cycling. **Figure 13** shows an automotive power module named SKiM by Semikron, which is designed with high reliability to meet the demands of automotive applications in terms of shock and vibration stability, as well as high-temperature capability and service life [31].

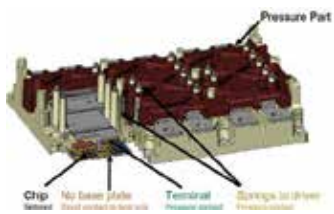

Figure 13. Baseplate and solder-free automotive power module [31].

The module features a pressure-contact low-profile housing that boasts the advantages of 100% solder-free module, Pb-free, and spring contacts for auxiliary contacts. The chips are sintered by silver on substrate, achieving a very high-power cycling capability. The sinter joint is a thin silver layer whose thermal resistance is superior to that of a soldered joint. Due to the high melting point of silver (960°C), no joining fatigue occurs, resulting in an increased service life [31].

The pressure contact of bus bar and auxiliary pins results in very low thermal and ohmic resistance and high thermal reliability. The laminated sandwich main terminals as shown in **Figure 14** benefits to a very low stray inductance and therefore improves the reliability, efficiency, and electrical performance. The single chip is connected symmetrically in **Figure 15**, leading to similar stray inductances for the individual chips and a homogeneous current distribution [31]. The baseplate-free structure has advantages of low volume and lightweight, but a thermal interface layer must be applied to improve the contact between substrate and heat sink, which deteriorates the thermal performance and reliability.

Figure 14. Main terminals with sandwich structure and low inductance [31].

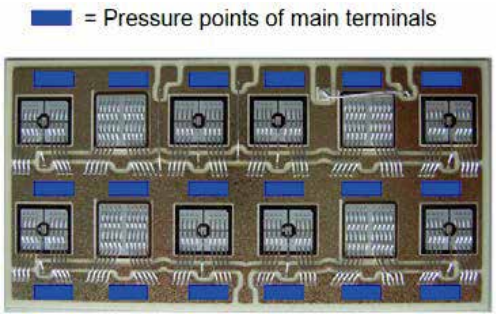

Figure 15. The substrate with symmetrically chip layout and terminal pressure contact areas [31].

4.3. Direct lead bond automotive module

A Transfer-mold power (TPM) packaged by direct lead bond (DLB) technology was released to automotive power electronics market by Mitsubishi and Bosch [20, 21, 41], which makes HEV/EV applications more reliable and compact. **Figure 16** shows the power module samples, the low profile, and compact package achieved by the concept.

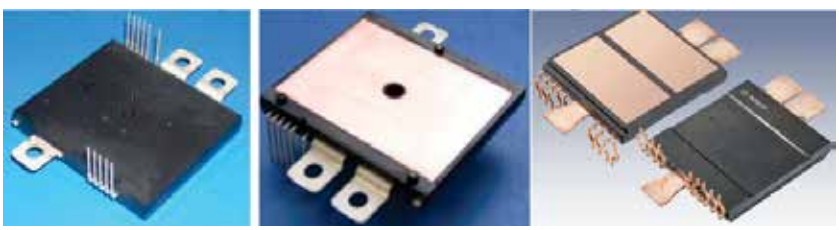

Figure 16. TPM automotive module prototypes from Mitsubishi and Bosch (Right) [20, 41].

The internal cross section of the packaging structure is shown in **Figure 17**. The transfer-mold case chips are bonded on heat spreader and on lead frame directly (DLB) by lead-free solder, the TCIL is attached on the heat spreader for electrical isolation and contact with external heat sink.

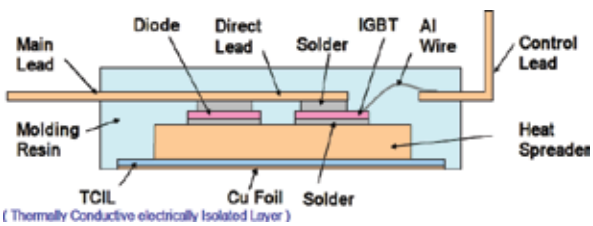

Figure 17. The internal cross section of TPM module with DLB [20].

http://dx.doi.org/10.5772/64173

DLB is the key feature of the module, by which the internal lead resistance is decreased to 50% and the self-inductance is decreased to 60% compared with the classically wire-bonded TPM module. The large solder contact area of DLB results in a uniform chip surface temperature distribution and a small thermal resistance. The integrated heat spreader reduces the contact thermal resistance and transient thermal impedance. The construction provides a larger area of heat flow between junction and case. The features of DLB TPM automotive has enhanced almost 30 times of power and thermal cycling capability compared with the conventional module case assembled with wire bond technology. In addition, the on-chip temperature and current sensors are integrated into the IGBT die, enabling a precise, safe, and fast over temperature protection, and detects and turns off a short-circuit situation without the IGBT entering a de-saturation phase [20, 21, 41].

As the evolution of the first generation of DLB module, a six-in-one HEV/EV module bonded by DLB and integrated with direct water-cooled Al fin was developed [21]. The adoption of these innovative technologies has led to improved thermal performance of 30%, and has reduced the footprint by 40% and the module weight by 76%. **Figure 18** shows the module prototypes and internal structure. The Al cooling fin was integrated into module for direct liquid cooling. DLB is employed that has extensive advantages to power density, thermal and electrical performance, reliability, etc. The Al cooling fins have lower thermal conductivity compared to Cu pin-fin structure, but they have high durability when exposing directly to coolant and are much lighter. Compared to the first-generation DLB modules of **Figure 16**, as much as 76% weight reduction and 30% thermal performance improvement were achieved based on the same current and voltage for three-phase HEV/EV motor drives [21].

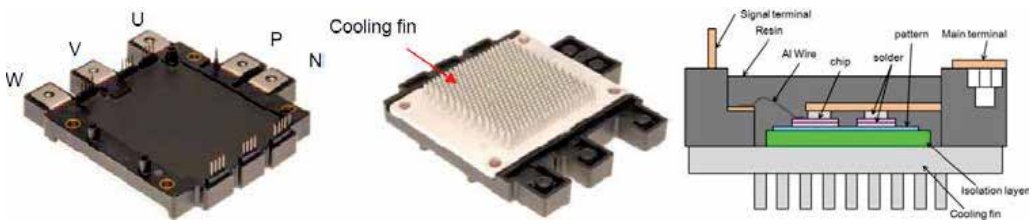

Figure 18. The prototypes and package structure of a high performance, compact size, and light-weight HEV/EV power module [21].

The custom power module in Nissan LEAF pure EV shown in **Figure 19** has the same concept of DLB [2]. The power semiconductor dies are attached onto Cu plate, which is an electrical terminal and is wire bonded to other terminals to form a half-bridge configuration. The large-area Cu bus bars act as heat spreader and are mounted onto external cold plate through a separated electrical insulator sheet. The sheet has a special composition and offers high thermal conductivity.

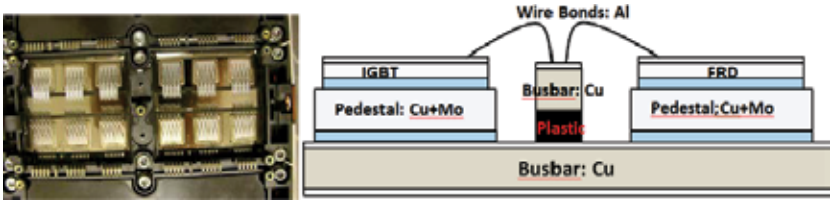

Figure 19. The custom module for Nissan LEAF and its schematic of cross-sectional view [2].

4.4. Planar interconnection and double-sided-cooled automotive module

In a conventional module packaging, the top electrodes of die are electrically interconnected by bonding Al wires, while the whole bottom metal surfaces are soldered onto insulating ceramic with direct bond copper or aluminum surfaces. This asymmetric package structure has a series of drawbacks such as large parasitic electric parameters, deformation of die subjected to thermomechanical stress, small thermal conduction path through the top of die, etc.

Therefore, changing the top interconnection configuration to a planar or symmetric package will bring comprehensive benefits to thermal, electrical, and reliability. With a planar interconnection, the die can be connected to cold plates at both sides to achieve double-sided cooling, and the thermal performance can be enhanced accordingly. This will eliminate the traditional bonding wires but require that front metal of chips must be solderable [19].

The concept of planar IGBT packaging without bonding wires is shown in **Figure 6**, and the planar modules were developed for HEV/EV and aerospace industries. By soldering or sintering semiconductor chips to copper leads directly or to DBC system, the module can be cooled by liquid or forced air at both sides, which provides 70% higher cooling efficiency than a conventional single-side cooling module. A joining layer on a chip active area will spread heat easily and result in low-junction temperature and high reliability [15, 19]. The removal of bonding wires has advantages on reliability as wire bonds are prone to failure during operation because of the high intermittent temperature cycling from the junction. On the other hand, the parasitic resistance and inductance are reduced accordingly by large area contact, which improves efficiency and dynamic performance such as the safe operating areas of RBSOA and SCSOA [2, 6].

IR has presented a new power management platform approach for HEV/EV to help address the need to reduce the size, weight, and system cost of electric power-train components while increasing system reliability for long lifetime, low maintenance, and low warranty cost. The packaging platform named CooliR^{2TM} characterizes wire bond frees and transfer-mold technologies that addresses all the HEV/EV module packaging challenges. The IGBT and diode called CooliR^{2}DIE were designed for the platform. The IGBT has reduction of conduction and switching losses, increases of blocking voltage, and compatibility with wire bond-free interconnection techniques, and the switching frequency and maximum T_j were increased to

http://dx.doi.org/10.5772/64173

20 kHz and 175°C, respectively. The diode was optimized for automotive traction by fast-speed soft recovery with oscillation-free behavior [15, 19, 42].

Figure 20 shows the CooliR²DIE as building blocks and the construction of a half-bridge package by using the die. The building-block approach of CooliR^{2TM} platform has advantages of cost reduction and mechatronics enabler. The electrical performance of package is improved with lower resistance and parasitic inductance. The cooling method is flexible for no baseplate cooling, or attaching a baseplate or direct liquid-cooled heat sink to substrate. The transient thermal impedance and die temperature distribution are improved in the packaging. In addition, the reliability and power density are increased by the wirebond less, dual-sided cooling and higher T_{jmax} solutions.

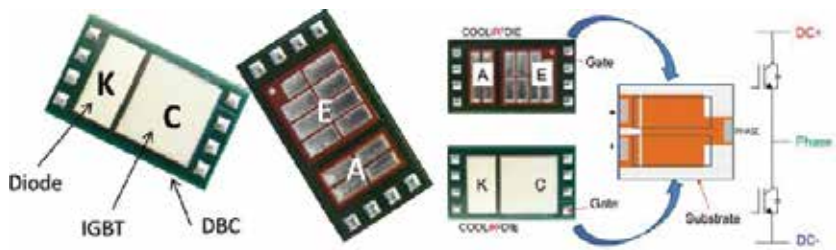

Figure 20. CooliR²DIE building block and the construction of a half-bridge package by using CooliR²DIE [42].

Figure 21 shows a custom automotive power module for Toyota LS600, in which two planar Cu plates are directly soldered onto power electrodes on the dies from both surfaces. The module is encapsulated with transfer-molded compound while keeping the Cu plates exposed to the outside for acting as heat sinks to transfer device heat to a cold plate (cooling tube) from two surfaces [2]. Therefore, the module's thermal resistance is reduced dramatically. Insulator layers are required at both sides between power module and cold plate as the module is nonelectrically isolated.

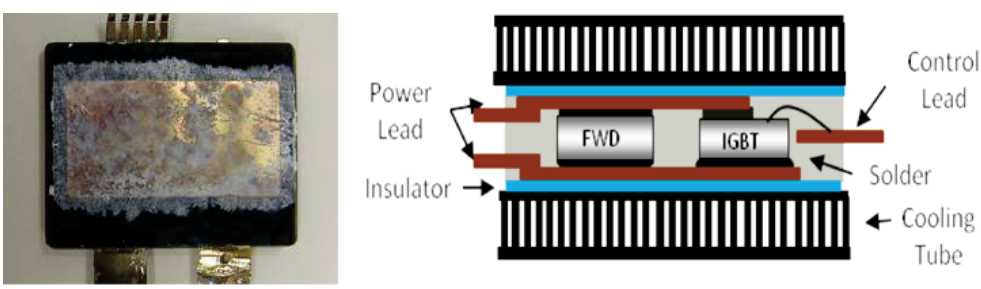

Figure 21. Custom power modules of Toyota LS600 and its schematic of cross-sectional view [2].

In **Figure 22**, Delphi planar [36] power module for dual-side cooling is shown. The DBC isolates module to external heat sink. It is a co-packaged IGBT and diode unit that needs next-level

interconnection to form power inverters, so the pressure must be controlled to ensure the press contact between all package units and cold plates for double-sided cooling. However, the assembly complexity of electrical interconnections is difficult and costly at inverter-level packaging.

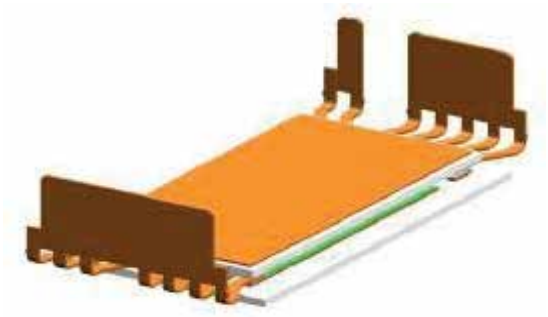

Figure 22. Delphi planar bond power module with dual-side cooling [36].

The Semikron double-sided planar power module using SkiN technology is shown in **Figure 23**. The die top connection is a flex circuit board, and all the joining interfaces between two sides of die and substrate, and DBC and heat sink, are bonded by Ag-sintering process. This provides very high thermal and power cycling reliability, as well as good thermal and electrical performance [43].

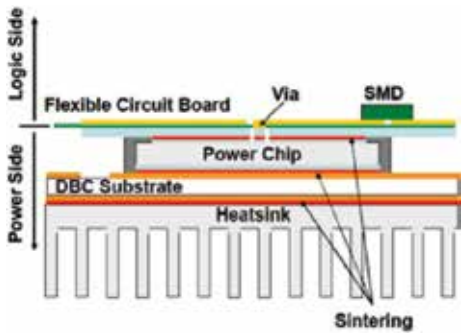

Figure 23. Schematic of cross-sectional view of Semikron SKiN power module [43].

5. Packaging trend of HEV/EV power module

The standard of power module for passenger car is stringent than industrial and CAV (Commercial, construction, and agricultural vehicles) products. Therefore, the advanced packaging structure, material, and technology must be investigated.

http://dx.doi.org/10.5772/64173

5.1. Novel structures in automotive module packaging

As mentioned above, the direct liquid cooling power module is becoming a standard solution to HEV/EV power packaging. The power density is improved as its excellent thermal performance and compact integration with heat sink, which is also the volume and weight. $T_{j\ max}$ can be well controlled by reduction significantly of $R_{th\ j\text{-}h}$, so the reliability and lifetime are enhanced. By using the advanced cooling structures into module baseplate such as the two-phase change flat pipe, vapor chamber and microchamber, etc., the heat transfer efficiency, volume, and weight are further improved.

The baseplate-free module has the advantages in volume, weight, and cost, which is preferred by automotive customers. However, the module with direct substrate cooling structures is more attractive for cooling efficiency, thermal performance together with the benefits of baseplate-free module.

The planar structure is a more advanced packaging trend for automotive module, a top isolation substrate, a flexible PCB or contacting leads are bonded to chip-top contact areas. The bonding wires are eliminated resulting in series benefits in parasitics reduction, temperature uniformity, and reliability. Therefore, the power density, thermal performance, reliability, volume, and weight are improved. By using a top substrate, the module can be cooled from both sides of a chip, increasing the cooling efficiency by more than 30% of a traditional one-side cooling structure.

5.2. Advanced materials for automotive module packaging

The selection of advanced packaging materials is essential to module performance and reliability, the advanced materials for power semiconductor die, substrate, baseplate, interconnection, and housing are proposed for automotive power packaging.

SiC devices such as MOSFET and Schottky Barrier Diode (SBD) are becoming popular in automotive power module market as its excellent material performance in electrical and thermal. The high bandgap makes SiC devices competent to high-temperature, high-voltage, and high-efficiency applications. Its thermal conductivity is about three times than Si, which is beneficial to high-temperature and high-power density requirements. The doubled electron saturation speed in SiC leads it as best candidate to high-frequency applications. In addition, the GaN devices are developed quickly for automotive product as the same reasons of SiC devices.

Si_3N_4 substrate is proposed for high performance and reliability power module packaging as its trade-off advantages of CTE, thermal, and mechanical performance. Although Si_3N_4 is not selected widely at the moment, the reduction of cost in the near future will make it a first choice in automotive module packaging.

AlSiC baseplate with direct liquid cooling pin-fin structure has been extensively proposed in passenger car and sport-racing cars. The reasons also lie in its overall performance advantages of CTE match with semiconductor and substrate materials, good thermal and mechanical features, and lightweight, etc. The advanced interconnection materials such as lead-free solder

and copper bonding wire are developed for enhancing reliability and lifetime of automotive module.

The new housing materials are applied in injection molding, transfer molding, and hematic supply high temperature and high mechanical reliability, which are becoming the mainstream housing of automotive module.

5.3. The trend of assembly technology

The assembly technology is essential to power module performance and reliability, so advanced joining and interconnection technologies are being developed for automotive packaging. The trends of joining interfaces between die, substrate, and baseplate are high and stable tensile strength solder layer formed by SnSb, high temperature and reliability intermetallic solder layer formed by transient liquid phase sintering (TPLS), or superior silver-sintered layer. SnSb soldering is an easy and cost-effective way by traditional process; however, TPLS and silver sintering have more reliability benefits.

The conventional Al wire bonding interconnection technique will be replaced by copper wire bonding and planar contacts such as direct lead and flexible PCB bonding. Copper wire bonding improves current and thermal capability, and the reliability, which the planar packaging results in high current, low parasitics, low loss, uniform temperature, and high reliability.

The interconnection of bus bar and pin is usually soldered to substrate in an industrial power module, which have low thermal and mechanical reliability. Recently, ultrasonic welding, which results in quite high bonding strength and pressure contact, is proposed in automotive power packaging. Both enhance thermal and mechanical reliability significantly by eliminating interface layers.

6. Summary

Development of hybrid and electric vehicles (HEV/EV) has brought challenges to power semiconductor industry in automotive power module packaging. As the essential role of power module plays in HEV/EV power-train system, people have made great efforts to improve electrical and thermal performance, reliability, volume/weight, and cost of automotive module. Many innovative designs in power module structure, material, and assembly technology have been proposed based on conventional power module packaging.

In this chapter, the status and trend of automotive standard power module packaging are reported. We have discussed the importance and functionality of power electronics and module in HEV/EV power-train system, and summarized the performance requirements by automotive industry. The designs of structure, material, and packaging technologies for high thermal, electrical performance, and high reliability for HEV/EV module are investigated. An overview of the typical state-of-the-art commercial and custom HEV/EV power modules, including direct liquid cooled, baseplate, and solder free, direct lead bonded, planar intercon-

nection and double-sided cooled, are analyzed. The details of novel structures, advanced packaging materials, and trends of assembly technology are proposed to instruct automotive module designs.

Author details

Yangang Wang[1,2*], Xiaoping Dai[1,2], Guoyou Liu[1,2], Yibo Wu[1,2], Yun Li[1,2] and Steve Jones[1,2]

*Address all correspondence to: yangang_wang@dynexsemi.com

1 Power Semiconductor R&D Centre, Dynex Semiconductor Ltd, CRRC Times Electric co. Ltd, Lincoln, UK

2 State Key Laboratory of Advanced Power Semiconductor Devices, CRRC Times Electric co. Ltd, Shifeng District, Zhuzhou, Hunan, P. R. China

References

[1] Technology Roadmap Electric and plug-in hybrid electric vehicles, International Energy Agency, https://www.iea.org/publications/freepublications/publication/EV_PHEV_Roadmap.pdf

[2] Z. Liang, Status and trend of automotive power packaging, *24th International Symposium on Power Semiconductor Device & ICs (ISPSD)*, ISPSD, Bruges, Belgium. pp. 325–331, Jun. 2012.

[3] Y. Wang, X. Dai, Y. Wu, S. Jones, Integrated liquid cooling automotive IGBT module for high temperature coolant application, *International Conference in Power Electronics, Intelligent Motion, Renewable Energy and Energy Management (PCIM Europe)*, pp. 1197–1203, May 2015.

[4] Y. Wang, S. Jones. X. Dai, G. Liu, Reliability enhancement by integrated liquid cooling in power IGBT modules for hybrid and electric vehicles, *Microelectronics Reliability*, vol. 54, no. 9–10, pp. 1911–1915, 2014.

[5] A. Christmann, M. Thobe, K. Mainka, Reliability of power modules in hybrid vehicles, *PCIM Europe*, pp. 359–366, May 2009.

[6] R. John, O. Vermesan, R. Bayerer, High temperature power electronics IGBT modules for electrical and hybrid vehicles, *IMAPS, High Temperature Electronics Network (HiT-EN)*, vol. 1, pp. 199–204, 2009.

[7] D. Hirschmann, Reliability prediction for inverters in hybrid electrical vehicles, *IEEE Transactions on Power Electron*ics, vol. 22, pp. 2511–2517, Nov. 2007.

[8] M. Thoben, F. Sauerland, K. Mainka, S. Edenharter, L. Beaurenaut, Lifetime modeling and simulation of power modules for hybrid, *Microelectronics Reliability*, vol. 54, no. 9–10, pp. 1806–1812, 2014.

[9] A. Chaudhary, S. Singh, Reliability comparison of inverters in hybrid electrical vehicles under different switching pattern, *International Journal of Scientific & Technology Research*, vol. 1, no. 2, pp. 63–66, 2012.

[10] K. Vogel, A. Ciliox, A. Schmal, IGBT with higher operation temperature-power density, lifetime and impact on inverter design, *PCIM Europe*, pp. 621–626, May 2011.

[11] M. Thoben, K. Mainka, R. Bayerer, I. Graf, M. Munzer, From vehicle drive cycle to reliability testing of power modules for hybrid vehicle inverter, *PCIM Europe*, May 2008.

[12] R. Bayerer, Higher junction temperature in power modules – a demand from hybrid cars, a potential for the next step increase in power density for various Variable Speed Drives, *PCIM Europe*, May 2008.

[13] M. Ciappa, F. Carbognani, W. Fichtner, Lifetime prediction and design of reliability tests for high-power devices in automotive applications, *IEEE Transactions on Device and Material Reliability*, vol. 3, pp. 191–196, 2003.

[14] Y. Wang, X. Dai, G. Liu, D. Li, S. Jones, An overview of advanced power semiconductor packaging for automotive system, *9th International Conference on Integrated Power Electronics Systems (CIPS)*, March 2016.

[15] J. Marcinkowski, CooliR^{2} ™ – New power module platform for HEV and EV traction Inverters, http://www.infineon.com/dgdl/coolir2b.pdf?fileId=5546d462533600a401535743770b3f01

[16] Power Electronics in Electric and Hybrid Vehicles, *Yole Development*, 2014.

[17] http://www.semiconductor-today.com/news_items/2013/FEB/YOLE_110213.html

[18] A. Morozumi, H. Hokazoni, Y. Nishimura, Y. Ikeda, Y. Nabetani, Y. Takahashi, Direct liquid cooling module with high reliability solder jointing technology for automotive applications, *25th ISPSD*, ISPSD, Ishikawa Ongakudo Kanazawa, Japan. pp. 109–112, 2013.

[19] J. Marcinkowski, Dual-side cooling of power semiconductor modules, *PCIM Europe*, pp. 1179–1185, May 2014.

[20] M. Ishihara, K. Hiyama, K. Yamada, T. Radke, M. Honsberg, T. Nakano, New transfer-mold power module series for automotive power-train inverters, *PCIM Europe*, pp. 1408–1413, May 2012.

[21] M. Ishihara, N. Miyamoto, K. Hiyama, T. Radke, T. Nakano, New compact-package power modules for electric and hybrid vehicles (J1 series), *PCIM Europe*, pp. 1093–1097, May 2014.

[22] S. Adachi, A. Odaka, F. Nagaune, P. Dietrich, A. Toba, N. Nishiura, Application technologies of direct cooling IGBT for electric and hybrid vehicles, *PCIM Europe*, pp. 825–832, 2013.

[23] T. Hitachi, G. Hiromichi, F. Nagaune, Direct liquid cooling IGBT module for automotive applications, *Fuji Electric Review*, vol. 58, pp. 55–59, 2012.

[24] F. Nagaune, H. Ghara, S. Adachi, T. Hitachi, H. Shibata, M. Morozumi, Small size and high thermal conductivity IGBT module for automotive applications, *PCIM Europe*, pp. 785–790, 2011.

[25] S. Adachi, F. Nagaune, H. Gohara, T. Hitachi, A. Morozumi, P. Dietrich, High thermal conductivity technology to realize high power density IGBT modules for electric and hybrid vehicles, *PCIM Europe*, pp. 1378–1384, 2012.

[26] M. Reeves, J. Moreno, P. Behcher, S.-J. Loong, D. Brown, Investigation on impact on thermal performance of new pin and fin geometries applied to liquid cooling of power electronics, *PCIM Europe*, pp. 772–778, 2011.

[27] J. Lutz, H. Schlangenotto, U. Scheuermann, R. De Doncker, Semiconductor power devices – physics, characteristics, reliability, *Springer*, Springer, Verlag Berlin Heidelberg 2011.

[28] G. Majumdar, Power modules as key component group for power electronics, *Power Conversion Conference*, pp. 1–8, April 2007.

[29] H. Rüthing, F. Hille, J. Niedernostheide, J. Schulze, 600 V Reverse conducting (RC-) IGBT for drives applications in ultra-thin wafer technology, *19th ISPSD*, ISPSD, Jeju Island. pp. 89–92, May 2007.

[30] IGBT4 – 650V, 1200V, 1700V state of the art IGBT technology http://www.bdtic.com/download/infineon/Infineon-IGBT4_650V_1200V_1700V_Modules-PB-v3.0-en.pdf

[31] SKiM 63/93 IGBT Modules, Technical Explanations, https://www.semikron.com/dl/service-support/downloads/download/semikron-technical-explanation-skim0-63-93-igbt-modules-en-2013-10-rev1-51

[32] N. Zhu, M. Chen, D. Xu, A simple method to evaluate substrate layout for power modules, *8th CIPS*, CIPS, Nuremberg, Germany. pp. 267–272, February 2014.

[33] R. Bayerer, T. Herrmann, T. Lutz, J. Lutz, M. Feller, Model of power cycling lifetime of IGBT modules – various factors influencing lifetime, *5th CIPS*, CIPS, Nuremberg, Germany. March 2008.

[34] M. Held, P. Jacob, G. Nicoletti, P. Scacco, M. H. Poech, Fast power cycling test for IGBT modules in traction application, *Power Electronics and Drive Systems*, vol. 1, pp. 425–430, 1997.

[35] Y. Wang, S. Jones, D. Chamund, G. Liu, Lifetime modelling of IGBT modules subjected to power cycling tests, *PCIM Europe*, pp. 802–809, May 2013.

[36] R. Taylor, Building blocks and opportunities for power electronics integration, *26th IEEE Applied Power Electronics Conference and Exposition (APEC)*, APEC, Fort Worth, Texas, USA. March 2011.

[37] C. Alexander, V. Klaus, N. F. Josef, H. Andreas, Next step towards higher power density with new IGBT an diode generation and influence on inverter design, *PCIM Europe*, pp. 357–365, May 2013.

[38] R. Schmidt, U. Scheuermann, Separating failure modes in power cycling tests, *7th CIPS*, CIPS, Nuremberg, Germany. pp. 97–102, March 2012.

[39] Y. Nishimura, K. Kido, F. Momose, T. Goto, Development of ultrasonic welding for IGBT module structure, *22nd ISPSD*, ISPSD, Hiroshima, Japan. pp. 293–296, 2010.

[40] K. Higuchi, A. Kitamura, H. Arai, T. Ichimura, H. Gohara, P. Dietrich, A. Nishiura, An intelligent power module with accuracy control system and direct liquid cooling for hybrid system, *PCIM Europe*, pp. 39–46, May 2014.

[41] http://mobile.bosch-semiconductors.com/pdf/MH6560C_Product_Info_140211.pdf

[42] J. Marcinkowski, Innovative CooliR^{2} ™ packaging platform with dual-side cooling advances HEVs and EVs, http://www.infineon.com/dgdl/coolir2d.pdf?fileId=5546d462533600a4015357439da93f03

[43] T. Stockmeier, P. Beckedahl, C. Goebl, T. Malzer, Skin: double side sintering technology for new packages, *23rd ISPSD*, ISPSD, Paradise Point Resort & Spa San Diego, CA, USA. pp. 324–327, May 2011.

Chapter 3

Passenger Exposure to Magnetic Fields in Electric Vehicles

Pablo Moreno-Torres, Marcos Lafoz,
Marcos Blanco and Jaime R. Arribas

Additional information is available at the end of the chapter

http://dx.doi.org/10.5772/64434

Abstract

In electric vehicles, passengers sit very close to an electric system of significant power, usually for a considerable amount of time. The relatively high currents achieved in these systems and the short distances between the power devices and the passengers mean that the latter could be exposed to relevant magnetic fields. This implies that it becomes necessary to evaluate the electromagnetic environment in the interior of these vehicles before releasing them in the market. Moreover, the hazards of magnetic field exposure must be taken into account when designing electric vehicles and their components. For this purpose, estimation tools based on finite element simulations can prove to be very useful. With appropriate design guidelines, it might be possible to make electric vehicles safe from the electromagnetic radiation point of view.

Keywords: electric vehicles, electromagnetic radiation, magnetic field exposure, occupational safety

1. Introduction

The traction drive of an electric car is an electrical system of considerable power, ranging from 40 to 120 kW. Even higher power levels are found in high-end models or in other vehicles such as electric buses. These power levels are usually achieved with high currents rather than voltages. Specifically, most commercial vehicles nowadays work with voltage levels below 400 V, which implies currents of the order of hundreds of amperes. This means that these traction drives could generate magnetic fields of considerable strength when compared to other conventional sources.

At the same time, distances between these magnetic field generators and the passengers are relatively short in most vehicles; for instance, it is usual to place the battery pack as far as possible from the bodywork to minimize the risk of battery damage and its consequences in case of crash; this implies positioning them just under or behind the passenger seats [1]. Consequently, there could be hundreds of amperes circulating some centimeters away from the passengers during strong accelerations or deep regenerative braking.

The combination of high currents and short distances involves some risks due to the presence of strong magnetic fields. These fields can potentially have undesired effects on electric and electronics devices, but also on living beings inside the vehicle, or close to it. The first effects are known as electromagnetic interference (EMI) and are analyzed within the discipline of electromagnetic compatibility (EMC), whose main goal is to ensure proper operation of operational equipment in a common electromagnetic environment. This is usually done by limiting or conditioning the electromagnetic fields (EMFs) emitted by each device, but mostly by immunizing them so that they are not affected by EMI coming from the rest of the devices.

The second effects are named electromagnetic radiation (EMR) and belong to the field known as bioelectromagnetism or bioelectromagnetics, which studies all kinds of interactions between EMFs and biological systems. EMR is usually classified into ionizing and nonionizing radiation, depending on its capability to ionize atoms and therefore to break chemical bonds. This is only possible if the radiation carries a high amount of energy, and hence ionizing capability is directly associated with wavelength and thus with frequency. The boundary between nonionizing and ionizing EMR is located in the ultraviolet range of the electromagnetic spectrum. In this sense, all the radiation emitted by an electric vehicle is nonionizing.

The relationship between nonionizing EMR and human health has been studied for decades. In 1996, the World Health Organization (WHO) established the *International EMF Project* to assess the scientific evidence of possible health effects of low-frequency EMR (from 0 to 300 GHz), encouraging focused research to fill important gaps in knowledge and the development of internationally acceptable standards limiting EMF exposure [2]. At present, some possible consequences of low-frequency EMF exposure are still Unclear. Namely health effects caused by long-term exposure (such as cancer or neurodegenerative disorders) are mentioned in the literature, although conclusive results have not been obtained. Many long-term studies have been described as questionable and of low repeatability. Moreover, it could be argued that long-term effects are impossible to determine with certainty, since they take years or even decades to appear. Hence, long-term consequences are a source of discussion within the scientific community.

On the other hand, short-term nonionizing effects are well established, and their mechanisms are well known. These biological effects occur as soon as the exposure begins, and they disappear when it ceases, or shortly after. They are caused by extremely strong low-frequency (up to a few hundred kHz) and strong medium-frequency EMFs (radio waves and microwaves up to 300 GHz), and thus they are also known as acute effects. They may be classified into two main groups: electrostimulant effects and thermal effects. The former are a consequence of the coupling between low-frequency fields and living matter, an example of this would be induced currents in some organic tissues generated by an external magnetic field. The latter are due to

http://dx.doi.org/10.5772/64434

energy exchange between medium-frequency fields and biological tissues, which produces a temperature increase in those body parts affected. Thermal effects are usually negligible for field frequencies below 100 kHz, but become increasingly significant as frequency grows. Current standards, guidelines, and recommendations regarding maximum exposure values are developed considering these acute effects.

This chapter is intended to introduce the reader to the topic of magnetic field exposure in electric vehicles (EVs). For further information, a considerable number of references are provided at the end. The chapter is divided into different sections as follows:

- Section 2, Problem description, describes the main sources of magnetic field within an EV and the corresponding properties of those fields.
- Section 3, Prevention guidelines and standards, presents the two most accepted criteria for limiting magnetic field exposure.
- Section 4, State of the art, summarizes the most relevant studies published to date about magnetic field exposure in electric vehicles, as well as their main conclusions.
- Section 5, Design guidelines, lists some design modifications and considerations that can help improve the safety on an EV from the EMR point of view.
- Section 6, Discussion, presents some arguable ideas about magnetic field exposure in EVs.

2. Problem description

Electric vehicles are one of the most relevant applications in which power devices and general public share a common space. Other well-known precedents are power lines close to houses or buildings, electric trains and trams, and household appliances, to cite a few examples. However, the specific characteristics of EVs could make this issue particularly worrying from the point of view of magnetic field exposure. The combination of high current levels, short average distances between equipment and passengers, and long exposure duration is especially detrimental in this application.

As mentioned in the "Introduction" section, power levels in electric vehicles are of the order of tens of kW, while voltage levels rarely exceed 600 V, as shown in **Table 1**. This implies that current levels usually reach hundreds of amperes. There are not many applications in which people are close to wires or devices carrying such high currents. Besides, the present trend in EVs nowadays consists in reducing voltage levels as much as possible, which implies even higher currents. Paradoxically, lower voltages imply improved safety in case of short circuit or electrocution, but also reduced safety from the point of view of magnetic field exposure.

Second, distances between the traction drive and the passengers are usually short. For a typical electric car, values range from 0.2 to 3.0 m depending on the location of all the power devices and power cables. In this sense, the topology and the configuration of the vehicle (i.e., how the power devices are located within the available space) are particularly relevant:

- For instance, there are some differences between those vehicles that add a DC-DC converter connecting the batteries and the inverter as those who do not (see **Figure 1**). Without such DC-DC, the battery must have enough voltage for the inverter to drive the electrical machine in every required operating point (torque-speed). This is usually done reaching a compromise between battery voltage, which should not be too high (using too many cells in series increase balancing and safety requirements) and machine voltage, which should not be too low (lower voltages imply higher currents and lower number of turns in the windings). In general, adding a DC-DC allows for higher voltages in the drive, which improves magnetic field exposure but could worsen electric field exposure. However, in most cases the DC-DC aims to reduce battery voltage, and thus battery current increases. Hence, if the batteries are placed close to the passengers, they could suffer from higher magnetic fields.
- There are also some differences between pure electric vehicles and hybrid electric vehicles. The former have simpler traction systems, with fewer devices and mechanisms, which can be easily accommodated within the available space. On the other hand, the power train of the latter comprises more equipment, and thus they are more prone to suffer from room issues. Having more flexibility to distribute the power devices within the vehicle is always a good thing, and magnetic field exposure is another aspect that benefits from it, since certain parts can be moved away from the passengers. Nevertheless, pure electric vehicles use more electric power than their counterparts. Considering that voltage levels are similar (see **Table 1**), this means that pure EVs use higher currents and thus they generate stronger magnetic fields. In general, it could be expected that the second factor (stronger fields) weighs more than the first one (longer distances), so that pure EVs should imply higher exposure levels than hybrid vehicles.
- Finally, the type of drive also has some influence over passenger field exposure, namely those vehicles with rear-wheel drives usually place most of the traction equipment (i.e., the electrical machine and the inverter) in the rear part of the vehicle, while front-wheel vehicles place it in the front part. As cars are given aerodynamic shapes to minimize aerodynamic drag, the front part is usually longer than the rear part, and distances between the front wheels and the front seats are usually longer than those between the rear wheels and the rear seats, as shown by the two examples in **Figure 2**. This means that vehicles with front-wheel drives will usually have longer distances between these power devices and the closest passengers.

Third, regarding the duration of the exposure, it is important to note that general public is subject to electromagnetic fields generated by EVs for a considerable amount of time, significantly longer than other daily exposures such as household appliances. From the results presented in [5, 6], it can be concluded that European citizens spend an average of 1 h and 25 min per working day driving their cars. Even if an appreciable part of that time is spent with the vehicle stopped (e.g., traffic lights or traffic jams), situation in which magnetic fields should be minimum, the duration of the exposure is still rather long. In the United States of America, these average times are probably even longer, up to 2 hours in average. It is important to note here that, in the case of low-frequency magnetic fields and health effects, it is not

http://dx.doi.org/10.5772/64434

necessary to take exposure duration into account at the moment, since there is no scientific proof of any health consequences due to this type of exposure.

Model	Type	Drive	Power level	Voltage level
Mitsubishi i-MiEV				
Peugeot iOn	BEV	Rear wheel	49 kW	400 V_{DC}
Citroën C-Zero				
Nissan LEAF	BEV	Front wheel	80 kW	400 V_{DC}
BMW i3	BEV	Rear wheel	125 kW	500 V_{DC}
Tesla model S	BEV	Rear wheel	235 kW	650 V_{DC}
Toyota Prius (3rd gen.)	HV	Front wheel	74 kW	400 V_{DC}
Toyota Prius PHV	PHV	Front wheel	60 kW	350 V_{DC}
Chevrolet Volt	PHV	Front wheel	55 kW (x2)	400 V_{DC}

BEV = battery electric vehicle; HV = hybrid vehicle; PHV = plug-in hybrid vehicle.

Table 1. Power and voltage levels of some commercial models of hybrid and electric vehicles.

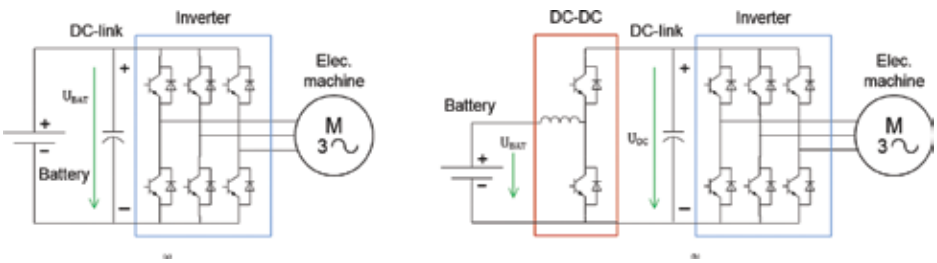

Figure 1. (a) Most common topology in electric cars nowadays. (b) Alternative topology, in which a DC-DC converter is added between the batteries and the inverter.

Figure 2. Schematics of two well-known pure EVs, showing the position of the main power devices: batteries, inverter, and electrical machine. (a) Rear-wheel drive and (b) front-wheel drive. Original images extracted from [3, 4] and modified by the authors.

In summary, magnetic fields in EVs could become an issue from the point of view of human health due to a combination of three factors: average and peak current levels, short distances between field generators and the passengers, and lengthy exposures.

2.1. Characteristics of the magnetic field generated by an EV

Under static electromagnetic conditions, electric fields basically depend on the voltage levels and on the distances between the passenger and the corresponding power equipment (Coulomb's law). Similarly, magnetic fields depend on the current levels and on that same distances (Biot-Savart law). In other words, when these physical magnitudes do not change over time, both fields are not coupled and they can be studied separately.

However, most electrical systems, EVs included, are characterized by time-varying electric magnitudes. In the most general case, and according to Maxwell's equations, both fields are coupled and their dependence with respect to variables such as voltages and currents is much more complex than those given by Coulomb and Biot-Savart laws. Fortunately, it is not necessary to work with Maxwell's equations in many cases, in which quasistatic approximations are applicable. Specifically, when the frequencies of the electromagnetic phenomena are low—so that propagation speed can be considered infinite [7]—a quasistatic model can be used, which provides an intermediate solution between the most general dynamic case (Maxwell's equations) and the purely static case (Coulomb and Biot-Savart laws). In this sense, a quasistatic system evolves from one state to another as if it was a static system [8].

Depending on the particular quasistatic model employed (each variant represents a different approximation of Maxwell's equations), the simplifications adopted will vary. In this particular case, Darwin's model is used, which considers both capacitive and inductive effects and which incorporates magnetic field contribution to total electric field (Faraday's law) [8]. In Darwin's model, Biot-Savart law is directly applicable, the only difference being that currents and magnetic fields are time-varying variables. However, Coulomb's law must be extended to account for magnetic induction. In other words, magnetic fields still depend on currents and distances, but also on time, while electric fields depend on voltages, distances, time, and on magnetic fields.

Electric vehicles constitute an application in which quasistatic models are appropriate, since frequencies are generally low. There are basically two types of frequencies in an electrical drive, such as those propelling EVs:

1. Fundamental frequencies: These are the lowest frequencies in the system, and they are related to the operating point of the drive. For example, in a steady-state situation, fundamental frequency would be roughly 0 Hz (DC) for the battery current and 100 Hz for a 2000-rpm 50 Hz synchronous machine working at 4000 rpm in the flux-weakening region. During transients, some of these fundamental frequencies will show harmonic content. One example of this is power peaks in the batteries, which involve low-frequency harmonics in battery current. In general, fundamental frequencies will be very low, of the order of hundreds of Hertz at most. However, the absence of steady state in some situations, such as urban driving, implies a wide-frequency spectrum.

http://dx.doi.org/10.5772/64434

2. Switching frequencies: These frequency values and their corresponding harmonic components are given by the operation of power semiconductors such as insulated-gate bipolar transistors (IGBTs) and diodes. They are defined by many factors, starting with the modulation technique (hysteresis band, pulse width modulation (PWM), space vector modulation (SVM), direct torque control (DTC), etc.), and also on the inductance value of the corresponding filters. For those which use variable-switching frequency, its values will depend on the operating point as well.

   More importantly, switching frequencies change significantly with power electronics technology. For instance, there is a huge difference between conventional IGBTs, fast IGBTs, and silicon carbide (SiC) metal-oxide-semiconductor field-effect transistors (MOSFETs). The former usually work at frequencies ranging from 2 to 20 kHz. Fast IGBTs can reach up to 50 kHz in many applications, while SiC MOSFETs are already exceeding frequencies over 150 kHz. Given the voltage levels usually employed in commercial EVs, there is no way to exclude any of the above three major technologies, so all of them are eligible for this application.

In summary, magnetic field frequencies can change considerably from one vehicle to another. According to current EV designs, and considering the technologies implemented in them (conventional IGBTs, and synchronous or asynchronous machines), it seems reasonable to expect fundamental and switching frequencies up to 10 kHz, with relevant harmonic components up to 300 kHz. These values are classified as "low and extremely low frequencies" from the point of view of electromagnetic exposure. Be that as it may, electromagnetic fields generated by EVs present a relatively wide-frequency spectrum, from 0 Hz to hundreds of kHz.

2.2. Other considerations

There are many magnetic field generators in a vehicle, besides the traction drive itself. Examples present not only in EVs but also in conventional ICE-based vehicles are other power equipment such as the air-conditioning system, but also magnetized steel-belted tires, which are one of the main sources of extremely low-frequency magnetic fields in conventional vehicles. This unintentional magnetization is a consequence of the manufacturing process, and the result is a magnetic field whose frequency depends on the vehicle speed, ranging from 0 to 20 Hz [9, 10]. This field is of considerable strength but attenuates very quickly as distance increases. Hence, maximum exposure values usually take place in the area of the feet [11, 12]. According to some authors, this source of magnetic field is negligible when considering magnetic field exposure inside hybrid and electric cars [13], but this point is not completely clear.

Nonetheless, all magnetic field generators contribute to overall magnetic field exposure, and therefore should be included in EMR studies. It is important to state here that magnetic field exposure must be assessed globally (total magnetic field), and not individually (magnetic field generated by each device or piece of equipment). See Section 3.1 for further information and corresponding references about exposure assessment.

There are other factors that may influence magnetic field exposure in a positive way. For instance, the results presented in Ref. [14] suggest that the car body shell could behave as a minor magnetic shield for some frequencies. Therefore, constructive aspects such as the shape, material, and thickness of the body shell could affect magnetic exposure.

It is also convenient to consider which operating points are potentially more hazardous for human health. Under normal operation of the vehicle, power/current peaks will be higher during strong accelerations than during deep regenerative braking. This is due to two main reasons: the passive nature of some of the movement resistances (rolling resistance and aerodynamic drag), which implies that both of them will always oppose movement, and the global energy efficiency of the traction drive. Notice that driving style will heavily impact total magnetic exposure in EVs: the more aggressive the driving style the higher the magnetic fields within the vehicle.

Nevertheless, there is another situation which could involve potentially hazardous exposure for passengers, or even for pedestrians that are close to the vehicle: fast charging. As battery technology improves, higher recharge rates are achieved, which obviously imply higher currents, and hence stronger magnetic fields. Nowadays, charge rates of 2–4 C are already usual, with even higher values reachable in the near future [15, 16]. Therefore, magnetic field generation must be studied not only during normal operation of the vehicle but also during fast charging. As a general rule, it is highly advisable to remain outside of the vehicle, and at some distance from it, while fast charge is in process.

Finally, it is important to consider the wide variety of electric vehicles that exit nowadays, and how their different configurations, topologies, and power levels affect magnetic field exposure. Some considerations have already been mentioned in this chapter about vehicle configuration (front-wheel vs. rear-wheel traction, for instance; another example would be battery placement), and also about the power topology (significant differences arise when adding a DC-DC converter, or when using hybrid energy storage systems that combine batteries and supercapacitors for increased performance [17]). The largest differences, however, appear when considering electric vehicles of different types, such as motorbikes, buses, racing cars, or even electric planes [18, 19]. Magnetic exposure in these other vehicles could be very different when compared to electric cars, depending on the power levels involved and on the distances between the power equipment and the closest passengers.

3. Prevention guidelines and standards

Magnetic field exposure assessment is a two-step process: first, one must characterize the magnetic field inside the vehicle (either by estimation or by measurement). The second step involves determining whether the obtained values could be hazardous for the passengers. Both tasks can prove very challenging, and thus any guidance is welcome. In this sense, there are some standards and guidelines that help with the second step. This section is dedicated to these documents.

http://dx.doi.org/10.5772/64434

Concern regarding potentially hazardous consequences of nonionizing EMR started to raise some decades ago, around the 1950s and 1960s, first about radio waves and microwaves, and more recently about low-intensity fields as well, such as those generated by power lines, cell phones, and Wi-Fi devices. The effects of nonionizing electromagnetic fields on the human body have been studied for many years already, and the results are conclusive in some cases and inconclusive in others [20–23].

Basically, there are two types of effects that electromagnetic fields can have on biological tissues: short-term and long-term effects. Short-term effects, also known as acute effects, are those that appear instantaneously, or minutes after the beginning of the exposure. In general, these effects only take place under fields of considerable intensity, and disappear as exposure ceases. The biological mechanisms involved in these short-term effects are relatively well known, as well as the field values (intensity and frequency) that cause them [24–27]. They are usually classified into two main groups: electrostimulant effects and thermal effects. The former are caused by the interaction between low-frequency fields and living matter, either by polarization and dipole reorientation produced by electric fields, or due to induced currents generated by magnetic fields (for instance, a strong alternate magnetic field can induce electrical currents capable of stimulating nerves and muscles in an undesired way). The latter refer to the exchange of energy between fields and tissues, which rises their temperature. These thermal effects are completely negligible for frequencies under 100 kHz, but become relevant at higher frequencies (consider, for the sake of illustration, the operating principle of a microwave oven, whose working frequency is around 2.45 GHz). Electrostimulant effects are instantaneous, while thermal effects have a time constant of minutes.

Long-term effects, on the other hand, are those that could appear after months or years of exposure. Several studies have tried to determine the relationship between long-term exposure to electromagnetic fields and different pathologies (cancer, neurodegenerative disorders, etc.), without finding conclusive evidence for it. Approximately half of these studies show small correlations, just statistically significant, between long-term exposure and these illnesses [28]. In any case, the possibility of such relationships made the International Agency for Research on Cancer (IARC) to classify low-intensity, low-frequency electromagnetic fields, and also radiofrequency electromagnetic fields, as "possibly carcinogenic to humans (Group 2B)" [24, 25].

Generally speaking, it is extremely difficult to establish direct biological effects caused by long-term exposure, and to obtain reproducible results [23]. As a consequence, standards and guidelines to limit human exposure are elaborated based only on well-known, scientifically proven, short-term effects (with appropriate safety factors), and therefore long-term effects are not taken into account. This applies to the two most extended guidelines nowadays, those from the International Commission on Non-Ionizing Radiation Protection (ICNIRP) and those from the Institute of Electrical and Electronic Engineers (IEEE). Both are briefly described subsequently.

3.1. ICNIRP's guidelines

The most extended criteria for recommended exposure limit to EMFs were first proposed by the International Commission on Non-Ionizing Radiation Protection (ICNIRP) in 1998 [22]. These guidelines are based on current scientific evidence, as well as risk analysis performed by the World Health Organization (WHO). They establish protection recommendations considering well-known mechanisms and appropriate security factors, the latter being due mostly to scientific uncertainty.

Eleven years after their first publication, no new scientific evidence of any adverse effects had been found [29], a reason why a review of the guidelines on limitation to exposure to high-frequency EMFs (100 kHz to 300 GHz) was considered unnecessary. Nevertheless, concerning static EMFs and extremely low-frequency EMFs (1 Hz to 100 kHz), special guidelines were published in 2009 [30] and 2010 [31], respectively, in an attempt to include the results of the main scientific publications during those 11 years. The referred publications not only established recommended exposure limits to EMFs but also include explanations concerning the ways these fields could affect human health. These two guidelines suggest recommended exposure limits (which are defined in terms of in-body quantities such as electrical fields and induced currents in a given tissue, which complicates exposure assessment), but they also provide reference levels for the electromagnetic environment (external electrical and magnetic field values). These levels are extremely helpful to assess magnetic field exposure, since the following consideration is usually applied: if the exposure environment complies with the field reference levels, then it can be assumed that the exposure limits are not infringed. Certainly, exceeding these reference levels does not necessarily imply that the corresponding exposure limits have been breached. In such cases, further analysis is required.

Frequency (Hz)	Magnetic field H (Am^{-1})	Magnetic flux density B (T)
1–8 Hz	$3.2 \times 10^4/f^2$	$4 \times 10^{-2}/f^2$
8–25 Hz	$4 \times 10^3 / f$	$5 \times 10^{-3}/f$
25–400 Hz	1.6×10^2	2×10^{-4}
400–3 kHz	$6.4 \times 10^4/f$	$8 \times 10^{-2}/f$
3 kHz to 10 MHz	21	2.7×10^{-5}

Notes: H and B in unperturbed RMS values. In addition, reference levels relating to tissue-heating effects need to be considered for frequencies above 100 kHz.

Table 2. ICNIRP's reference levels for general public exposure to time-varying magnetic fields.

Regarding exposure limits to EMFs, different considerations arise depending on the person affected. Thus, there is an "occupational exposure," which is applied to those individuals who are exposed to EMFs as a result of performing their regular job activities. There is also a "general public exposure," which refers to the rest of the population. In summary, ICNIRP's reference levels for static magnetic fields are 400 mT for general public (EVs passengers

http://dx.doi.org/10.5772/64434

included) and 2 T for occupational public [30], whereas the Earth's magnetic field ranges from 30 to 60 μT, depending on the region on the Earth. Concerning time-variant fields, the exposure limits to EMFs for "general public" are given in **Table 2** and also in **Figure 3** [31]. Notice that these values correspond to a sinusoidal, single-frequency, homogeneous magnetic field exposure.

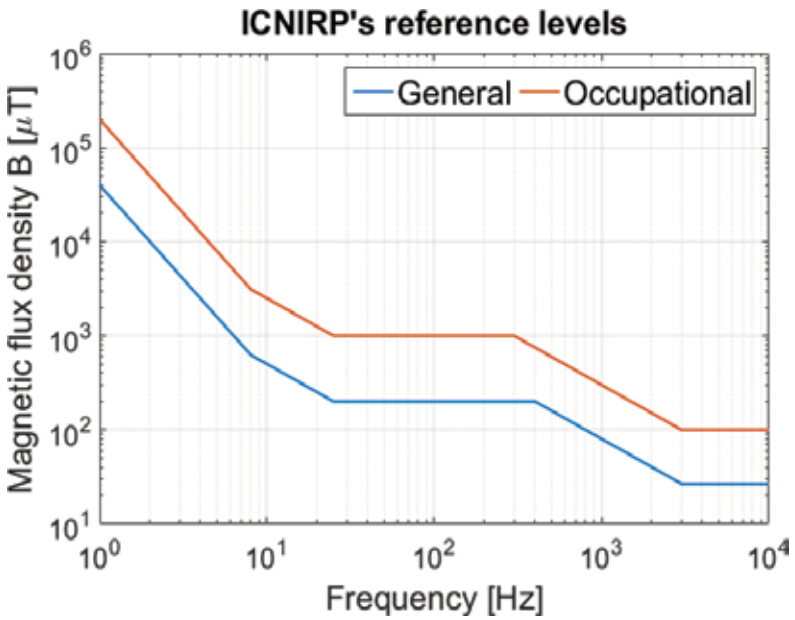

Figure 3. ICNIRP's reference levels for sinusoidal magnetic field exposure as a function of frequency (up to 10 kHz).

Notice that the above reference levels are not given as a function of time (exposure duration). They are maximum or absolute values that must never be breached. This is consistent with the fact that their corresponding exposure limits have been established based on short-term effects only. In other words, the above reference levels should guarantee the absence of harmful biological effects in the short term, based on current scientific evidence and in accordance to the experts' consensus-based criteria.

Regarding multiple frequency sinusoidal exposure, ICNIRP states that all contributions should be considered cumulative, so that the following global limit should be met:

$$\sum_{j=1\ \mathrm{Hz}}^{10\ \mathrm{MHz}} \frac{B_j}{B_{\mathrm{max},j}} \leq 1 \tag{1}$$

where B_j is the field magnitude at each given frequency, and $B_{\mathrm{max},j}$ is the reference level corresponding to that frequency. The expression for the magnetic field H is analogous.

In the case of nonsinusoidal exposure, the evaluation procedure consists in performing a frequency analysis to obtain the corresponding harmonic decomposition. After this, all harmonic components must be considered at the same time by means of Eq. (1). This methodology is simple, but very conservative, given that it assumes that all harmonic components are in phase (worst-case scenario), which is hardly real. This assumption is so pessimistic that even background noise can result in a breach of ICNIPR's reference levels if enough harmonic components are included in the calculation [32]. Consequently, a second method is recommended instead for those cases in which the number of harmonic component is considerable [31]. This alternative method consists in weighting the field components with a filter function (inverse Fourier transform) related to the reference levels [33]:

$$\left| \sum_i \frac{B_i}{EL_i} \cos(2\pi f_i \cdot t + \theta_i + \varphi_i) \right| \leq 1 \tag{2}$$

where EL_i is the reference level corresponding to the *i*th harmonic, whose frequency is f_i, while B_i and θ_i are the field amplitude and phase corresponding to that frequency, respectively, φ_i is the filter phase (also for that frequency), and t is the time. An example of implementation of the above method can be found in [9] and also in [34], in which Eq. (1) yields 99% with respect to ICNIRP's reference levels, while Eq. (2) decreases this result to 19%.

As aforementioned, ICNIRP's values are given for homogeneous exposure with respect to the whole extension of the human body. However, this assumption is not valid when magnetic field sources are close to the people affected, as might occur in an EV. Again, considering a heterogeneous exposure as homogeneous (taking maximum values as average values) results in a conservative approach. Other methods involve spatial averaging [35] or dosimetric analysis [31].

It is also important to clarify that these guidelines are not legally mandatory, and that become legally binding only if a country incorporates them into its own legislation [36]. At present, many countries and organizations have adopted these security limits. For example, the European Commission uses ICNIRP's guidelines to write regulations about EMR emission limits, applicable within the European Union [37]. Most member countries have therefore adopted these regulations, and some of them have even applied more restrictive criteria or have developed measures to legally enforce them.

3.2. IEEE's exposure standard

This subsection briefly describes the standard IEEE C95.6 [38]. This standard defines exposure levels to protect against adverse effects in humans from exposure to electric and magnetic fields at frequencies from 0 to 3 kHz.

Regarding long-term exposures to magnetic fields, the most recent reviews considered in the standard are the following: the International Commission on Non-Ionizing Radiation Protection (ICNIRP) [22], the International Agency for Research on Cancer (IARC) [24], the US

National Research Council (NRS) [39], the US National Institute of Environmental Health Sciences (NIEHS) [20, 40] the Health Council of the Netherlands [41], the Institution of Electrical Engineers [42], and the Advisory Group on Non-Ionizing Radiation (AGNIR) of the UK National Radiological Protection Board [43].

Because none of the above reviews concluded that any hazard from long-term exposure has been confirmed, this standard does not propose limits on exposures that are lower than those necessary to protect against adverse short-term effects. The purpose of this standard is just to define exposure standards for the frequency regime 0–3 kHz. For pulsed or nonsinusoidal fields, it may be necessary to evaluate an acceptance criterion at frequencies outside this frequency regime by means of a summation from the lowest frequency of the exposure waveform, to a maximum frequency of 5 MHz, as detailed in the standard itself [38].

Frequency (Hz)	Magnetic field H (Am^{-1})	Magnetic flux density *B* (T)
<0.153 Hz	9.39×10^4	118×10^{-3}
0.153–20 Hz	$1.44 \times 10^4/f$	$18.1 \times 10^{-3}/f$
20–759 Hz	719	0.904×10^{-3}
759 Hz to 3 kHz	$5.47 \times 10^5/f$	$687 \times 10^{-3}/f$

Notes: *f* is the frequency in Hz; MPEs refer to spatial maximum.

Table 3. IEEE's maximum permissible exposure to sinusoidal magnetic fields for general public: head and torso.

Frequency (Hz)	Magnetic field H (Am^{-1})	Magnetic flux density *B* (T)
<10.7 Hz	–	353×10^{-3}
10.7 Hz to 3 kHz	–	$3790 \times 10^{-3}/f$

Note: *f* is the frequency in Hz.

Table 4. IEEE's maximum permissible exposure to sinusoidal magnetic fields for general public: arms and legs.

In addition to the in situ electric field restrictions collected in the standard, but not discussed in this chapter, the in situ magnetic field below 10 Hz should be restricted to a peak value of 167 mT for the general public and up to 500 mT in a controlled environment. For frequencies above 10 Hz, a basic restriction on the in situ magnetic field is not specified in IEEE's standard. **Table 3** lists maximum permissible magnetic field limits (flux density *B*, and magnetic field strength *H*) corresponding to head and torso exposure for general public. The averaging time for a root-mean-square (RMS) measure is 0.2 s for frequencies above 25 Hz. For lower frequencies, the averaging time is such that at least five cycles are included in the average, but with a maximum of 10 s. In the same way, **Table 4** shows arm and leg exposure limits, also for general public. All these maximum exposure limits are based on avoidance of the following short-term reactions [38]:

- Aversive or painful stimulation of sensory or motor neurons.
- Muscle excitation that may lead to injury while performing potentially hazardous activities.
- Excitation of neurons or direct alteration of synaptic activity within the brain.
- Cardiac excitation.
- Adverse effects associated with induced potentials or forces on rapidly moving charges within the body, such as in blood flow.

IEEE's maximum permissible exposure values must be understood in the same way as INCIRP's reference levels. In this sense, compliance with **Tables 3** and **4** ensures compliance with the basic restrictions, which are defined in terms of in-body quantities. However, lack of compliance with these tables does not necessarily imply lack of compliance with the basic restrictions, but rather that it may be necessary to evaluate whether the basic restrictions have been met [38]. For more information, the reader is referred to the standard itself.

The information contained in **Tables 3** and **4** is also shown in **Figure 4** for clarity. Besides, ICNIRP's reference levels for general public are also included in the figure for comparison.

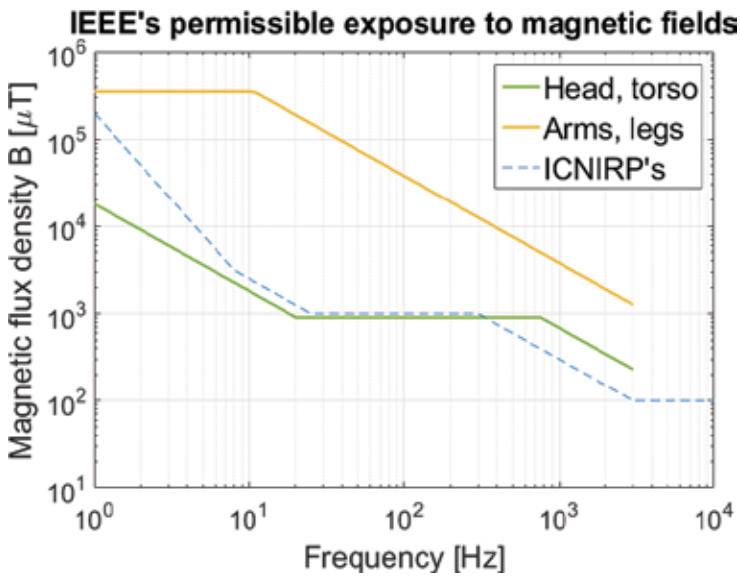

Figure 4. IEEE's maximum permissible exposure to sinusoidal magnetic fields as a function of frequency (up to 3 kHz).

4. State of the art

This section is devoted to a brief overview of recent publications that deal with EMR and magnetic field exposure in EVs. Some main conclusions, drawn for these studies, are sum-

marized here as well. Related publications, such as those that analyze EMC in electric vehicles or EMR in other applications, are also mentioned.

In general, there are not many publications about magnetic field exposure in electric and hybrid cars. Most works about electromagnetic fields and EVs address problems belonging to the field of EMC. Some examples of such studies can be found in [44–48]. There are certainly several publications that deal with EMFs and its potentially hazardous effects on human health, both from the medical and from the engineering points of view, but for other applications. A review of the medical literature is certainly out of the scope of this chapter, and hence the reader is referred to specialized bibliography such as [23–26, 28] for that purpose. Regarding engineering publications, one classical field of study are power lines [49–52], substations, and other transformation centers [49–54]. Most of these works focus on the effects of EMFs on workers (i.e., occupational exposure). Medical equipment in hospitals is another typical example of electromagnetic evaluation, again focusing on the people operating these machines on a daily basis. More recently, some studies have approached electromagnetic exposure from the point of view of general public, for example, in buildings and urban environments [55, 56]. The first studies in vehicles were probably those about electrical trains and trams, and also about conventional ICE-based cars [57–59].

In general, publications about EVs and EMR can be classified into two main groups: studies that perform measurements in vehicles (experimental approach) and studies that use analytical approximations or numerical simulations, usually based on the finite element method (FEM) (simulation approach). These two groups are treated separately in the following sections.

4.1. Magnetic field measurement in electric vehicles

One of the first publications specifically dedicated to EMR in hybrid and electric cars is the one by *ElectromagneticHealth.org* [60], which focuses on the 2004 Toyota Prius (second gene-ration). This preliminary study, which was motivated by a press article published in 2008, titled "*Fear, But Few Facts, on Hybrid Risks*," concludes that it is considerably difficult to perform repetitive and accurate measurements in a moving vehicle without the proper means. The magnetic field values obtained during this study were not high (always below 1 μT), but possibly higher than those found in conventional ICE-based cars. The rear seats were the most exposed, according to this work. One year later, in 2009, two more studies were published which included measurements in an electric car and in a hybrid bus, respectively, under dynamic driving conditions [13, 61].

The next two noteworthy publications, Ref. [58] from 2010 and Ref. [34] from 2013, describe some issues that should be taken into account when measuring magnetic fields in vehicles. The work in Ref. [58] deals mainly with trains and trams, but hybrid cars are also considered. Previous measurements performed in trains, locomotives, and railway stations by different researchers are summarized in that paper. Average results are provided for each type of vehicle considered in the study: 200 trains and trams (both urban and suburban), and also one hybrid car. Train and tram measurements were taken in varied conditions: weekdays and weekends, day and night, inside and outside. Regarding the hybrid car, different positions (front and rear parts, left and right sides, floor, seat, and head levels) were taken into account. Frequency

spectrum ranges from 5 Hz to 100 kHz. Magnetic field values found in the car are low (in the order of a few μT), especially when compared to ICNIRP's reference levels, although it is not clear which method was used to account for multifrequency exposure (see Subsection 3.1). In average, highest magnetic field values were found at the rear left side of the hybrid car. The maximum levels of recorded magnetic field strength are emitted at 12 Hz, which is a very low frequency. About the study published in [34], it provides an example of how to deal with multifrequency exposure in accordance to ICNIRP's recommendations. This work focuses on electric vehicles exclusively, and the magnetic field values obtained are in line with those from [13], around 15–20% of ICNIRP's reference levels. The paper also presents simulation results (see Subsection 4.2).

In 2015, two journal papers were published with measurement results from a wide variety of hybrid and electric cars [9, 10]. Some of their authors participated in the two publications from the previous paragraph. The study in [9] comprises a total of three conventional cars and eight electric vehicles, including some based on fuel cells instead of batteries. Both laboratory measurements and road measurements were taken and compared to INCIRP's reference levels with a wide-frequency range, up to 10 MHz. The vehicle that showed highest values reached 18% of ICNIRP's levels. Unsurprisingly, the researchers found that magnetic field exposure was higher in EVs than in ICE-based vehicles in average. However, the position of maximum exposure within each vehicle (front vs. rear part, foot vs. seat level) was different. This position is probably influenced by the configuration and topology of the vehicle, as described in Section 2. The main sources of magnetic field are identified in this study: at frequencies below 1 Hz, hundreds of μT are present (most likely due to battery current). Between a few Hz and 1 kHz, fields up to 2 μT were found, generated by most sources (combustion engine, steering pump, and wheels are mentioned in the paper, but probably fundamental currents in the inverter and in the electrical machine were also responsible). Finally, above 1 kHz, less than 100 nT was measured, and the authors identified the inverter as the only source (which makes sense, since it is the only power electronics device in the traction drive).

The open-access study in Ref. [10] focuses on diesel, gasoline, and hybrid cars. Up to 10 vehicles are analyzed, and the results are consistent with previous investigations. Results are presented separately for different seats and for different engine types. In general, magnetic field exposure was higher in hybrid cars, and then in gasoline cars. The authors state that magnetic field exposure depends on the operating conditions (speed, acceleration, etc.), which is unsurprising.

4.2. Magnetic field estimation by numeric simulations

Other research projects take a different approach and analyze the problem by means of finite element method (FEM) simulations and even analytical approximations. FEM simulations are helpful to better understand the problem, to analyze magnetic field exposure dependence on certain parameters (for instance, by performing sensitivity analysis), and to develop a predictive methodology. Being able to estimate magnetic field exposure without actually having to perform measurements could prove extremely useful for EV designers. As proposed in Ref.

http://dx.doi.org/10.5772/64434

[62], a fully operational estimation tool would allow for optimized predesign even before building the first prototype, thus reducing engineering time and cost.

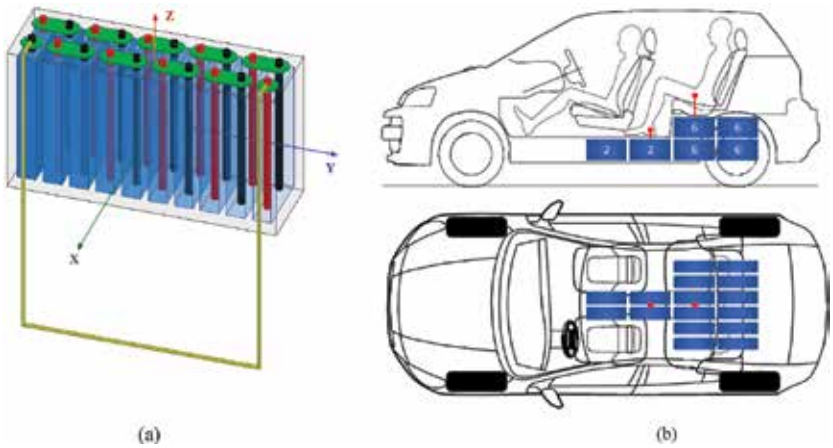

Figure 5. (a) FEM model used in Ref. [64] to estimate the magnetic field generated by one single NiMH battery cell. (b) Hypothetical battery pack belonging to a hypothetical EV analyzed in Ref. [64]. Both figures have been reused with permission.

This is the approach taken in Refs. [63, 64], works that analyze the magnetic field generated by the inverter and by the batteries, respectively, of a hypothetical EV via FEM simulations (**Figure 5**). Simulation results are validated with experimental measurements in both cases, and then they are used to estimate the worst operating points from the point of view of passenger exposure. Similarly, Refs. [14] and [34] contain two examples of how FEM simulations can be used for estimation and prediction purposes (**Figure 5**).

5. Design guidelines

In this section, some design guidelines and recommendations to minimize magnetic field exposure in EVs are provided. Note that all these measures are of pure electric nature, and therefore they may not be applicable when considering other factors. They are based on the ALARP principle ("As Low As Reasonably Practicable"). In other words, the goal is to maintain exposure levels as low as reasonably possible with the available means, both in a technical and in an economic sense. This criterion allows the implementation of safety strategies at an acceptable cost, and it should preferably be applied during the first design stages of the EV and its components.

These guidelines are classified into two groups, depending on whether they involve major changes in the vehicle or not. The first group contains measures that do not change the topology nor the configuration of the vehicle, and that do not increase its weight nor its cost:

- A general design guideline is to place the power devices and their connections as far from the passengers as possible. However, a vehicle usually provides little room to maneuver in this sense, especially in the case of hybrid electric vehicles. The battery stack, the electronic converters, and the motor should be as far away as possible from the passengers. Batteries are usually placed just under the seats, in order to minimize risks in case of crash. However, this involves bringing them closer to the passengers. A compromise should be reached.
- Complementary, power devices should be oriented so that the magnetic field suffered by the passengers is minimized. As described in Section 4, some power equipment such as batteries and inverters could generate stronger fields in some specific directions [63, 64]. Therefore, their relative direction with respect to the passengers should be carefully chosen.
- Wires of the same type should be as close as possible of each other: both DC wires must be taped together; similarly, the three-phase AC wires must be taped together, preferably in a triangular disposition. This way, the magnetic field generated by each cable in the interior of the vehicle will be cancelled by the rest.
- Wires should be as short as possible, except when this involves bringing them closer to the passengers.
- When placing batteries below the seats, the battery pack can be redesigned in order to allow terminals to be placed at the bottom. This would increase the distance from the stack connections to the passengers in a value equal to the height of the battery cells. This is very convenient, given that those connections are usually close to the occupants, they carry currents up to hundreds of amperes, and it is very difficult to place them together so the magnetic field generated by all of them as a whole is cancelled out. Naturally, the chemistry of the batteries must allow this inverted position, which is not a problem with lithium-based technologies. Notice that this action does not necessarily increase the distances between the passengers and the cells themselves.

If further actions were necessary in order to reduce the magnetic field generated by the EV, these additional measures may prove helpful:

- Longer distances between power equipment and passengers are always welcome. As discussed in Section 2, front-wheel traction drives are usually better suited to provide such longer distances.
- In the same sense, in-wheel motor technology [65] allows the devices inside an EV to be distributed in a much more flexible way. The space reserved for the conventional internal combustion motor could be occupied by the battery stack instead, which would mean that no field-generating devices would be placed under the seats.
- The higher the voltages, the lower the currents and the magnetic field, but the electric field could become higher (considering a quasistatic approximation [8], higher voltages, and higher du/dt will imply higher Coulomb electric field, but lower currents involve lower magnetic fields and thus lower Faraday electric field during transients [62]). Nonetheless, high on-board voltages may be hazardous in case of a crash, so once again a compromise would be necessary.

http://dx.doi.org/10.5772/64434

- A magnetic shield can be placed around the main devices responsible for the magnetic field in the interior of the car. Alternatively, the whole interior could be shielded, yielding higher protection at the expense of increased shield weight and cost. In both cases, the efficacy of the shield will be determined by its properties, and especially by its thickness. In the first case, a ferromagnetic alloy of high magnetic permeability, such as Mu-metal or similar, could be used [66]. For shielding the whole interior, ferromagnetic sheets such as those used to shield hospital rooms and some laboratories are recommended instead [67]. Notice that if switching frequencies grow above 100 kHz (by using SiC power devices, for instance), Faraday shielding could become necessary. This consist in radiofrequency shields made of copper or similar [67], such as those found in microwave ovens.

6. Discussion

Magnetic field exposure is a matter of growing concern in the society. Recently, low-intensity exposure is receiving much attention due to its possible hazardous effects on human health in the long term. However, uncertainty is high and there is still much research to be done. In this sense, short-term effects are proven and well known, while long-term effects remain to be found (although some theoretical bases and some experimental results point to the existence of potential hazardous effects [23]). With respect to EVs in particular, results presented so far in the scientific literature suggest that this concern is not scientifically justified, at least according to current standards and guidelines, which only take short-term exposure into account. In general, exposure levels in EVs are low when compared to ICNIRP's and IEEE's recommended levels, but high when compared to other daily exposures such as those suffered at home or at work. This increase in overall magnetic field exposure is what generates concern, despite the lack of scientific proof.

Uncertainty is not the only worrying aspect of magnetic field exposure in EVs. Some emerging and promising technologies, such as SiC power electronics, could pose a significant threat, given that they allow for higher switching frequencies. Certainly, there are many aspects involved, and therefore deep analysis is required before drawing any conclusions. However, it is clear that replacing silicon-based IGBTs with SiC MOSFETs could change the spectrum of the magnetic field inside the vehicle drastically, for better or for worse. In this sense, there are already a few publications that alert about a worsening in EMC phenomena when using SiC technology [68].

Paradoxically, some scientific results suggest that low-intensity low-frequency magnetic fields could have beneficial effects on human health. Certainly, these usually refer to medical treatments based on EMFs, but still knowledge is scarce about what will happen to EV passengers in the long term. Other experts have mentioned that even if magnetic fields have undesired effects on humans, it is perfectly possible that our bodies have inbuilt mechanisms to compensate for these effects [23]. Once again, further research is needed.

Finally, the authors would like to state that driving style has a strong influence on magnetic field exposure. In this regard, those drivers that favor aggressive styles (strong accelerations

and deep regenerative braking) will be exposed to stronger magnetic fields. Efficient driving does not only reduce fuel consumption and maintenance needs; it also reduces magnetic field exposure.

Acknowledgements

This work was partially supported by the Community of Madrid, which contributed to it through the SEGVAUTO-TRIES-CM Program (S2013/MIT-2713).

Author details

Pablo Moreno-Torres[1*], Marcos Lafoz[1], Marcos Blanco[1] and Jaime R. Arribas[2]

*Address all correspondence to: pablo.morenotorres.05@gmail.com

1 Electrical Engineering Department, CIEMAT (Spanish National Research Centre on Energy, Environment and Technology), Madrid, Spain

2 Technical University of Madrid, Spain

References

[1] B. Frieske, M. Kloetzke, F. Mauser. Trends in vehicle concept and key technology development for hybrid and battery electric vehicles. World Electric Vehicle Symposium and Exhibition (EVS27), Barcelona (Spain), 17–20 Nov. 2013.

[2] World Health Organization (WHO). The International EMF Project 1996. Available from: http://www.who.int/peh-emf/project/en/

[3] Car review specification: 2012 Mitsubishi I-MiEV. Available from: http://carspecprice.blogspot.com.es/2012/06/2012-mitsubishi-i-miev.html

[4] J. Cobb. Nissan Testing 250-Plus-Mile Range Leaf Mule With New Battery Chemistry. 14 Jun. 2015. Available from: http://www.hybridcars.com/nissan-testing-250-mile-range-leaf-with-new-battery-chemistry/

[5] G. Pasaoglu, D. Fiorello, A. Martino, L. Zani, A. Zubaryeva and C. Thiel. Travel patterns and the potential use of electric cars – Results from a direct survey in six European countries. Technological Forecasting and Social Change, Vol. 87, Issue 0, pp 51–59, 2014.

[6] G. Pasaoglu, A. Zubaryeva, D. Fiorello, C. Thiel. Analysis of European mobility surveys and their potential to support studies on the impact of electric vehicles on energy and infrastructure needs in Europe. Technological Forecasting and Social Change, Vol. 87, Issue 0, pp 41–50, 2014.

[7] J. D. Jackson. Classical Electrodynamics (3rd ed). Wiley, 1999. ISBN-13: 978-0471309321.

[8] J. Larsson. Electromagnetics from a quasistatic perspective. American Journal of Physics, Vol 75, Issue 3, pp 230–239, 2007.

[9] A. Vassilev, A. Ferber, C. Wehrmann, O. Pinaud, M. Schilling, A. R. Ruddle. Magnetic Field Exposure Assessment in Electric Vehicles. IEEE Transactions on Electromagnetic Compatibility, Vol 57, Issue 1, pp 35–43, 2015.

[10] R. Hareuveny, M. Sudan, M. Halgamuge, Y. Yaffe, Y. Tzabari, D. Namir and L. Kheifets. Characterization of Extremely Low Frequency Magnetic Fields from Diesel, Gasoline and Hybrid Cars under Controlled Conditions. International Journal of Environmental Research and Public Health, Vol 12, Issue 2, pp 1651–1666, 2015.

[11] S. Milham, J. B. Hatfield, R. Tell. Magnetic fields from steel-belted radial tires: Implications for epidemiologic studies. Bioelectromagnetics, Vol 20, Issue 7, pp 440–445, 1999.

[12] S. Stankowski, A. Kessi, O. Bécheiraz, K. Meier-Engel and M. Meier. Low frequency magnetic fields induced by car tire magnetization. Health Physics, Vol 90, Issue 2, pp 148–153, 2006.

[13] G. Schmid, R. Überbacher, P. Göth. ELF and LF magnetic field exposure in hybrid- and electric cars. Bioelectromagnetics Conference, Davos (Switzerland), 2009.

[14] A. R. Ruddle, L. Low. Impact of bodyshell on low frequency magnetic fields due to electric vehicle power cables. International Symposium on Electromagnetic Compatibility (EMC EUROPE), Rome (Italy), 17–21 Sept. 2012.

[15] M. Yilmaz, P. T. Krein. Review of Battery Charger Topologies, Charging Power Levels, and Infrastructure for Plug-In Electric and Hybrid Vehicles. IEEE Transactions on Power Electronics, Vol 28, Issue 5, pp 2151–2169, 2013.

[16] G. Pistoia (editor). Lithium-Ion Batteries. Advances and Applications. Elsevier, 2014. ISBN-13: 978-0-444-59513-3.

[17] A. Ostadi, M. Kazerani. Optimal Sizing of the Battery Unit in a Plug-in Electric Vehicle. IEEE Transactions on Vehicular Technology, Vol 63, Issue 7, pp 3077–3084, 2014.

[18] K. Rajashekara. Parallel between More Electric Aircraft and Electric/Hybrid Vehicle Power Conversion Technologies. IEEE Electrification Magazine, Vol 2, Issue 2, pp 50–60, 2014.

[19] A. Ostadi, M. Kazerani. A Comparative Analysis of Optimal Sizing of Battery-only, Ultracapacitor-only, and Battery-Ultracapacitor Hybrid Energy Storage Systems for a

City Bus. IEEE Transactions on Vehicular Technology, Vol 64, Issue 0, pp 4449–4460, 2014.

[20] National Institute of Environmental Health Sciences (NIEHS). Health Effects from Exposure to Power–Line Frequency Electric and Magnetic Fields. 1999. Available from: http://niremf.ifac.cnr.it/docs/niehs99.pdf

[21] World Health Organization (WHO). Electro-magnetic fields and public health: exposure to extremely low frequency fields. Geneva (Switzerland), 2007.

[22] International Commission on Non-Ionizing Radiation Protection (ICNIRP). Guidelines for Limiting Exposure to Time-Varying Electric, Magnetic, and Electromagnetic Fields (up to 300 GHz). Health Physics, Vol 74, Issue 4, pp 494–522, 1998.

[23] F. Barnes and B. Greenenbaum. Some Effects of Weak Magnetic Fields on Biological Systems: RF fields can change radical concentrations and cancer cell growth rates. IEEE Power Electronics Magazine. Vol 3, Issue 1, pp 60–68, 2016.

[24] International Agency for Research on Cancer (IARC). Non-Ionizing Radiation, Part 1: Static and extremely low frequency electric and magnetic fields (3rd ed). Lyon (France), 2002.

[25] IARC. Non-Ionizing Radiation, Part 2: Radiofrequency electromagnetic fields. Lyon (France), 2013.

[26] ICNIRP. Exposure to static and low frequency electromagnetic fields, biological effects and health consequences (0–100 kHz). Munich (Germany), 2003. ISBN-13: 978-3-934994-03-4.

[27] WHO. Environmental Health Criteria 238. Extremely low frequency (ELF) fields. Geneva (Switzerland), 2007.

[28] L. Kheifets and R. Shimkhada. Epidemiological studies of extremely low frequency electromagnetic fields. Chapter 6 in Biological and Medical Aspects of Electromagnetic Fields, pp 227–264. CRC Press, 2007. ISBN–13: 978-0-8493-9538-3.

[29] ICNIRP. Statement on the Guidelines for limiting exposure to time-varying electric, magnetic and electromagnetic fields (up to 300 GHz). Health Physics, Vol 97, Issue 3, pp 257–259, 2009.

[30] ICNIRP. Guidelines on limits of exposure to static magnetic fields. Health Physics, Vol 96, Issue 4, pp 504–514, 2009.

[31] ICNIRP. Guidelines for Limiting Exposure to Time-Varying Electric and Magnetic Fields (1 Hz – 100 kHz). Health Physics, Vol 96, Issue 6, pp 818–836, 2010.

[32] J. J. Nelson, W. Clement, B. Martel, R. Kautz and Nelson KH. Assessment of active implantable medical device interaction in hybrid electric vehicles. IEEE International Symposium on Electromagnetic Compatibility (EMC 2008), Detroit (USA), 18–22 Aug. 2008.

http://dx.doi.org/10.5772/64434

[33] K. Jokela. Restricting exposure to pulsed and broadband magnetic fields. Health Physics. 2000, Vol 79, Issue 4, pp 373–388.

[34] A. R. Ruddle, L. Low, A. Vassilev. Evaluating low frequency magnetic field exposure from traction current transients in electric vehicles. International Symposium on Electromagnetic Compatibility (EMC Europe 2013), Brugge (Belgium), 2–6 Sept. 2013.

[35] K. Jokela. Assessment of complex EMF exposure situations including inhomogeneous field distribution. Health Physics, Vol 92, Issue 6, pp 531–540, 2007.

[36] WHO. Framework for Developing Health-Based EMF Standards. Geneva (Switzerland), 2006.

[37] 1999/519/EC. Council Recommendation of 12th July 1999 on the limitation of exposure of the general public to electromagnetic fields (0 Hz to 300 GHz). Official Journal of the European Communities, pp 59–70, 1999.

[38] IEEE. Standard for Safety Levels with Respect to Human Exposure to Radio Frequency Electromagnetic Fields, 3 kHz to 300 GHz. IEEE Std C951-2005 (Revision of IEEE Std C951-1991), 2006.

[39] Committee on the Possible Effects of Electromagnetic Fields on Biologic Systems (NRC). Possible Health Effects of Exposure to Residential Electric and Magnetic Fields. National Academy Press, 1997.

[40] National Institute of Environmental Health Sciences (NIEHS). Assessment of Health Effects from Exposure to Power-line Frequency Electric and Magnetic Fields. 1998.

[41] K. Olden. Health Effects from Exposure to Power-Line Frequency Electric and Magnetic Fields. 1999.

[42] Health Council of the Netherlands. Exposure to Electromagnetic Fields (0 Hz–10 MHz). The Hague (Netherlands), 2000.

[43] The Institution of Electrical Engineers Biological Effects Working Party. The possible harmful biological effects of low level electromagnetic fields of frequencies up to 300 GHz. 2000.

[44] Advisory Group on Non-ionising Radiation (AGNIR). Report of an Advisory Group on Non-ionising Radiation. ELF Electromagnetic Fields and the Risk of Cancer. National Radiological Protection Board, 2001.

[45] M. C. Di Piazza, A. Ragusa, G. Vitale. Effects of Common-Mode Active Filtering in Induction Motor Drives for Electric Vehicles. IEEE Transactions on Vehicular Technology, Vol 59, Issue 6, pp 2664–2673, 2010.

[46] D. Hamza, M. Pahlevaninezhad, P. K. Jain. Implementation of a Novel Digital Active EMI Technique in a DSP-Based DC/DC Digital Controller Used in Electric Vehicle (EV). IEEE Transactions on Power Electronics, Vol 28, Issue 7, pp 3126–3137, 2013.

[47] A. R. Ruddle, R. Armstrong. Review of current EMC standards in relation to vehicles with electric powertrains. International Symposium on Electromagnetic Compatibility (EMC Europe 2013), Brugge (Belgium), 2–6 Sept. 2013.

[48] S. Jeschke, H. Hirsch. Investigations on the EMI of an electric vehicle traction system in dynamic operation. International Symposium on Electromagnetic Compatibility (EMC Europe 2014), Gothenburg (Sweden),1–4 Sept. 2014.

[49] M. C. Di Piazza, M. Luna, G. Vitale. EMI Reduction in DC-Fed Electric Drives by Active Common-Mode Compensator. IEEE Transactions on Electromagnetic Compatibility, Vol 56, Issue 5, pp 1067–1076, 2014.

[50] R. G. Olsen, P. S. Wong. Characteristics of low frequency electric and magnetic fields in the vicinity of electric power lines. IEEE Transactions on Power Delivery, Vol 7, Issue 4, pp 2046–2055, 1992.

[51] R. G. Olsen, D. C. James, V. L. Chartier. The performance of reduced magnetic field power lines: theory and measurements on an operating line. IEEE Transactions on Power Delivery, Vol 8, Issue 3, pp 1430–1442, 1993.

[52] A. R. Memari, W. Janischewskyj. Mitigation of magnetic field near power lines. IEEE Transactions on Power Delivery, Vol 11, Issue 3, pp 1577–1586, 1996.

[53] G. Filippopoulos, D. Tsanakas. Analytical calculation of the magnetic field produced by electric power lines. IEEE Transactions on Power Delivery, Vol 20, Issue 2, pp 1474–1482, 2005.

[54] W. Joseph, L. Verloock, L. Martens. General Public Exposure by ELF Fields of 150–36/11-kV Substations in Urban Environment. IEEE Transactions on Power Delivery, Vol 24, Issue 2, pp 642–649, 2009.

[55] A. S. Safigianni, C. G. Tsompanidou. Electric- and Magnetic-Field Measurements in an Outdoor Electric Power Substation. IEEE Transactions on Power Delivery, Vol 24, Issue 1, pp 38–42, 2009.

[56] K. H. Mild, M. Saudstrom, A. Johnsson. Measured 50 Hz electric and magnetic fields in Swedish and Norwegian residential buildings. IEEE Transactions on Instrumentation and Measurement, Vol 45, Issue 3, pp 710–714, 1996.

[57] D. Clements-Croome. Electromagnetic Environments and Health in Buildings (1st ed). Routledge, 2003. ISBN-13: 978-0415316569.

[58] Y. A. Kopytenko, N. G. Ptitsyna, M. I. Tyasto, V. Ismaguilov, G. Villoresi. Monitoring and Analysis of Magnetic Fields Onboard Transport Systems: Waveforms and Expo-

sure Assessment. 7th International Symposium on Electromagnetic Compatibility and Electromagnetic Ecology, 26–29 June 2007.

[59] M. Halgamuge, C. D. Abeyrathne, P. Mendis. Measurement and analysis of electromagnetic fields from trams, trains, and hybrid cars. Radiation Protection Dosimetry, Vol 141, Issue 3, pp 255–268, 2010.

[60] N. Dapeng, Z. Feng, X. Changwei, Q. Riqiang. Measurement and analysis of low frequency magnetic field in multiple unit train. IEEE 5th International Symposium on Microwave, Antenna, Propagation and EMC Technologies for Wireless Communications (MAPE 2013), 29–31 Oct. 2013.

[61] Electromagnetic Health Organization. EMF test of 2007 Toyota Prius hybrid. Available from: www.electromagnetichealth.org.

[62] R. Überbacher, G. Schmid, P. Göth. ELF magnetic field exposure during an inner-city hybrid bus ride. Bioelectromagnetics Conference, Davos (Switzerland), 2009.

[63] P. Moreno-Torres. Analysis and Design Considerations of an Electric Vehicle Powertrain regarding Energy Efficiency and Magnetic Field Exposure. PhD dissertation. Universidad Politécnica de Madrid, 2016. Available from: http://oa.upm.es/41040/.

[64] P. Concha Moreno-Torres, J. Lourd, M. Lafoz, J. R. Arribas. Evaluation of the Magnetic Field Generated by the Inverter of an Electric Vehicle. IEEE Transactions on Magnetics, Vol 49, Issue 2, pp 837–844, 2013.

[65] P. Moreno-Torres Concha, P. Velez, M. Lafoz, J. R. Arribas. Passenger Exposure to Magnetic Fields due to the Batteries of an Electric Vehicle. IEEE Transactions on Vehicular Technology, Vol 65, Issue 6, pp 4564–4571, 2015.

[66] C. Versèle, O. Deblecker, J. Lobry. Multiobjective Optimal Design of an Inverter Fed Axial Flux Permanent Magnet In-Wheel Motor for Electric Vehicles. In Electric Vehicles - Modelling and Simulations (1st ed). InTech, 2011. Available from: http://www.intechopen.com/books/electric-vehicles-modelling-and-simulations

[67] Magnetic Shield Corporation. All about shielding. 2015. Available from: http://www.magnetic-shield.com/faqs-all-about-shielding.html

[68] S. Celozzi, R. Araneo, G. Lovat. Electromagnetic Shielding. Wiley-IEEE Press, 2008. ISBN-13: 9780470055366.

[69] N. Oswald, P. Anthony, N. McNeill, B. H. Stark. An Experimental Investigation of the Tradeoff between Switching Losses and EMI Generation With Hard-Switched All-Si, Si-SiC, and All-SiC Device Combinations. IEEE Transactions on Power Electronics, Vol 29, Issue 5, pp 2393–2407, 2014.

Chapter 4

State of the Art of Magnetic Gears, their Design, and Characteristics with Respect to EV Application

Daniel Fodorean

Additional information is available at the end of the chapter

http://dx.doi.org/10.5772/64174

Abstract

This chapter briefly explains the advantage of using magnetic gears (MGs) for transportation applications. Usually, a traction EV unit consists of, besides the engine or motor, a mechanical gear. The drawbacks of using mechanical gears have been emphasized, especially with respect to high-speed motorization, where high transmission ratio can be reached only by connecting multiple gears in series. A magnetic gear is capable of overcoming these issues. The chapter presents a state of the art on the available MGs, with fixed or variable transmission ratio, pointing out their applicability. Next, the possible design approaches (harmonic, magnetic reluctance equivalent circuit, and vector potential) are introduced. Furthermore, the output performances (power and torque) of two types of studied MGs are evaluated, with emphasis on the main loss criteria: iron losses in all the active parts of the MG. Finally, the influence of several materials is observed by means of numerical computation in order to decide, based on specific configuration, the most suited variant for transportation and aeronautic applications.

Keywords: EV application, state of the art of magnetic gears, design, FEM numerical computation, iron loss

1. Introduction

Electric vehicles (EVs) offer promising solutions for sustainable transport, but their development is hampered by a number of technological challenges [1–10]. To be competitive with internal combustion engines, EVs must offer the same dynamics, range, comfort conditions, and be cost effective [1, 2].

Since 2012, there has been an increase in the number of electric cars running on highways [3, 6, 8]. Most of them are powered by permanent magnet synchronous machines (PMSM)—due to their high energy from rare earths materials used for excitation—and sometimes by DC motors (DCM), for Renault ZOE model, induction machines (IM), or Tesla-S model. **Table 1** presents few of the best-selling electric cars, in series production, with some technical characteristics and their cost/unit. Apart from Tesla-S model, which is extremely expensive, car manufacturers are generally proposing motorization variants with approximately the same performance and features. The best sold model today is the Nissan Leaf, launched in December 2010; by December 2016, it should reach over 200,000 units sold globally. Among European variants, Renault-Zoe and BMW-i3 are the bestsellers, noting that the German car manufacturer entered the market in the autumn of 2013 and by the end of this year, 2016, it should surpass 60,000 sold-ordered units. The number of electric units sold (globally surpassed the amount of 1 million units) is far from the number of internal combustion engine variants sold, one reason being the cost, in addition to the issue of autonomy. Basically, because of reduced autonomy and the reduced number of electric cars sold, the production cost/unit for EVs is high. Nevertheless, the trend is clear and with the increase in the number of supplying stations, the number of electric cars sold should increase exponentially.

Model	EM	EM power	Top speed	Autonomy	Other characteristics and price
Renault ZOE	DCM	43/65 kW	135 km/h	100 km	22 kWh/400 V Li-I battery; **27k€**;
Citroen C-ZEROs	PMSM	47 kW	130 km/h	100 km	Li-I battery; **30€**;
Peugeot iOn	PMSM	47 kW	130 km/h	100 km	Li-I battery; 0–100km/h:16s; **30k€**
Nissan Leaf	PMSM	80 kW	150 km/h	121 km	24 kWch Li-Manganate battery; **29k$**;
BMW-i3	PMSM	65 kW	150 km/h	130 km	360 V Li-I battery; 0–60 km/h:< 4 s; **41k$**;
Smart electric	PMSM	35 kW	125 km/h	145 km	Li-I battery; 0–60 km/h: 4.8 s; **20k$**
Mitsubishi i-MiEV	PMSM	49 kW	130 km/h	100 km	16 kW/330 V Li-I battery; **34k$**
Tesla S	IM	225 kW	193 km/h	335 km	60 kWh battery; 0–100km/h:<6s; **71k$**

Table 1. Some of the best-selling electric cars, in series production: propulsion's characteristics and approximate cost/unit.

An interesting perspective was presented by the EVIG institute in 2013, see **Figure 1**. In their estimation, at the end of 2016 the number of cars sold should reach 2 million, and by the end of 2020 we should expect to have about 6 million electric cars running on streets. It looks promising, and we need to leave it to time to confirm their estimation.

The autonomy range of electric cars is affected by the load capacity and the energy storage capability, which is directly influenced by the total weight of the car and the propulsion's efficiency [2]. Thus, a closer look at the propulsion system should be considered.

The components of the drive chain are the electrical propulsion (electrical machine and transmission), the converter, and the battery—the energy flow within the system's components

http://dx.doi.org/10.5772/64174

is bidirectional. The largest share of losses is in the electrical propulsion, 72%, on the static converter the loss is about 19%, and at the battery level the loss is about 9% (**Figure 2**).

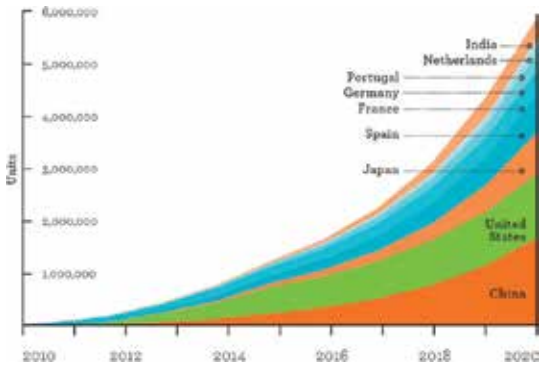

Figure 1. Perspective on the sold electric cars, worldwide.

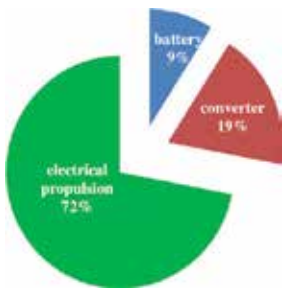

Figure 2. Losses in the propulsion system.

Therefore, acting mainly on the electrical propulsion by improving its efficiency and power density will improve the overall autonomy of the EV [3–5].

With regard to the existing propulsion solution, it can be seen that over time, the operating speed has substantially increased [11–19]. As an example, let us take a look at few series-manufactured cars: if in 2003, the electric motor of the Toyota-Prius-Hybrid was at 6000 r/min, the latest model is running at 12,000 r/min [9]; for the BMW-i3 model, the nominal speed is 4000 r/min, while the maximum speed (in flux-weakening operating conditions) is 11,800 r/min; for the present Mitsubishi-iMiev model, the speed of the motor is 9000 r/min. We can conclude that all car manufacturers are looking at increasing the speed of motorization, having in mind the improvisation of power density of the traction chain, as well as EV's autonomy.

In this context, we should recall that higher speeds are not easily and efficiently possible, since attached to the electric motor a gear is placed in order to transfer the torque-speed to the car's traction wheels. For a tire diameter of about 0.6 m and a circumferential speed of 1500 r/min coming from the gear, the vehicle's traveling speed is 47 m/s, meaning 169 km/h. In such a

case, even if we would like to increase the speed of the propulsion motor, a classic mechanical gear with high transmission ratio is difficult to obtain; usually, we consider cascaded gear units, but this will affect the global power density of the traction system and its efficiency. Thus, a solution is needed to overcome this drawback. In this context, the use of a magnetic gear (MG) could be the right solution.

In **Table 2**, a weight comparison of the possible motorization solutions is presented, based on personal experience or technical data found on the available equipment.

Component	**Electric propulsion**		
	Classic (low speed) with mechanical gear	**High speed (26000 r/min, water cooled) with mechanical gear in steps**	**High speed (26000 r/min, water cooled), magnetic gear with 1 fix step**
Motorization (30 kW)	130 kg	16 kg	16 kg
Gear	≈50 kg	≈80 kg	33 kg
Converter (30 kW/water cooled)		≈8 kg	
Battery (380 Vcc, 18 kWh)		≈200 kg	
Total weight	**≈388 kg**	**≈304 kg**	**≈257 kg**
Remarks	Increased volume and weight, acceptable efficiency	Decreased volume and weight, efficiency affected by the gear in steps	Reduced volume and weight, increased efficiency, limitation for wide-speed operation

Table 2. Comparison of traction chain weights for different configurations containing classic or magnetic gears.

For the sake of comparison, we have considered three possible variants: one motorization with 6500 r/min, another one with high-speed motor (running at 26,000 r/min), while the traction is used with a fixed mechanical gear ratio, or with multilevel gear (to reach the desired ratio), or when, for the same high-speed machine, we have a magnetic gear (MG) excited with rare earth material. **Table 2** shows how for the same converter and battery pack, high-speed motorization has a reduced weight with about 80 kg (with fixed mechanical gear). Otherwise, when using an MG with high transmission ratio, the performance and power density are high, while the weight of the entire propulsion system is decreased by about 130 kg—which is a huge win for an EV.

The detailed structure of a magnetic gear will be presented in the next section. Here, we should recall that the main materials found on a magnetic gear are the permanent magnet for excitation, and the steel. Thus, the MG has one important disadvantage: it is extremely expensive because the excitation (on both rotating parts—the low-speed rotors—which are interacting for the production of the torque) is generally made of Nd-Fe-B. According to **Table 3**, at the present time, the most important rare earth resources are found in Asia, particularly in China; even the European production is under Hitachi license—meaning that it is again an Asian license. Due to the monopoly imposed by Asian countries, the price of this type of

http://dx.doi.org/10.5772/64174

material reached 130 €/kg in 2010–2011 (from 50 €/kg in 2002), now being stabilized after a slight decrease at 100–110 €/kg. As a consequence, the European and other countries are trying to avoid this monopoly. Moreover, the global earth resources in terms of rare earth materials cannot cover today's industry needs.

Nd-Fe-B worldwide production, in 2013	×1000 (Tons)	%
China	70	~80
Japan	17	~19
EU	1.5	~1
Total	88.5	100

Table 3. Worldwide production of Nd-Fe-B at the 2013-year level.

As a result, an important decision was first taken in 2012, when the European Research Agency (ERA) said that it will not fund research projects that use rare earth materials, such as Nd-Fe-B or Sm-Co type; it is for this reason that research institutes and universities have lately reconsidered the use of ferrite material (5 €/kg) or the possibility to avoid any excitation material, by means of passive rotors, such as reluctance synchronous machines (RSM). Some others are trying to reduce the volume of rare earth materials, calling such machines as PM-assisted ones.

Otherwise, from previous research experience and information found in the literature, it has been observed that a magnetic gear with specific configuration of poles/teeth will induce specific torque ripples in the propulsion system [25–31]. Thus, when thinking of an MG, we are interested in finding an appropriate configuration which produces the lowest vibration and noise level. These elements will be considered with respect to the MG topic, while considering it for the EV application.

2. Principal of operation of magnetic gears, available topologies, and design approaches

A classic gear, meaning a mechanical one, which relies on the contact of two wheels with different number of iron teeth (see **Figure 3** left), has some important drawbacks. First of all, physical contact is needed, which involves local friction and heat (and consequently losses). Besides, lubrication is needed from time to time, in appropriate quantity. Moreover, the teeth are physically and irreversibly damaged with time due to material friction and fatigue. Thus, the losses increase after several hours/years of operation. All these disadvantages are eliminated in the case of a magnetic gear (MG). Above all, another important benefit of MG use should be indicated here: in order to obtain high transmission ratio, one should use complex gears, with more than two integrated wheels. Usually, two or more mechanical gears are cascaded (linked) in the transmission chain. Such configurations drastically affect the power

density and the efficiency of mechanical transmission. This is not the case for MGs: the most important amount of loss is found in the iron loss component, while the mechanical one (due to friction with the air and on the bearings) is in the same range as that of mechanical gears.

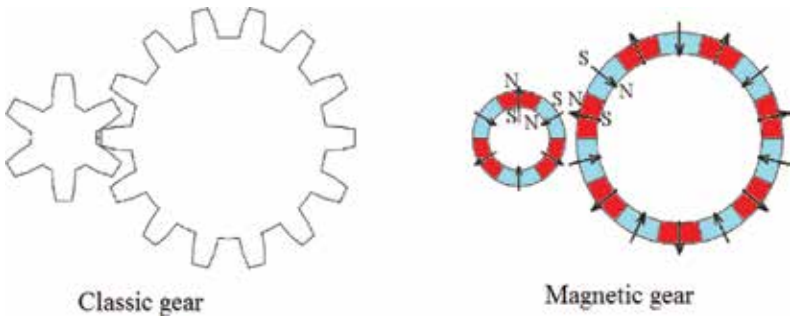

Figure 3. The classical (left) and magnetic (right) gears.

The first reference of a gear without mechanical contact dates back to 1916 [20, 34]. Since then, the benefits of MG were highlighted, namely: no need for lubrication, no local heating (no friction losses), and no risk of breaking the elements used to transfer power [20–41]. However, the first built viable solution dates to the 1980s (see a similar configuration of such an MG in **Figure 3** right)—evaluated from the torque capability point of view in [35]—but its efficiency was somewhere in the 25–30% range (only a part of magnetic poles was in active magnetic contact). The first efficient MG solution that fully exploits all the gear magnets dates back to early 2000 [20]—see **Figure 4**. Numerous other configurations of MGs have been proposed with time [21–41]. Some of these variants will be shown here in order to have a clue about the state of the art, but before that, we will see the principal of operation of a regular MG.

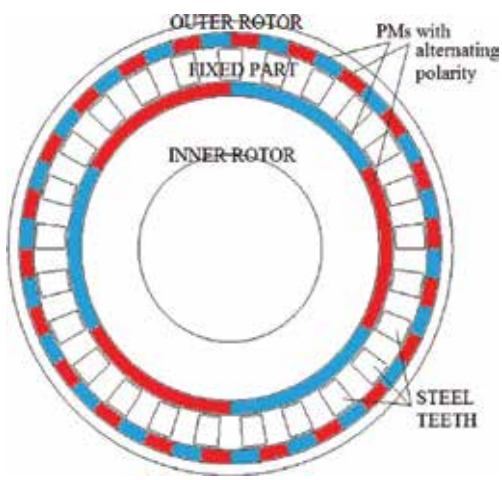

Figure 4. Cross section of the main elements of the active parts of an efficient MG.

http://dx.doi.org/10.5772/64174

2.1. Principal of operation

The operation of the MG is based on the modulation of the magnetic field created by the rotating magnetic poles of the high-speed rotor within the iron poles of the static part [20, 33]. The main components of such MG are shown in **Figure 4**. The field developed in the static iron will interact with the field created by the magnetic poles of the low-speed (outer) rotor and will force it to run in the opposite direction [20, 33].

It has been shown that the highest torque transmission is obtained with the following equality [20]:

$$p_{out} = N_s - p_{in} \tag{1}$$

where p_{in}, N_s, and p_{out} are the number of poles pair for the inner (high-speed) rotor, of the fixed iron part and of the outer (low-speed) rotor, respectively. The correspondences between the output (ω_{out}) and input (ω_{in}) speed and the gear ratio (gr) are:

$$\omega_{out} = -gr \cdot \omega_{in} \tag{2}$$

$$gr = -\frac{\omega_{out}}{\omega_{in}} = \frac{p_{in}}{p_{out}} \tag{3}$$

Besides, with a specific configuration of the MG, it is possible to obtain smooth mechanical characteristics—the lowest possible torque ripples are obtained if the ripples coefficient (k_r) equals unity (the ideal case) [33].

$$k_r = \frac{2 \cdot p_{in} \cdot N_s}{LCM(2 \cdot p_{in}, N_s)} \tag{4}$$

where *LCM* denotes the 'least common multiple' between the number of poles of the inner rotor and the fixed iron teeth.

These are just a few elements showing the operating principle of an MG in general. The analytical modeling of different MGs found in the literature will be summarized later, after the presentation of a detailed state of the art on the existent configurations.

2.2. State of the art of magnetic gears with fixed or variable transmission ratio

The first efficient MG, having radial configuration, was proposed by Attalah [20]. Next, other variants have been proposed. For example, in [34] a concentrated flux variant (or the so-called *spoke configuration*) was considered for the inner (high-speed) rotor; for the low-speed and high-torque rotor, the surface-mounted variant is almost exclusively used—because the surface-

mounted topology proposes the best power density, and because at low speed the risk of magnet's detaching is reduced. Such a topology, like the one presented in [34], is shown in **Figure 5**. This variant is again of radial flux. Thus, one could imagine all types of configurations for the high-speed rotor, which are usually used for classic permanent magnet synchronous machines (PMSM)—see different rotor configurations in **Figure 6**.

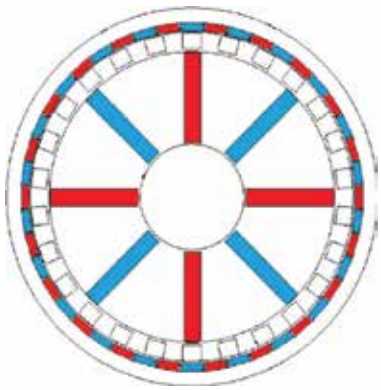

Figure 5. Cross section of flux-concentrated MG (spoke variant for the high speed rotor).

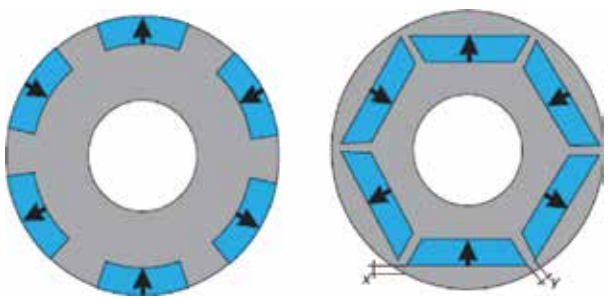

Figure 6. Possible rotor configurations for the radial flux MG: partially inset (left) and buried magnet (right) variants.

Since in an MG we are not interested in the flux-weakening capabilities of the structure itself, the structure with surface-mounted magnets based on Nd-Fe-B material on the high-speed rotor (shown in **Figure 4**) is almost exclusively used. When cheaper magnet material such as the ferrite is used, the concentrated flux (or spoke) variant can be considered (**Figure 5**). The partially or entirely inset magnet variants in **Figure 6** could be appropriate solutions when very high speeds are to be considered, in order to avoid the use of a consolidating ring of carbon or Titan material—which increases the air gap of the MG and drastically reduces its capability of producing the torque.

Axial flux variants [28, 29], such as the ones shown in **Figure 7**, have also been analyzed, since the axial configuration offers the best power density (due to reduced volume and weight on the passive elements: shaft and housing).

http://dx.doi.org/10.5772/64174

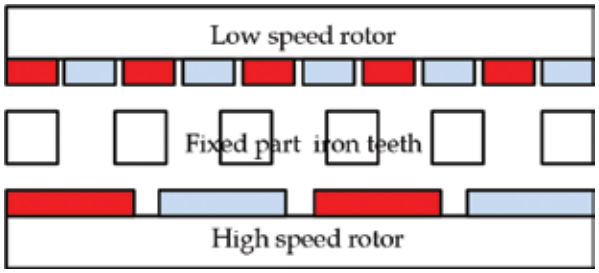

Figure 7. Axial flux MG configuration.

Usually, the MG is attached at the inner rotor side to an electric motor, to transfer the desired speed and torque to a load. In order to reduce the passive elements, some researchers have proposed integrated configurations. Such configurations are usually built on in-wheel motor variants, meaning that the motor has an inner stator and an outer rotor. Next, attached to the outer rotor is the inner rotor of the MG above, the static part with iron teeth, and on top of it the second rotor of the MG. Such compact variants have been studied in [26, 30, 31, 39, 40]. The transition from in-wheel motor to integrated MG-motor is shown in **Figure 8**.

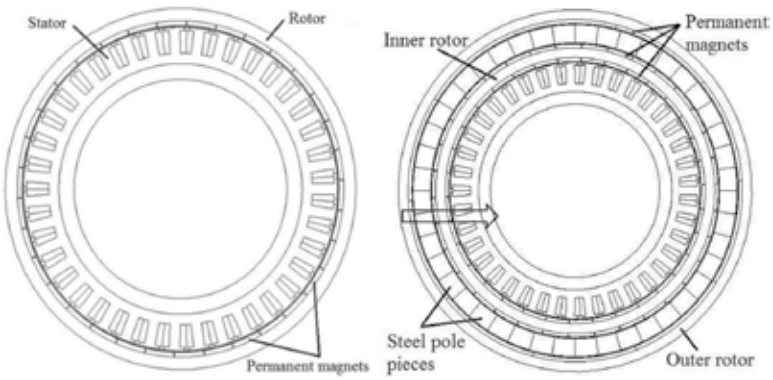

Figure 8. Transition from in-wheel motor to integrated MG-motor configuration [40].

Other types of MGs, such as the cycloid [27] and even the ones with variable transmission ratio [24, 29] have been proposed. Thus, we can emphasize that this topic is of real interest in the field of EVs (for the majority of applications) and power generation for wind turbines [39]. Next, the reader's attention will be focused on the existent analytical approaches that can be used for MG's design and modeling.

2.3. Analytical approaches for the design of MGs

There are three main design techniques for the analytical modeling of magnetic gears, similar to the case of electrical machines: the harmonic approach [25, 27, 30, 36], the magnetic reluctance equivalent circuit [22, 38], and vector potential algorithm [26, 28, 37, 41].

2.3.1. Analytical design of MG through harmonic approach

For the solution presented in [20], later we had the formularization of the operating principal, given by Atallah [36] and others [25, 27 , 30]. In order to express the torque produced by the two rotors rotating in opposite direction, we first need to express the flux density in the air gap. This flux density has two components: a radial and a tangential one. Also, the influence of the stationary part (the iron teeth) has to be evaluated as a modulating component.

The two components of flux density, the radial and tangential one, produced by the inner rotor of the MG, are:

$$\begin{cases} B_{rin} = \sum_{n=1,3,5}^{\infty} a_n \cdot \cos(n \cdot p_{in} \cdot (\theta - \omega_{in} \cdot t + \alpha_0)) \\ B_{tin} = \sum_{n=1,3,5}^{\infty} b_n \cdot \sin(n \cdot p_{in} \cdot (\theta - \omega_{in} \cdot t + \alpha_0)) \end{cases} \tag{5}$$

where a_n, b_n, and α_0 are the Fourier coefficients and the initial shift angle of the rotor. Next, the modulating component of the fixed iron teeth, similarly obtained, is function of Fourier coefficients and initial shift angle of this armature, meaning a_n, b_n, and α_0:

$$\chi = c_0 + \sum_{m=1}^{\infty} c_m \cdot \cos(m \cdot N_s \cdot (\theta + \beta_0)) \tag{6}$$

Similar to (5), one can get the flux density components to the outer rotor of the MG. In [30] some detailed formulation was given for the harmonic components with the pole pair number equal to ($n \cdot p_{in}$) and ($m \cdot N_s$ - $n \cdot p_{out}$), or equal to ($n \cdot p_{out}$) and ($m \cdot N_s$ - $n \cdot p_{in}$).

The torque produced by the inner and outer rotor is a function of the pull-out torque, T_{min} and T_{mout} (γ_0 is the shift angle of the outer rotor of the MG) [30]:

$$\begin{cases} T_{in} = T_{\min} \cdot \sin\left(\dfrac{N_s \cdot \beta_0 - p_{out} \cdot \gamma_0 - p_{in} \cdot \alpha_0}{p_{in}} \right) \\ T_{out} = T_{mout} \cdot \sin\left(\dfrac{N_s \cdot \beta_0 - p_{out} \cdot \gamma_0 - p_{in} \cdot \alpha_0}{p_{out}} \right) \end{cases} \tag{7}$$

2.3.2. Analytical design of MG through magnetic reluctance equivalent circuit

Based on the literature research, we have found a first approach on MG modeling through magnetic reluctance equivalent circuit in [22]. This approach is interesting because it also takes into account the steel material characteristic (through curve fitting). Actually, this paper was an adaptation of the method presented in [38] where the analytical design approach was applied to a brushless permanent magnet machine.

http://dx.doi.org/10.5772/64174

The method consists in computing the torque, as a function of a flux (Ψ_m) and magneto-motive force (F_m) product, produced in each element of the equivalent circuit. Such a magnetic reluctance equivalent circuit is shown in **Figure 9**.

$$T = \frac{n_\theta}{2 \cdot \pi} \cdot \sum_{j=1}^{n_\theta} \Psi_{mj} \times \Delta F_{mj} \tag{8}$$

where n_θ is the number of elements of reluctances on the considered equivalent circuit.

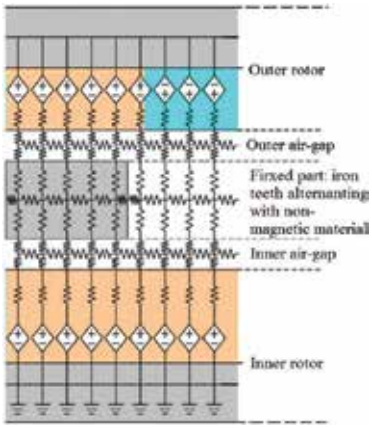

Figure 9. Magnetic reluctance equivalent circuit for MG design [22].

The magnetic flux is a function of the magnetic reluctance, which can be expressed through curve fitting for each specific material. For a certain iron sheet, the magnetic reluctance can be expressed as:

$$R(\Psi_m) = a_1 \cdot \frac{h}{S^1} \cdot \Psi^0 + a_n \cdot \frac{h}{S^n} \cdot \Psi^{n-1} \tag{9}$$

where h is the length of the flux for a specific trajectory and the S is the area of the flux on a specific element of the geometry—a or n index varies the function of material. These reluctances (and finally the fluxes) are calculated on radial and tangential direction.

The magneto-motive force, F_m, can be computed as well on each specific element, recalling that:

$$F_m = H_m \cdot h \tag{10}$$

where H_m is the magnetic field intensity calculated on each element of the magnetic circuit.

2.3.3. Analytical design of MGs through vector potential algorithm

The vector potential expressions, in both air gaps of the MG, have been detailed for radial and axial flux topologies in [28, 41]. Since the mathematical modeling for such an approach is quite laborious and goes beyond the scope of this state-of-the-art presentation of MGs, it will not be presented here. (It's worth mentioning that even the integral coefficients are detailed in the previous references; thus, the reader can investigate this topic if needed.)

With this, we have concluded a short presentation on the available analytical models used in the design of process of MGs. Next, we will consider two of the available configurations to evaluate their performances (in terms of iron loss and torque) and we will rapidly investigate the influence of certain materials used in the construction of MGs.

3. Characteristics of MGs with respect to their use in EV application

Two of the previously presented MG variants will be investigated here: the first one is an integrated motor-gear variant having an in-wheel configuration for the electric motor, and the second MG will be a high-speed variant with buried permanent magnets. Evaluation of the performances of these two topologies in terms of iron loss and torque (or output power) will be employed numerically, by means of finite element method (FEM) and the Flux2D software.

3.1. Integrated in-wheel motor magnetic gear topology

The considered in-wheel motor gear topology is the one presented in **Figure 8**. The motor is a fractional slot permanent magnet synchronous machine (FS-PMSM)—17 pairs of poles and 39 slots. Above the outer rotor of the FS-PMSM and attached to it, we have an inner rotor of the MG, having the same number of pairs of poles (p_{in}=17), and a reduced number of pairs of poles for the outer rotor of the MG (p_{out}=5). It means that the magnetic transmission will produce a higher speed, at a lower torque: it is a multiplier, or reversed gear [40]. Numerically computed results are shown in **Figures 10–12**.

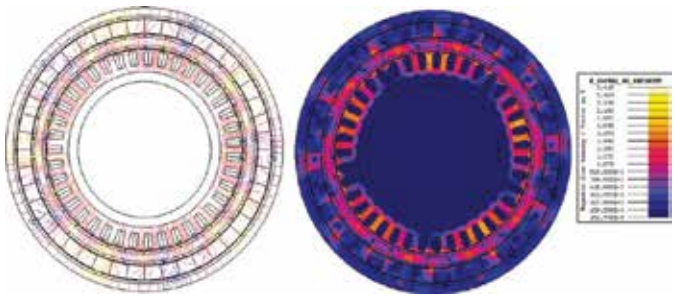

Figure 10. Integrated motor-gear analyzed variant, based on in-wheel motor: field lines (left) and flux density distribution (right) within the active parts.

http://dx.doi.org/10.5772/64174

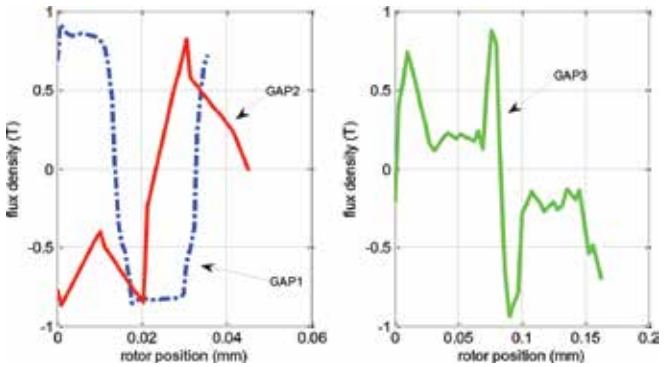

Figure 11. Air-gap flux density in the integrated motor-gear studied variant [40].

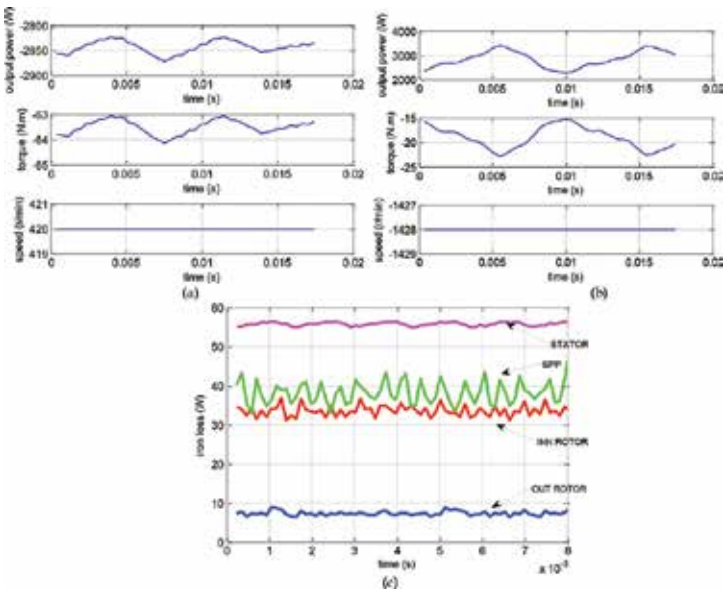

Figure 12. Performances of the integrated motor-gear studied variant: the speed-torque-power on the low speed rotor of the MG (a), for the high-speed outer rotor (b), and the iron loss in the active parts.

A first result of this analyzed integrated motor-gear variant is shown in **Figure 10**, where the field lines and flux density distribution within the active parts of the topology are presented. The reader can observe the influence of modulated teeth in the transfer of the flux (torque) from the inner to outer rotor. In the air gap layers of this machine-gear topology, the FEM software computed the following air gap flux densities, plotted in **Figure 11**: here, Gap1 refers to the in-wheel motor's air gap, Gap2 stands for the inner rotor air gap of the MG and Gap3 refers to its outer rotor air gap. More results are plotted in **Figure 12**.

The delivered torque and power, as well as the iron loss within the active parts of the integrated motor-gear studied variant are plotted in **Figure 11**. Some torque ripples can be identified, both on the inner and on the outer rotors of the integrated motor-gear variant. Since the major loss component within an MG is the iron loss, it is obvoius that the efficiency of the transmission is very low. One could sum the iron loss components (for the inner and outer rotor, as well as for the static part poles or teeth—SPP) and of the in-wheel motor to get 130 W. These results are not optimized. Based on the image of the flux density distribution (**Figure 10** right), we could consider to reshape the teeth's geometry and the outer rotor yoke, in the perspective of increasing the efficiency.

In order to prove the important advantage of MGs against classic mechanical gear, that is the possibility to obtain a very high transmission ratio for high-speed applications, and to get a very compact magnetic traction system with very good power density, the reader's attention will be oriented toward a high-speed MG.

3.2. MG with buried permanent magnets for high-speed applications

The second analyzed MG is with high-speed inner rotor, running at 26,000 r/min (with p_{in}=1), and outer rotor for low-speed rotor (with p_{out}=15) running at approximately 1500 r/min. The number of static part iron teeth is N_s=16. The magnets are buried in order to avoid the surface-mounted pieces which need a consolidating ring. A preliminary check on the mechanical resistance of the inner rotor steel needs to be employed numerically, to check if the iron bridges have not been damaged during MG's operation. A cross section of the high-speed MG is shown in **Figure 13**.

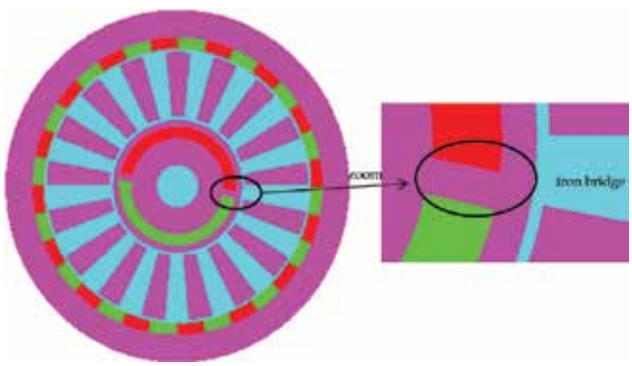

Figure 13. The high-speed MG studied variant.

This MG will be evaluated for different steel material characteristics (M335, M400, and Vacoflux48), and permanent magnet types (Nd-Fe-B, Ferrite, Alnico). As a reference variant, the MG with Nd-Fe-B and M400 steel is considered. The first result of this configuration is shown in **Figure 14**, where the field lines and flux density distribution are shown. An obvious saturation is found on the inner rotor core, on the iron's bridge, which is normal behavior since the flux needs to pass the air gap.

http://dx.doi.org/10.5772/64174

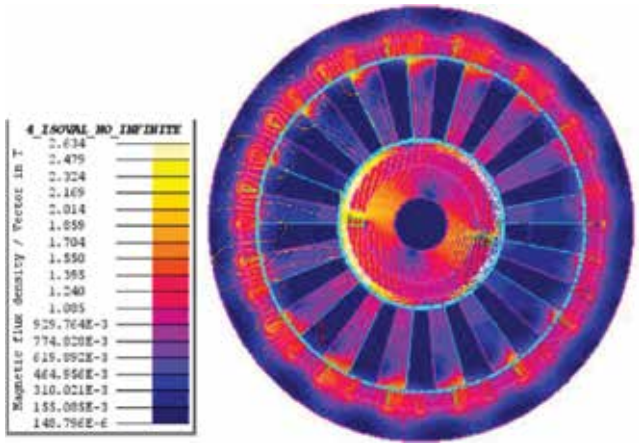

Figure 14. The field lines and flux density distribution within the active parts of the high-speed MG.

Some transient simulations were carried out in Flux2D. In **Figures 15–17** are presented the simulated results for the case of an MG with M400 steel used for all cores and armature, and Nd-Fe-b as magnet material. Here, the output power and torque as well as the iron losses in the active parts of the structure are plotted. Very smooth mechanical performances have been obtained with such configuration of MG, with 1/16 ratio. The amount of iron loss in this case is about 800 W.

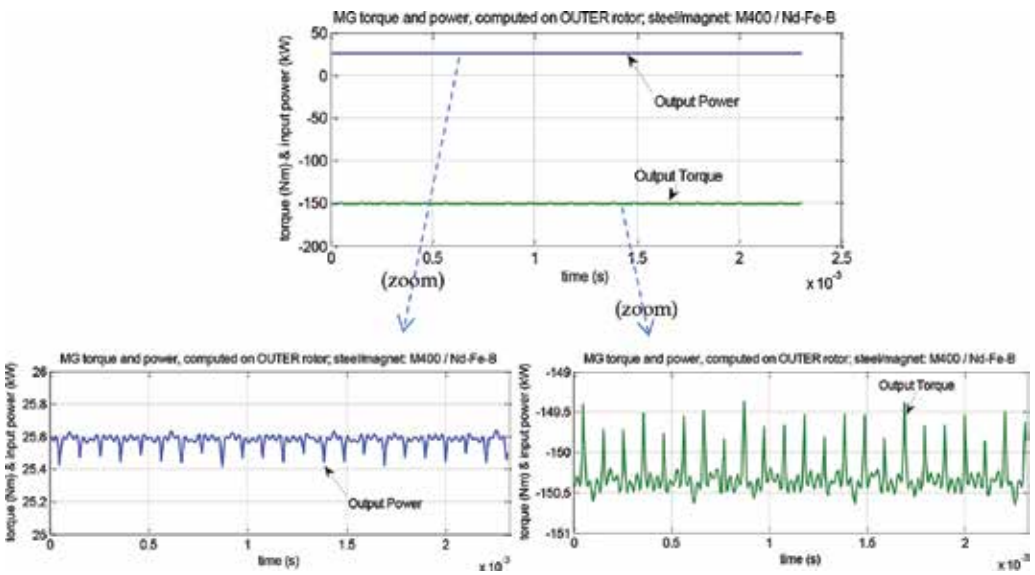

Figure 15. Simulated results for the MG with M400 steel and Nd-Fe-B magnet: input and output power [40].

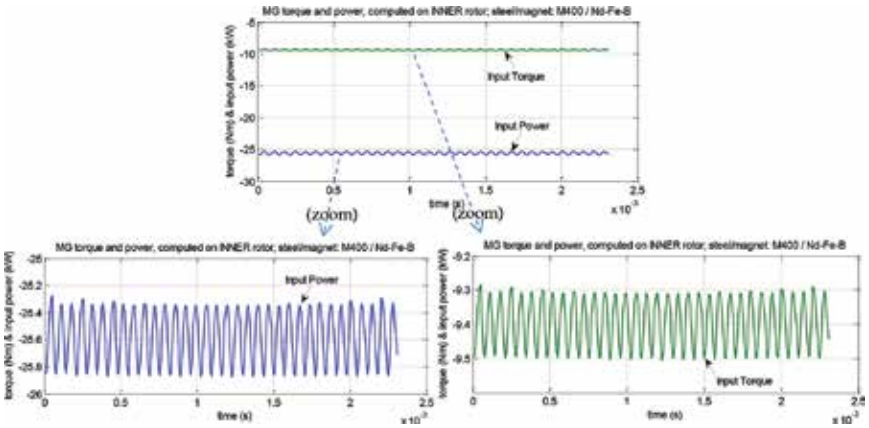

Figure 16. Simulated results for the MG with M400 steel and Nd-Fe-B magnet: input and output torque [40].

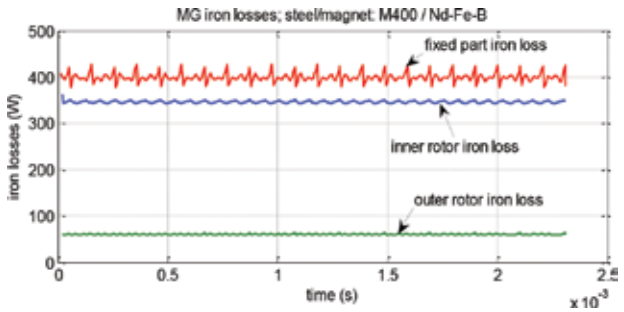

Figure 17. Simulated results for the MG with M400 steel and Nd-Fe-B magnet: iron losses in the active parts [40].

Now, let us see what happens if better material is used, such as the Vacoflux48 steel, which has a very narrow hysteresis curve. The iron loss results are given in **Figure 18**. (The mechanical output performances are not given here; only the amount of iron loss in the fixed iron teeth, inner, and outer rotor of the MG.)

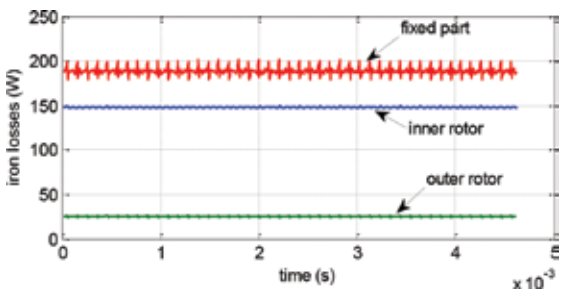

Figure 18. Simulated iron losses for the MG with Vacoflux48 steel and Nd-Fe-B magnet [40].

An amount of 365 W of iron loss was computed here. By comparing these iron losses (for the M400 steel, given in **Figure 17**, and the ones from **Figure 18**, for Vacoflux48), the huge advantage of the structure equiped with Vacoflux material is obvious, for which the iron loss is less than half of the M400—which is neither a bad material nor a cheap one. Of course, products based on Vacoflux48 are rather exclusive units and meant for special applications (like racing cars)—the cost of one prototype is almost prohibitively expensive. For ordinary applications, even the M400 steel is considered an expensive material—it is usually used for prototypes and low series manufacturing. Otherwise, a cheaper variant based on M335 is suitable in terms of output performances, giving similar results as the ones using M400.

A more complete comparison of the performances of the high-speed MG, when equipped with different types of materials and their magnetical characteristics is given in **Tables 4** and **5**—the width of the considered steel sheet (0.2, 0.35, and 0.5mm) is given also in **Table 4**.

Property	Material					
	PM			Steel		
	Nd-Fe-B	Alnico	Ferrite	M400 (0.5 mm)	M335 (0.35 mm)	Vacoflux48 (0.2 mm)
Remnant flux-density	1.35 T	1.27 T	0.45 T			
Relative magnetic permeability	1.05	1	16	~4000	~4000	~4000
Magnetic field intensity (coercivity at saturation)	−930 kA/m	−51.5 kA/m	−300 kA/m	50 kA/m	5 kA/m	1.9 kA/m
Saturation flux-density				2 T	1.6 T	2.25 T

Table 4. The properties of the materials used in the construction of the high-speed MG.

Materials	Parameter				
	T_{in} (Nm)	T_{out} (Nm)	Ripple of T_{in} (%)	Ripple of T_{out} (%)	Total Pfe (W)
Nd-Fe-B + M400	9.34	150.3	2.14	0.79	806.9
Alnico + M400	0.82	13.14	1.82	0.68	51.9
Ferrite + M400	0.637	10.18	3.3	0.98	22.9
Nd-Fe-B + M335	9.34	150.3	2.35	0.86	870
Nd-Fe-B + Vacoflux48	9.34	150.3	1.68	0.84	396.6

Table 5. Comparison of different configurations (material based) of MGs.

Some comments need to be made with respect to the Alnico and ferrite, the results of which are summarized in **Table 4**: for this specific configuration of the MG, because of the iron bridge which needs to support important centrifugal forces (we recall that the high-speed rotor is running at 26,000 r/min), and the low level of remanent flux density (for Ferrite material) or

coercivity (for Alnico), the magnetic flux is not sufficiently strong to cross the air gap. Different rotor configurations (with concentrated flux or halback array) need to be considered—which means that a topology with more than one pair of poles is requested. To prove this, one can investigate the field lines and the flux densities depicted in **Figure 16**, given within the active parts of the MG while ferrite or Alnico materials are used (**Figure 19**).

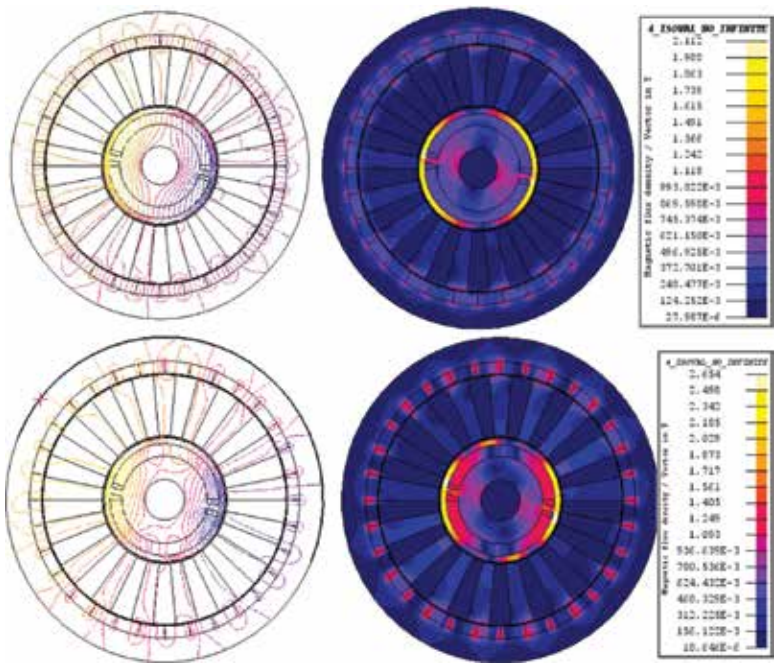

Figure 19. Investigation of the MG field lines and flux density distribution, when ferrite (top) and Alnico (bottom) magnets were considered.

As 15 years have passed since the first efficient MG proposition, we could expect, in the next years, improvements in the field of MGs, especially for the ones with variable transmission ratio, which could be extremly useful in transportation and aeronautical domains. With the advancement in the field of materials, for rare earth materials and ferromagnetic steel, the future of fully electromagnetic propulsion systems could be considered as a viable industrial solution, and not only a new research subject.

4. Conclusions

This chapter proposes an overview of the challenges in EV application, where the speed limits were pushed forward in the last decade. Practically, all the car manufacturers are proposing mobility solutions based on electrically propelled traction systems, which are limited because of the drawbacks of the mechanical gear, which needs to be continuously lubricated, presenting

important heat and local losses; moreover, higher speeds drastically decrease the power density of motorization. To overcome these drawbacks, researchers have proposed in the last decade possible solutions based on magnetic gears (MGs). We have presented in this chapter the existent configuration of fixed transmission ratio MGs, we have also indicated some references in which the variable transmission was studied and we have presented the main analytical approaches used for the design of MGs: the harmonic, magnetic reluctance equivalent circuit, and vector potential algorithms. A quasi-complete reference list was given with respect to this topic. Next, we have investigated two variants of MG, one with integrated motor and a second one for high-speed applications and a transmission ratio of 1/16. Through numerical computation we have investigated the output mechanical performances of the studied MGs, as well as the major loss component of such devices: the iron loss within the active parts of the MG. The influence of different materials on the active parts, meaning ferromagnetic steel and permanent magnets, was evaluated and a comparison of the obtained performances was depicted.

The research on MG has gained interest in the last decade and we expect that based on advancements in materials, the performances of these devices will be even more improved and will be of real interest, especially in the field of transportation and aeronautics.

Acknowledgements

This work was supported by a grant of the Romanian National Authority for Scientific Research and Innovation, CNCS—UEFISCDI, project number PN-II-RU-TE-2014-4-1143 (TE30/2015).

Author details

Daniel Fodorean

Address all correspondence to: daniel.fodorean@mae.utcluj.ro

Faculty of Electrical Engineering, Department of Electrical Machines and Drives, Technical University of Cluj-Napoca, Cluj-Napoca, Romania

References

[1] A.E. Fuhs. Hybrid vehicle and the future of personal transportation. Boca Raton, Florida, USA: CRC Press, 2009.

[2] J. Larminie and J. Lowry. Electric vehicle technology explained. 2nd edition. West Sussex, England: Wiley, 2012.

[3] D. Fodorean, F. Jurca, M. Ruba, and D.C. Popa. Motorization variants for light electric vehicles – design, magnetic, mechanical and thermal aspects. Cluj-Napoca, Romania: AlmaMater June 2013.

[4] J. De Santiago, et al. Electrical motor drivelines in commercial all-electric vehicles: a review. IEEE Transactions on Vehicular Technology, vol. 61, no. 2, pp. 475–485, Feb. 2012.

[5] I. Husain. Electric and hybrid vehicles: design fundamentals. 2nd edition. Boca Raton, Florida, USA: CRC Press, 2011.

[6] M. Ehsani, Y. Gao, and A. Emadi. Modern electric, Hybrid electric, and Fuel cell vehicles: fundamentals, theory, and design – 2nd edition, CRC Press, Boca Raton, Florida, USA, 2010.

[7] C.W. Wessner. Building the U.S. battery industry for electric drive vehicles. The National Academies Press, USA, 2012.

[8] G. Pistoia. Electric and hybrid vehicles: power sources, models, sustainability, infrastructure and the market. Boca Raton, Florida, USA: CRC Press, 2010.

[9] R. James. Hendershot tutorial at ICEM conference, Berlin, 2–5 September, 2014: Electric Machine Design Strategies to Achieve IE2, IE3 & HEM (IE4) Efficiencies.

[10] 17th of June, 2016 http://www.osvehicle.com.

[11] D. Fodorean. Study of a high speed motorization with improved performances dedicated for an electric vehicle. IEEE Transactions on Magnetics, vol. 50, no. 2, Feb. 2014, paper no. 7022804.

[12] F. Luise, et al. Design and technology solutions for high-efficiency high-speed motors, ICEM 2012, Marseille, France, Sep. 2012, pp. 157–163.

[13] A. Tenconi, S. Vaschetto, and A. Vigliani. Electrical machines for high-speed applications: design considerations and tradeoffs. IEEE Transactions on Industrial Electronics, vol. 61, no. 6, pp. 3022–3029, 2014.

[14] G. Pellegrino, A. Vagati, B. Boazzo, and P. Guglielmi. Comparison of induction and PM synchronous motor drives for EV application including design examples. IEEE Transactions on Industry Applications, vol. 48, no. 6, pp. 2322–2332, Nov/Dec. 2012.

[15] D. Gerada, A. Mebarki, N.L. Brown, K.J. Bradley, and C. Gerada. Design aspects of high-speed high-power-density laminated-rotor induction machines. IEEE Transactions on Industrial Electronics, vol. 58, no. 9, pp. 4039–4047, Sept. 2011.

[16] K. Sung-Il, K. Young-Kyoun, L. Geun-Ho, and H. Jung-Pyo. A novel rotor configuration and experimental verification of interior PM synchronous motor for high-speed applications. IEEE Transactions on Magnetics, vol. 48, no. 2, pp. 995–998, 2012.

[17] D.P. Marcetic, I.R. Krcmar, M.A. Gecic, and P.R. Matic. Discrete rotor flux and speed estimators for high-speed shaft-sensorless IM drives. IEEE Transactions on Industrial Electronics, vol. 61, no. 6, pp. 3099–3108, June 2014.

[18] R.R. Moghaddam, F. Magnussen, and C. Sadarangani. Theoretical and experimental reevaluation of synchronous reluctance machine. IEEE Transactions on Industrial Electronics, vol. 57, no. 1, pp. 6–12, Jan. 2010.

[19] J.-H. Seo, T.-K. Chung, C.-G. Lee, S.-Y. Jung, and H-K. Jung. Harmonic iron loss analysis of electrical machines for high-speed operation considering driving condition. IEEE Transactions on Magnetics, vol. 45, no. 10, pp. 4656–4659, Oct. 2009.

[20] K. Atallah and D. Howe. A novel high-performance magnetic gear. IEEE Transactions on Magnetics, vol. 37, no. 4, pp. 2844–2845, Jul. 2001.

[21] M. Aubertin, A. Tounzi, and Y. Le Mach. Study of an electromagnetic gearbox involving two permanent magnet synchronous machine using 3-D-FEM. IEEE Transactions on Magnetics, vol. 44, no. 11, pp. 4381–4384, Nov. 2008.

[22] M. Fukuoka, K. Nakamura, and O. Ichinokura. Dynamic analysis of planetary type magnetic gear based on reluctance network analysis. IEEE Transactions on Magnetics, vol. 47, no. 10, pp. 2414–2417, Oct. 2011.

[23] E. Gouda, S. Mezani, L. Baghli, and A. Rezzoug. Comparative study between mechanical and magnetic planetary gears. IEEE Transactions on Magnetics, vol. 47, no. 2, pp. 439–450, Feb. 2011.

[24] D. Fodorean. Magnetic gear with transmission ration in steps (original title in Romanian) – patent proposal, A/00869/17.11.2014.

[25] J. Rens, R. Clark, S. Calverley, K. Atallah and D. Howe. Design, analysis and realization of a novel magnetic harmonic gear. In: Proceedings of the 2008 International Conference on Electrical Machines Paper ID 1454, Villamoura, Portugal, 2008.

[26] Linni Jian, Guoqing Xu, Chunting Chris Mi, K.T. Chau, and C.C. Chan. Analytical method for magnetic field calculation in a low-speed permanent-magnet harmonic machine. IEEE Transactions on Energy Conversion, vol. 26, no. 3, pp. 862–870, Sept. 2011.

[27] F.T. Jørgensen, T.O. Andersen, and P.O. Rasmussen. The cycloid permanent magnetic gear. IEEE Transactions on Industry Applications, vol. 44, no. 6, pp. 1659–1665, Nov/Dec. 2008.

[28] T. Lubin, S. Mezani, and A. Rezzoug. Development of a 2D analytical model for the electromagnetic computation of axial-field magnetic gears. IEEE Transactions on

Magnetics, Institute of Electrical and Electronics Engineers, 2013, DOI: 10.1109/TMAG.2013.2267746.

[29] Mu Chen, Kwok-Tong Chau, Christopher H. T. Lee, and Chunhua Liu, Design and analysis of a new axial-field magnetic variable gear using pole-changing permanent magnets. Progress in Electromagnetics Research, vol. 153, pp. 23–32, 2015.

[30] Linni Jian, K.T. Chau, and J.Z. Jiang, An integrated magnetic-geared permanent magnet in-wheel motor drive for electric vehicles. IEEE Vehicle Power and Propulsion Conference (VPPC), September 3–5, 2008, Harbin, China.

[31] P.O. Rasmussen, H.H. Mortensen, T.N. Matzen, T.M. Jahns, and H.A. Toliyat. Motor integrated permanent magnet gear with a wide torque-speed range. IEEE Energy Conversion Congress and Exposition, 2009. ECCE 2009, 20–24 September 2009, San Jose, California, USA. pp. 1510–1518.

[32] D. Fodorean, C. Irimia, and P. Minciunescu. Performances evaluation of a magnetic gear with high transmission ratio used for high speed applications, Progress in Electromagnetics Research Symposium, Prague, Czech Republic, 06–09 July, 2015, pp. 627–631.

[33] D. Fodorean. Study of a high speed motorization with improved performances dedicated for an electric vehicle. IEEE Transactions on Magnetics, vol. 50, no. 2, paper no. 7022804, Feb. 2014.

[34] P. Rasmussen, T. Andersen, F. Jorgensen, and O. Nielsen. Development of a high-performance magnetic gear. IEEE Transactions on Industry Applications, vol. 41, no. 3, pp. 764–770, May/June 2005.

[35] Yi-Chang Wu and Chih-Wen Wang. Transmitted torque analysis of a magnetic gear mechanism with rectangular magnets. Applied Mathematics & Information Sciences, vol. 9, no. 2, pp. 1059–1065, 2015.

[36] K. Atallah, S.D. Calverley, and D. Howe. Design, analysis and realisation of a high performance magnetic gear. IEEE Proceedings-Electric Power Applications, vol. 151, no. 2, pp. 135–143, Mar 2004.

[37] L. Jian and K. T. Chau. Analytical calculation of magnetic field distribution in coaxial magnetic gears. Progress in Electromagnetics Research, PIER 92, pp. 1–16, 2009.

[38] K. Nakamura, M. Ishihara, and O. Ichinokura. Reluctance network analysis model of a permanent magnet generator considering an overhang structure and iron loss, ICEM 2006, Chania, Greece, paper no. 311, September 2006.

[39] L. Jian and G. Xu. Electromagnetic design and analysis of a novel magnetic-gear-integrated wind power generator using time-stepping finite element method. Progress in Electromagnetics Research, vol. 113, pp. 351–367, 2011.

http://dx.doi.org/10.5772/64174

[40] C.V. Pop and D. Fodorean. In-wheel motor with integrated magnetic gear for extended speed applications. IEEE SPEEDAM 2016, Capri, Italy, 22–24 June 2016, accepted for publication.

[41] T. Lubin, S. Mezani, and A. Rezzoug. Analytical computation of the magnetic field distribution in a magnetic gear. IEEE Transactions on Magnetics, Institute of Electrical and Electronics Engineers, vol. 46, no. 7, pp. 2611–2621, 2010.

Chapter 5

Switched Reluctance Drives with Degraded Mode for Electric Vehicles

Pablo Moreno-Torres, Marcos Lafoz, Marcos Blanco,
Gustavo Navarro, Jorge Torres and
Luis García-Tabarés

Additional information is available at the end of the chapter

http://dx.doi.org/10.5772/64431

Abstract

There are many types of electrical machines suitable for electric vehicles. Nowadays, most manufacturers and researchers tend towards two major alternatives: permanent magnet synchronous machines and induction machines. However, these are not the only competitive candidates. Reluctance machines, which have been well-known for some decades already, present some interesting advantages. For instance, switched reluctance machines are intrinsically redundant and fault-tolerant, which makes them attractive for applications in which robustness is compulsory. In this sense, switched reluctance drives can keep working even when one of their phases loses its functionality for any reason. In an electric vehicle, this would mean being able to keep driving the vehicle even after some failures, although with reduced performance (in degraded mode). In this chapter, switched reluctance drives for traction applications are analyzed, focusing on their capability to operate in degraded mode (with m-1 phases available).

Keywords: switched reluctance machine, traction drive, fault-tolerant drive, degraded mode

1. Introduction

In electric vehicles (EVs), the component responsible for providing mechanical torque is the motor. The main requirements for EV motors are high peak power, power density, compactness, high torque over a wide speed range, fast torque response, energy efficiency, reliability, robustness, fault tolerance, low maintenance and low cost [1].

Various motors have been considered for EV applications [2]: DC machines, induction machines (IMs), permanent magnet synchronous machines (PMSM) and switched reluctance machines (SRMs). DC machines are not used any more due to the high maintenance required and the lack of reliability associated to the commutator and the brushes. IMs, commonly used in industrial applications, are a robust option with more reliability and better efficiency than DC machines. However, they present a clear disadvantage which is the heat produced by the losses in the rotor, difficult to extract, requiring a special cooling system and reducing the overload capacity of the motor. PMSMs, and particularly Interior PMSMs (IPMSMs), are the most popular choice for EVs [3, 4]. These motors have higher efficiency, compactness, high-power density, fast dynamics and high torque-to-inertia ratio. However, they show some drawbacks due to the presence of rare earth permanent magnets. The price and the availability of rare earth material are considered a potential problem for EVs massive development [5]. Besides, PMSMs are more sensitive to high temperatures, and they suffer from risk of demagnetization.

Switched reluctance drives (SRDs) are getting increased attention recently, including in the EV industry [6]. SRMs have been well known for many years due to its simple operation principle. Relatively, advances in static switches and digital control devices have fostered its applications in many different fields, even replacing other types of electrical machines.

2. State of the art

A rotary switched reluctance machine consists of a stator, in which an even number of coils are placed in an laminated iron yoke, and a rotor, which comprises only a laminated iron yoke with no coils. Both parts have a polar configuration with different number of poles in each one. Only a restricted combination of pole number for rotor and stator is allowed to run the machine properly. The name of this type of machine comes from the fact that every time a coil is activated, the rotor moves trying to align one of its poles with the corresponding stator one, minimizing the overall reluctance of the magnetic circuit. The SRM is based on the concept of switching the stator coils sequentially. If the coil is switched on before the closest rotor pole is aligned with the active stator one, then the machine acts as a motor, while if it is switched after, then it acts as a generator.

Structural simplicity, high efficiency compared with the induction motor, low cost and control flexibility, rugged motor construction, large starting torque, wide speed range, inherent fault-tolerance capability, and high operating efficiency are some of the characteristics that make the SRM a remarkable candidate for electric drive of electric vehicles and hybrid electric vehicles (HEVs) [7]. The authors of [2] also refer to the SRM suitability for high-speed applications as well as for harsh environment such as EVs, considering high temperature and vibrations. Another important advantage of SRMs is their intrinsic fault tolerance, in the sense that they will continue to operate in a satisfactory manner, without the other phases being affected, after sustaining some types of faults [8]. Moreover, most SRMs can operate even if one of the phases is broken down (degraded mode or “m-1phases” mode), which means that

http://dx.doi.org/10.5772/64431

they are intrinsically redundant [9–11]. Consequently, the SRM combines many desirable qualities of induction machines as well as PM brushless machines. Its performance and inherently low manufacturing cost make it a competitive option for this application.

On the other hand, SRMs have also some disadvantages, such as lower specific torque, high-torque ripple, low efficiency compared with IPMSM and high noise and vibrations [12]. Most authors claim that PMSMs can reach up to twice the power density of SRMs. However, this is only true when the comparison is done in unfair terms: PMSMs are not fault tolerant by default, but they must be for some applications. The good news is that they can be designed to be fault tolerant (although not for high-speed applications); the bad news is that doing so decreases their power density significantly [8]. Besides, PMSM lose torque capability with temperature due to permanent magnets flux reduction [13], much more than SRMs and IMs. As high temperatures could become a common requirement for electric motors in EVs, this fact will further reduce the difference between PMSMs and the other two alternatives. After considering these two points, PMSMs could achieve "only" 25–50% more power density than SRMs [8].

Having a SRM with a higher number of rotor poles than stator poles results in higher efficiency and torque to weight ratio [14, 15]. This is particularly convenient for outer-rotor machines, usually used in in-wheel designs. In such case, a better performance is achieved if a segmented rotor topology is used [16]. Segmented rotor SRMs have a stator with full pitch coils and a rotor with discrete segments embedded in nonmagnetic material.

Regarding torque ripple, several alternatives related to rotor geometry have been extensively studied [17], based on slanting, serration, chamfering or skewing, demonstrating a certain improvement in torque ripple. Other studies have been accomplished varying yoke thickness, stator pole width, internal stator diameter [17, 18] and pole shapes [19].

Various SRM have been designed and built during the last two decades for EV and HEV applications; examples are found in [11, 20–27]. The key points to improve a SRM efficiency are to increase the number of stator and rotor poles, reduce iron losses using 0.1-mm-thick high-silicon steel laminations and use continuous current mode (single pulse) operation above rated speed [20]. It seems that torque density and efficiency cannot be improved at the same time: for instance, [26] achieved an efficiency of 96% but torque density was 25 Nm/l, while [27] reported a torque density of 38 Nm/l, although the efficiency was 90% due to the low-grade iron steel utilized to maximize torque density. As usually in electrical machines, getting both high-torque density and high-energy efficiency is difficult without rare earth permanent magnets.

In SRDs, the power electronics topology is usually chosen as a compromise between performance and the number of power semiconductor devices. The higher the number of switches, the higher the cost and the failure rate, but the controllability of the system increases, improving performance. Different power topologies with specific advantages and disadvantages are usually found in the literature [1, 28, 29]. The most common one is the asymmetric bridge converter, comprising two switching devices and two power diodes per phase. **Figure 1** shows the circuit schematic of this converter for a 4-phase SRM. The main advantage of this topology is the capability of supplying each phase individually. This, in turn, allows efficient phase

overlapping, increasing average torque and reducing torque ripple. For the same reason, this circuit is very convenient for achieving fault-tolerant SRDs. In terms of cost, the main drawback of this topology is the high number of switching devices in comparison with other alternatives.

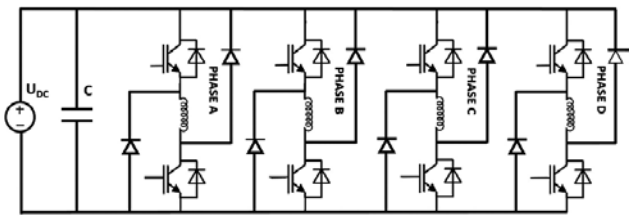

Figure 1. Asymmetric bridge converter topology for 8/6-pole switched reluctance machine.

The above topology requires two more diodes per phase compared with the most conventional topology used for PMSMs and IMs [30]. As aforementioned, some alternative topologies have been proposed in order to reduce the number of devices, including one that uses the SRM phases as inductive filters to charge the EV battery [31], which adds an additional value to this type of machine over IMs and PMSMs. However, these alternatives reduce the controllability and efficiency of the drive and are generally avoided in applications with demanding torque ripple requirements.

SRMs require very precise position determination, since the activation of the phases must be synchronized with rotor position to achieve good performance. Conventionally, SRDs have a measuring device (either an encoder or a resolver) to determine the speed and position of the rotor. These sensors are accurate and relatively inexpensive and have very good performance. However, it would be desirable to remove them (without deteriorating performance considerably) in order to make the drive cheaper, less voluminous, less noise-sensitive and more reliable [32, 33]. This can be done by means of a "position sensorless control", also known as "position self-sensing control" given that the external sensor is replaced by the electrical machine itself, which acts as its own position sensor [34].

As the cost and the volume of an external position sensor is not significant when compared to the whole traction system, the main advantage of position self-sensing in SRMs for EVs is the possibility to continue operation in case the external sensor is out of service. This redundancy increases the fault tolerance of the whole drive, which is critical in traction applications and one of the main approaches of this chapter.

During the last decades, many self-sensing techniques have been proposed for rotating electrical machines in general [32, 33] and SRMs in particular [35, 36]. Commonly, these methods perform well either at high speed (such as BEF-based, flux linkage-based or inductance-based techniques) or at low speed/standstill (such as injection-based or di/dt-based techniques). This implies that at least two of these methods are usually combined in the same drive, the transition between both being particularly delicate.

Besides, self-sensing normally causes a slight reduction in performance, since the position is estimated with some error. This in turn implies that phase activations and deactivations are not applied exactly when desired, leading to a reduction in average torque, an increase in torque ripple and its consequences, and a decrease in energy efficiency. Of course, all these disadvantages are minor when compared to having the possibility to operate the EV even after the external position sensor fails.

Electromagnetic interference (EMI) and electromagnetic compatibility (EMC) are also very important aspects of an EV. In this sense, SRMs could present worse EMC behavior due to higher di/dt and higher switching frequencies in general. Ample research is missing on this topic.

3. SRM under analysis: starting values for the design process

In this chapter, a SRM is analyzed from a preliminary point of view. For the sake of comparison, this SRM has been designed to replace the original PMSM of a Nissan Leaf, whose main specifications are listed in **Table 1**. Therefore, a SRM has to be pre-designed with the aim of achieving similar performance to that of the PMSM of the Nissan Leaf. This SRM must have the same torque-speed capabilities than the original motor. Besides, both machines should have the same outer diameter, while keeping current density at similar values, in an attempt to keep the comparison as fair as possible. As SRMs have significant lower power density than PMSMs, this means that the proposed SRM will be longer and heavier than the original motor.

Magnitude	Value (units)	Comments
Type of machine	PMSM	
Power (rated)	80 kW	
Torque (rated/max)	254/280 Nm	
Speed (rated/max)	3000/9800 rpm	Maximum speed estimated from vehicle parameters.
Transmission	7.94:1	Transformation ratio
DC voltage	300 V	Batteries rated voltage is 360 V, and batteries voltage ranges from 280 to 400 V depending on state of charge and current
Weight (PMSM)	82 kg	Estimated
Weight (inverter)	15 kg	Estimated
Stator outer diameter	250 mm	Estimated
Rotor outer diameter	170 mm	Estimated

Table 1. Nissan Leaf motor specifications.

The first decision to make when designing an electrical motor is obviously the machine type and topology (number of phases and number of poles). In this case, a conventional radial-flux inner-rotor non-skewed SRM is selected for consistency with the original PMSM. Regarding

the topology, an 8/6-pole configuration is chosen as a compromise between torque density + cost (the less number of phases/poles, the better) and torque ripple + degraded capability (the more phases/poles, the better) [2]. The minimum number of phases that can ensure that the machine will be able to start with m-1 phases available (degraded mode) from any rotor position is four (although a especial starting routine will sometimes be needed, which could also work for 3-phase SRMs; see Section 5). Hence, an 8/6-pole topology makes for a good candidate for fault tolerant EVs.

Input parameters		**Output parameters**	
Magnitude	**Symbol**	**Magnitude**	**Symbol**
Rated power	P_r	Number of turns per coil	N
Rated speed	ω_r	Phase current during activation; see **Figure 11a**	I_{AVG}
Number of stator phases	m	Rotor outer radius	R_R
Number of stator pairs per pole	N_{sp}	Active length	L
Stator outer radius	R_S	Stator pole width	$W_S = 2 \cdot a$
Air gap	g	Stator pole height	H_S
Operational current density	I_ρ		

Table 2. Input and output parameters for the analytical pre-design model.

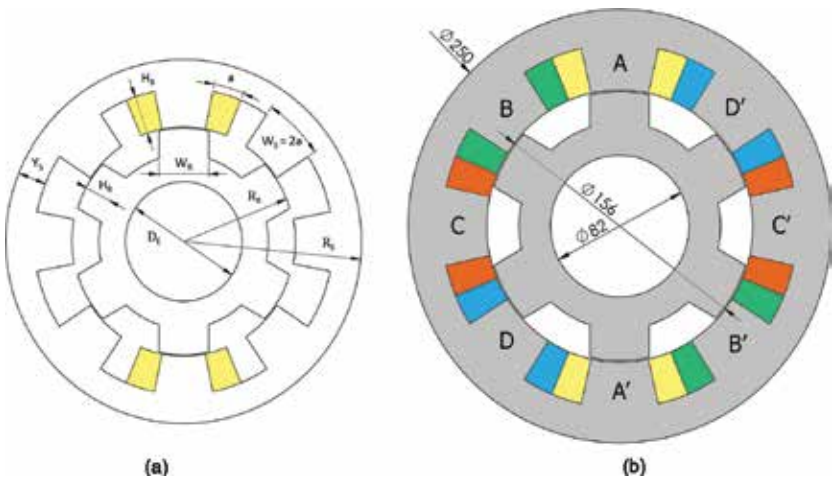

Figure 2. (a) Cross section of a 8/6-pole SRM with curved coils. (b) 80-kW SRM considered in this work (after FEM pre-design). Rotor position in both figures is 0° (phase AA′ aligned position).

Once the type of machine is fixed, the design process starts with analytical calculations based on some of the methodologies proposed in the literature, such as [35, 37, 38]. The main dimensions of a given SRM can be easily computed using a simple analytical model, which

http://dx.doi.org/10.5772/64431

starts from some initial specifications and several simplifications. Obviously, the results need to be checked with more refined tools such as finite element method (FEM) codes. Input parameters to perform the pre-dimensioning and output parameters to be provided by the model are given in **Table 2** and **Figure 2**.

Regarding the assumptions and simplifications in which the model is based, they can be listed as:

- The machine is fully saturated and works at a magnetic field B in the air gap, which leads to use a simple equation for the produced torque T, in the form:

$$T_{em} = \frac{P_r}{\omega_r} = 2 \cdot K_T \cdot N \cdot N_{sp} \cdot I_{AVG} \cdot B \cdot R_R \cdot L \tag{1}$$

  where K_T is a torque constant related to the machine saturation level, which varies from 0.5 in non-saturated machines up to 0.8 in heavily saturated ones. Additionally, the voltage V_k applied to each phase is:

$$V_k = 2 \cdot N \cdot N_{sp} \cdot \omega \cdot B \cdot R_R \cdot L \tag{2}$$

- Coils are curved for a better use of the slot between poles. They have the shape shown in **Figure 2**. Under this approach, it must be satisfied that:

$$N \cdot I_{AVG} = I_\rho \cdot a \cdot H_S \tag{3}$$

- The return yoke width Y_S must be the same as half the pole width in order to work at the same magnetic flux density at the return yoke, without increasing the saturation level. Alternatively, a certain correction empirical factor K_f can be introduced to achieve more realistic results. This simplification, together with some geometrical considerations, leads to the following expressions:

$$Y_S = K_f \cdot a \tag{4}$$

$$a = \frac{2 \cdot \pi \cdot R_R}{8 \cdot N_{sp} \cdot m} \tag{5}$$

$$R_S = R_R + H_S + Y_S \tag{6}$$

- Both coil ends can be considered as a complete circular ring with inner radius a and outer radius $2a$. This assumption allows an easy estimate of the overall length and weight of the coils.

Combining expressions (4)–(6), (3) and (1), one can derive an equation with two unknowns, the rotor radius R_R and the active length L :

$$R_S \cdot {R_R}^2 - {R_R}^3 \cdot \left(1 + \frac{\pi \cdot K_f}{4 \cdot N_{sp} \cdot m}\right) - \frac{T_{em} \cdot 2 \cdot m}{\pi \cdot K_T \cdot B \cdot L \cdot I_\rho} = 0 \xrightarrow{\text{fixing } L} -A \cdot {R_R}^3 + B \cdot {R_R}^2 - C = 0 \tag{7}$$

The procedure to dimension the machine consists in fixing the length L , and then finding the zeros of the polynomial function given by the above equation to calculate R_R. If the value chosen for L is too low, there will be no real solutions for the rotor radius R_R, meaning that for a given stator radius R_S there is no machine able to provide the required torque. Beyond that limit, there will be two main options: one with a small rotor radius and a large coil with many ampere-turns and another with a large rotor radius and a smaller coil. The optimum solution in terms of the shortest machine will be the one for which both rotor radiuses are the same. Alternatively, the criteria for finding the optimum machine could be to select the lightest one. In that case, the weight of the coil ends should be taken into account.

As an example, a pre-dimensioning of a SRM with the input specifications listed in **Table 3** has been performed.

Magnitude	Value (units)	Comments
Type of machine	8/6-pole SRM	m = 4, N_{sp} = 1
Power (rated)	80 kW	T_{em} = 254 Nm
Speed (rated)	3000 rpm	
Current density	7 A/mm^2	
Air gap magnetic field	1.8 T	
Pole to return Yoke factor	1	

Table 3. 8/6-pole SRM pre-design specifications.

Figure 3 shows the results obtained using the previous model, particularly the calculation of the optimum active length with its corresponding overall weight, for different stator outer radiuses. It can be seen that, for this simple approach, there is an optimum stator radius which minimizes the overall weight. Nevertheless, further and deeper analysis should be performed, since this solution can be far from being the optimum in terms of efficiency, for instance. In this regard, the evaluation of the coil resistance and inductance, end-winding included, is essential to estimate the behavior of the machine, including its overall efficiency.

http://dx.doi.org/10.5772/64431

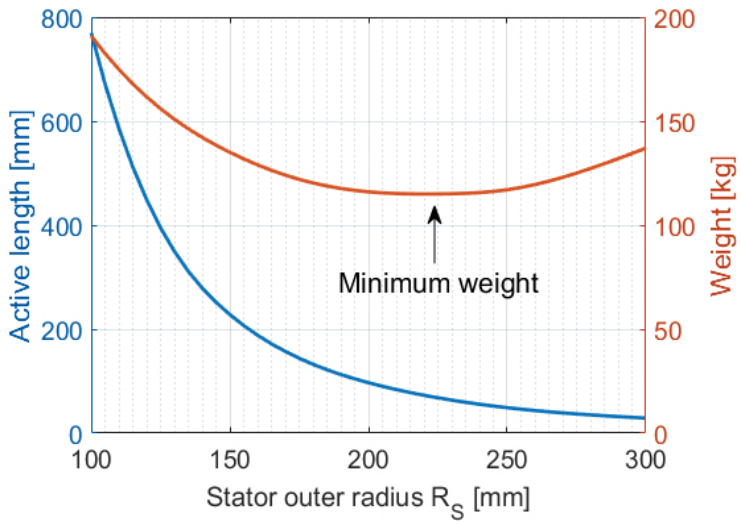

Figure 3. Calculation of active length and overall weight for the proposed SRM.

Magnitude	**Minimum weight (analytical)**	**R_S = 125 mm, as the original PMSM (analytical)**	**R_S = 125 mm (FEM-tuned, Figure 2(b))**
Active length **(mm)**	68	395	300
Stator radius **(mm)**	225	125	125
Rotor radius **(mm)**	124	72	78
Air gap	–	–	0.6
Stator pole width **(mm)**	49	28	34.3
Stator pole height **(mm)**	77	39	26.4
Turns per coil	29	8	10
Phase current I_{AVG} **(A)**	451	482	360
Current density (**A/mm²**)	7.0	7.0	7.7
Rotor pole width **(mm)**	–	–	35
Rotor pole height **(mm)**	–	–	18.5
Active weight **(kg)**	115 (est.)	156 (est.)	101

Table 4. Comparison between two possible analytical solutions for the proposed SRM and the tuned solution after the FEM simulations described in Section 4.

Table 4 provides the calculated output parameters for the minimum weight machine, along with those computed for a 250-mm outer stator diameter, which is the one designed to replace the original PMSM in the Nissan Leaf. **Table 4** also includes the parameters corresponding to the final pre-design, obtained after the design tuning achieved by FEM simulations and time-domain simulations such as those described in next section. This last design is the one that will be analyzed in detail for the rest of the chapter.

4. Pre-design analysis and validation

This section is devoted to the analysis and validation of the pre-design described in Section 3. This analysis was carried out only from an electrical engineering point of view, corresponding to an early-stage in the design process: electromagnetics, power electronics, modulation technique, control strategy and power losses. Therefore, other crucial aspects such as mechanical behavior, cooling, EMC, certification testing, series production, quality assurance, useful life and recyclability are not considered.

4.1. FEM analysis

The first step consists in analyzing and optimizing the preliminary design by means of FEM simulations. This task is usually divided into two different parts:

1. Verification of the analytical pre-design: The aim is to validate the topology, the main stator/rotor dimensions and the winding properties (e.g., number of turns) of the analytical pre-design. This means checking whether the machine provides rated torque at low speed with the specified current and current density, calculating the back-EMF (electromotive force) and the maximum speed for a given DC voltage, and other verifications such as air gap flux density, magnetic saturation or inductances.
2. Mild optimization of the geometrical design: FEM simulations are extremely useful to tune certain geometric parameters, such as stator and rotor pole widths and heights. This can be carried out in a very simple but suboptimal manner, or by considering an optimization problem which can be solved by conventional methods: from brute force (small number of design variables) to evolutionary algorithms.

For the purposes of this chapter, focus is placed on torque, both in normal and "m-1 phases" mode: average torque, torque ripple and minimum torque to start the vehicle (especially significant in degraded mode, when one of the phases is out of service). For such an analysis, 2D simulations are normally sufficient, especially for machines with a large ratio between magnetic length and rotor outer diameter ($L/D_R > 1$), which is the case analyzed here.

One of the first results that should be obtained by FEM simulations is the instantaneous torque as a function of both rotor position and current. It is sufficient to calculate it for half an electric period, since this function is periodical and asymmetrical with respect to the rotor angle. This period is calculated as follows:

$$\Delta\theta = \frac{360°}{N_R} \tag{8}$$

which yields 60° for an 8/6-pole SRM. Results for the 80-kW 8/6-pole SRM are depicted in **Figure 4**; rated current is 360 A. Notice how raising the current increases the saturation level

http://dx.doi.org/10.5772/64431

of the machine, which in turn "deforms" the torque pulse. This deformation implies higher torque ripple under constant current profiles, as described later.

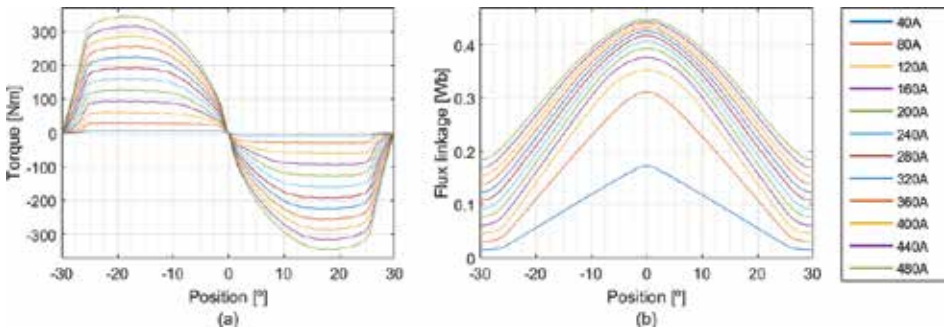

Figure 4. (a) Instantaneous torque and (b) flux linkage during an electric period for different current values.

It is also very interesting to calculate the flux linkage of each phase as a function of rotor position and current, as shown in **Figure 4**. This information is extremely useful to build a simulation model of the whole traction drive, as described in Section 4.3. Notice that most SRM models found in the literature neglect cross-coupling between phases, which implies that each phase is supposed to be independent of the rest. This assumption is not valid under operating conditions in which two phases conduct simultaneously. This is especially relevant when torque is generated by two phases (such as phase overlapping in torque-sharing functions to reduce torque ripple).

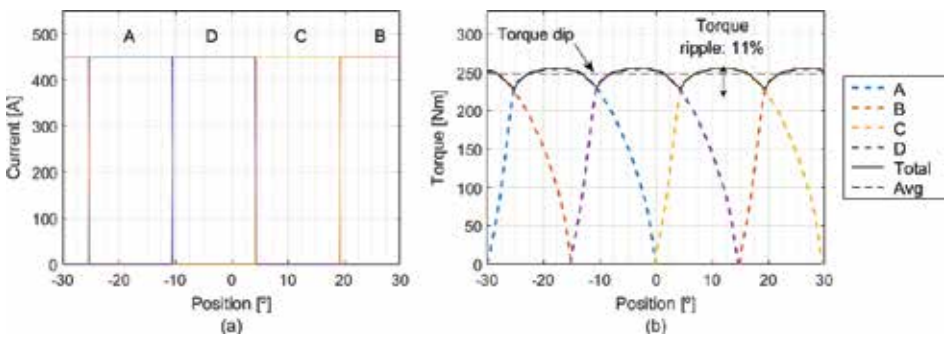

Figure 5. (a) Ideal current pulses and (b) corresponding torque profile at 100% load.

Next, torque curves from **Figure 4** can be post-processed to estimate the instantaneous torque profile in steady state for different current levels. Usually, this is carried out under the assumption of ideal current pulses, such as those depicted in **Figure 5**. Of course, this ideal supply is far from being real, but it gives a first estimation without using a full model of the drive, such as the one described later in the chapter. In this ideal case, the activation and deactivation angles θ_{ON} and θ_{OFF} are given by the intersection of the torque curves corre-

sponding to different phases, so that there is no overlapping (the previous phase is turned off when the next one is turned on). The torque profile corresponding to these ideal current profiles is shown in **Figure 5** for rated current. Notice how a constant current profile without overlapping cannot generate a constant torque profile in non-skewed SRMs, even at low current levels (low saturation levels).

Finally, FEM results can also be used to assess the degraded capability of an SRM. **Figure 6** shows the current profile under ideal current pulses when one of the phases is out of service. Compared to normal operation (**Figure 5**), m-1 mode presents lower torque and extremely high-torque ripple under ideal current pulses supply. It is worth mentioning that switching angles should be specifically optimized for degraded operation, so that the control strategy can adapt to the new topology when a phase losses its function. Therefore, the average torque and torque ripple values included in **Figure 6** are not final, as presented later in this chapter.

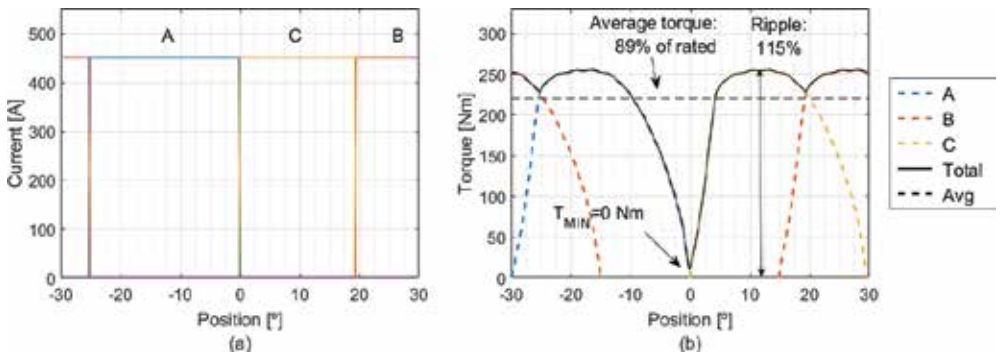

Figure 6. Torque profile in degraded mode of operation (m-1 phases).

Speed (rpm)	Mode	Conduction losses (W)	Switching losses (W)	Total losses (W)	Efficiency (%)
3000	Normal	2254	1161	3415	96.8
9800	Normal	2102	305	2407	97
3000	m-1 phases	1256	771	2050	97.43
9800	m-1 phases	912	368	1280	98.4

Table 5. Power electronics losses in steady state at rated and maximum speed, both for normal and degraded modes.

Similarly, it is convenient that the torque dip generated by the missing phase is above 0 at every angle to ensure that the vehicle can start regardless of rotor position (this is not possible with 6/4-pole and 8/6-pole SRMs). Otherwise, special starting routines must be implemented in the control system, as proposed in **Table 5**. There are many factors that influence the capability of a given SRM to start an EV besides rotor position: inertia, load torque (including the grade of the road α), overloading capability of the traction drive and the control strategy, which can be adapted to the particular conditions in which the vehicle must be

started. Further analysis regarding the self-starting capability under degraded operation is presented in section 5.

4.2. Power electronics pre-design

Power electronics to drive the 8/6-pole SRM comprises an asymmetric power converter connecting to the common DC link for all electric phases and a DC filter to improve voltage ripple. The electrical machine is current-controlled by means of a hysteresis band strategy. Other usual alternatives are closed-loop pulse-width-modulation (PWM) [39] and direct torque control (DTC) [40].

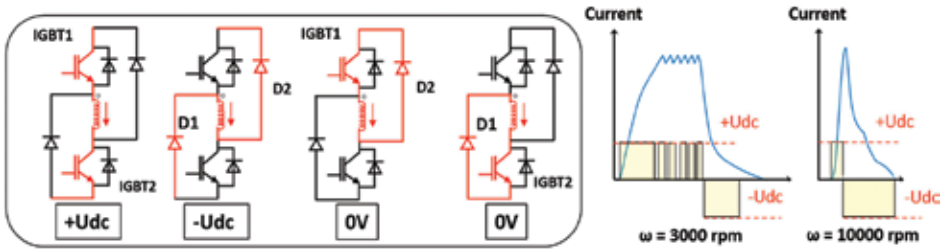

Figure 7. SRM power converter topology and switched selection for rated and maximum speed operation.

Motor mode operation requires the use of $+U_{DC}$ and 0 V to keep the current within the reference band, using $-U_{DC}$ to switch the current off rapidly when the phase is deactivated, as **Figure 7** illustrates. Current is individually controlled in each machine phase with an asymmetric bridge topology, allowing total independence between phases. During EV braking, the machine works as a generator, requiring $+U_{DC}$ to increase rapidly the current and then it is kept within the reference band using 0 V and $-U_{DC}$. At higher speeds, the machine is designed to achieve single-pulse operation, where just $+U_{DC}$ and $-U_{DC}$ are sufficient to control the current whilst the commutation frequency is reduced [41].

Since the power level and the DC-link voltage are usually defined, simulation-based analysis can be used to determine the voltage and current levels of the power converter devices. The semiconductor technology is selected to fulfill the following electrical specifications: DC-link voltage, current carrying capacity, maximum switching frequency, load cycle and isolation requirements.

4.3. Drive modeling and analysis

When analyzing electrical drives, simulation models in the time-domain comprising the electrical machine, the power electronics converter, the control strategy, the switching technique and the equivalent load are extremely useful. When the machine model is built with data extracted from FEM simulations (employing tools such as look-up tables or LUTs), these kind of simulations allow for fast and accurate calculations. In the case of SRDs, such a model is an excellent way to calculate average torque and torque ripple under real current pulses and

also to optimize switching angles under different operating conditions and optimization criteria. **Figure 8** shows a schematic of the time-domain simulation model used in this work.

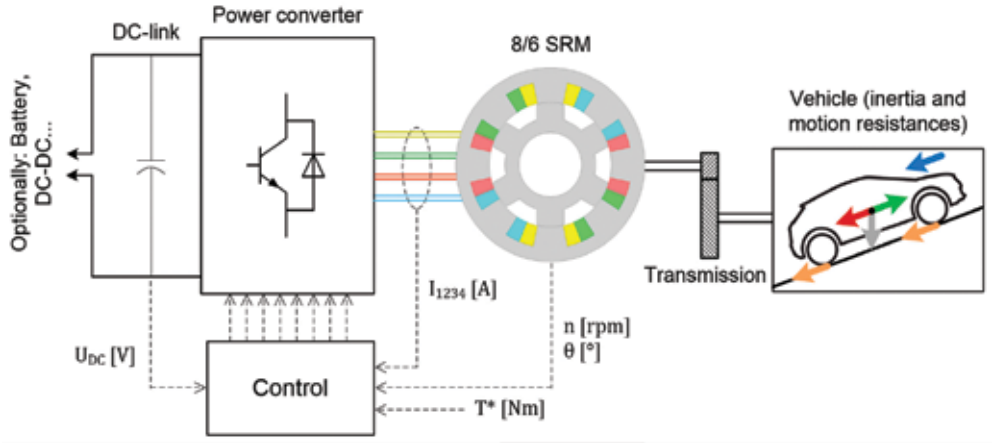

Figure 8. SRM-based traction drive model.

SRDs and EVs modeling is outside the scope of this chapter, and therefore, the reader is referred to publications that deal with these aspects, such as [1, 42–45]. For convenience, the most relevant equations are included next, starting with the voltage equation for each machine phase:

$$u_k = R_S \cdot i_k + \frac{d\lambda_k}{dt}; \quad k = 1 \ldots m \tag{9}$$

The flux linkage λ_x of each phase depends on the current of that phase i_x, of the current of the previous/next phase i_y (when simultaneous conduction takes place) and rotor position θ. Neglecting cross-coupling yields:

$$\lambda_k = f(i_k, i_{k\pm1}, \theta) \approx f\left(i_k, \theta\right) \tag{10}$$

the relationship between flux linkage, current and rotor position being the one given by **Figure 4**, usually implemented via a LUT. Similarly, the torque provided by each phase is given by **Figure 4** and a second LUT, the total torque being the sum of each phase torque (again, cross-coupling is neglected):

$$T_{em} = T_k + T_{k+1}; \qquad T_k \approx g\left(i_k, \theta\right) \quad \text{and} \quad T_{k+1} \approx g(i_{k+1}, \theta) \tag{11}$$

http://dx.doi.org/10.5772/64431

Notice that the above expression considers up to two phases because it will be the maximum number of phases conducting simultaneously. Finally, the mechanical equation of the drive is as follows:

$$T_{em} - T_{load} = J \cdot \frac{d\omega_{mec}}{dt} + B \cdot \omega_{mec} \tag{12}$$

The vehicle model represents both the total inertia and the load torque as seen by the motor:

$$J \approx J_{rotor} + \frac{J_{wheels}}{i_{GEAR}^2} + \frac{M \cdot ERR^2}{i_{GEAR}^2} \tag{13}$$

$$T_{load} = \frac{ERR}{i_{GEAR} \cdot \mu_{GEAR}} \cdot F_T \ (traction\ mode) \tag{14}$$

where M is the total mass of the vehicle [kg], ERR [m] is the effective rolling radius, i_{GEAR} [−] is the transmission gear ratio and μ_{GEAR} [−] is the transmission energy efficiency (assumed to be constant and equal to 0.95).

The vehicle motion resistances include rolling resistance, aerodynamic drag and gradient resistance; the last one being of active nature (may take negative values and contribute to the movement of the vehicle):

$$F_T = F_{aero} + F_{roll} + F_{grav} \rightarrow \begin{cases} F_{aero} = \frac{1}{2} \cdot \rho \cdot A_F \cdot C_D \cdot v^2 \geq 0 \\ F_{roll} = \mu_{rod} \cdot M \cdot g \cdot \cos(\alpha) > 0 \\ F_{grav} = M \cdot g \cdot \sin(\alpha) \end{cases} \tag{15}$$

Regarding the control strategy and the switching technique, this work considers hysteresis current control with optimized switching angles as a function of speed and the desired torque, as illustrated in **Figure 9**.

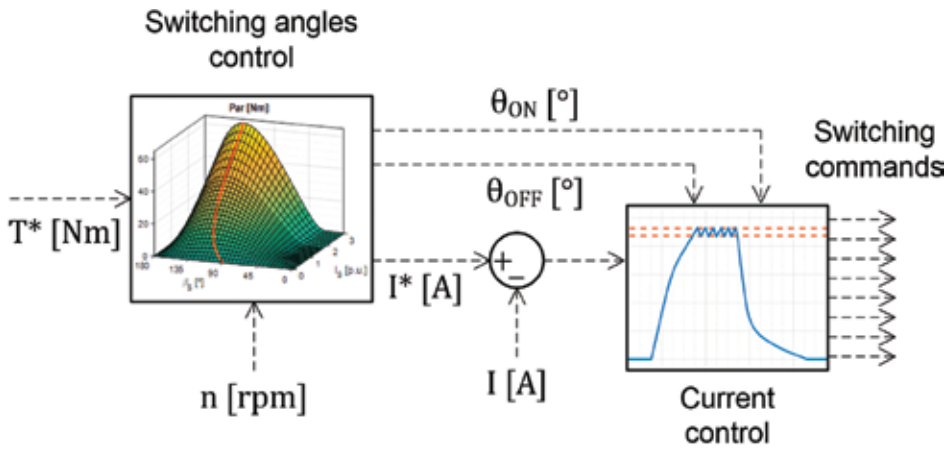

Figure 9. Torque control scheme with switching angles controller.

A simulation model such as the one described above is useful to optimize switching angles considering different optimization criteria. In this particular case, a compromise between average torque and torque ripple was chosen, which yields the torque-speed characteristic depicted in **Figure 10** (angle resolution of ±0.25°).

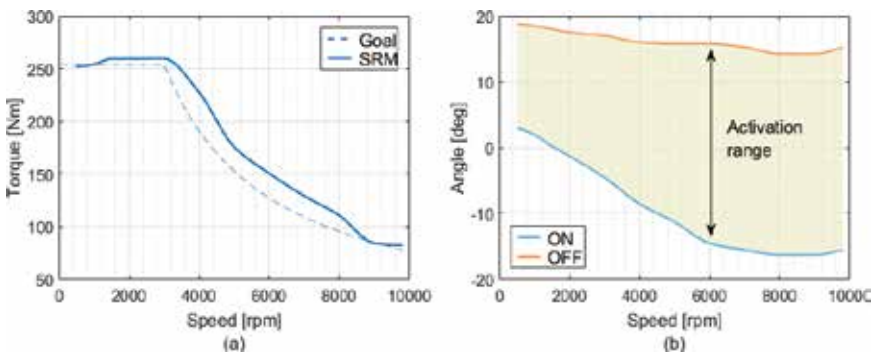

Figure 10. (a) Torque-speed characteristic of the 8/6-pole SRM analyzed in this chapter. (b) Corresponding switching angles as a function of speed (all phases are equal but phase-shifted).

Traditionally, one of the biggest disadvantages of SRMs is torque ripple and its consequences (vibrations, efficiency and acoustic noise) with respect to other electrical machines. However, there has been a lot of research on this topic in the last two decades. As a result, torque ripple has improved considerably and it is no longer an issue in many applications that use SRMs. Basically, there are two main approaches to reduce torque ripple (which can be complementary): machine design and machine control. The former include techniques such as skewing (see Section 2 for references). These modifications reduce overall performance (torque density and efficiency) and could increase the cost of the machine.

http://dx.doi.org/10.5772/64431

The second alternative consists in improving the control strategy. These methods can be classified into two categories, depending on whether the converter topology is conventional or advanced [44]. Examples of control strategies belonging to the first category are current profiling or current shaping (CP), torque-sharing function (TSF) and direct torque control (DTC). The first two basically consist in adapting the shape of the real current pulses so that torque dips/peaks are minimized [35]. Of course, this adaptation will be feasible depending on the available voltage, the back-EMF of the machine, and the inductance. In other words, the feasibility will decrease with the speed of the machine. This is convenient, given that torque ripple is more detrimental at low speed, both mechanically and from the point of view of comfort. Advanced topologies use a second DC source to increase the available voltage under certain operating conditions, thus allowing for higher *di*/*dt* [44].

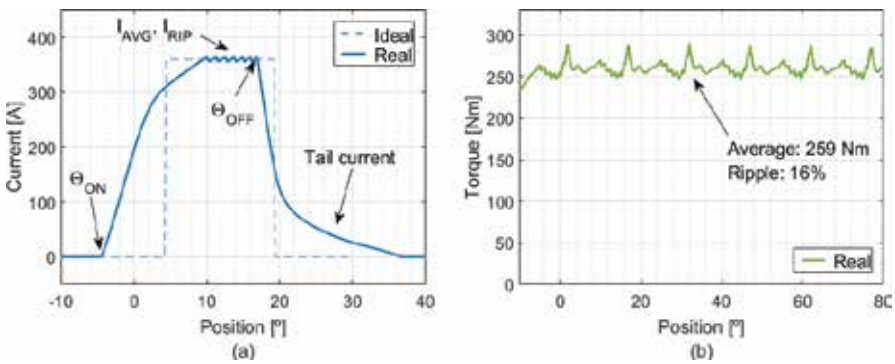

Figure 11. (a) Current pulse considered in this work (no current profiling) and (b) corresponding torque profile, both at 3000 rpm and 100% load.

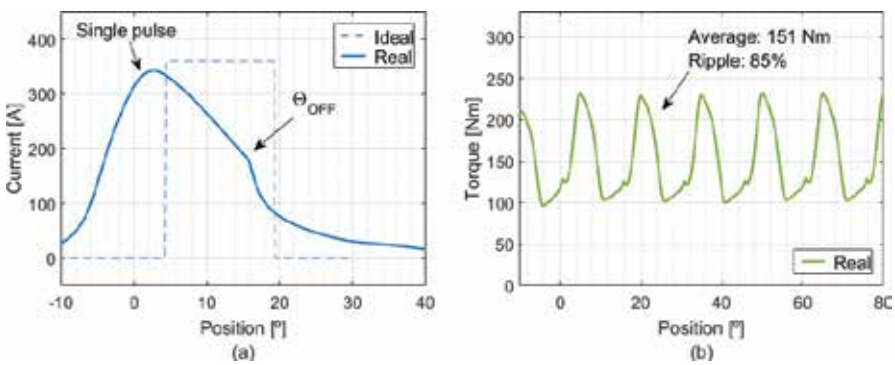

Figure 12. (a) Current in single pulse mode and (b) corresponding torque profile, both at 6000 rpm and 100% load.

For the sake of simplicity, and unless otherwise stated, all the results presented are given for a current control scheme which operates with unshaped current pulses such as that depicted in **Figure 11**, defined by θ_{ON}, θ_{OFF}, I_{AVG} and I_{RIP}. Consequently, torque ripple values given in

this chapter are noticeably high and should not be considered as reference values for EV applications.

Finally, **Figure 12** contains the same information as **Figure 11** but for a high-speed operating point. As speed increases, the time available for each phase activation reduces and at the same time the phase back-EMF increases, which makes the machine work in single pulse mode (also known as advance angle control or AAC by some authors, although this name could be confusing because turn-on angles are advanced in a wide range of speed, and not only under single pulse operation).

4.4. Power losses analysis

Power losses in SRDs present some differences when compared to those based in IMs or PMSMs. When a machine works with sinusoidal current supply, simplified loss models based on single-frequency models of the machine are usually sufficient to estimate resistive losses in the electrical circuit and iron losses in the magnetic circuit. However, SRMs have pulsed supply, which invalidates the single-frequency approach.

Resistive losses (also known as Joule or copper losses) depend on three main factors: the current i, the DC resistance of the winding R_{DC} (defined by its cross-sectional area, its total length and its conductivity) and the skin effect and proximity effect factor k_{AC} (which gives the AC resistance of the winding and depends on its geometrical properties and the frequency of the current) [37]. Therefore, the instantaneous power dissipated in each coil is:

$$P_{Cu,1}(t) = f\left(i, R_{DC}, k_{AC}\right) = k_{AC} \cdot R_{DC} \cdot i(t)^2 = R_{AC} \cdot i(t)^2 \tag{16}$$

In steady state, average power losses may be estimated analytically using the RMS value of the current and the total number of phases m:

$$\overline{P_{Cu}} = m \cdot R_{AC} \cdot {I_{RMS}}^2 \approx m \cdot R_{AC} \cdot \left(\frac{I_{AVG}}{\sqrt{m}}\right)^2 = R_{AC} \cdot {I_{AVG}}^2 \tag{17}$$

In practice, resistive losses will be higher to those estimated by the above equation, since it assumes ideal current pulses and therefore neglects current tails and phase overlapping. A simulation model such as that described in Section 4.3 can prove accurate to estimate resistive losses with real current profiles, provided that the skin and proximity effects factor k_{AC} has been properly considered. Notice that such factor depends on the switching frequency, and hence an iterative process may be required. For the SRM analyzed in this work, $k_{AC} \approx 3$.

Both skin and proximity effects are caused by eddy currents in the windings of the machine. High-power low-voltage SRMs such as those used for EV applications are usually strongly affected by these phenomena due to the combination of low number of turns, large cross-sectional area in the conductors and currents with high-frequency components in the frequen-

http://dx.doi.org/10.5772/64431

cy domain. As the wire dimensions increase, eddy currents gain importance and neglecting them can lead to significant overestimation of machine performance [46]. As it is well-known, methods such as conductor division and transposition, employing parallel paths or using Roebel bars or Litz wire, help reduce k_{AC}.

Iron losses are also very relevant in high-speed rotating machines. They depend on the magnetic flux density amplitude and frequency, and thus on the machine current and speed:

$$P_{Fe} = f_1(B, f) = f_2(I_{AVG}, n) \tag{18}$$

Again, conventional iron loss estimation techniques based on single-frequency models are not suitable for SRMs, whose current is pulsated and not sinusoidal [47]. In general, SRMs have higher frequencies and higher harmonic content than other machines at comparable speed and power, but less iron volume in high-speed applications [48]. Another distinctive aspect of SRMs is that some iron regions work with bidirectional magnetic flux, while in others the flux is unidirectional. In this sense, the number of flux reversals in the rotor can be minimized using negative current pulses. Hence, designing a SRD with bidirectional current supply can greatly improve rotor iron losses, at the expense of doubling the number of power switches.

Mechanical losses comprise bearing losses, windage losses and air-cooling losses when forced convection is used. Bearing and air-cooling losses in SRMs are comparable to other machines types and they are modeled in the same way. Windage losses, however, are usually higher in SRMs due to their doubly salient nature, and more specifically, to the aerodynamic behavior of the salient pole rotor. This is usually an issue in high-tangential speed applications, in which vacuum chambers or vacuum sleeves are sometimes used for this reason. Windage losses calculations that assume cylindrical rotor shape are not valid for conventional SRMs and hence specific expressions must be used:

$$P_{wind} = A \cdot \omega^B; B \in [2,3] \tag{19}$$

where A and $B \in [2, 3]$ are coefficients which depend on the rotor geometry, and in the case of A also on the operating conditions (pressure, temperature, etc.) [49].

Power electronics losses are also very relevant in electrical drives. They are usually divided into static and switching losses. The former refer to steady state (on- and off-states) while the latter refers to transients between states (switching). Conduction losses are of the first kind, as they correspond to the nonzero on-state voltage of the device V_{ON} (collector-emitter voltage in an IGBT (Isolated Gate Bipolar Transistor), emitter-collector voltage in a diode) while it carries a current I_{ON} [50]. The other static losses are those corresponding to the nonzero off-state current of a power semiconductor device when it blocks a voltage V_{OFF}. This reverse current I_{OFF} is a leakage current which in turn depends on V_{OFF} and which is usually very low for the power levels considered in this work. Therefore, blocking losses are conventionally

neglected in IGBTs except for high voltages (above 1000 V) and/or high temperatures (above 150°C) [50, 51].

$$P_{COND} = P_{ON} + P_{OFF} \approx P_{ON} = f(V_{ON}, I_{ON}, Temp.) \tag{20}$$

Complementary, the energy dissipated during each switching is called either turn-on energy E_{ON} or turn-off energy E_{OFF}. Neglecting parasitic effects, switching losses are given by the following expression [52]:

$$P_{SW} = P_{SW,ON} + P_{SW,OFF} = \left(E_{ON} + E_{OFF}\right) \cdot f_{SW} \tag{21}$$

f_{SW} being the switching frequency. Obviously, both E_{ON} and E_{OFF} highly depend on the current and on the voltage, since they are defined by a power peak that in turn is caused by current and voltage transients. They are also influenced by temperature. The switching frequency measures the number of turn-ons and turn-offs per time unit of a power semiconductor. It depends on the operating point (torque and speed) and on the electrical characteristic of the machine. In a 8/6-pole SRM, each phase is enabled six times per rotor revolution, so that knowing speed in the machine (e.g., 3000 rpm) and the number of commutations per phase activation n_C, the switching frequency is given as:

$$f_{sw,avg}(Hz) = \frac{3000 \text{ rpm}}{1 \text{ min}} \cdot \frac{1 \text{ min}}{60 \text{ s}} \cdot \frac{6 \text{ activation}}{1 \text{ revolution}} \cdot \frac{n_C}{\text{activation}} = 300 \cdot n_C \tag{22}$$

In single pulse mode, n_C is reduced to only two commutations per phase activation. As a result, switching losses decrease significantly.

For the sake of illustration, total power losses have been calculated for the SRD studied in this work under rated electrical conditions (U_{DC} = 300 V, I_{AVG} = 360 A and n = 3000 rpm) and maximum speed (n_{nom} = 9800) using simulation analysis. Besides, power losses have been calculated in degraded mode of operation (m-1 phases available) as well. **Table 5** shows the results for both modes of operation (normal and degraded).

5. Degraded mode (with m-1 phases available)

As mentioned along the whole chapter, "m-1 phases" operation is particularly interesting in EV applications and one potential advantage of SRMs over its counterparts. Degraded mode was one of the main reasons why a 4-phase topology was chosen in this work, given that

http://dx.doi.org/10.5772/64431

performance loss, when one phase losses functionality, is obviously more significant in machines with a low number of phases.

Performance priorities under these circumstances are different from those in normal operation. Degrade mode will be used only in case of emergency: it will allow the EV to keep driving, but the owner should take it to a repair workshop as soon as possible for proper fixing (similar to an emergency spare tire). This consideration has many implications. For instance, switching angles optimization should probably prioritize average torque over torque ripple, which will be huge anyway, or even over energy efficiency or IGBT (Isolated Gate Bipolar Transistor) aging.

Degraded mode is implemented by detecting that one phase cannot operate anymore (severe fault detection), by disabling it, and by adapting the control strategy to the new situation so that performance loss is minimized. Fault detection may be carried out in different ways, such as [53–55]. Faults that can be surpassed by the aforementioned m-1 phases mode include single coil faults, single IGBT faults and single converter branch faults, which are the most frequent. Notice that those faults that affect more than one phase simultaneously will generally prevent operation in degraded mode, unless the number of phases is high (five or more). In any case, grave faults such as DC-link short circuits will completely prevent operation.

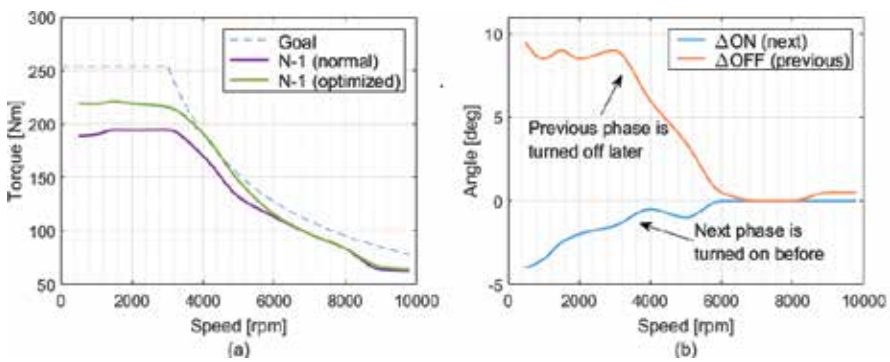

Figure 13. (a) Torque-speed characteristic of the 8/6-pole SRM in m-1 phases mode. (b) Modification of switching angles with respect to the normal mode.

Performance analysis under degraded mode can be carried out with the same methodology presented in Section 4.3. For instance, **Figure 13** shows the torque-speed characteristic of the 8/6-pole SRM in m-1 phases mode. Two curves are given: one corresponding to default switching angles (those used in normal mode) and a second obtained by optimizing the angles specifically for m-1 phases operation, thus increasing torque but also current loading in both the power converter and the machine. In this last case, one of the phases is disabled, and consequently the adjacent phases are used in a wider range of angular position, as depicted in **Figure 6** for an ideal case. Namely, the previous phase is turned off later than usual, while the next phase is activated before, as shown in **Figure 13**.

Complementary, **Figure 14** shows the current pulses in steady state in "m-1 phases" mode. The torque profile is also depicted. It is worth mentioning that increasing the conduction period of the adjacent phases implies overloading both the corresponding power electronics and some of the machine coils from the thermal point of view. Therefore, results from **Figures 13** and **14** could be invalid for long periods of operation (in this sense, angles corresponding to normal mode are a safer choice). However, in this work, current was kept constant for the sake of comparison.

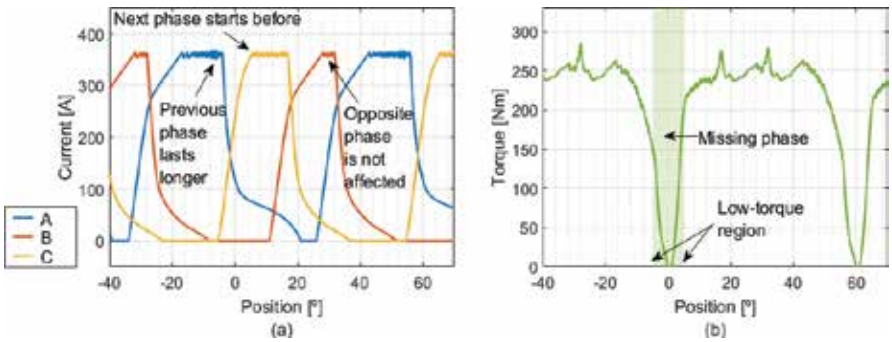

Figure 14. (a) Current pulses in m-1 phases mode (phase D is disabled) and (b) corresponding torque profile, both at 3000 rpm and 100% current.

It is important to notice that degraded mode should be able not only to keep the EV running, but also to start it from any rotor position and from different conditions, such as different road grade values. In this sense, when rotor position implies that a rotor pole is aligned with phase A in **Figure 2** (i.e., $\theta = 0° \pm k \cdot 60°$; see **Figure 6**), there is no available torque. In practice, torque is very low in a zone of ±5° around these zero-torque positions (see **Figure 14**), which constitute the worst situation to start the vehicle. There are at least three possible ways to proceed in such a case, depending on the road grade:

- Negative grade (gravitational force helps starting the vehicle): this is the best case, since it is sufficient to release the mechanical brakes and let the vehicle start going down the slope. After 10 mechanical degrees in the motor shaft, which imply barely 7 mm of linear displacement in this particular case, the motor can already provide enough torque to further accelerate the vehicle at reasonable rates.

- Positive grade (gravitational force opposes vehicle movement in the desired direction): this is the case which requires more torque and therefore the one in which the torque reduction, due to the faulty phase, will be more noticeable during acceleration. However, starting the vehicle is not so difficult, provided that it can move backwards for at least 7 mm. The starting process would comprise two steps: First, mechanical brakes are released and the vehicle reverses, down the slope, until the motor gets out of the low-torque zone, and then it is stopped. Second, high torque is provided by the motor to start the vehicle again, knowing that a torque dip will appear almost as soon as the vehicle starts moving. However, if the

http://dx.doi.org/10.5772/64431

speed of the vehicle is not enough to go through the whole low-torque region, the vehicle will stop due to the gravitational force. This would require repeating the process, but making the linear displacement in step 1 larger, so that higher speed can be achieved before facing the low-torque zone.

- Flat road (there is no gravitational force): the main problem here is that releasing the mechanical brakes will not start the vehicle. However, a two-step starting process similar to that described above could suffice: First, the phase opposite to the faulty one (if the activation sequence is A–B–C–D and D is the faulty phase, then B is the phase opposite to the faulty one), which has high negative torque capability precisely when the rotor is in the low-torque region, is used to reverse the vehicle for up to 7 mm. For this, it is very convenient that the SRM has an even number of phases, so that the phase opposite to the faulty one can provide high torque (although more than one phase can be used otherwise, as usually in SRMs). The second step is exactly the same as in the case of positive grade, but without the gravitational force opposing acceleration, which highly simplifies the starting process.

As an example, a starting process such as that described above is shown in **Figure 15**, corresponding to a flat road situation. As can be seen, the results suggest that the proposed starting protocol would successfully start a Nissan Leaf with the 8/6-pole SRM studied in this work.

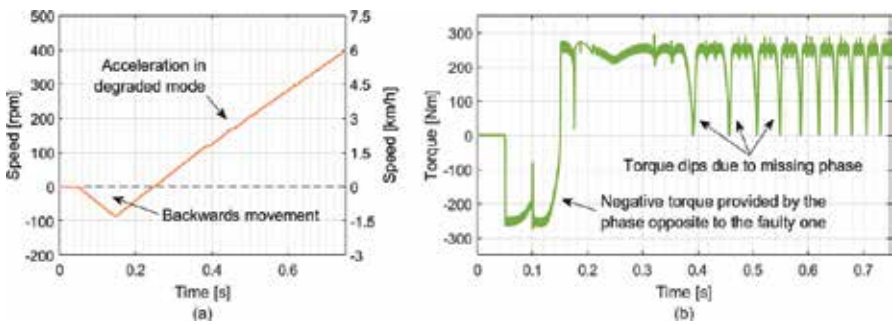

Figure 15. Vehicle start-up from the worst possible rotor position (none of the healthy phases produce torque) and under the worst possible conditions (flat terrain).

Author details

Pablo Moreno-Torres*, Marcos Lafoz*, Marcos Blanco, Gustavo Navarro, Jorge Torres and Luis García-Tabarés

*Address all correspondence to: pablo.moreno-torres@ciemat.es and marcos.lafoz@ciemat.es

Electrical Engineering Department, CIEMAT (Spanish National Research Centre on Energy, Environment and Technology), Madrid, Spain

References

[1] Krishnan R. Switched Reluctance Motor Drives: Modeling, Simulation, Analysis, Design, and Applications. 1st ed: CRC Press LLC Boca Raton, Florida, United States ; 2001.

[2] Petrus V, Pop AC, Martis CS, Gyselinck J, Iancu V, editors. Design and comparison of different Switched Reluctance Machine topologies for electric vehicle propulsion. In: 2010 XIX International Conference on Electrical Machines (ICEM); 2010 6–8 Sep. 2010.

[3] Takeno M, Chiba A, Hoshi N, Ogasawara S, Takemoto M, Rahman MA. Test Results and torque improvement of the 50-kW switched reluctance motor designed for hybrid electric vehicles. IEEE Transactions on Industry Applications. 2012;48(4):1327–34.

[4] Staunton RH, Ayers CW, Marlino LD, Chiasson JN, Burress TA. Evaluation of 2004 Toyota Prius Hybrid Electric Drive System. R. H. Staunton C. W. Ayers L. D. Marlino J. N. Chiasson T. A. Burress Prepared by the OAK RIDGE NATIONAL LABORATORY Oak Ridge, Tennessee 37831 managed by UT-BATTELLE, LLC for the U.S. DEPARTMENT OF ENERGY Under contract DE-AC05-00OR22725 Publication Date: May 2006 http://www.engr.uvic.ca/~mech459/Pub_References/890029.pdf

[5] Kiyota K, Sugimoto H, Chiba A. Comparing electric motors: an analysis using four standard driving schedules. IEEE Industry Applications Magazine. 2014;20(4):12–20.

[6] Anekunu AY, Chowdhury SP, Chowdhury S, editors. A review of research and development on switched reluctance motor for electric vehicles. In: 2013 IEEE Power and Energy Society General Meeting (PES); 2013 21–25 July 2013.

[7] Cheng H, Chen H, Yang Z. Average torque control of switched reluctance machine drives for electric vehicles. IET Electric Power Applications. 2015;9(7):459–68.

[8] Jack AG, Mecrow BC, Haylock JA. A comparative study of permanent magnet and switched reluctance motors for high-performance fault-tolerant applications. IEEE Transactions on Industry Applications. 1996;32(4):889–95.

[9] Stephens CM. Fault detection and management system for fault-tolerant switched reluctance motor drives. IEEE Transactions on Industry Applications. 1991;27(6):1098–102.

[10] Mir S, Islam MS, Sebastian T, Husain I. Fault-tolerant switched reluctance motor drive using adaptive fuzzy logic controller. IEEE Transactions on Power Electronics. 2004;19(2):289–95.

[11] Hennen MD, Niessen M, Heyers C, Brauer HJ, Doncker RWD. Development and control of an integrated and distributed inverter for a fault tolerant five-phase switched reluctance traction drive. IEEE Transactions on Power Electronics. 2012;27(2):547–54.

[12] Zeraoulia M, Benbouzid MEH, Diallo D. Electric motor drive selection issues for HEV propulsion systems: a comparative study. IEEE Transactions on Vehicular Technology. 2006;55(6):1756–64.

[13] Sebastian T. Temperature effects on torque production and efficiency of PM motors using NdFeB magnets. IEEE Transactions on Industry Applications. 1995;31(2):353–57.

[14] Desai PC, Krishnamurthy M, Schofield N, Emadi A. Novel switched reluctance machine configuration with higher number of rotor poles than stator poles: concept to implementation. IEEE Transactions on Industrial Electronics. 2010;57(2):649–59.

[15] Bilgin B, Emadi A, Krishnamurthy M. Design considerations for switched reluctance machines with a higher number of rotor poles. IEEE Transactions on Industrial Electronics. 2012;59(10):3745–56.

[16] Rallabandi V, Fernandes BG. Design procedure of segmented rotor switched reluctance motor for direct drive applications. IET Electric Power Applications. 2014;8(3):77–88.

[17] Moallem M, Ong CM, Unnewehr LE. Effect of rotor profiles on the torque of a switched-reluctance motor. IEEE Transactions on Industry Applications. 1992;28(2):364–69.

[18] Krzysztof Bieńkowski JS, Bogdan Bucki, Adam Biernat, Adam Rogalski. Influence of Geometrical Parameters of Switched Reluctance Motor on Electromagnetic Torque. Berichte Und Informationen Hochschule fur Technik und Wirtschaft; Dresten 2004.

[19] Sundaram M, Navaneethan P, Vasanthakumar M, editors. Magnetic analysis and comparison of Switched Reluctance Motors with different stator pole shapes using a 3D finite element method. In: 2009 INCACEC 2009 2009 International Conference on Control, Automation, Communication and Energy Conservation; 2009 4–6 June 2009.

[20] Chiba A, Kiyota K, Hoshi N, Takemoto M, Ogasawara S. Development of a rare-earth-free SR motor with high torque density for hybrid vehicles. IEEE Transactions on Energy Conversion. 2015;30(1):175–82.

[21] Uematsu T, Wallace RS, editors. Design of a 100 kW switched reluctance motor for electric vehicle propulsion. In: 1995 APEC '95 Conference Proceedings of Applied Power Electronics Conference and Exposition;1995, Tenth Annual; 1995 5–9 Mar 1995.

[22] Rahman KM, Schulz SE. Design of high-efficiency and high-torque-density switched reluctance motor for vehicle propulsion. IEEE Transactions on Industry Applications. 2002;38(6):1500–07.

[23] Watanabe K, Aida S, Komatsuzaki A, Miki I, editors. Driving force characteristics of 40 kW switched reluctance motor for electric vehicle. In: 2007 ICEMS International Conference on Electrical Machines and Systems; 2007 8–11 Oct. 2007.

[24] Shuanghong W, Qionghua Z, Zhiyuan M, Libing Z. Implementation of a 50-kW four-phase switched reluctance motor drive system for hybrid electric vehicle. IEEE Transactions on Magnetics. 2005;41(1):501–04.

[25] Kalan BA, Lovatt HC, Prout G, editors. Voltage control of switched reluctance machines for hybrid electric vehicles. Power Electronics Specialists Conference, 2002 pesc 02 2002 IEEE 33rd Annual; 2002 2002.

[26] Watterson PA, Wei W, Kalan BA, Lovatt HC, Prout G, Dunlop JB, et al., editors. A switched-reluctance motor/generator for mild hybrid vehicles. In: 2008 ICEMS 2008 International Conference on Electrical Machines and Systems; 2008 17–20 Oct. 2008.

[27] Miller JM, Gale AR, McCleer PJ, Leonardi F, Lang JH, editors. Starter-alternator for hybrid electric vehicle: comparison of induction and variable reluctance machines and drives. Industry Applications Conference, 1998 Thirty-Third IAS Annual Meeting The 1998 IEEE; 1998 12–15 Oct. 1998.

[28] Ellabban O, Abu-Rub H, editors. Switched reluctance motor converter topologies: a review. In: 2014 IEEE International Conference on Industrial Technology (ICIT); 2014 Feb. 26 2014-March 1 2014.

[29] Barnes M, Pollock C. Power electronic converters for switched reluctance drives. IEEE Transactions on Power Electronics. 1998;13(6):1100–11.

[30] Miller TJE. Converter volt-ampere requirements of the switched reluctance motor drive. IEEE Transactions on Industry Applications. 1985;IA-21(5):1136–44.

[31] Hu Y, Song X, Cao W, Ji B. New SR drive with integrated charging capacity for plug-in hybrid electric vehicles (PHEVs). IEEE Transactions on Industrial Electronics. 2014;61(10):5722–31.

[32] Holtz J. Sensorless control of induction motor drives. Proceedings of the IEEE. 2002;90(8):1359–94.

[33] Holtz J. Sensorless control of induction machines—with or without signal injection? IEEE Transactions on Industrial Electronics; 2006;53(1):7–30.

[34] Wu S, Reigosa DD, Shibukawa Y, Leetmaa MA, Lorenz RD, Li Y. Interior permanent-magnet synchronous motor design for improving self-sensing performance at very low speed. IEEE Transactions on Industry Applications. 2009;45(6):1939–46.

[35] Chau KT. Switched Reluctance Motor Drives. Electric Vehicle Machines and Drives Design, Analysis and Application: Wiley-IEEE Press; © 2015 John Wiley & Sons Singapore Pte. Ltd. p. 108–46.

[36] Fahimi B, Suresh G, Ehsani M, editors. Review of sensorless control methods in switched reluctance motor drives. In: 2000 Conference Record of the 2000 IEEE Industry Applications Conference; 2000.

[37] Pyrhonen J, Jokinen T, Hrabovcova V. Design of Rotating Electrical Machines. 2nd ed: Wiley; Chichester, West Sussex, PO19 8SQ, United Kingdom; 2013.

[38] Krishnan R, Arumugan R, Lindsay JF. Design procedure for switched-reluctance motors. IEEE Transactions on Industry Applications. 1988;24(3):456–61.

[39] Nakao N, Akatsu K, editors. A simple unipolar excitation strategy for switched reluctance motors by using PWM current control. In: 2013 IEEE ECCE Asia Downunder (ECCE Asia); 2013 3–6 June 2013.

[40] Jeyabharath R, Veena P, Rajaram M, editors. A novel DTC strategy of torque and flux control for switched reluctance motor drive. In: 2006 PEDES '06 International Conference on Power Electronics, Drives and Energy Systems; 2006 12–15 Dec. 2006.

[41] Kioskeridis I, Mademlis C. Maximum efficiency in single-pulse controlled switched reluctance motor drives. IEEE Transactions on Energy Conversion. 2005;20(4):809–17.

[42] Schaltz E. Chapter 1. Electrical Vehicle Design and Modeling. Electric Vehicles—Modelling and Simulations: InTech; 2011. p. 1–24.

[43] Pacejka HB. Tyre and Vehicle Dynamics: Butterworth-Heinemann. The Boulevard, Langford Lane, Oxford OX5 1GB, UK; 2006.

[44] Lee D-H. Advanced torque control scheme for the high speed switched reluctance motor. In: Ahmad M, editor. Advances in Motor Torque Control: InTech; 2011. p. 87–114.

[45] Moreno-Torres P, Blanco M, Lafoz M, Arribas J. Educational project for the teaching of control of electric traction drives. Energies. 2015;8(2):921.

[46] Carstensen C. Eddy Currents in Windings of Switched Reluctance Machines. Christian Carstensen 2007 http://publications.rwth-aachen.de/record/49862/files/Carstensen_Christian.pdf.

[47] Barbisio E, Fiorillo F, Ragusa C. Predicting loss in magnetic steels under arbitrary induction waveform and with minor hysteresis loops. IEEE Transactions on Magnetics. 2004;40(4):1810–19.

[48] Miller TJE. Switched Reluctance Motors and their Control. 2nd ed: Magna Physics Publications. Oxford, England; 1993.

[49] Calverley SD, Jewell GW, Saunders RJ. Aerodynamic losses in switched reluctance machines. IEE Proceedings: Electric Power Applications. 2000;147(6):443–48.

[50] Grbovic PJ. Interfase DC-DC Converters. Ultra-Capacitors in Power Conversion Systems: Analysis, Modeling and Design in Theory and Practice: Wiley-IEEE Press. Chichester, West Sussex, PO19 8SQ, United Kingdom; 2013. p. 216–316.

[51] Wintrich A, Nicolai U, Tursky W, Reimann T. Application Manual Power Semiconductors Dr.-Ing. Arendt Wintrich Dr.-Ing. Ulrich Nicolai Dr. techn. Werner Tursky

Univ.-Prof. Dr.-Ing. Tobias Reimann Published by SEMIKRON International GmbH, Germany ISBN 978-3-938843-83-3 2nd revised edition https://www.semikron.com/dl/service-support/downloads/download/semikron-application-manual-power-semiconductors-english-en-2015 2011.

[52] ABB Switzerland Ltd. Thermal runaway during blocking Application Note 5SYA 2045-01 ABB Switzerland Ltd Semiconductors https://library.e.abb.com/public/4839b96959e24e32b59b08285a11bff0/Thermal%20runaway%20during%20blocking_5SYA%202045-01NLay.pdf 2013.

[53] Torkaman H, Afjei E. Sensorless method for eccentricity fault monitoring and diagnosis in switched reluctance machines based on stator voltage signature. IEEE Transactions on Magnetics. 2013;49(2):912–20.

[54] Marques JF, Estima JO, Gameiro NS, Cardoso AJM. A new diagnostic technique for real-time diagnosis of power converter faults in switched reluctance motor drives. IEEE Transactions on Industry Applications. 2014;50(3):1854–60.

[55] Yihua Hu CG, Wenping Cao and Stephen Finney. Fault diagnosis of switched reluctance motors in electrified vehicle applications. In: Chomat M, editor. New Applications of Electric Drives: InTech; 2015. p. 59–86.

Chapter 6

Load Leveling Utilizing Electric Vehicles and their Used Batteries

Muhammad Aziz and Takuya Oda

Additional information is available at the end of the chapter

http://dx.doi.org/10.5772/64432

Abstract

The increase of electric vehicles (EVs) has led to some challenging problems and opportunities, especially related to electricity issues. The uncontrolled charging and discharging of EVs can reduce the quality of electricity grid due to frequency and voltage instabilities. However, the optimized utilization of EVs also offers high potential for ancillary service including frequency control and storage. The adoption of EVs and used EV batteries is expected to be able to improve the total economic performance of EVs as well as reduce the environmental impact. In this chapter, the utilization of EVs, together with their used batteries, to support the electricity (load leveling) in a small-scale energy management system (EMS) is analyzed and demonstrated. The demonstration bed consists of five EVs, five used EV batteries, and photovoltaic (PV) panels. The EMS forecasts the load of the office building and the possibly generated power from PV panels. In addition, it also calculates the potential of EVs which are available for joining the load leveling program. EMS will control all the charging and discharging behaviors of connected EVs and used EV batteries, therefore the grid load can be maintained to be lower than the calculated peak-cut threshold. It is found that the utilization of EVs to support small-scale EMS through direct contract is feasible, and hence applicable. At the end of the chapter, some suggestions earned from demonstration test are also listed for further consideration.

Keywords: vehicle-to-grid, used battery, load leveling, small scale, energy management system

1. Introduction

The massive dissemination of electric vehicles (EVs) is believed to be able to improve the total energy efficiency of the vehicles as well as reduce the emission of greenhouse gases and oil

consumption [1]. In Japan, considering that the gasoline price, total annual driving distance, electricity price during night time, and fuel consumption of both gasoline-fueled vehicle and EV are 110 JPY l^{-1}, 10,000 km, 12 JPY kWh^{-1}, and 15 km l^{-1} and 6 km kWh^{-1}, respectively, the total operational cost of EV may be less than 30% of gasoline-fueled vehicle. Furthermore, the acceleration in the development of EV also has been influenced strongly by some various factors including fluctuating oil and gas prices, successful advancements in battery technology, and broader supporting infrastructure [2,3]. Unfortunately, there are still some challenging problems to expand in a broader scope of the community including high capital cost, long charging time, and relatively short travelable distance [4]. In addition, although the operational cost of EVs is cheaper than the conventional gasoline-fueled vehicles (internal combustion engine–based vehicles), the initial cost of EV is still higher due to high production cost.

To further reduce the initial and operational costs of EV (increase its economic performance), innovative value-added utilization of EV is requested. Furthermore, massive deployment of EVs can disturb significantly the grid electricity, especially when individual charging of EVs in large capacity and number occurred. According to [5], in case that a half of vehicles in Kanto (Tokyo and its surroundings) area are transformed to EVs and half of them are demanding a quick charging simultaneously, about 7.31 GW of additional electricity supply is required. Recently, to give an answer to the above problems, the idea of vehicle-to-grid (V2G) has been proposed and investigated [6–8].

The adoption of EVs to support the electricity of grid or any electricity-related system becomes possible because of controllable charging and discharging behaviors resulting in the possibility of scheduled and coordinated charging and discharging. Therefore, the parked and connected EVs can be assumed as a largely bundled battery which is able to consume (absorb) the electricity from the grid, store it, and release back to the grid. In addition, V2G can be achieved when minimally three fundamental preconditions are totally satisfied: (1) an electricity line connecting both EV and power grid, such as charging station, (2) a communication system transferring the information and control command between EV and grid operator, and (3) an accurate and trusted metering system facilitating fair service measurement [9]. Furthermore, in case that there is any demand for electricity, the grid operators and/or energy management system (EMS) are able to dispatch a control command instructing the connected EVs to discharge their stored electricity to the grid. On the other hand, they can instruct the connected EVs to absorb the electricity due to surplus of electricity or decrease of electricity demand. Therefore, the balance between supply and demand, as well as quality of grid electricity can be maintained.

V2G provides various possible ancillary services to the electricity grid or any electricity-related system such as load leveling and spinning reserve. In addition, the distributed EVs also can be assumed as a large-scale energy storage (battery) which is potential to be bundled and utilized to minimize the effect of fluctuating supply. As EVs are moving from and to different times and places, they also could be employed as an energy carrier transporting the electricity in different places and times due to some factors such as electricity price difference and emergency condition. From the economic analysis, the massive adoption of EVs to give ancillary service to the grid (V2G) is considered beneficial because the projected profit is still

http://dx.doi.org/10.5772/64432

significantly higher than the initial cost of EVs, especially the battery including the consideration of battery wear and life cycle [4]. This feasibility study has been performed based on the actual data of EVs, especially the life cycle of battery.

Until now, battery cost stands as the highest share in total EV production cost. In addition, as the number of produced EVs increases, the number and total capacity of the used batteries increase accordingly. According to [10], the EV batteries are generally replaced after their storage capacity drops to about 70–80% of its initial capacity. The decrease in battery capacity leads to shorter possible driving range. Therefore, although these used EV batteries are not appropriate anymore for EVs, they can be reutilized as a stationary energy storage (stationary battery). This kind of battery utilization is believed to be able to further improve the overall economic performance of EV as well as reduces their impacts to the environment because it can lengthen the battery end-of-life. The study on the utilization of EV batteries acting as stationary battery to take part in ancillary service to certain EMS or grid can be found in several literature [11, 12].

Several studies focusing on theoretical analyses of the application of both EVs and used EV batteries have been conducted well. However, those studies are generally lack of experimental investigation including demonstration tests and real application. This chapter deals mainly with the employment of EVs and used EV batteries in supporting the electricity in any typical small-scale EMS including both theoretical and experimental studies. In addition, the results from the demonstration test are also studied and analyzed.

2. Energy management system

Charging of EVs basically can be categorized into three different capacities: (a) slow charging with capacity lower than 4 kW, (b) fast charging with capacity of 10–20 kW, and (c) ultrafast charging with a maximum capacity of 50 kW or higher [13]. Ultrafast charging is conducted generally under high DC voltage and current. In Japan, this ultrafast charging follows the standard of CHAdeMO (the acronym of "charge de move", equivalent to "move by charge") which offers charging capacity of 10–50 kW. Until the end of 2015, there are about 6000 ultrafast chargers following CHAdeMO standard across Japan [14]. CHAdeMO chargers can facilitate bidirectional electricity flows resulting in possible charging and discharging of EVs. In addition, intelligent controlling system is also generally installed inside the charger, hence high level communication and control can be achieved.

The management of energy, especially the electricity, is usually coordinated and controlled by certain independent operator. In North America, independent system operator (ISO) and regional transmission operator (RTO) act as the independent and neutral organizations that are responsible to coordinate, control, and monitor the electric transmission throughout the state or region [15]. In addition, ISO and independent transmission operator (ITO) were established in Europe which are quite similar with ISO/RTO in North America. The main differences between the US-type ISO/RTO and the EU-type ISO/ITO are the absence of profit motives, and participation and transparency of all the involved stakeholders [16]. ITO in

Europe owns the assets and it belongs to certain stakeholders, but has a regulation to guarantee its independence. On the other hand, ISO is fully unbundled operator having no assets although still belongs to certain stakeholders.

In Japan, community energy management system (CEMS) has been proposed and demonstrated. The main purpose of CEMS is realizing a resilient and smart community, especially related to efficiency in energy utilization and minimization of CO_2 emission. The concept of CEMS comes from the demand to optimize the energy services, maximize the potential economy, and minimize the environmental impacts. CEMS coordinates and monitors all the energy supply and demand throughout the community, hence improving the comfort, security, and safety of the whole community members. In CEMS, the streams of energy and information are flowing simultaneously covering supply, demand, storage, and distribution. As a system, CEMS must be robust and secured because it deals with individual information and its authentication.

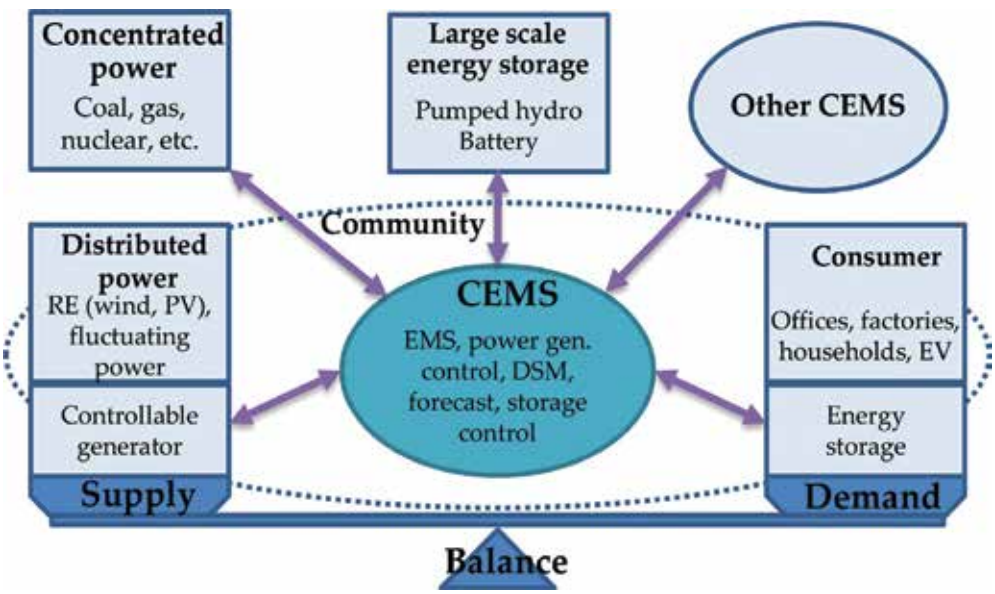

Figure 1. Basic concept of CEMS.

Figure 1 shows the basic concept of CEMS. CEMS has an important role of monitoring and controlling all the energy involved in the community. It becomes the core of efficient, secured, and optimized energy utilization throughout the community. CEMS is able to communicate with other entities inside and outside its authority. Inside the community, CEMS communicates intensively with its lower EMSs such as home energy management system (HEMS), building energy management system (BEMS), and factory energy management system (FEMS). In addition, it also may communicate directly with EVs distributed in the community which are not controlled under certain EMS. CEMS is also able to communicate with other

http://dx.doi.org/10.5772/64432

CEMS, large-scale energy providers (utilities), transmission operators, and energy storage operators.

Inside the community, CEMS initially forecasts both energy supply, especially generable renewable energy (RE) and demand. This forecast is usually performed based on historical (for several years before) and meteorological data. Furthermore, it calculates the most optimized energy balance in terms of quality, security, and economic cost. In case the energy balance between the supply and demand cannot be self-achieved inside the community due to lack of power generation capacity, high and fluctuating demand, and emergency condition, CEMS communicates with other CEMS, utilities, and energy storage providers to deliver or increase their power to the community. On the other hand, in case there is surplus electricity inside the community (due to high supply and/or low demand), CEMS can offer to other CEMS or utilities to buy this surplus electricity.

CEMS is also performing a demand side management (DSM). DSM includes efficient energy usage and demand response (DR) in demand side, instead of adding larger generation capacity at the supply side. DSM can be considered as a dispatchable resource, in which the consumer lower voluntarily their demand, therefore the grid quality can be maintained without any additional power supply.

3. EV involvement in energy management system

EVs can be applied to support the grid electricity, mainly providing energy storage and ancillary services, due to the above-mentioned characteristics. As energy storage, EVs can be charged when the electricity price is relatively low because of surplus electricity in supply side, including RE and excess power, and lower demand (such as during night time). Furthermore, the ancillary services which can be performed by EVs to support the grid electricity mainly cover frequency regulation (up and down regulations), electricity storage, and spinning (synchronous) reserve. Compared to other energy storages or generators, EVs have a very advantageous characteristic which is its ability to charge and discharge instantaneously their electricity once they received the command from the operator or EMS. The above-mentioned ancillary services are required to preserve the balance between supply and demand of electricity, therefore the electricity can be appropriately reliable.

To participate in the ancillary services, the EV owners are requested to have any service contract with the operator or EMS. Possible utilization contract schemes of EVs to support the grid electricity or any electricity-related system are shown in **Figure 2**. In general, the participation of EVs in the electricity market could be conducted through two types of participation contracts, they are direct and aggregator-based contracts. To facilitate a communication between EVs and operators, a real time data collection is conducted by vehicle information system (VIS) in a certain time interval from EVs covering battery state of charge (SOC), position (GPS data), and predicted arrival time. VIS might be owned and managed directly by EMS, aggregator or it is independent as service operator which provides EV information services to EMS and aggregator.

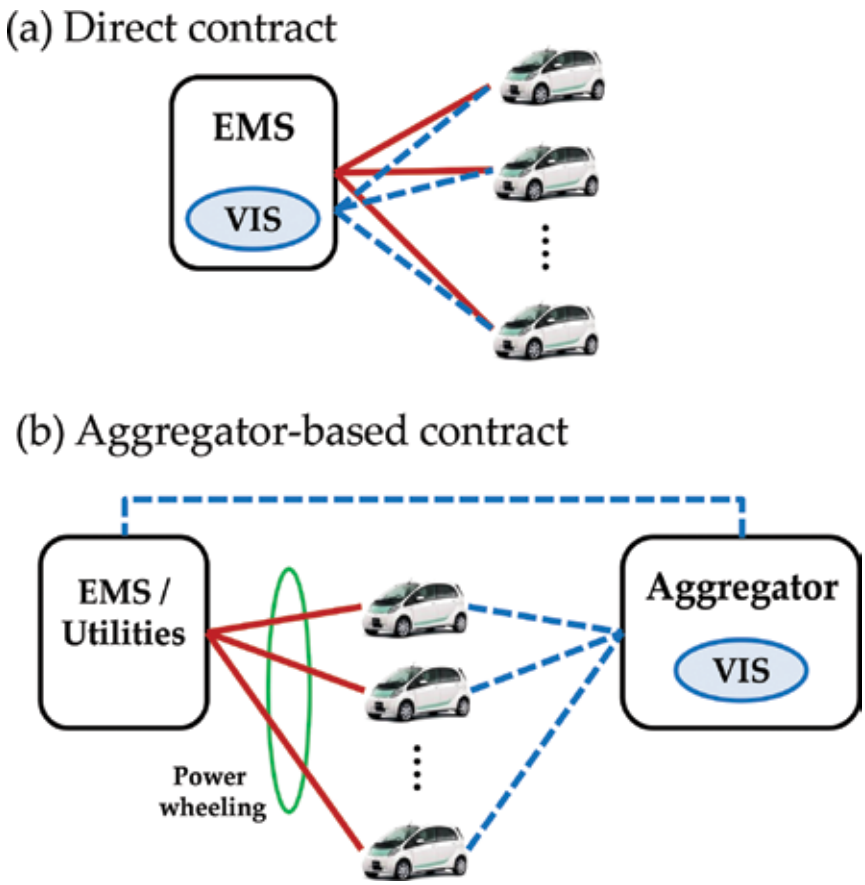

Figure 2. Possible contract schemes of EV in EMS: (a) direct contract and (b) aggregator-based contract.

In a direct contract, the EV owners have the service contract directly with the energy service providers (EMS). In this contract scheme, both the electricity and information are transferred privately and directly between EVs and energy service provider. Therefore, this type of contract is considered applicable for a relatively small-scale EMS, including BEMS and FEMS, and in where EVs are parked and connected to the chargers for relatively long time, for example during working hours. The main advantage of this type of contract scheme is the ability to optimize the profit for the involving entities (EV owners and EMS). Furthermore, controls for both charging and discharging are more simple and faster as EVs are directly and fully under control of EMS. The report in this chapter describes mainly on this type of contract scheme.

On the contrary, in an aggregator-based contract scheme, EV owners have service contracts with the aggregators which are providing and managing electricity services. Therefore, there is no direct contract between EV owners and EMS or other electricity-related entities. The information including EV position (GPS), battery condition (SOC), and estimated arrival time is basically coordinated by aggregator via VIS. Based on these data, the aggregator calculates

http://dx.doi.org/10.5772/64432

the available number of EVs as well as the total capacity of the battery which is potential for power services. Furthermore, the aggregator can offer and negotiate for electricity services with other electricity-related entities including aggregators, EMS, and/or electricity utilities. It is assumed that this kind of contract scheme is suitable to be adopted for comparatively large-scale EMS or electricity utilities. The participating EVs are not only located in certain single place, but they might be distributed in different places as long as both electricity connection and communication are available and possible to perform ancillary services. The electricity absorbed from and discharged to the grid can be transferred through power wheeling service utilizing the available distribution and transmission lines. Aggregator acts as service operator, hence they offer some possible ancillary services to the EV owners. On the contrary, the EV owners have the right to select the offered ancillary service programs and receive the service fee from the aggregator.

Load leveling has a strong correlation with the management of both electricity demand and supply. The main objective is to lower the total grid load (electricity purchased from grid) during peak-load hours and avoid the electricity usage higher than the contracted power capacity by shifting the load from peak to off-peak-load hours. In this study, load leveling is conducted by employing both peak-shift and peak-cut. The former is defined as dislocating the electricity load during peak-load time to off-peak-load time. It can be performed by utilizing the stationary battery or other power storage devices which can absorb and store the electricity during off-peak-load time and discharge it during peak-load time. The latter is described as the effort to reduce the electricity which is purchased from the grid. In real practice, this can be conducted by generating its own energy supply especially during peak-load hours, such as RE, or by purchasing the electricity from other entities including the connected EVs. In the case that additional power supply is purchased from EVs, EVs are considered as energy storage and carrier which are storing and transporting the electricity from and to different times and places. Therefore, the economic performance of EVs can be improved by participating in this kind of ancillary services.

4. Charging behavior of EVs

Almost all of EVs adopt lithium-ion batteries to store the electricity with consideration of high-energy density, high stability, long lifetime, and relatively lower environmental impact. Charging and discharging behaviors of EVs are influenced by some factors including SOC and temperature [13]. Temperature influences some interface properties of the batteries including viscosity, density, dielectric strength, and ion diffusion capability [17]. Lower temperature results in poor charging and discharging performances because of lower performances of those properties as well as electrolyte limitation [18]. In addition, as temperature decreases, the transfer resistance increases [19].

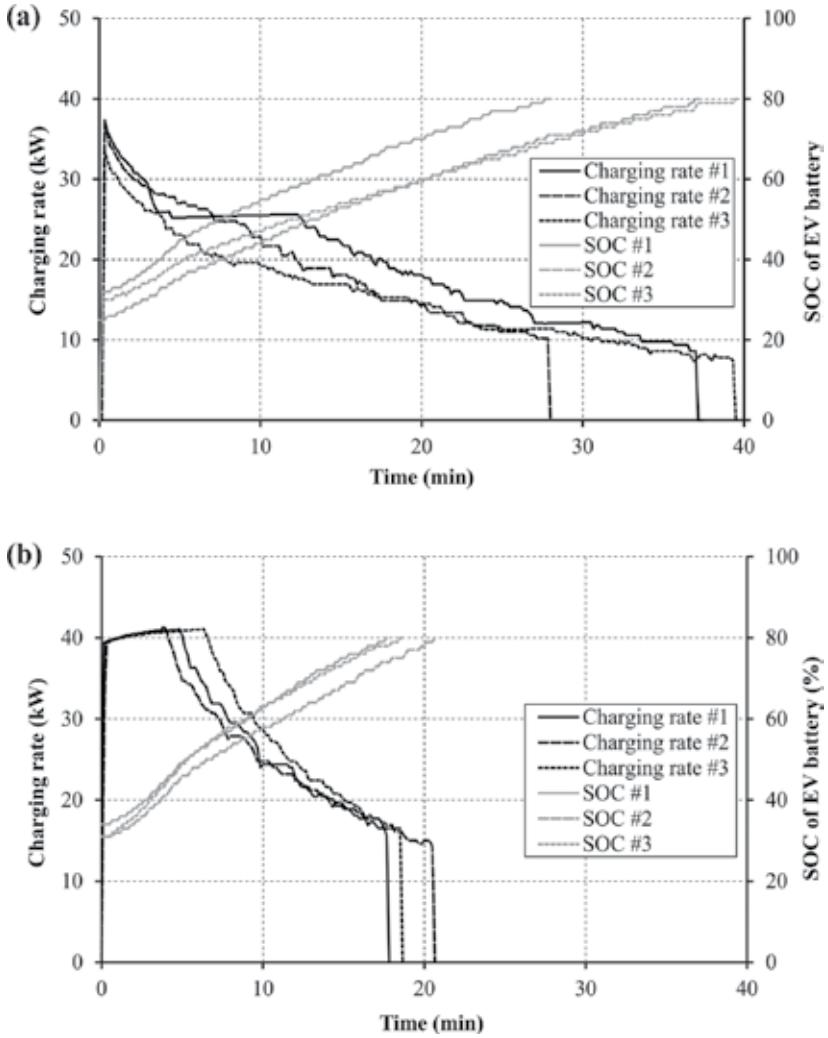

Figure 3. Relationship among charging rate, battery SOC, and charging time during EV charging in different seasons: (a) winter and (b) summer.

Aziz et al. [13] have performed an experimental study confirming the effect of battery SOC and temperature to the charging behavior of EVs in both summer and winter using DC ultrafast charger (maximum charging rate of 50 kW). **Figure 3** shows their experimental results, i.e., the relationship among the charging rate, battery SOC, and charging time. Generally, charging rate is influenced strongly by the SOC of battery. EVs with lower battery SOC can absorb higher electricity and their charging rate decreases gradually as their battery SOC increases. In addition, charging in relatively higher temperature (summer) results in higher charging rate, therefore shorter charging time can be achieved. Lithium-ion batteries are generally charged employing a constant current (CC)-constant voltage (CV) method. Charging under higher temperature leads to higher charging current, therefore shorter charging time can be realized.

http://dx.doi.org/10.5772/64432

5. Integration of EVs and their used batteries to small-scale EMS

The conceptual diagram of integration of EVs and used EV batteries in supporting the electricity in a small-scale EMS is presented in **Figure 4**. To take part in the ancillary services coordinated by EMS, there must be an initial contract between the EV owners EMS, either direct contract or aggregator-based contract through third entity such as an aggregator. Because of the mobility characteristic of EVs, their charging and discharging behaviors can be fully controlled by EMS in case EVs are connected to the designated charging stations. In addition, the used EV batteries are employed as stationary storage which are always connected to and managed completely by EMS. These used EV batteries are utilized mainly for peak-shift. Therefore, they are charged when the electricity price is low, such as during night time, and discharged during peak-load time or when the electricity price is relatively high, such as noon time. Hence, the amount of electricity which is purchased from the grid during peak-load time can be reduced, resulting in total low electricity cost.

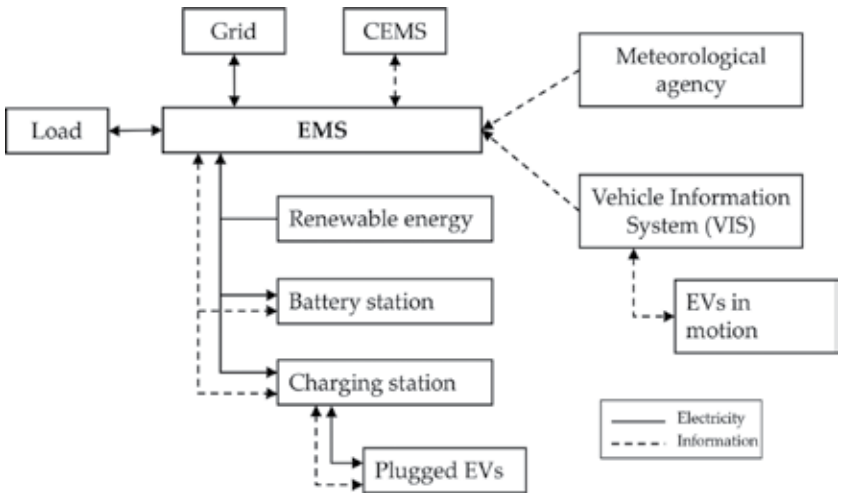

Figure 4. Conceptual diagram of integration of EVs and their used batteries to small-scale EMS.

EMS is basically controlling all the electricity flows including demand and supply sides. Some types of small-scale EMSs include BEMS, FEMS, and HEMS. A direct contract scheme is adopted in this case. EMS requests the required information from different sources covering its own demand (load), weather information from meteorological agency, EV information from VIS, electricity condition in the community from CEMS, and grid electricity condition from utility. Regarding the weather information, EMS generally has a service contract with certain meteorological agency providing the weather forecast in a certain interval of time in a day. Based on the received weather forecast, EMS will estimate its own load, including base load and fluctuating load. The former is generally defined as the minimum load which is required to run the system for sequential 24 hours. Therefore, this kind of load is usually constant along the day and insignificantly effected by the weather or human behavior. On the contrary, the

latter is determined as the load which is influenced strongly by the surrounding weather and human behavior. The fluctuating load includes air conditioning, heating, and lighting. Moreover, the possibly generated electricity from RE, such as wind and solar, is also predicted by EMS utilizing the weather information received from meteorological agency.

Figure 5 represents the average total load of the office building, especially in Japan, in four different seasons. The highest total building load takes place in summer, and is followed by one in winter, due to air conditioning demand. In addition, building loads in both spring and autumn are almost similar, which are lower than one in winter. Furthermore, daily peak-loads occur twice in a day (weekday), i.e., before noon and afternoon peak-loads. This is because of the immediate drop of load following the lunch break for about 1 hour. The afternoon peak-load mostly takes place in a longer duration, which is about 3 hours, and is higher than the before noon peak-load. Moreover, the highest value of peak-load during summer takes place during afternoon time (13:00–16:00) due to cooling demand. On the contrary, this highest value of peak-load moves to evening time (16:00–17:00) during other three seasons (autumn, winter, and spring) due to heating demand.

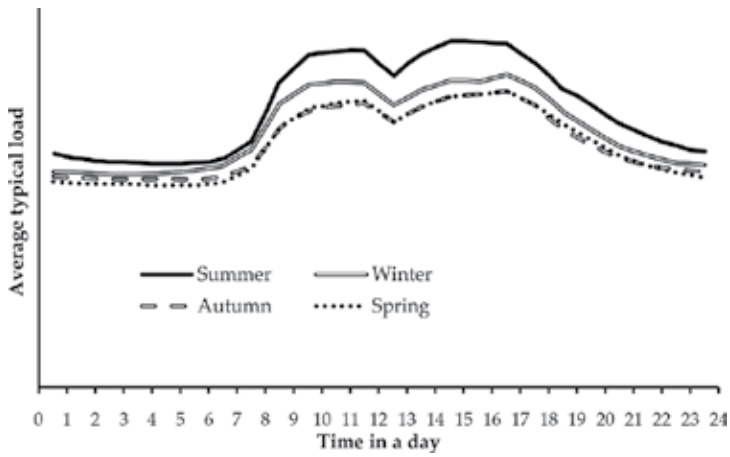

Figure 5. Average electricity loads for office building in different seasons.

EMS also receives the EV information from VIS including their position (GPS data), battery SOC, and predicted arrival time. In addition, VIS monitors and collects the information from its EV members wirelessly. It might be an independent service operator and a part of EMS or aggregator. It is responsible to communicate with each EV and provide the collected data to the EMS or aggregator in which VIS has a contract with. In addition, these data are used for coordinating both charging and discharging of EVs, maintaining the balance of electricity and avoiding any peak-load in EMS. Furthermore, VIS is also able to provide additional services to the EV drivers/owners concerning the available ancillary service programs which are being offered by EMS or aggregator. Hence, the EV owners can select according to their interests or conditions. Furthermore, EMS can request the electricity utilities to provide the information including the electricity condition and price in advance (such as one day ahead). This infor-

http://dx.doi.org/10.5772/64432

mation is important to plan and optimize the electricity supply as well as calculate the amount of electricity which should be purchased from utilities. In addition, EMS also calculates the charging and discharging behaviors of both EVs and used EV batteries which are available according to the information provided by VIS.

Figure 6 shows the assumed one day specific curve of EV battery SOC during a weekday. EVs are departed in the morning and they reach the destination (office building) at around 9 am. In this study, EVs are used for peak-cut during the afternoon peak-load due to higher peak-load and limited number of EVs in a demonstration test. EV discharging is stopped in case that the peak-cut (load leveling) finishes or the SOC of EV batteries drops to minimum SOC (SOC_{min}). SOC_{min} might be determined by the EV drivers/owners, EMS, or aggregator. In addition, EVs leave the office building at around 6 pm with minimum battery condition (SOC_{min}). On the other hand, in case that the total building load is relatively low (such as in the morning, lunch break, and night) EVs might be charged to enhance their discharging capacity or extending their traveling.

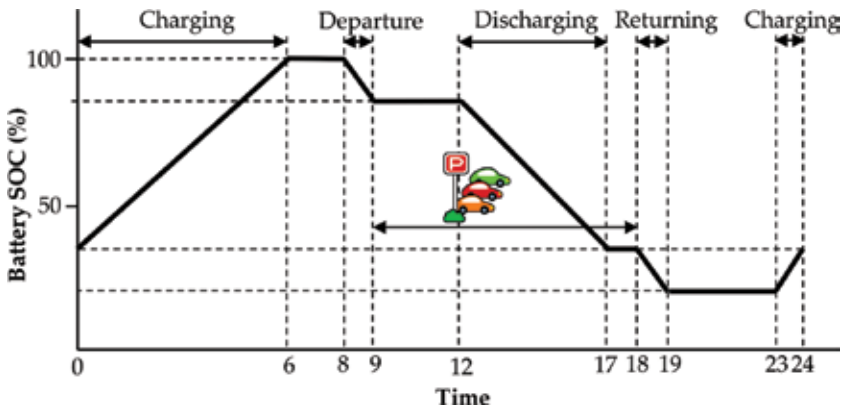

Figure 6. Typical SOC state of EVs in weekdays (commuting).

6. Suggested utilization system of EVs and their used batteries

Figure 7 presents the basic concept of load leveling which is developed for a small-scale EMS employing EVs, used EV batteries and RE generators including photovoltaic (PV) and wind. Four main continuous steps are proposed: (1) forecasting of the possibly generated RE and building load, (2) load leveling calculation including peak-shift and peak-cut, (3) value recalculation and correction, and (4) charging and discharging controls of both EVs and used EV batteries. The first step, load and RE forecasting, is basically conducted by EMS for 24 hours ahead. Furthermore, because the electricity amount in Japan is measured for a duration of 30 min, the electricity amounts (kWh) in this study are also measured and calculated as the total summation for a duration of 30 min.

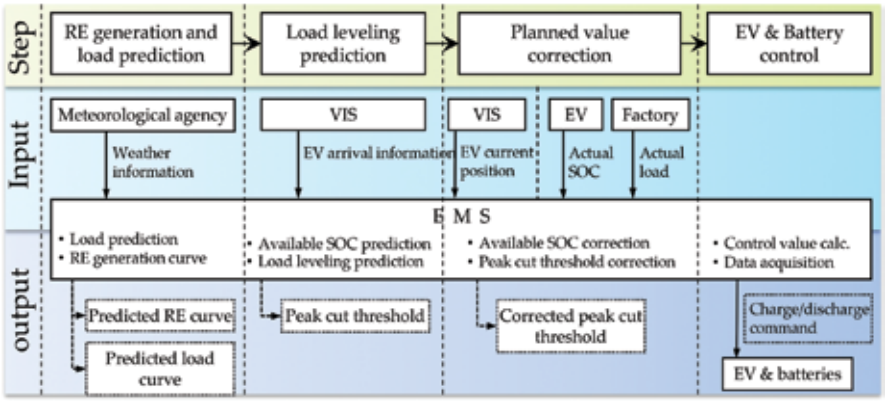

Figure 7. Developed load leveling concept utilizing EVs and their used batteries.

To forecast both load and possibly generated RE, EMS initially sends a request to meteorological agency to deliver the local weather forecast information. This weather information is very crucial for calculating the electricity which can be potentially generated by RE, such as PV and wind. Because the amount of RE generation is significantly smaller than the total load, in this study, this generated electricity from RE is used directly for peak-cut, hence it will be delivered directly and consumed entirely without being stored in the battery. Moreover, the weather information is also used to forecast the fluctuating load of the office building, especially to calculate the demand of air conditioning (cooling and heating) and lighting. The outputs from this first step include the predicted power generation from RE and daily load curves of the next day (defined as day starting from 00:00 to 24:00).

As the building load and possibly generated electricity from RE have been predicted, EMS will calculate the achievable load leveling (peak-cut) for the next day. In order to realize it, EMS sends a request to VIS to calculate and send the information related to the available EVs, including their battery SOCs, which will potentially participate for the load leveling program. This information is required to estimate the total available electricity which can be supplied by the EVs for load leveling.

In order to perform the given request by EMS, VIS initially collects the traveling schedule from the EV drivers (planned departure time and predicted arrival time). Next, EMS forwards this information, as well as calculates the total availability of EVs and their batteries, together with basic information including EV's ID. This registration of traveling schedule is conducted up to 24 hours before the planned departure. Finally, using the data from the first and second steps, EMS is able to estimate the peak-cut threshold which can be applied for the next day.

In this study, a peak-cut threshold is determined as the maximum electricity which is purchased from the electricity grid. To calculate this peak-cut threshold, some important factors need to be considered including price of electricity at the corresponding time, contracted power capacity, possibly generated electricity from RE, available electricity supply from other sources with low price, and potential energy storage.

http://dx.doi.org/10.5772/64432

In case that the electricity which is consumed by the office building rises resulting in the condition that the purchased electricity from the grid increases and reaches nearly the calculated peak-cut threshold, EMS immediately sends the control command to both connected EVs and used EV batteries to release their electricity supporting EMS to cover the demand. Therefore, the electricity purchased from the grid can be kept to be the same to or lower than the calculated peak-cut threshold. As a result, a higher price of electricity during peak-load time or penalty due to higher capacity than the contracted one can be avoided.

When EVs are not connected to the designated charging stations, such as in motion or being parked in other places, the information of EVs is sent wirelessly to VIS in an interval of several seconds to minutes (adding and renewing the information). Thereafter, VIS transmits the updated data to EMS. EMS will recalculate the potential availability of electricity from EVs. Moreover, EMS also recalculates the building load based on the present real load of building and real weather which is measured using thermometer and hygrometer. Next, EMS renews its energy management plan, especially the calculated peak-cut threshold.

Furthermore, when EVs arrive at the office building and are plugged to the designated charging stations, EV start to communicate directly with EMS and bypassing VIS through the charging lines. EMS will read the information from EVs and update the previous data received from VIS, especially the battery SOC. As EVs are connected directly to EMS via charging station, EVs are completely under EMS management. Therefore, their charging and discharging behaviors are controlled completely by EMS. After receiving the updated data from EVs, EMS recalculates the peak-cut threshold accurately. As the electricity demand reaches the updated peak-cut threshold, EMS sends the control command to EVs and used EV batteries to discharge their electricity. After finishing the load leveling, EMS can manage the charging for EVs, hence another peak-load due to uncoordinated EV charging can be avoided.

7. Demonstration test

Figure 8 shows the schematic diagram of the demonstration test bed developed in this study. Solid and dotted lines represent the electricity and information flows, respectively. In addition, **Figure 9** shows the pictures of the developed test bed. This demonstration test bed was constructed in the factory area of Mitsubishi Motors Corporation which is located in Okazaki, Aichi prefecture, Japan. Due to limited number of EVs and used EV batteries in this study, this test bed is connected to the electricity of the main office building (office building is considered as BEMS), and not to the whole electricity of the factory. PV panels having total maximum capacity of 20 kW is installed at the rooftop of the test bed as RE generator. In addition, five Mitsubishi EVs, i-Miev G, are participating in this demonstration test. The drivers are the employees who are working in the factory and EVs are used for commuting purpose. Therefore, EVs are basically available during working hours, especially during the day. They are parked and plugged to charging stations installed in the test bed. Furthermore, five used EV batteries are also employed as stationary battery. These used EV batteries are basically detached from the same type of EVs after about one year usage.

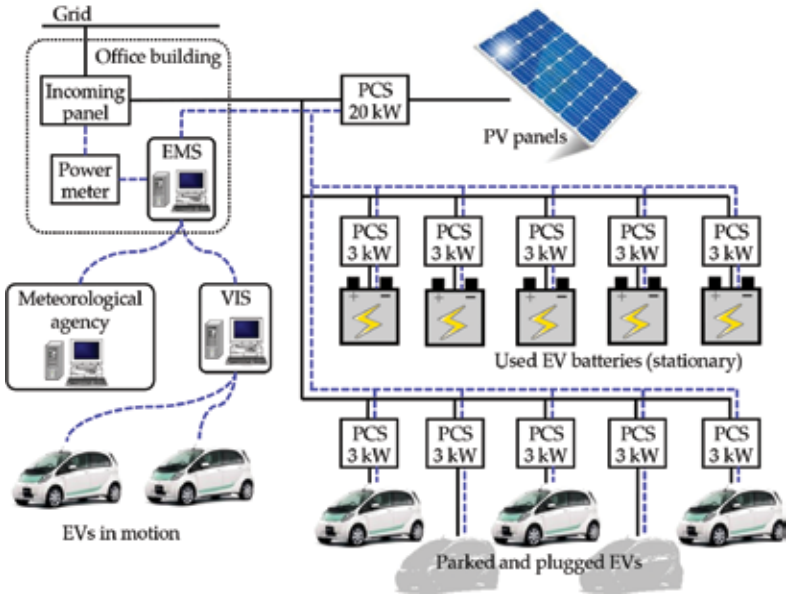

Figure 8. Schematic diagram of the developed test bed.

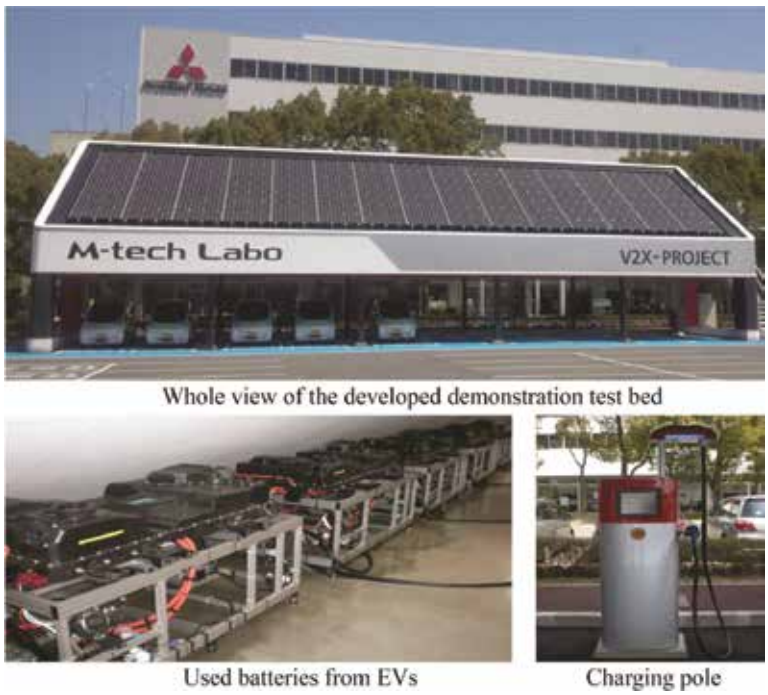

Figure 9. Overview of the developed system involving PV, EVs, and used EV batteries.

http://dx.doi.org/10.5772/64432

Components	Properties	Value
PV panels	Type	Monocrystalline
	Capacity	20 kW
	Direction, angle	South, 30°
	PCS capacity	AC 200 V, 100 A
EVs	Type	i-Miev G
	Number	5
	Battery capacity	16 kWh
	Charging capacity	DC 370 V, 15 A
	PCS capacity	AC 200 V, 15 A
Used EV batteries	Original EV	i-Miev G
	Number	5
	Condition	1-year usage
	Battery capacity	16 kWh
	Charging capacity	DC 370 V, 15 A
	PCS capacity	AC 200 V, 15 A

Table 1. Specifications of the developed test bed.

EMS is controlling the balance of both demand and supply of the main office building and test bed. EMS also forecasts and measures the demand of the office building. In addition, VIS is also developed as an independent system which communicates with EVs and transmits the received information to EMS. **Table 1** shows the detailed specifications of the developed demonstration test bed.

The drivers submit their daily traveling plans to VIS up to one day before the scheduled departure. To facilitate this, a web-based system has been developed facilitating the drivers to input and check their traveling plan from any computers or mobile devices. If EVs are not connected to the designated charging stations of EMS, such as in motion, EVs send their data to VIS in an interval of 10 s wirelessly. In addition, VIS transmitted the received data from EVs to EMS simultaneously. EMS receives EV data from VIS and weather information from meteorological agency. Although the weather information is received basically one day before, meteorological agency will update these data automatically once there is any renewal or correction in the weather information.

Used EV batteries are utilized for peak-shift. Charging of used EV batteries is practically performed from midnight to morning (00:00–06:00). Threshold for charging and discharging of both EVs and used EV batteries is set to SOC 90% and SOC 40%, accordingly. In addition, load leveling is designed to be conducted during afternoon peak-load time starting from 12:00 until 18:00 (6 hours duration) because the total amount of potentially available electricity from EVs and used EV batteries is limited and very small compared to the total load of the office

building. In addition, to diminish the effect of ambient temperature on charging and discharging behaviors of used EV batteries, the storage room of used EV batteries is controlled to have a temperature of 25 °C throughout the year at.

The load of office building is estimated as the sum of the base load and fluctuating load, especially the air conditioning demand. The air conditioning demand is calculated using historical data for several previous years and forecasted ambient temperature received from meteorological agency. The demand of office building in certain typical time, L_t, can be simply approximated as follows:

$$L_t = L_{BS} + f\left(\left[T_{OA} - T_{ST}\right]_t \left(\Delta\tau\right)\right) \tag{1}$$

where L_{BS}, f, T_{OA}, T_{ST}, and $\Delta\tau$ are the base load for 30 min interval (kWh) of the office building, functional relationship, outside ambient temperature (°C), room temperature inside the office building (°C), and time shift (h), respectively.

The available electricity from EVs, P_{EV}, which are in motion and not plugged in to the charging poles can be estimated as the correlation of SOC and the remaining distance (both are received from VIS), and can be represented as follows:

$$P_{EV,t} = \left(SOC_{EV,t} \times C_{EV} - d_t \times \eta_{EV}\right) - SOC_{\min} \times C_{EV} \tag{2}$$

where $SOC_{EV,t}$, C_{EV}, d_t, η_{EV}, and SOC_{min} are SOC of each EV (%), EV battery capacity (kWh), remaining travel distance to the designated charging station (km), power consumption of EV (kWh km^{-1}), and minimum SOC threshold for discharging (%), respectively.

To calculate the peak-cut threshold, a day load duration curve is initially created using the historical data of the averaged office building load for the same month in the last year. A peak-cut threshold, P_{thr}, can be approximated using Equation (3). **Figure 10** shows the illustration of a day load duration curve.

$$\begin{aligned} &for\ L_n > P_{thr} \\ &\Sigma L_n = n\ P_{thr} + \Sigma P_{ev,m} + \Sigma P_{bat,m} + P_{pv} \end{aligned} \tag{3}$$

where P_{bat}, n, and m are available power from used EV battery (kWh), number of load higher than peak-cut threshold, and number of EVs and used EV batteries, respectively.

In general, a load duration curve lines up all the loads in a descending order. Therefore, in this demonstration test, a day load duration curve is created by sorting all 30 min duration of office building loads from the largest to the smallest loads. Therefore, the plotted area represents the total electricity consumed by the office building for a day (starting from 00:00 to 24:00). Furthermore, the generated electricity from PV panels is directly delivered to the building

http://dx.doi.org/10.5772/64432

without being managed by EMS to be stored in the battery. In addition, the total electricity which can be obtained from connected EVs, used EV batteries, and PV panels is plotted on the top of a day load duration curve for the corresponding day while its bottom is kept to be straight at the same value of load. Therefore, the created straight line is a peak-cut threshold which is used in load leveling.

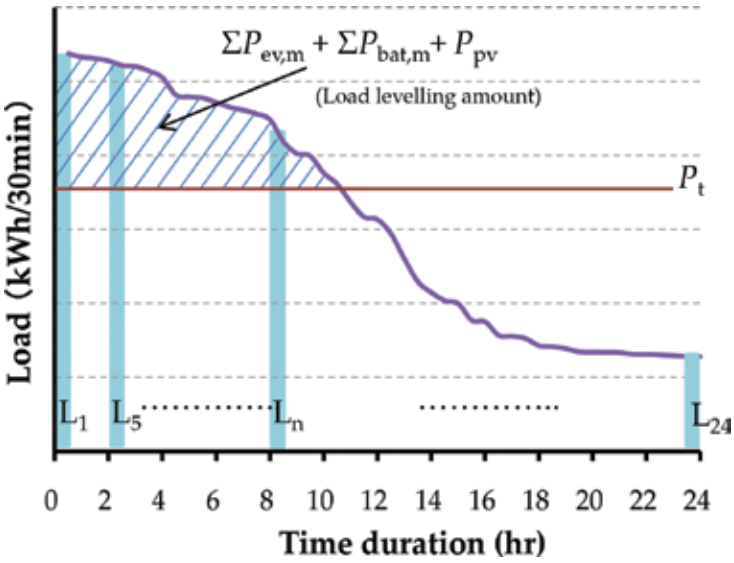

Figure 10. Typical load duration curve and the calculated peak-cut threshold.

8. Results of load leveling test

A result of load leveling demonstration test of one representative weekday is shown in **Figure 11**. It consists of the total grid load (net electricity purchased from the grid), building load (the total load consumed by the office building), electricity generated by PV panels, and total charging and discharging from and to EVs and used EV batteries. Charging and discharging of EV and used EV batteries are represented as dotted blocks in positive and negative sides, respectively. The total grid load during after-noon peak-load time (load leveling test from 13:00 to 16:00) is significantly lower than the building load. This is because of the power generated by PV panels and peak-cut threshold which order the EVs and used EV batteries to discharge their electricity.

Charging and discharging of EVs and used EV batteries in negative sides mainly occur due to charging of used EV batteries during the night time and EVs charging during morning time (before the peak-load time) and during lunch break time. As used EV batteries are charged during night time, the grid load during this time is higher than the building load. EVs generally arrive at the office building at around 08:00 and they are connected to the designated charging

stations of EMS. From this moment, charging and discharging behaviors are fully controlled by EMS. Because the building load is still lower than the calculated peak-cut threshold, EVs charging can be conducted until the building load reaches nearly the peak-cut threshold to increase the discharging capacity of the EVs during peak-cut. Moreover, additional charging starts again during noon break (12:00–13:00) because the building load drops drastically creating any marginal grid load.

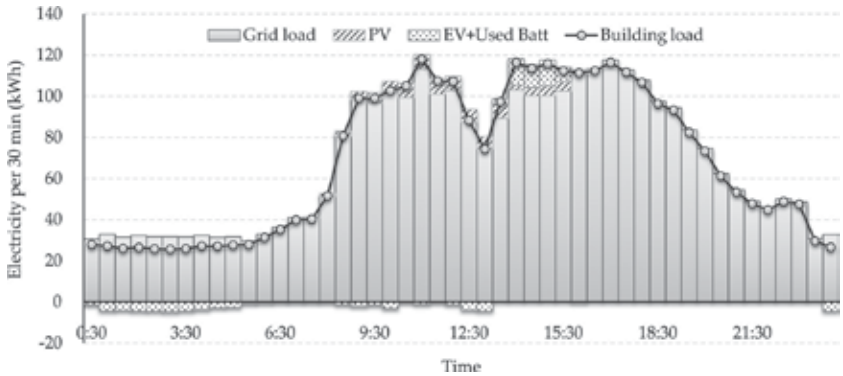

Figure 11. Results of load leveling test during weekdays.

From **Figure 10**, the peak-load occurs twice, i.e., before noon and afternoon, respectively. However, before noon peak-load is lower than the one in afternoon time. The generated electricity by PV is always consumed directly without being charged, hence peak-cut for the before-noon peak-load is conducted only by PV. In addition, the afternoon peak-load starts usually from 13:00 after the end of lunch break time. During this time, the building increases significantly and when it reaches approximately the calculated peak-cut threshold, EMS sends immediately the control command to EVs and used EV batteries to discharge their electricity according to the required amount for load leveling. Hence, the purchased grid load can be kept to lower than the contracted power capacity.

However, due to the limitation of available number of EVs and used EV batteries, load leveling only can be performed in a relatively short duration of time. It is estimated that as the number of EVs and used EV batteries taking part in this ancillary service program increases, more significant effect of load leveling can be achieved. In addition, a longer duration of load leveling and lower value of peak-cut threshold can be obtained accordingly.

Figure 12 shows the total amount of load leveling in a day by each PV panels, EVs, and used EV battery for 8 months of duration of demonstration test. Furthermore, **Figure 13** shows the averaged total load leveling by each PV panels, EVs, and used EV battery in different months. The used EV batteries have the largest and most stable load leveling share compared to EVs and PV. On the other hand, the generated electricity from PV is quite fluctuating because it is influenced strongly by the weather condition, especially solar intensity. Furthermore, the share of EVs in load leveling is also strongly influenced by their main usage as vehicle because it will affect significantly their SOC (available electricity for load leveling).

http://dx.doi.org/10.5772/64432

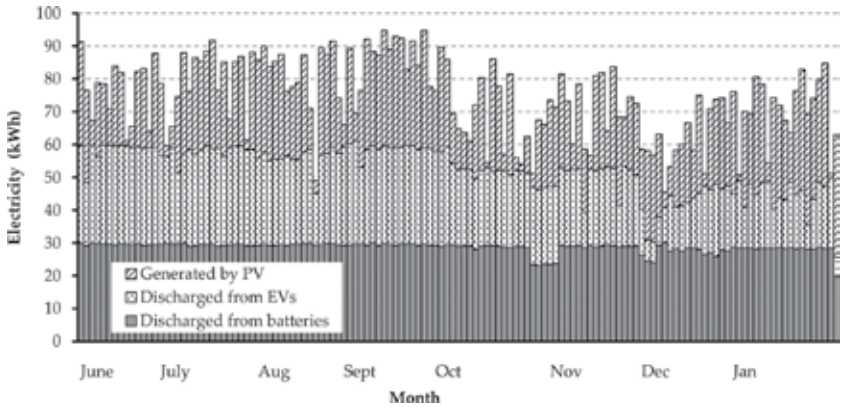

Figure 12. The amount of load leveling in a day by each component (PV, EVs, and used EV batteries).

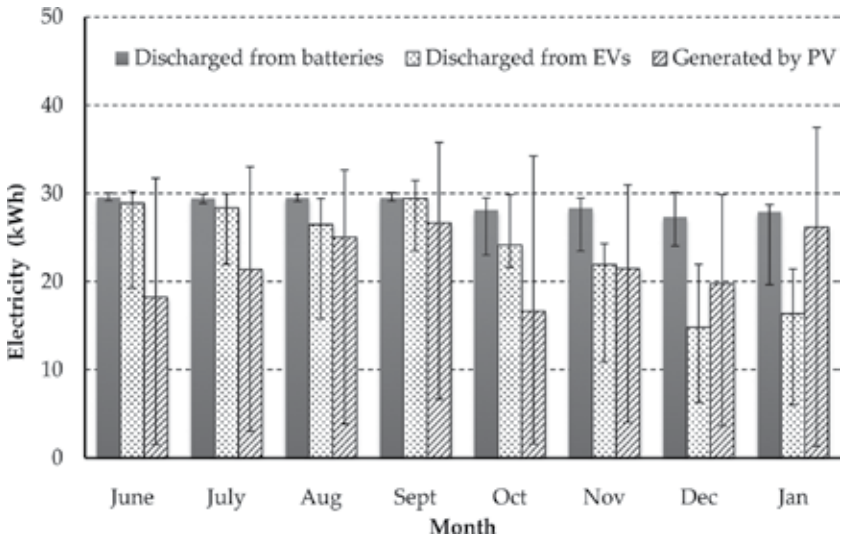

Figure 13. Averaged total load leveling by each component (PV, EVs, and used EV batteries).

The uncertainties are brought mainly by three factors: EVs, PV, and building load. These factors result in divergence between the predicted and real values. In this demonstration test, because the capacity of office building load is significantly larger than the total electricity which can be provided by PV panels, EVs, and used EV batteries, it is assumed that the strongest factor influencing this uncertainty is the building load, especially demands for air conditioning. Moreover, PV also gives an additional influence to this uncertainty due to its fluctuation.

As the results of conducted demonstration test, the predicted grid load showed a relatively high similarity with the real grid load. However, the difference between the predicted building load and its real load is relatively large due to the above-mentioned uncertainties.

The divergences in office building load and generated electricity from PV panels can be lowered by controlling the charging and discharging amounts from both EVs and used EV batteries. In addition, in this demonstration test, the uncertainty related to EV availability and its capacity do not show any significant impact. It is because the drivers of EVs are basically the employees who are working in the office building and almost the commuting routes are constant every day. It is considered that although there is an uncertainty on EVs' availability and their capacity, the divergence between the predicted and real grid loads could be reduced as long as the capacity of the used EV batteries which are owned by EMS are able to cover those fluctuating factors.

9. Some findings and suggestions

There are some important findings and suggestions which can be derived from the above theoretical study and demonstration test which are related to the employment of EVs and their used batteries to support the electricity in a small-scale EMS.

a. To calculate an optimum peak-cut threshold, an accurate forecast of both demand and supply is required. The demand forecast is influenced strongly by two main factors (especially the fluctuating load): weather condition and human behavior inside the building. To achieve more accurate weather forecast, timely update of weather information from meteorological agency and utilization of historical meteorological data are considered very important. In addition, regarding the forecasting of the human behavior, a construction of database and knowledge of specific behavior patterns of the office building is demanded. In case that the measurement of behavior patterns is relatively difficult to be performed, the method of guiding the behavior of the residence by establishing some regulations or policies might be taken.

b. Objective and accurate metering system to measure the amount of charged and discharged electricity to and from EVs is crucially demanded to enhance the trust and transparency. It can be performed by independent third party which is trusted by both EV owners and EMS/aggregator, especially in an aggregator-based contract scheme. The measurement can also include the participating duration, including stand-by time.

c. The increase in EVs number taking part in this ancillary service results in larger available capacity for load leveling (peak-cut). Unfortunately, this phenomenon is also potential to cause higher risk of larger fluctuation in case that EMS cannot forecast accurately the number of EVs. Installation of larger amount of stationary battery (used EV batteries) is considered potential to buffer and absorb this fluctuation through charging and discharging controls.

d. If some EVs which are participating in the ancillary service stop suddenly their service and demand an emergence charging due to some factors, such as traveling distance which will be traveled, EMS also must be able to coordinate this kind of sudden charging demand for EVs. The uncoordinated charging can result in creation of a new peak-load.

http://dx.doi.org/10.5772/64432

e. Compared to peak-load during summer, peak-load during winter is generally lower. However, peak-load during winter occurs mainly during evening time, around 17:00. This is because the heating demand inside the office building increases following the decrease in ambient temperature. It is important to note that the basic working hour also ends in this time, therefore there is any possibility that some EVs are demanding an additional charging before leaving the office. As a result, a new peak-load can occur during this time if the demand for EV charging is high. EMS must be able to also predict this kind of emergency and uncoordinated charging, hence a new peak-load can be prevented.

f. Additional number of EVs and total capacity of used EV batteries will be required when the amount of electricity generated by REs, including PV and wind, increase due to larger amount of fluctuating electricity in the supply side.

10. Conclusion

This chapter discussed the enhanced utilization of EVs and their used batteries to participate in ancillary service to support the electricity, especially in a small-scale EMS. In addition, experimental study based on the real data collected from the demonstration test bed has also been described. The study showed that it is feasible to utilize EVs and used EV batteries in supporting small-scale EMS. Furthermore, load leveling which determines initially the peak-cut threshold and, then controls both charging and discharging behaviors of EVs and used EV batteries based on peak-cut threshold is considered as a valid technique. As a result, the purchased electricity from the grid can be kept to be lower than the contracted power capacity.

Accurate forecast of both load and supply is considered as one of the important issues in this utilization, in addition to the availability forecast of EVs and their batteries. The supply includes the condition of electricity market, possible generated power by REs, and available electricity which can be supplied by EVs. Furthermore, highly accurate load forecast, especially the fluctuating load including human behavior and air conditioning, is also very essential to achieve an optimum target condition as it has been estimated by EMS.

Author details

Muhammad Aziz* and Takuya Oda

*Address all correspondence to: maziz@ssr.titech.ac.jp

Institute of Innovative Research, Tokyo Institute of Technology, Ookayama, Meguro-ku, Tokyo, Japan

References

[1] Aziz M, Oda T, Kashiwagi T. Extended utilization of electric vehicles and their re-used batteries to support the building energy management system. Energy Procedia 2015;75:1938–1943. DOI: 10.1016/j.egypro.2015.07.226.

[2] Schott B, Puttner A, Muller M. The market for battery electric vehicle. In: Scrosati B, Garche J, Tillmetz W, editors. Advances in battery technology for electric vehicles. Cambridge: Elsevier; 2015. p. 35–54.

[3] Barkenbus JN. Our electric automotive future: CO2 savings through a disruptive technology. Policy and Society. 2009;27(4):399–410. DOI: 10.1016/j.polsoc.2009.01.005.

[4] Aziz M, Oda T, Mitani T, Watanabe Y, Kashiwagi T. Utilization of electric vehicles and their used batteries for peak-load shifting. Energies. 2015;8:3720–3738. DOI: 10.3390/en8053720.

[5] Paul TK, Aisu H. Management of quick charging of electric vehicles using power from grid and storage batteries. In: IEEE International Electric Vehicle Conference (IEVC) 2012; 4–8 March 2012; Greenville, SC. 2012. p. 1–8.

[6] Aziz M, Oda T, Morihara A, Murakami T, Momose N. Utilization of EVs and their used batteries in factory load leveling. In: 2014 IEEE PES Innovative Smart Grid Technologies Conference (ISGT); 19–22 Feb. 2014; Washington, DC: IEEE; 2014. p. 1–5. DOI: 10.1109/ISGT.2014.6816370.

[7] Tomic J, Kempton W. Using fleets of electric-drive vehicles for grid support. Journal of Power Sources 2007;168:459–468. DOI: 10.1016/j.jpowsour.2007.03.010.

[8] Kempton W, Letendre SE. Electric vehicles as a new power source for electric utilities. Transportation Research Part D: Transport and Environment. 1997;2(3):157–175. DOI: 10.1016/S1361-9209(97)00001-1.

[9] Drude L, Pereira Jr LP, Ruther R. Photovoltaics (PV) and electric vehicle-to-grid (V2G) strategies for peak demand reduction in urban regions in Brazil in a smart grid environment. Renewable Energy 2014;68:443–451. DOI: 10.1016/j.renene.2014.01.049.

[10] Viswanathan VV, Kintner-Meyer M. Second use of transportation batteries: maximizing the values of batteries for transportation and grid services. IEEE Transactions on Vehicular Technology. 2011;60(7):2963–2970. DOI: 10.1109/TVT.2011.2160378.

[11] Alimisis V, Hatziargyriou ND. Evaluation of a hybrid power plant comprising used EV-batteries to complement wind power. IEEE Transactions on Sustainable Energy. 2013;4(2):286–293. DOI: 10.1109/TSTE.2012.2220160.

[12] Neubauer J, Pesaran AA, Howell D. Secondary use of EV and PHEV batteries - Opportunities and challenges. In: Proceedings of the 10th Advanced Automotive Battery Conference; 19–21 May 2010; Orlando, FL: NREL; 2010.

[13] Aziz M, Oda T, Ito M. Battery-assisted charging system for simultaneous charging of electric vehicles. Energy 2016;100:82–90. DOI: 10.1016/j.energy.2016.01.069.

[14] Oda T, Aziz M, Mitani T, Watanabe Y, Kashiwagi T. Actual congestion and effect of charger addition in the quick charger station—case study based on the records of expressway. IEEJ Transactions on Power and Energy. 2016;136(2):198–204. DOI: 10.1541/ieejpes.136.198 (in Japanese).

[15] ISO/RTO Council. About the IRC. Available from: www.isorto.org/Pages/Home [Accessed: 8 Mar 2016].

[16] Bohne E. Clash of regulatory cultures in the EU: the liberalization of energy markets. In: Bohne E, Karlsson C, editors. Repositioning Europe and America for Growth: The Role of Governments and Private Actors in Key Policy Areas. Berlin: LIT Verlag; 2010. p. 145–190.

[17] Jansen AN, Dees DW, Abraham DP, Amine K, Henriksen GL. Low-temperature study of lithium-ion cells using a LiySn micro-reference electrode. Journal of Power Sources 2007;174:373–379.

[18] Ping P, Wang Q, Huang P, Sun J, Chen C. Thermal behaviour analysis of lithium-ion battery at elevated temperature using deconvolution method. Applied Energy 2014;129:261–273.

[19] Liao P, Zuo P, Ma Y, Chen X, An Y, Gao Y, Yin G. Effects of temperature on charge/discharge behaviors of $LiFePO_4$ cathode for Li-ion batteries. Electrochimica Acta 2012;60:269–273.

Chapter 7

V2G Services for Renewable Integration

Mahmoud Ghofrani, Eric Detert,
Negar Niromand Hosseini, Amirsaman Arabali,
Nicholas Myers and Phasith Ngin

Additional information is available at the end of the chapter

http://dx.doi.org/10.5772/64433

Abstract

With the proliferation of renewable energy sources (RES) and the growing consumer demand for plug-in hybrid (PHEV) and total electric vehicles (EV), the limitations of the aging electrical grid distribution infrastructure is becoming more and more apparent. The development of better infrastructure, therefore, is at the forefront of research. The development of a smart grid, a bidirectional distribution infrastructure, will allow for two-way "communication" of power distributors and aggregators with multiple smart platforms, such as smart buildings, homes, and vehicles. The focus of this chapter is to outline the means of (electrical) vehicle to (smart) grid (V2G) interactions and how attaining a synergistic relationship is vital to improving the way power is distributed. The ability of fleets of EVs to act as a unit for excess power storage allows for the increased integration of RES into existing grid infrastructure and smart grids in the future through the bidirectional communication; providing support, giving back stored power into the grid to lessen the load felt by generation utilities, augment stochastic RES when generation is not meeting demands, lowering costs for both sellers and buyers, and above all, working toward the betterment of Earth.

Keywords: electric vehicles, renewable energy, vehicle-to-grid, optimization, smart grid

1. Introduction

The world is presently facing many energy problems. Fossil fuels have been the main dominant energy source for both the transportation sector and power generation industry even if this energy source produces greenhouse gases (GHGs) which have a negative impact on climate

change [1]. With fossil fuel prices increasing and its negative environmental impact, oil is becoming less of a long-term energy solution, and more renewable sources of energy are being sought. Wind and photovoltaic solar are renewable energy (RE) sources that are rapidly replacing conventional power sources. On the other hand, electric vehicles (EVs) are becoming more and more popular due to the fewer emission and low oil dependency.

The electrical vehicle is a zero emission vehicle because it does not produce the pollution associated with internal combustion engines (ICEs). However, the charging through fossil-fuelled electrical generation still makes an environment impact since most electricity is generated by burning fossil fuels. But comparing with cars operated by gas power, cars operated by batteries are cleaner because they produce less carbon emissions. Moreover, battery-powered motors cost less to operate. The other advantage of EVs is safety and efficiency. EVs use the advance technology to maintain the vehicle adequately and to keep the right supplies on hand in case of emergencies. EVs offer benefits to the transportation sector and the electric power system. They help strengthen the economy, are more environmentally friendly, and can reduce strain on the petroleum industry by using renewable generation, especially photovoltaic solar and wind, which is an important part of the transition to cleaner sources of power. EVs are the best option for greener and economic driving [2].

An electric vehicle (EV) is considered an electrical drive vehicle which uses one or more electrical motors or traction motor for propulsion. An EV is powered through a collector system by electricity from a self-contained battery or generator to convert fuel to electricity. These are termed battery electric vehicles (BEVs), or if powered with an off vehicle source, termed plug-in hybrid electric vehicles (PHEVs) [3].

The battery electric vehicle is one type of electrical vehicle that uses chemical energy stored in rechargeable battery packs. There are three major parts in the typical architecture of BEVS: electric motor, rechargeable battery, and controller. The electric motor uses a rechargeable battery as an energy source to generate propulsion. The controller manages the power supplied to the electric motor. Another important part of a BEV is the inverter, which is for converting the electricity stored in the battery (DC) power to alternating current (AC) power [3]. The Nissan Leaf is a battery electric vehicle which relies on the grid to recharge its battery. Its battery packs can be charged from fully discharged to 80% capacity in about 30 minutes using DC fast charging. It does not produce pollution or GHGs, and also helps to reduce dependence on petroleum [4].

The plug-in hybrid electric vehicle is a hybrid electrical vehicle that can use rechargeable batteries or another energy storage device. They are usually equipped with both an electric motor and an additional internal combustion engine for propulsion. PHEVs can be driven in two modes: charge depleting (CD) and charge sustaining (CS). PHEVs produce energy from on-board battery packs when they operate in CD mode, and they switch to CS mode and utilize the ICE system for further propulsion if the charge of the battery has been depleted to a predetermined level. There are three categories of plug-in hybrid vehicle: parallel hybrid, series hybrid, and power-split hybrid. The parallel hybrid is the most commonly adopted. They use both electric motor and an engine to power the driven wheels in a car [3]. The Toyota Prius is a hybrid car with an internal combustion engine. Its large on-board battery recharges

http://dx.doi.org/10.5772/64433

while the gasoline-fuelled ICE is running. It is fully self-sufficient and does not rely on the grid. It can use its large on-board battery for 34–40 miles before the on-board gasoline generator kicks in. It is fully capable of making long trips, but can also go short distance powered entirely by the battery without any gasoline [5].

2. Vehicle to grid (V2G)

2.1. Concept

The advancement of EV technology has brought on additional attention into the integration of the transportation sector into the power grid. The control and management of EV loads by the power utility using the communication between vehicles and the power grid is referred to as vehicle to grid. Some other similar concepts are vehicle to home (V2H) and vehicle to vehicle (V2V). These involve exchanging power between an individual's home power network and their vehicle, or exchanging power within a community of electric vehicles [6].

Currently, the transportation sector is primarily using gasoline or petrol for propulsion, and does not have any interconnection capabilities with the power grid. However, with the advancing adoption of EV into the transportation market, the idea of allowing EVs to plug into the power grid, to not only charge their vehicles, but also discharge energy back into the grid, becomes more practical [2].

The V2G concept could provide many services to power grid but presents some challenges as well. The benefits of such a system include peak load shaving, load leveling, and voltage regulation, which will ultimately result in maximizing profits. The challenges include the logistics of retrofitting the current infrastructures and gaining the support of the public and policy makers.

One issue includes the accelerated battery degradation due to increasing the charging cycles of each vehicle's battery. Studies are being conducted to collect more accurate data on battery lifecycles. These studies will provide more information so that policy makers can either prevent consumers' battery degradation, or more accurately consider the cost of that wear and implement that into the pricing scheme. The battery degradation scenario is part of the social barrier that V2G may present. Skeptical EV owners may wonder how they can be assured they will have enough energy stored in their vehicle to accommodate their transportation needs. There are also concerns of how the consumers will be fairly compensated for discharging their energy back into the grid.

The challenge of retrofitting the power grid infrastructure could be the biggest hurdle. Implementing V2G would be a large investment. Improving hardware and software in the grid system would be one major cost. Another would be adding a bidirectional battery charger to each EV. Bidirectional chargers consist of a complex controller and high tension cabling with stringent safety requirements. V2G implementation would mean frequent charge and discharge cycles resulting in more losses from energy conversions. A large fleet of EV's charging and discharging would add up to large energy losses for the power system [6].

The overall concept of V2G began with the idea of tapping into the underutilized power capacity of the passenger vehicle fleet. Whether it is internal combustion or all electric, the vehicle fleet in the United States has much more energy capacity than all the U.S. electrical generating plants combined and they sit idle nearly 95% of the day. As the automobile industry begins to shift more toward electric and hybrid vehicle production, the utilities have begun to consider using these vehicle batteries as a storage cell. Studies have shown that even with unfavorable assumptions about cost and lifecycles of batteries, over a wide range of conditions, the value to the utility of tapping vehicle electrical storage exceeds the cost of a two-way hook-up and reduced battery life. It has been considered to offer incentives to the vehicle owner as a purchase subsidy, lower electric rates, or purchase and maintenance of successive vehicle batteries [7].

A possible configuration for an EV participating in V2G technologies would have a user interface with the vehicle allowing the owner to disable or limit the discharge to the grid. An intelligent charge controller could have several options for the owner to charge and discharge the vehicle. Some options could be to charge now or charge when cheap, or to set a minimum threshold to maintain enough charge for the owner to be able to cover a particular driving distance. This would allow for more flexibility for owners to participate as much as their lifestyle allows. An incentive-based program would hopefully garner more favor from consumers [7].

2.2. Smart grid

A smart grid is a modernized electrical power grid that involves communication technology between the utility and the consumers using computer-based remote control and automation to improve reliability, efficiency, and sustainability of the power supply. Two-way communication between the utility and its customers by way of sensors and smart meters throughout the smart grid are used for real-time data acquisition. The data collected from these sensors and smart meters are then used by intelligent and autonomous monitoring control to supervise and optimize the overall operations of the interconnected components [2].

An additional characteristic that separates the smart grid from the conventional grid is that consumers can actively participate in the grid operation. The smart grid would contain advanced metering infrastructure that would allow for consumers to access the real-time information about electricity usage, tariff, and incentive information. They can use this information for their own gain by adjusting electricity usage patterns and preferences. These adjustments would likely help to balance out the overall energy supply and demand. The smart grid concept also incorporates a widely dispersed distribution of generation units from various forms of renewable generation and conventional power sources. This variety of generation sources will provide better overall reliability and reduce risks from attacks and natural disasters [2].

The ability to accommodate renewable energy sources more efficiently is another attractive characteristic of the smart grid. Wind and PV solar energy has unpredictable and intermittent supply of power to the grid. Due to varying weather conditions, the power produced from these sources can be much higher than the power demand in some cases and much lower in

http://dx.doi.org/10.5772/64433

other cases. They are variable with time and unable to dispatch on command. However, these sources are practically viable if able to store and later discharge excess energy. The promise of balancing the electricity generation from renewable sources with consumer load is realistic with energy storage systems and controllable dispatch loads. A smart grid that communicates supply and demand data will make renewable sources with energy storage systems a practical solution [1].

The smart grid can improve grid reliability and power quality but implementing it into existing infrastructure will be a challenge. In the meantime, there are several smart grid projects underway all over the world. According to the Global Smart Grid Federation Report, the leading projects are taking place in Australia; Ontario, Canada; London, Great Britain; Ireland; South Korea; and Houston, TX, in the United States [8].

2.2.1. Smart charging/discharging

As EVs become more prevalent, a high concentration of vehicles charging over a small period of time will inevitably lead to overload conditions in local nodes of the grid. This could lead to interruptions and/or imbalances that would degrade the service quality, increase line losses, or damage equipment. Smart grids are fundamental in smart charging management strategies that can reduce peak load on the grid. This will also allow for the advantage of coordinating vehicle charging in order to store surplus grid energy at a given instant and inject it into the grid when needed [9].

The potentially undesirable effects of uncontrolled EV charging such as overloading the power system facility would lead to an unregulated, less efficient electrical supply. To alleviate this condition, some smart charging schemes have been developed to minimize charging costs. Some optimization algorithms have been developed to create a better solution for EV's charging and discharging into the grid. Some smart charging concepts include using day-ahead energy resource scheduling for smart grid by considering all the dispersed energy resources (i.e., wind, solar, conventional, etc.) and the V2G participants. An optimization approach could be used for intelligent optimal scheduling. To facilitate this intelligent charging concept, a radio frequency identification (RFID) tag technology would be used to ID those plugging into the grid. Some options could be considered where EV owners could control and monitor their charging through a mobile web application. Parameters could be adjusted such as the desired state of charge, arrival and departure times, or options for the V2G services to maximize profit. Other intelligent charging models use consumption historical statistics with data mining approaches. This method could include using the GPS function on an EV owners' mobile device to help determine driving characteristics [1].

Efforts have been made in developing smart charging strategies to account for the efficiency of the charging process. An effective dispatching strategy needs to account for the losses in the charging process to accurately estimate the amount of energy fed to the battery from the grid. Accounting for these nonideal conditions will allow for better overall system performance. Currently, the charging efficiency of batteries for electric transportation still is largely dependent on the charging rate due to the internal battery resistance. On a typical lithium-ion cell, the charging rate is normalized with respect to the battery capacity. The efficiency will

decrease significantly with the charging rate due to the internal battery resistance power dissipation with the charging current. These charging characteristics need to be taken into account to develop smart charging strategies [9].

2.2.2. Advanced communication and control

The critical portion of the smart grid is the communication and control aspect. A two-way communication network enables demand response technologies which can control distributed energy resources over dispersed geographical areas [1]. As smart grid capabilities increase with newer automation and communication networks, power utilities and aggregators are able to see real-time distribution and load demands on the network and, via the bidirectional communication, control and optimize the supply of power. A key benefit with EV is that they can act as energy storage units that interact with the smart grid, through "smart" charging stations. This dual-channel communication is only available through the use of bidirectional communication, not unilateral, which among other reasons makes the switch from non-EV to EV even more practical. These interactions can help optimize power distribution, decreasing degradation and increasing quality of deliverable power through active power support and reactive power compensation [2]. With an infrastructure of smart meters, the power system can obtain the information of power demand and consumption in the system to better schedule generation and distribution for locational pricing. With a large number of smart meters, fiber optics as a medium would not be feasible due to cost, and wireless communication would be the preferred method between smart meters and control centers [8]. The benefits of wireless include low cost infrastructure and wide area coverage [1]. Perhaps a hybrid wired/wireless system can be used in the future for security concerned consumers [10].

In comparison with traditional data networks, the smart meter network of a smart grid would have some unique challenges. One challenge would be the volume of traffic and limited bandwidth due to the large number of smart meters. Another would be the requirement for real-time data transmission. The power grid is a very dynamic system and it is critical to have current data. Delays in data transmission could result in instability to the power market. Another challenge would be taking the characteristics of the power systems into account for charge scheduling. Traditional scheduling algorithms that maximize the throughput or minimize the average delay may not be valid in a smart grid. Addressing these challenges could include introducing locational marginal pricing and a model of power load variation into a scheduling algorithm [10].

On the consumer side, there are several ideas on how EV owners can exercise control of their vehicle's charging schedule while still allowing the power grid to benefit from the EV battery source. One idea would consider equipping each V2G compatible EV with a user interface device to allow the driver to receive instructions or seek advice for charging/discharging processes. An alert would be issued in the event when the EV's battery capacity is below a predetermined threshold level. This alert can include near-by charging stations, distance, their energy price, etc. The alert can also provide the driver with instructions to bringing the vehicle to appropriate charging stations to serve as a backfill battery. All of this information exchange would be accomplished through wireless communication and hall-effect current sensors.

http://dx.doi.org/10.5772/64433

System architecture of a vehicle to grid communication system would possibly include several road side units that would communicate between passing vehicles, nearby charging stations, and the smart grid. The road side units would allow communication between vehicles and charging stations when the transmission ranges would not be sufficient. The data transfer would be triggered by the driver or a recommendation system. With a driver-triggered scenario, the driver checks the state of charge and seeks advice on charging through the user interface on board the EV. The communication module will send a message to the nearest road side unit to request information of near-by charging stations. The inquiry would generate a reply back to the vehicle with its geographical location and/or current energy price. The on-board controller would collect data through the message exchanges and start the recommendation system. This recommendation system would decide whether it is the right time to charge or not based on the vehicle's state of charge, energy prices, and grid status. It would either recommend to charge or defer to off-peak hours when energy rates would likely be lower.

With a system-triggered scenario, the recommendation of energy charging depends on factors such as the grid load, the state of charge of the vehicle, and real-time energy prices. The system would receive alarms from sensors on the vehicle (for battery capacity), and then send messages to the road side units to start a recommendation process [11].

3. V2G services for renewable energy (RE) integration

V2G systems can provide a variety of services to power utilities, grid operators and aggregators, as well as the EV owner and even the environment. These services include ancillary services, time shifting, active power support, and reactive power compensation through voltage regulation. These services will become invaluable due to their mitigation of the increasing uncertainties and intermittencies of the grid due to the renewable energy integration [12, 13].

3.1. Ancillary services: spinning reserve

Ancillary service refers to the supporting service supplied to the power grid in order to improve upon and maintain the reliability and efficiency of the power grid, this also increases sustainability. There are several ancillary services that are required for the security, reliability, and stability of the grid. These services make up reactive supply, voltage control, regulation, operating spinning reserve, operating supplemental reserve, and restoring energy imbalance [14]. V2G technology inputs ancillary services to the power grid through a spinning reserve service, where the energy stored in the grid-connected EVs is utilized as an additional generation capacity to make up for the generation deficiencies due to generation outages [15]. The spinning reserve service provided by V2G technology provides a platform to initiate failure recovery, as well as reduce the backup generation capacity [16, 17].

3.2. Time shifting

In time shifting services, storage capabilities and technologies are required to necessitate and provide energy within a timeframe of 5–12 hours. In this particular case, energy storage

systems are required to absorb and assimilate all of the energy from RESs during off-peak demand periods. This absorbed energy may be supplemented with cheaper alternative power sources brought from the network if necessary, and then selling it during peak power demand periods; mitigating the activation or update of other conventional and more mainstream peak power generation plants [18].

3.3. Active power support

EV can provide numerous methods of active power support. Through bidirectional communication, the excessive EVs energy that would otherwise be wasted can be sent back to the utilities and aggregators via the smart grid through specialized charging stations, parking lots, etc. The goal of active power support is to ease the demand on the power utilities. The demand for power is not constant, in that demand ebbs and flows, with a decrease in the late nights and sizable demands during the mid-day and early mornings. This fluctuation degrades the generative power of utilities. In addition, utility customers see the prices of electricity change in accordance to the demands; having to pay a premium price for electricity usage during peak hours. Power systems are designed for worst-case conditions, that is, assuming maximum load and demand. It follows that whenever the demand is less than maximum, the systems are being underutilized. Operating at maximum capacity also wears out the system over its life time. EVs are able to provide two kinds of active power support, load leveling and peak shaving, to prolong power system longevity and lower the economic strain on consumers and EV owners [2].

3.3.1. Load leveling

Load leveling is the goal to "spread out" the high demand curve during peak hours, thus decreasing the operational strain on the systems. EVs act, when on the V2G scale, as a collective distribution network to supply excess power back through the smart grid to level out the load peak. By using smarter distribution networks, the demand for sole generation and distribution felt by power utilities and aggregators is lessened, prolonging system life and mitigating unnecessary costs of repairs or upgrades. Utilizing the power systems at a level less than peak for a longer period of time will lead to less loses overall, prolonging usability and lowering overloading chances. Due to the stochastic nature of weather-dependent renewable resources, the output power is unreliable to constantly meet the load. Using distribution networks to store excess energy, like EVs, to act as a buffer to provide power whenever levels of renewable generation is not at demand will allow year-round operation of renewables through lowered reliance on perfect weather conditions [19].

3.3.2. Peak shaving

By allowing the power systems to not operate at worst-case peak levels, the degradation of the systems is lessened and the overall life of the system and its generative abilities are increased. This allows for longer and higher quality power distribution. EV connected to the grid during peak hours increases the load at the low-voltage network. This increases the demand for current and consequently the need for power from the medium and high-voltage networks.

http://dx.doi.org/10.5772/64433

The increased load will force more current through transmission cables and transformers from high- and medium-voltage networks down to low-voltage networks, which in turn increases transmission losses and thermal wear on components, decreasing usability. By peak shaving, this load is lessened through coordinated EV charging and EV-based distribution networks through bidirectional infrastructure. The power delivered back to the utilities and aggregators through V2G will decrease the peak demand, the degradation of generation resources, distribution resources, and, by allowing the system to operate at a lower level, the premium price of electricity faced by EV owners during peak demand hours [19].

3.4. Reactive power compensation: voltage regulation

A constant problem facing power utilities and aggregators is ensuring that the voltage and current distributed through the network are in phase. However, with each load attached, a disparity between the two can occur, resulting in a decrease in the deliverable power factor which requires corrective measures. Reactive power support is able to supply voltage and current to meet reactive load at the distribution level that would otherwise has to be supplied by generators. Without reactive power support, supply voltages would fall below minimum levels and more current would be needed to push through transmission lines, resulting in thermal wear and potential blackouts [20].

Specialized capacitor banks are used by utilities to locally supply reactive power at the load bus to lessen the load felt at the utility level. This specialized volt-ampere reactive (VAC) compensator banks are costly and difficult to upgrade. By using the DC-link capacitors present in EV chargers, utilities through the smart grid would be able to use the V2G distribution network as a reactive power support system in addition to active power support network via the bidirectional communication infrastructure. Since the DC-link capacitors supply the reactive power, no strain is placed on the EV battery [21].

4. Optimization of V2G services for RE integration

4.1. Optimization techniques for V2G services

Mathematical modeling of systems allows for variable change while trying to maintain a maximization or minimization of a criterion or many criteria. This modeling allows for experimental change without potential risks to the actual system. Finding an optimal middle ground between maximized efficiency and minimized cost is achievable through mathematical modeling using various optimization techniques and functions. The different techniques are summarized in the following sections.

4.1.1. Classical optimization techniques

Classical techniques are utilized when the optimization function is a continuous and/or differentiable function. The solutions of optimization are found using differential calculus. The most utilized types of classical models are: linear programming (LP), nonlinear programming

(NLP), dynamic programming (DP), mixed-integer programming (MIP), stochastic programming (SP), convex programming (CP), and analytical modeling (AM).

4.1.2. Metaheuristic optimization techniques

Metaheuristic optimization techniques find, generate, or select a heuristic in this case a method of searching for an optimization strategy that may provide the best solution to the optimization problem with nonderivative, noncontinuous objective functions These metaheuristic methods sample from a much larger sample set to find a solution that best fits the entire set. It is based off of random operators to find the best solution to the set of variables faster than iterative or simple heuristics. The common types of metaheuristic techniques are: genetic algorithms (GA), particle-swarm optimization (PSO), ant colony optimization (ACO), simulated annealing (SA), and Tabu search [3].

4.1.3. Hybrid optimization techniques

Hybrid optimization techniques are techniques that combine two or more of the previously described methods, either classical or metaheuristic. Typically, they combine iterative approaches to heuristic solutions.

4.2. Optimization objectives

The focus on optimization for V2G services are cost, efficiency, and emission optimization. Through the use of the optimization techniques listed above, significant gains can be made toward producing the most efficient and cost-effective EVs, maximizing V2G interactions, and improving smart grid technologies and power generation and distribution.

4.2.1. Cost optimization

Cost optimization is focused on minimizing the costs of interaction between EVs and RES providers through the smart grid. Providers wish to reduce costs and maximize profit while EV owners wish to minimize the cost of charging and vehicle maintenance [3].

4.2.1.1. Operational cost minimization

Operational costs and their minimization are crucial for all market participants including the generation, transmission, and distribution providers and users [3]. **Table 1** summarizes the related research works, their objective functions, techniques in use for optimization, and their main findings.

Reference	Objective function(s)	Optimi-zation technique	Findings
[22]	$\min C_{\mathrm{Iso},T}^{C}=\sum_{i=1}^{n}C_i^d P_i^d v_i T + C_B^d P_B^d T + \sum_{k=1}^{m} C_k P_k z_k T$ $\max C_{\mathrm{Iso},T}^{P}=\sum_{i=1}^{n}\left(-C_i^C P_i^C\right)v_i T - C_B^C P_B^C T$ $C_{\mathrm{Iso},T}^{C}$ is the islanded operating cost over a horizon of length T; C_i^d, P_i^d are the discharging price and power of the ith EV; C_B^d, P_B^d are the discharging price and power of battery swapping stations (BSS); P_k, C_k are the amount of load shedding of the kth interruptible load (IL) user and its service price; v_i, z_k are in binary with v_i being a 1 if the ith EV is connected to the microgrid after islanding while fixed to zero when the ith EV is not available; z_k is 1 when the interruption time of the kth IL does not exceed the longest time per interruption while it is enforced to be zero if the time limit on load shedding is violated.	Classical (Mathe-matical progra-mming)	On a regional level, a management strategy is proposed by this paper for minimizing costs and maximizing profits of an islanded microgrid with renewable resources. The strategy is beneficial for managing the load of EV fleets and optimizing the operation to mitigate the load impact by leveling and peak shaving. The strategy uses fuzzy systems to obtain the charging price EVs.
[23]	$\min TSC=\sum_{T}^{t=1}\left(u_{j,t}^{\mathrm{DG}}P_{j,t}^{\mathrm{DG}}B_{j,t}^{\mathrm{DG}} + S_j^{\mathrm{DG}}\left\| u_{j,t}^{\mathrm{DG}}-u_{j,t-1}^{\mathrm{DG}}\right\|\right)]$ $+\sum_{T}^{t=1}\left(\sum_{L}^{i=1}P_{i,t}^{\mathrm{PHEV}}B_{i,t}^{\mathrm{PHEV}} + P_t^{\mathrm{Grid}}B_t^{\mathrm{Grid}}\right)$ TSC is the total schedule cost; L is the total number of PHEV; M is the total number of DG units; $u_{j,t}^{\mathrm{DG}}$ is the status of the jth DG unit at hour t; $P_{j,t}^{\mathrm{DG}}$ (kW) is the active power production of the jth DG unit at hour t; $S_{j,t}^{\mathrm{DG}}$ ($) is the start-up or shut-down cost of the jth DG unit; $B_{i,t}^{\mathrm{PHEV}}$ ($) is the bid of the jth PHEV at hour t; $B_{j,t}^{\mathrm{DG}}$ ($) is the bid of the jth DG unit at hour t; B_t^{Grid} ($) is the energy bid of the utility at hour t.	Metaheu-ristic (GA)	The proposed planning model provides the DNO (distribution network operator) a set of optimal solutions over a range of operating conditions and uncertainties.
[24]	$\min_{\{l_k\},\{z_k\}}\sum_k p_B^T l_k + \frac{\rho}{2}\left\| l_k - z_k\right\|_2^2 + C_2 f_0\left(\sum_k z_k\right)$ z_k is the auxiliary variable; p_B is the base price; l_k is the kth user load; ρ is the quadratic coefficient for augmented	Classical (NLP)	Demand curve can be flattened after numerical examples of optimization

Reference	Objective function(s)	Optimi-zation technique	Findings
	Lagrangian; C_2 is the coefficient for fluctuation price; f_0 is the variance of aggregated demand load.		
[25]	$\min_{n,p}\sum_{t=1}^{T}\sum_{i=1}^{N}\left[H_{i,t}(n)+\left(A_i n_{i,t}+\sum_{j=1}^{J} p_{i,j,t}B_{i,j}\right)\right]$ i is the generator group; t is the time intervals; $H_{i,t}$ is the start-up cost of group i at time t; A_i is the no-load cost of one unit of group i; $B_{i,j}$ is the marginal cost of segment j of the group i's cost function; $n_{i,t}$ is the integer of commitment decisions; $p_{i,j,t}$ is the output for segment j of group i at time t.	Classical (MILP)	Controlled charging can substantially reduce the cost of supplying additional EV demand due to lowered usage of peak generators, avoiding wind/solar curtailment, reduce carbon emission and associated costs, and reduce thermal generator start-up times.
[26]	$\min\{Cost-Revenue\}$ $=\left\{\left(\sum_{N}^{i=1}\sum_{T}^{h=1} Cost_{i,h}^{\mathrm{CHP}}+\sum_{N}^{i=1}\sum_{T}^{h=1} Cost_{i,h}^{b}\right.\right.$ $\left.+\sum_{N}^{i=1}\sum_{T}^{h=1} Cost_{i,h}^{\mathrm{PV}}+\sum_{T}^{h=1} ep_h * grid_h^{\mathrm{buy}}\right)$ $\left.-\left(\sum_{T}^{h=1} SC * ep_h * grid_h^{\mathrm{sell}}\right)\right\}$ $Cost_{i,h}^{\mathrm{CHP}}$ is the cost of electricity production by CHP systems; $Cost_{i,h}^{b}$ is the cost of heat production by the boilers; $Cost_{i,h}^{\mathrm{PV}}$ is the total operation cost of PV generation systems; $grid_h^{\mathrm{buy}}$ and $grid_h^{\mathrm{sell}}$ are the purchased and sold electricity from/to the upstream network; ep_h is the electricity price at hour h in the upstream network; SC is the sell coefficient; N is the number of buses; T is the number of intervals (hour).	Classical (NLP)	The introduction of PV (photovoltaic) generation systems coupled with PV storage systems in IMGs (industrial microgrid) could have positive effects on their scheduling solution and minimizing the overall cost.
[27, 28]	$\min_{I_i(t),N_{V2G(t)}} TC=W_c\times(Fuel+Start-Up)$ $+W_e\times Emission$ $=\left\{E\left(\sum_{s\in S}\sum_{i=1}^{N}\sum_{t=1}^{H}[W_c(FC_i(P_i(t))\right.\right.$ $+SC_i(1-I_i(t-1)))$ $\left.+W_e(\psi_i EC_i(P_i(t))]I_i(t))\right\}$	Metaheu-ristic (PSO)	PSO was utilized to generate a successful schedule considering the stochastic nature of renewable energies, load and GVs in a smart grid. Valid

Reference	Objective function(s)	Optimization technique	Findings
	$I_I(t)$, $N_{V2G(t)}$ are the decision variables for the on/off state of units and number of GVs connected to the grid at time *t*; $FC_i(P_i(t))$ is the fuel cost of a thermal unit *i* with $P_i(t)$ being the output power of unit *i* at time *t*; $SC_i(t)$ is the start-up cost for restarting the de-committed thermal unit *i*; ψ_i is the emission penalty factor of unit *i*; $EC_i()$ is the emission cost function for unit *i*; weight factors W_c and W_e are used to increase the flexibility of the system; *N* is the number of units; *H* is the scheduling hours; *S* is the set of scenarios; $E(.)$ is the expectation.		scenarios are derived from prior statistics, heuristics, and anecdotal experiences of the authors.
[29]	$\min\Big[\sum_t\sum_i \left(p^b \cdot F_{c,i}(P_{i,t}) + SU_{i,t} + SD_{i,t}\right) + \sum_t\sum_k p^b \cdot (SU_{k,t} + SD_{k,t}) + \sum_t\sum_v p^b \cdot C_{v,t}\Big] + \Big[\sum_t\sum_i \left(F^r_{c,i}\left(\Delta^{\max\times}_{i,t}\right)\right)\Big] + \sum_s p^s \cdot \Big[\sum_t\sum_i F_{c,i}\left(P^s_{i,t}\right) + \sum_t\sum_k (SU^s_{k,t} + SD^s_{k,t}) + \sum_t\sum_v C^s_{v,t}\Big]$ p^b, p^s are the probabilities of the base case solution, and the probability of a scenario *s*; $F_{c,(.)}$, $F^r_{c,(.)}$ are the production/availability cost function of a thermal unit; $C^{(.)}_{(.)}$ is the operation cost of PEV fleet; $\Delta^{\max\times}_{(.)}$ is the maximum permissible power adjustment of a unit; $P^{(.)}_{(.)}$ is the generation of a unit; *s* denotes a scenario; $SD^{(.)}_{(.)}$ is the shutdown cost a unit; $SU^{(.)}_{(.)}$ is the startup cost of a unit; $b_{m,(.)}$ is the slope of segment *m* in a linearized charge/discharge curve; *i* denotes a thermal unit; *t* is the hour index; *v* denotes a PEV fleet.	Classical (MIP)	Numerical tests demonstrate the effectiveness of the proposed approach for analyzing the impact of PEVs on the grid operation cost and hourly wind energy dispatch.

Table 1. Optimization of V2G services for minimizing operational cost.

Reference	Objective function	Optimi-zation technique	Findings
[30]	$\min_{u_1,u_2} \sum_{T}^{t=1} \{C_{\text{energy}}(u_1) + C_{\text{reserve},s}(R_s) + C_{\text{reserve},d}(R_d)\}$ u_1 is the electricity generation; u_2 is the scheduling of wind power; C_{energy} is the cost of electricity generation; $C_{\text{reserve},s}$ is the reserve scheduling; $C_{\text{reserve},d}$ is the expected reserve dispatch; R_s is the scheduling of conventional reserve (MW); R_d is the expected dispatch of conventional reserve (MW).	Classical (DP)	Demonstrated the value of fully exploring the synergy between PEV and wind power using a three-level controller; with the top-level minimizing generation costs, mid-level allotting charging time and power based on battery SOC, and bottom-level using real-time feedback to attempt grid frequency synchronization.
[31]	$\min_{P_{G_i}^{(t)}, P_{L_j}^{(t)}, E_{VB_j}^{(0)}, \Delta E} \sum_{t=i}^{T} \sum_{i} n_{G_i} \cdot P_{G_i}^{(t)}$ P_{G_i} is the power produced by generator G_i; n_{G_i} is the marginal cost of generator G_i; P_{L_j} is the power consumed by load L_j; E_{VB_j} is the energy content of the virtual battery; ΔE is the shift in the energy content of the aggregation of virtual batteries.	Hybrid (Classical and scenario method)	Compared to a pure cost-optimizing strategy, part of the charging has to be moved from the night to more expensive hours to reduce the SOC swing. This leaves enough flexibility to compensate the forecast error.
[32]	$\min E \mid C_{total} \mid$ $C_{\text{total}} = \sum_{i=1}^{N_c} C_i(P_{s,i}) + \sum_{i=1}^{N_w} C_{w,i}(W_{s,i}) + \sum_{i=1}^{N_w} C_{w,u,i}(W_{s,i}, W_i) + \sum_{i=1}^{N_w} C_{w,o,i}(W_{s,i}, W_i) + \sum_{i=1}^{N_e} C_{e,i}(P_{e,s,i}) + \sum_{i=1}^{N_e} C_{e,u,i}(P_{e,i}, P_{e,s,i}) + \sum_{i=1}^{N_e} C_{e,o,i}(P_{e,i}, P_{e,s,i})$	Hybrid (Interior point based PSO)	By studying the statistical properties of charging and discharging EVs along with formulating a power system economic dispatch model, which takes into account impacts of EVs and wind

Reference	Objective function	Optimization technique	Findings
	N_c is the number of conventional generators; N_w is the number of wind generators; N_e is the number of buses with V2G facilities installed; C_i is the conventional generator cost; $P_{s,i}$ is the scheduled output of the conventional generator i; $C_{w,i}$ is the wind generator cost; W_i is the available wind power; $W_{s,i}$ is the scheduled output of the wind generator i; $C_{w,u,i}$ is the underestimating penalty cost coefficient; $C_{w,o,i}$ is the overestimating penalty cost coefficient; $P_{e,}i$ is the available V2G power at bus i; $P_{e,s,i}$is the scheduled V2G power at bus i.		generators, a novel algorithm is proposed to solve nonlinear and nonconvex optimization problems.
[33]	$\min_{u_1,u_2} \sum_t \left\{ C_{\text{conv}}.\left(u_1 + r'\right) + CA.S.(r) \right\}$ *Cconv* is the cost of conventional generators; $C_{A.S.}$ is the cost of ancillary services; u_1, u_2 are the control variables representing the scheduling of conventional generators and ancillary services; r is the scheduling of ancillary services; r' is the expected dispatch of ancillary services.	Classical (DP)	The proposed integration is an implementable algorithm to realize the synergy of PEV charging and wind energy. It can also be made to reflect other inherently stochastic RESs.
[34]	$\min\left(\sum_{i \in NG} \alpha_i \Delta P_{gi} + \sum_{i \in ND} \beta_i \Delta P_{di} \right)$ i^{th} is the index bus bar; α_i is the coefficient of generation curtailment; β_i is the coefficient of load shedding; ΔP_{di} is the load shedding; ΔP_{gi} is generation curtailment; *NG*, *ND* are the sets of generation and load demand.		It is found that active network management (ANM) strategies achieved through intelligent EV charging can further reduce generation curtailment; allowing for more absorption of renewable energy.

Table 2. Optimization of V2G services for minimizing generation cost.

4.2.1.2. Generation cost optimization

Generation cost optimization is crucial to both power distributors, charging station operators, and the EV owners. Interactions between EVs and RESs through the smart grid are at the center of intensive research. Maximizing the profit for distributors, minimizing cost of operation/ generation, and the cost of ownership and charging of EV is crucial with the proliferation of

green energy [3]. **Table 2** summarizes the related research works, their objective functions, techniques in use for optimization, and their main findings.

4.2.1.3. Profit/benefit optimization

By maximizing the profit for generators/providers, or the benefits for providing energy, the effects are felt by the supply chain through aggregators, charging stations, etc. down to the EV owners. Optimization is referenced from the viewpoint of increasing investments in RESs or electricity delivery management. **Table 3** summarizes the related research works, their objective functions, techniques in use for optimization, and their main findings.

4.2.1.4. Charging cost optimization

Minimizing costs is crucial to both distributors and EV owners. Ensuring that the costs stay low on the distribution side ensures that costs stay low on the consumer side. Maximizing the synergy between stochastic RES generation and EV charging loads is the key to minimizing the costs surrounding EVs [3]. **Table 4** summarizes the related research works, their objective functions, techniques in use for optimization, and their main findings.

Reference	Objective function	Optimi-zation technique	Findings
[35]	$\max_{x,b,d,y,g} P(x,\ d)=\sum_{n=0}^{N-1} p^{e}(n)[x(n)+d(n)]$ x is the energy supplied directly to the grid; b is the energy transferred to the batteries; d is the energy transferred from the batteries; y is the needed storage capacity; g is the energy transferred to the batteries as payment; $P()$ is the revenues raised by the virtual power plant (VPP) from the electricity sold at market; $p^{e}(n)$ is the wholesale price of electricity.	Classical (Iterative LP)	VPP formed with EVs can maximize profits by optimizing the schedule of supply to the grid based on the wind energy production and the available storage.
[36]	$\min_{u} -\left\{\sum_{h} p^{h}\sum_{i} x_{i}^{h}-\sum_{h} c^{h}\cdot y^{h} -E_{\xi}\sum_{h}\left\{r^{h}(\xi)\cdot z^{h*}(\xi)-q^{h}\cdot v^{h*}(\xi)\right\}\right\}$ x_{i}^{h} is the allocation of energy to EV i for hour h; y^{h} is the amount of purchased bulk energy for hour h; p^{h} is the price per energy unit at which energy is charged to the EVs during hour h by the aggregator; c^{h} is the price of bulk	Classical (SP)	A stochastic-based framework is proposed for smart grid operators to determine optimal charging control of EVs and energy purchasing to

Reference	Objective function	Optimi-zation technique	Findings
	energy for hour h; $r^h(\xi)$ is the price of energy in the real-time market; q^h is the price at which excess energy is purchased back; z^h is the real-time energy purchased back by the aggregator; v^h is the excess energy sold back.		maximize performance.
[37]	$\min_{I \in \mathrm{I}} \frac{S_{\text{online}}(I)}{S^*_{\text{offline}}(I)} \geq \alpha$ I is the input set fixed for all input instances I with finite sizes; $S_{\text{online}}(I)$ is the total profit obtained by the online scheduler; $S^*_{\text{offline}}(I)$ is the optimal offline scheduler.	Classical (Threshold admission and greedy scheduling (TAGS))	It is shown that, when the price offered to the EV customers is higher than the purchasing price of electricity from the grid, TAGS achieves the competitive ratio of 1.
[38]	$\max_{POP_i(t),MxAP_i(t),MnAP_i(t)} In - C$ $In = \alpha \sum_t \left(P_{\text{regUp}}(t) R_{\text{Up}}(t) + P_{\text{regDown}}(t) R_{\text{Down}}(t)\right)$ $+ Mk \sum_i \sum_t \left(E\left(PD_i(t)\right)\right)$ $In - C$ is the aggregator income minus costs; Mk is the aggregator markup over wholesale energy price; α is the percentage of regulation revenue taken by the aggregator; R_{Up} is the bid regulation up capacity of the aggregator; R_{Down} is the bid regulation down capacity of the aggregator; PD_i is the power draw of the battery of the ith EV.	Classical (CP)	Simulations of hourly, daily, and yearly show that the optimal algorithms increase aggregator profits, lower load demand, and reduce costs to customers.
[17]	$\max \text{V2G Income} = \sum_{t=1}^{T} \left[\left(\sum_{V=1}^{N_V} \left(P_{\text{Discharge}(V,t)}\right) \right) \times C_{\text{Discharge}(V,t)} - P_{\text{Charge}(V,t)} \times C_{\text{Charge}(V,t)} \right) \times \Delta t \right]$ N_V is the total number of vehicles V; $P_{\text{Discharge}(V,t)}$ is the power discharge of vehicle V in period t; $c_{\text{Discharge}(V,t)}$ is the discharge price of vehicle V in period t; $P_{\text{Discharge}(V,t)}$ is the power charge of vehicle V in period t; $c_{\text{Discharge}(V,t)}$ is the charge price of vehicle V in period t.	Metaheur-istic (parallel PSO)	The parallelization approach presented provides promising results to model EV loads on distribution networks for future incorporation of smart grid technologies

Table 3. Optimization of V2G services for maximizing profits/benefits.

Reference	Objective function	Optimization technique	Findings
[39]	$\min_{u_{i,t}} \sum_{t=1}^{N_t} \left(C_t^N + \alpha_t\right) Q_{EV,t} + \beta Q_{EV,t}^2$ $u_{i,t}$ is the optimization variable representing the charging rate of vehicle i out of a total number of vehicles at time t; C_t^N is the time-dependent network tariff; α_t is the baseline electricity price at time t; $Q_{EV,t}$ is the extra demand of the EVs; $\beta Q_{EV,t}^2$ is the EV-dependent part.	Classical (Rolling horizon optimization scheme)	An analysis of EV-caused distribution network congestion management is presented and a mathematical model of optimization is proposed.
[40]	$\min_{x_g(t)} V\gamma(t)y(t) - \sum_{g=1}^{G}\left[Q_g(t)\left(1+\frac{\eta}{R_g}\right) + Z_g(t)\right]x_g(t)$ $x_g(t)$ is the control variable; V is a parameter that is used to tune the tradeoff between cost and queue backlog growth; $\gamma(t)$ is the electricity price at time t; $y(t)$ is an auxiliary variable; $Q_g(t)$ the total charging tasks in timeslot t of g queues; $Z_g(t)$ is the virtual queue; R_g is the max charging time; η is a constant to adjust the growth rate of the virtual queue.	Classical (Lyapunov optimization)	A stochastic optimization problem is formulated to describe the queuing problem for EV charging requests and minimize the time average cost of using other energy sources when renewable sources are unable to meet demand.
[41]	$\min(EC) = \min\left(\sum_{t=t_a}^{t_b} P_t \times SP_t\right)$ EC is the energy costs of the PEV; P_t is the charge/discharge power at hour t; SP_t is the spot hour price at hour t; t_a is the starting hour of charge/discharge for the PEV; t_b is the ending hour of charge/discharge for the PEV.	Classical (Sequential quadratic programming)	The optimization method presented has shown that PEV charging/discharging during optimal spot market times minimize energy costs on low wind-generated power days.
[42]	$\min \sum_{t=1}^{T} \alpha q_t + \beta q_t^2$ q_t are the total purchases and sales of the aggregator; α, β are variables linearly relating price to load.	Classical (Quadratic programming)	This paper offers to aggregators a framework of optimizing charging and discharging of EV fleets given driving patterns and spot market prices.

Table 4. Optimization of V2G services for minimizing EVs' charging cost.

4.2.1.5. Other cost-related optimization

Other cost-related optimizations include minimizing overall costs related to system lifetime, transmission, materials and resources, upgrades, losses, and renewable imbalances [3]. **Table 5** summarizes the related research works, their objective functions, techniques in use for optimization, and their main findings.

4.2.2. Efficiency optimization

The efficient utilization of renewables can reduce the use of fossil energy quite substantially. This can elicit several benefits including air pollution reduction and cost savings for consumers. The efficiency-related optimization objectives in regards to EVs interactions with RESs are maximizing RES utilization, optimizing energy dispatch, optimizing energy management, minimizing power loss, and minimizing energy loss. Sections 4.2.2.1 and 4.2.2.2 provide details regarding the efficiency-related optimization works for EVs interacting with RESs.

Reference	Objective function	Optimization technique	Findings
[43]	$\min_{\Omega}([f_1(\Omega)f_2(\Omega)])$ $f_1(\Omega)=NPV_{\text{uprgrades}}+NPV_{\text{losses}}$ $f_2(\Omega)=E_{\text{grid}}+E_{\text{DG}}-E_{\text{PEV}}$ *NPV*uprgrades is the net present value (NPV) of the costs of upgrades; *NPV*lossses is the NPV of the costs of losses; E_{grid} are the emissions due to energy purchased from the grid; E_{DG} are the emissions of distributed generation (DG) units; E_{PEV} are the emission reductions of the PEV.	Metah-euristic (Nondo-minated sorting genetic algorithm (NDSGA))	A planning method is presented that can accommodate a high penetration of PEV and renewable DG into preexisting distribution networks.
[44]	$\min C=C_{\text{DG}}+C_{\text{S}}+C_{\text{G}}+C_{\text{M}}$ C is the lifecycle cost of the system; C_{DG} and C_{S} are the initial capital costs for the renewable DG and the storage unit; C_{G} is the cost associate with getting energy from the grid; C_{M} is the maintenance cost of the system.	Classical (MILP)	A methodology is presented to design grid-interfaced PEV charging stations that integrate RE generation and distribution networks
[45]	$\min\sum_{t=1}^{24}aP_{\text{Conv}}^2(t)+bP_{\text{Conv}}(t)+c$	Metahe-uristic (GA)	This paper generates a smart energy management system

Reference	Objective function	Optimi-zation technique	Findings
	a, b, c are cost coefficients; $P_{\mathrm{Conv}}(t)$ is the generation of the conventional generator at time *t*.		(EMS) that allows distributors a more economical means of incorporating wind resources and EV storage solutions into existing generation resources.
[46]	$\min \{C_{\mathrm{Pen.}} + C_{\mathrm{V2G}} - R_{\mathrm{V2G}}\}$ $C_{\mathrm{Pen.}}$ is the penalty cost for wind power imbalances; C_{V2G} is the cost for V2G services; R_{V2G} is the revenue for V2G services.	Hybrid (GA-based Monte Carlo simulation (MCS))	The proposed optimization provides collaboration between wind participants and EV aggregators to minimize the sum of the penalty cost associated with wind power imbalances and V2G expenses associated with purchased energy, battery degradation and capital costs as well as increasing the EVs' revenues and incentives.
[47]	$\min \sum_{k=1}^{K} C_{\mathrm{Pen}.}(t_k)$ C_{pen} is the penalty cost for PV power imbalances; *K* is the number of time steps.	Hybrid (PSO-based Monte Carlo simulation (MCS))	This paper proposes a coordinated charging/discharging scheme to optimally utilize V2G capacities of EVs to minimize the penalty cost for PV power under-/overproduction.

Table 5. Optimization of V2G services for minimizing costs.

http://dx.doi.org/10.5772/64433

4.2.2.1. RES utilization maximization

The excessive power generated by RESs can be stored in batteries of the EV fleets and DC-link capacitors in specialized charging stations to supply the necessary power through V2G infrastructure when the renewable energy generation is insufficient to meet load demands. An optimization strategy is required to coordinate the EVs' charging/discharging with RESs uncertainties to maximize the use of renewable generation. **Table 6** summarizes the related research works, their objective functions, techniques in use for optimization, and their main findings.

Reference	Objective function	Optimization technique	Findings
[48]	$\max_{\varphi_t} \rightarrow \overline{\mathrm{RES}} = \sum_{t=1}^{T} res_t \cdot \varphi$ res_t is the share of RES of total load in time step t (%); φ_t is the charge parameter for time step t.	Classical (LP)	Through the optimization objective of maximizing amount of charging power coming from RES through the smart grid during optimal times, the authors were able to see that RES made up 83% of the EVs' charging demand.
[49]	$\min_{\varphi,\, ramp_t ramp,\, isOn} f = \sum_{t \in 1..T} CG_t$ CG_t is the conventional generation in time slot $[t-1, t]$; $ramp_t$ is the occurrence of ramping for time slot $[t-1, t]$; φ is the maximum charge amount in one time slot; $isOn_t$ is the binary state variable for conventional generation.	Classical (MIP)	The findings presented suggest that through an optimal charging algorithm controlling the scheduling of EV fleet charging, the usage of renewables can double; with wind alone supplying 67.2%.

Reference	Objective function	Optimi-zation technique	Findings
[50]	$C_{\text{tot}}(t)=\min\left(\sum_{n=1}^{NTU}\left(C_{\text{start},n}+(PC_n(P_{TUn})_{NTU}\right.\right.$ $\left.\left.+C_{ems,n}(P_{TUn}).t_{\text{int}}\right)\right)$ is the number of thermal units; $C_{\text{tot}}(t)$ is the total production cost; $C_{\text{start},n}$ is the startup cost of unit n; PC_n is the production cost of unit n; $C_{ems,n}$ is the CO_2 emission cost of unit n; P_{TUn} is the output power of unit n; t_{int} is the time period share in an hour.	Classical (MIP)	This paper suggests a strategy to fully supply the EVs' charging load by RESs within a microgrid composing of a photovoltaic plant, a thermal unit, battery energy storage systems, and electric vehicle charging stations.
[51]	$J\tilde{u}^*(x_0)=\max_{\tilde{u}\in U} J\tilde{u}(x_0)$ $J\tilde{u}(x_0)=\lim_{T\to\infty}\frac{1}{T}E\left\{\int_0^T r(x(t),\, a(t))\mathrm{d}t\right\}$ $\tilde{u}^*$ is the optimal charging policy; $r(x(t),\, a(t))$ is the reward for the action $a(t)$ taken in a state $x(t)$.	Classical (LP)	The authors developed an optimal charging policy strategy to maximize renewable energy utilization within preexisting distribution infrastructure despite stochastic generation potential.
[52]	$\min_{x_t^k}\left\{\sum_{t=1}^{T} C_t\left(\sum_{k=1}^{K} x_t^k\right)+\sum_{k=1}^{K}\sum_{t=1}^{T} D_t^k(x_t^k)\right\}$ $C_t(.)$ is the imbalance cost; $D_t^k(.)$ is the disutility of the subscribers that aid in balancing; x_t^k is the energy demand of subscriber k during time slot t.	Classical (Convex optimi-zation–quadratic) progr-amming	The authors proposed an optimal distributed algorithm to balance the synergy of smartgrid interactions between RES supply and EV charging demand.

Reference	Objective function	Optimization technique	Findings
[53]	$\text{Min}\left\{J=\sum_{h=1}^{H}\sum_{p=1}^{h-1}\left((x_{h,p}-b_{h,p})\cdot\left(K_\rho\rho_P-\sum_{r=1}^{NG}K_rP_{r,p}\right)\right)\right\}$ J is the objective function; $x_{h,p}$ is the purchased and charged energy at hour p; $b_{h,p}$ is the available energy in the batteries of EDVs that is used in hour h; H is the number of hours in the assessed time period; $P_{r,p}$ is the production of RES r in hour p among NG RESs; ρ_P is the purchase energy price in the market in hour p; K_ρ and K_r are the optimization parameters that regulate the objective function J.	Classical (LP)	Higher transportation costs for EDV users present a tradeoff for a cleaner environment through reduced emissions as a result of more intensive RES exploitation in transportation.

Table 6. Optimization of V2G services for maximizing RES utilization.

4.2.2.2. Other efficiency-related optimization

Other efficiency-related optimizations include minimizing imported electricity [54], minimizing power loss [55], minimizing loss energy, and optimizing energy management [56], etc. Table 7 below summarizes the related research works, their objective functions, techniques in use for optimization, and their main findings.

Reference	Objective function	Optimization technique	Findings
[54]	$\min\left(\theta^T-\rho(h)\cdot\sum_{h=1}^{H}E(h)\right)$ $\rho(h)$ is the unit price of the electricity consumption; $E(h)$ is the electricity in (kwh) generated from renewable energy sources in time slot (hour) h; θ^T is the total daily electricity cost.	Classical (MILP)	The results of the simulations conducted in this paper show that intelligent, optimized scheduling of EV fleets drastically increases

Reference	Objective function	Optimi-zation technique	Findings
			overall distribution performance, reducing charging times and related costs.
[55]	$F = \min[(f_1 + f_2) + \sum_{i \in N_{DG}} (\max(V_i - V_i^{\max}, 0) + \max(V_i^{\min} - V_i, 0)) + \sum_{i \in N} \max + (\lvert S_i \rvert - \lvert S_i^{\max} \rvert, 0)]$ f_1 is the power losses of N-bus distribution system; f_2 is the error between rated voltage (1 p.u) and voltage of each bus; V is the voltage; N_{DG} is the total number of system suppliers.	Metahe-uristic (GA)	The focus of this paper is on improving the "smart parking lot," with a primary goal of efficiently reducing power losses through improving voltage profiles and optimized scheduling of EV fleet charging during peak and nonpeak hours.
[56]	$\text{Min } C = \sum_{Sc_{\text{wind}}}^{H} \pi(Sc_{\text{wind}}) \sum_{t=0}^{N-1} \left[\sum_{i=1}^{I} C_{DGU_{i,t}} \cdot (P_{DGU_{i,t,Sc_{wind}}}) + C_{\text{grid},t} \cdot (P_{\text{grid},t}) + \sum_{j=1}^{J} C_{GAR_{j,t}} \cdot (P_{GAR_{j,t,Sc_{\text{wind}}}}) \right]$ $\pi(Sc_{\text{wind}})$ is the probability/weight of wind scenario Sc_{wind}; Sc_{wind} is the index of wind power scenarios running from 1 to H; $C_{DGU_{i,t}}$ is the price of energy obtained from dispatch-able generating unit i at time t; $P_{DGU_{i,t,Sc_{\text{wind}}}}$ is the power output from dispatch able generating unit i at time t and under wind power scenario Sc_{wind}; $C_{\text{grid},t}$ is the price of energy obtained from the main grid at time t; $P_{\text{grid},t}$ is the power input/output for the main grid at time t; $C_{GAR_{j,t}}$ is the price of energy obtained from garage j at time t; $P_{GAR_{j,t,Sc_{\text{wind}}}}$ is the power input/output for garage j at time t and under wind power scenario Sc_{wind}	Classical (LP)	The practical model provided in this paper assesses the ability of V2G systems to provide power support to conventional grid operations, including small electric energy systems (SEESs).

Table 7. Optimization of V2G services for improving efficiency.

4.2.3. Emission optimization

Emission reduction is one of the most important objectives of EVs' adoption for transportation. This objective can be further satisfied through interactions between EVs and RESs. V2G implementation plays a key role in this scenario to decrease the power utility costs and protect the environment. Related research works include references [27] and [28] of **Table 1**, reference [43] of **Table 5**, and reference [57] whose objective function, optimization technique, and its main finding is provided in **Table 8**.

Reference	Objective function	Optimization technique	Findings
[57]	Minimize $J = \sum_{0}^{24} \left(\frac{CO_2}{gal} * m_f * \Delta t_{dr} + \frac{CO_2}{kWh} * P_b * \Delta t_{ch} \right)$ J is the optimization objective; m_f is the gasoline consumption; P_b is the battery charging power; Δt_{ch} is the charging time step Δt_{dr} is the driving time step.	Classical (DP)	The proposed integrated approach shows, through successful simulations, that with more wind-based power generation and integration into existing distribution infrastructure comes a reduction in carbon dioxide emissions.

Table 8. Optimization of V2G services for reducing emission.

Author details

Mahmoud Ghofrani[1*], Eric Detert[1], Negar Niromand Hosseini[1], Amirsaman Arabali[2], Nicholas Myers[1] and Phasith Ngin[1]

*Address all correspondence to: mrani@uw.edu

1 Electrical Engineering, Engineering and Mathematics Division, School of STEM, University of Washington Bothell, Bothell, Washington, USA

2 LCG Consulting, Los Altos, California, USA

References

[1] Mwasilu F., Justo J.J., Kim E., Do T.D., Jung J.W. Electrical vehicle and smart grid interaction: A review on vehicle to grid and renewable energy source integration. Renewable and Sustainable Energy. 2014; 34:501–516.

[2] Yong J.Y., Ramachandaramurthy V.K., Tan K.M., Mithulananthan N. A review on the state-of-the-art technologies of the electrical vehicle, its impacts and prospects. Renewable and Sustainable Energy Reviews. 2015; 49:365–385.

[3] Liu L., Kong F., Lui X., Peng Y., Qinglong W. A review on electric vehicles interacting with renewable energy in smart grid. Renewable and Sustainable Energy Reviews. 2015; 51:648–661.

[4] Wikipedia. Nissan Leaf [Internet]. [Updated: 4/15/2016]. Available from: https://en.wikipedia.org/wiki/Nissan_Leaf [Accessed: 4/17/2016]

[5] Wikipedia. Toyota Prius [Internet]. [Updated: 4/14/2016]. Available from: https://en.wikipedia.org/wiki/Toyota_Prius [Accessed: 4/17/2016]

[6] Tan K.M., Ramachandaramurth V.K., Yong J.Y. Integration of electrical vehicle in smart grid: A review on vehicle to grid technologies and optimization techniques. Renewable and Sustainable Energy Reviews. 2016; 53:720–732.

[7] Kempton W., Letendre S. Electric vehicles as a new power source for electric utilities. Transportation Research Part D- Transportation and Environment. 1997; 2(3):157–175.

[8] Canada NewsWire. Global Smart Grid Federation Publishes Report on Learning Smart Grid Project Around the World. 2012.

[9] Amoroso F., Cappuccino G. Advantages of efficiency-aware smart charging strategies for PEVs. Energy Conversation & Management. 2012; 54(1):1–6.

[10] Li H., Lai L., Qiu R.C. Scheduling of wireless metering for power market pricing in smart grid. IEEE Transactions on Smart Grid. 2012; 3(4):1611–1620.

[11] Kim T., Chang A.C.C., Li M., Rong C., Patrikakis C.Z., Sleza D. Communication and networking. In: International Conference, FGCN 2010, Held as Part of the Future Generation Information Technology Conference, FGIT 2010; December 13–15, 2010; Jeju Island, Korea. Berlin: Springer; 2010. pp. 199–206.

[12] Monterio V., Pinto J.G., Exposto B., Goncalves H., Ferreira J.C., Couto C., et al. Assessment of a battery charger for electric vehicles with reactive power control. In: Proceedings of the IEEE IECON 2012: 38th Annual Conference on Industrial Electronics Society; October 25–28, 2012. pp. 5142–5147.

[13] Han S., Han S., Sezaki K. Development of an optimal vehicle-to-grid aggregator for frequency regulation. IEEE Transactions on Smart Grid. 2010; 1(1):65–72.

[14] Mullan J., Harries D., Bräunl T., Whitely S. The technical economic and commercial viability of the vehicle-to-grid concept. Energy Policy. 2012; 48:394–406.

[15] Sortomme E., El-Sharkawi M.A. Optimal scheduling of vehicle-to-grid energy and ancillary services. IEEE Transactions on Smart Grid. 2012; 3(1):351–359.

[16] Ghanbarzadeh T., Goleijani S., Moghaddam M.P. Reliability constrained unit commitment with electric vehicle to grid using hybrid particle swarm optimization and ant colony optimization. In: Proceedings of the IEEE power and energy society general meeting; July 24–29, 2011. pp. 1–7.

[17] Soares J., Vale Z., Canizes B., Morais H. Multi-objective parallel particle swarm optimization for day-ahead vehicle-to-grid scheduling. In: Proceedings of the IEEE CIASG 2013: Symposium on Computational Intelligence Applications in Smart Grid; April 16–19, 2013. pp. 138–145.

[18] Díaz-González F., Sumper A., Gomis-Bellmunt O., Villafáfila R. A review of energy storage technologies for wind power applications. Renewable and Sustainable Energy Reviews. 2012; 16(4):2154–2171.

[19] Leemput N., Geth F., Claessens B., Van Roy J., Ponnette R., Driesen J. A case study of coordinated electric vehicle charging for peak shaving on a low voltage grid. IEEE Innovative Smart Grid Technologies (ISGT Europe); 2012.

[20] Kesler M., Kisacikoglu M.C., Tolbert L.M. Vehicle-to-grid reactive power operation using plug-in electric vehicle bidirectional off-board charger. IEEE Transactions on Industrial Electronics. 2014; 61(12):6778–6784.

[21] Yong J.Y., Ramachandaramurthy V.K., Tan K.M., Mithulananthan N. Bi-directional electric vehicle fast charging station with novel reactive power compensation for voltage regulation. International Journal of Electrical Power & Energy Systems. 2015; 64:300–310.

[22] Zhang M., Chen J. The energy management and optimized operation of electric vehicles based on microgrid. IEEE Transactions on Power Delivery. 2014; 29:1427–1435.

[23] Chen C., Duan S. Optimal integration of plug-in hybrid electric vehicles in microgrids. IEEE Transactions on Industrial Informatics. 2014; 10:1917–1926.

[24] Tan Z., Yang P., Nehorai A. An optimal and distributed demand response strategy with electric vehicles in the smart grid. IEEE Transactions on Smart Grid. 2014; 5:861–869.

[25] Aunedi M., Strbac G. Efficient system integration of wind generation through smart charging of electric vehicles. In: Proceedings of 8th International Conference and Exhibition on Ecological Vehicles and Renewable Energies (EVER); 2013. pp. 1–12.

[26] Derakhshandeh S., Masoum A.S., Deilami S., Masoum M.A., Hamedani Golshan M. Coordination of generation scheduling with PEVs charging in industrial microgrids. IEEE Transactions on Power Systems. 2013; 28:3451–3461.

[27] Saber A.Y., Venayagamoorthy G.K. Resource scheduling under uncertainty in a smart grid with renewables and plug-in vehicles. IEEE Systems Journal. 2012; 6:103–109.

[28] Saber A.Y., Venayagamoorthy G.K. Plug-in vehicles and renewable energy sources for cost and emission reductions. IEEE Transactions on Industrial Electronics. 2011; 58:1229–1238.

[29] Khodayar M.E., Wu L., Shahidehpour M. Hourly coordination of electric vehicle operation and volatile wind power generation in SCUC. IEEE Transactions on Smart Grid. 2012; 3:1271–1279.

[30] Li C.T., Ahn C., Peng H., Sun J. Synergistic control of plug-in vehicle charging and wind power scheduling. IEEE Transactions on Power Systems. 2013; 28:1113–1121.

[31] Vayá M.G., Andersson G. Integrating renewable energy forecast uncertainty in smart-charging approaches for plug-in electric vehicles. In: IEEE Grenoble PowerTech (POWERTECH); 2013. pp. 1–6.

[32] Zhao J., Wen F., Dong Z.Y., Xue Y., Wong K.P. Optimal dispatch of electric vehicles and wind power using enhanced particle swarm optimization. IEEE Transactions on Industrial Informatics. 2012; 8:889–899.

[33] Li C.T., Ahn C., Peng H., Sun J. Integration of plug-in electric vehicle charging and wind energy scheduling on electricity grid. In: IEEE Innovative Smart Grid Technologies (ISGT); 2011. pp. 1–7.

[34] Zhou L., Li F., Gu C., Hu Z., le Blond S. Cost/benefit assessment of a smart distribution system with intelligent electric vehicle charging. IEEE Trans. Smart Grid. 2014; 5:839–847.

[35] Vasirani M., Kota R., Cavalcante R.L., Ossowski S., Jennings N.R. An agent-based approach to virtual power plants of wind power generators and electric vehicles. IEEE Transactions on Smart Grid. 2013; 4:1314–1322.

[36] Goonewardena M., Le L.B. Charging of electric vehicles utilizing random wind: A stochastic optimization approach. In: IEEE Globecom Workshops (GC Wkshps); 2012. pp. 1520–1525.

[37] Chen S., Tong L. IEMS for large scale charging of electric vehicles: architecture and optimal online scheduling. In: Proceedings of IEEE 3rd International Conference on Smart Grid Communications (SmartGridComm); 2012. pp. 629–634.

[38] Sortomme E., El-Sharkawi M.A. Optimal charging strategies for unidirectional vehicle-to-grid. IEEE Transactions on Smart Grid. 2011; 2(1):131–138.

[39] Verzijlbergh R.A., de Vries L.J., Lukszo Z. Renewable energy sources and responsive demand. Do we need congestion management in the distribution grid? IEEE Transactions on Power Systems. 2014; 29 (5):2119–2128.

Edited by Mohamed Amine Fakhfakh

The book presents interesting topics from the area of modeling and simulation of electric vehicles application. The results presented by the authors of the book chapters are very interesting and inspiring. The book will familiarize the readers with the solutions and enable the readers to enlarge them by their own research. It will be useful for students of Electrical Engineering; it helps them solve practical problems.

ISBN 978-953-51-6678-8

Photo by Maxvis / iStock

IntechOpen